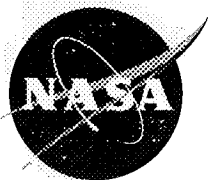


GSFC/CR-1998-206852



Vrije Universiteit

Linkages Between Global Vegetation and Climate

An Analysis Based on NOAA Advanced Very High Resolution Radiometer Data

Academisch Proefschrift

Sietse Oene Los

Contract NAS-31752

National Aeronautics and
Space Administration

Goddard Space Flight Center
Greenbelt, Maryland 20771

April 1998

VRIJE UNIVERSITEIT

Linkages between global vegetation and climate

An analysis based on

NOAA Advanced Very High Resolution Radiometer data

ACADEMISCH PROEFSCHRIFT

ter verkrijging van de graad van doctor aan
de Vrije Universiteit te Amsterdam,
op gezag van de rector magnificus
prof.dr. T. Sminia,
in het openbaar te verdedigen
ten overstaan van de promotiecommissie
van de faculteit der aardwetenschappen
op donderdag 4 juni 1998 om 15.45 uur
in het hoofgebouw van de universiteit,
De Boelelaan 1105

door

Sietse Oene Los

geboren te Groningen

Promotor : prof.dr. J.J. de Vries
Copromotor : dr. A.A. van de Griend



National
Aeronautics and
Space
Administration

NASA Scientific and Technical Document Availability Authorization (DAA)

The DAA approval process applies to all forms of published NASA Scientific and Technical Information (STI), whether disseminated in print or electronically. It is to be initiated by the responsible NASA Project Officer, Technical Monitor, author, or other appropriate NASA official for all presentations, reports, papers, and proceedings that contain NASA STI. Explanations are on the back of this form and are presented in greater detail in NPG 2200.2, "Guidelines for Documentation, Approval, and Dissemination of NASA Scientific and Technical Information."

☐ Original
☐ Modified

I. DOCUMENT/PROJECT IDENTIFICATION

TITLE

Linkages Between Global Vegetation and
Climate: An Analysis Based on NOAA
Advanced Very High Resolution Radiometer
Data

AUTHOR(S)

Sietse Los

ORIGINATING NASA ORGANIZATION

NASA's GSFC/Code 923

PERFORMING ORGANIZATION (If different)

CONTRACT/GRANT/INTERAGENCY/PROJECT NUMBER(S)

NAS5-31752

DOCUMENT NUMBER(S)

DOCUMENT DATE

1/5/98

For presentations, documents, or other STI to be externally published (including through electronic media), enter appropriate information on the intended publication such as name, place, and date of conference, periodical, or journal name, or book title and publisher in the next box. These documents must be routed to the NASA Headquarters or Center Export Control Administrator for approval (see Sections III and VIII).



II. SECURITY CLASSIFICATION

CHECK ONE (One of the five boxes denoting Security Classification must be checked.)

☐ SECRET ☐ SECRET RD ☐ CONFIDENTIAL ☐ CONFIDENTIAL RD ☒ UNCLASSIFIED

III. AVAILABILITY CATEGORY

☐ ITAR ☐ EAR

Export Controlled Document - USML Category

/CCL Export Control

Classification Number (ECCN)

(Documents marked in this block must have the
concurrence/approval of the NASA Headquarters or Center Export Control Administrator (see Section VIII).)

Confidential Commercial Document (check appropriate box at left and indicate below the appropriate limitation and expiration):

☐ TRADE SECRET
☐ SBIR
☐ COPYRIGHTED

☐ U.S. Government agencies and U.S. Government agency contractors only
☐ NASA contractors and U.S. Government only
☐ U.S. Government agencies only
☐ NASA personnel and NASA contractors only
☐ NASA personnel only
☐ Available only with the approval of issuing office:
☐ Limited until (date)

☒ PUBLICLY
AVAILABLE

Publicly available documents must be unclassified, may not be export controlled, may not contain trade secret or confidential commercial data, and should have cleared any applicable patents application process.

IV. DOCUMENT DISCLOSING AN INVENTION

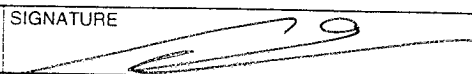
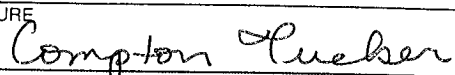
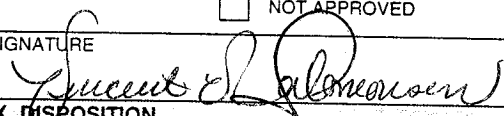
THIS DOCUMENT MAY BE RELEASED ON
(date)

NASA HQ OR CENTER PATENT OR INTELLECTUAL PROPERTY COUNSEL SIGNATURE

DATE

V. BLANKET RELEASE (OPTIONAL)

- ☐ All documents issued under the following contract/grant/project number may be processed as checked in Sections II and III.
- ☐ The blanket release authorization granted on (date)
- ☐ is RESCINDED - Future documents must have individual availability authorizations.
- ☐ is MODIFIED - Limitations for all documents processed in the STI system under the blanket release should be changed to conform to blocks as checked in Sections II and III.

VI. AUTHOR/ORIGINATOR VERIFICATION			
I HAVE DETERMINED THAT THIS PUBLICATION:			
<input type="checkbox"/> DOES contain export controlled, confidential commercial information, and/or discloses an invention for which a patent has been applied, and the appropriate limitation is checked in Sections III and/or IV.			
<input type="checkbox"/> does NOT contain export controlled, confidential commercial information, nor does it disclose an invention for which a patent has been applied, and may be released as indicated above.			
NAME OF AUTHOR/ORIGINATOR	MAIL CODE	SIGNATURE	DATE
Sietse Los	923		
VII. PROJECT OFFICER/TECHNICAL MONITOR/DIVISION CHIEF REVIEW			
<input type="checkbox"/> APPROVED FOR DISTRIBUTION AS MARKED ON REVERSE <input type="checkbox"/> NOT APPROVED			
NAME OF PROJECT OFFICER OR TECH. MONITOR	MAIL CODE	SIGNATURE	DATE
Compton Tucker	923		2/19/98
VIII. EXPORT CONTROL REVIEW/CONFIRMATION			
<input type="checkbox"/> Public release is approved <input type="checkbox"/> Export controlled limitation is not applicable			
<input type="checkbox"/> Export controlled limitation is approved <input type="checkbox"/> Export controlled limitation (ITAR/EAR) marked in Section III is assigned to this document:			
USML CATEGORY NUMBER	CCL ECCN NUMBER	HQ OR CENTER EXPORT CONTROL ADMINISTRATOR (as applicable)	DATE
IX. PROGRAM OFFICE OR DELEGATED AUTHORITY REVIEW			
<input checked="" type="checkbox"/> APPROVED FOR DISTRIBUTION AS MARKED ON REVERSE <input type="checkbox"/> NOT APPROVED			
NAME OF PROGRAM OFFICE REPRESENTATIVE	MAIL CODE	SIGNATURE	DATE
Vincent V. Salomonson	900		3/2/98
X. DISPOSITION			
THIS FORM, WHEN COMPLETED, IS TO BE SENT TO YOUR CENTER PUBLICATIONS OFFICE			

INSTRUCTIONS FOR COMPLETING THE NASA SCIENTIFIC AND TECHNICAL DOCUMENT AVAILABILITY AUTHORIZATION (DAA) FORM

Purpose. This DAA form is used to prescribe the availability and distribution of all NASA-generated and NASA-funded documents containing scientific and technical information (including those distributed via electronic media such as the World Wide Web and CD-ROM).

Requirements. The author/originator must provide either a suitable summary description (title, abstract, etc.) or a completed copy of the document with this form. This form is initiated by the document author/originator and that individual is responsible for recommending/determining the availability/distribution of the document. The author/originator completes Sections I through III, and VI. The author/originator is also responsible for obtaining information and signature in Section IV to the extent the document discloses an invention for which patent protection has been applied. Subsequent to completion of these sections, the author/originator forwards the document to the appropriate Project Manager/Technical Monitor/Division Chief for further review and approval in Section VII, including a re-review of the planned availability and distribution. Once this approval is obtained, the DAA is forwarded to the NASA Headquarters or Center Export Administrator for completion of Section VIII. It is then forwarded for completion of Section IX to the cognizant NASA Headquarters Program Office or Delegated Authority, who provides final review and approval for release of the document as marked.

When to Use This Form. Documents containing STI and intended for presentation or publication (including via electronic media) must be approved in accordance with the NASA STI Procedures and Guidelines (NPG 2200.2). Documents that are to be published in the NASA STI Report Series must be coordinated with the appropriate NASA Headquarters or Center Scientific and Technical Information Office in accordance with NPG 2200.2. Note that information on the Report Documentation Page (if attached) is not to be entered on the DAA except for title, document date, and contract number.

How to Use this Form. Specific guidelines for each section of this form are detailed below.

I. Document/Project Identification. Provide the information requested. If the document is classified, provide instead the security classification of the title and abstract. (Classified information must not be entered on this form). Include RTOP numbers on the Contract/Grant/Interagency/Project Number(s) line. Provide information on presentations or externally published documents as applicable.

II. Security Classification. Enter the applicable security classification for the document. Documents, if classified, will be available only to appropriately cleared personnel having a "need to know."

III. Availability Category for Unclassified Documents. Check the appropriate category or categories.

Export Controlled Document. If the document is subject to export restrictions (see NPG 2200.2, paragraph 4.5.3), the appropriate restriction must be checked, either International Traffic in Arms Regulations (ITAR) or Export Administration Regulations (EAR), and the appropriate United States Munitions List (USML) category or Commerce Control List (CCL), Export Control Classification Number (ECCN) must be cited.

Confidential Commercial Documents (Documents containing Trade Secrets, SBIR documents, and/or Copyrighted information). Check the applicable box (see NPG 2200.2 paragraph 4.5.7). When any of these boxes are checked, also indicate the appropriate limitation and expiration in the list to the right of these restrictions. These limitations refer to the user groups authorized to obtain the document. The limitations apply both to the initial distribution of the documents and the handling of requests for the documents. The limitations will appear on and apply to reproduced copies of the document. Documents limited to NASA personnel should not be made available to onsite contractors. If the Available Only With the Approval of Issuing Office limitation is checked, the NASA Center for Aerospace Information will provide only bibliographic processing and no initial distribution; CASI will refer all document requests to the issuing office.

Publicly Available Document - Unrestricted Distribution. Check this box if the information in the document may be made available to the general public without restrictions (unrestricted domestic and international distribution). If the document is copyrighted (see paragraph 4.5.7.3 in NPG 2200.2), also check the "Copyrighted" box in this section.

IV. Document Disclosing an Invention. This must be completed when the document contains information that discloses an invention (see NPG 2200.2, paragraph 4.5.9). When this box is checked, an additional appropriate availability category must be checked. Use of this category must be approved by NASA Headquarters or Center Patent Counsel or the Intellectual Property Counsel.

V. Blanket Release (Optional). Complete this optional section whenever subsequent documents produced under the contract, grant, or project are to be given the same distribution and/or availability as described in Sections II and III. More than one contract number or RTOP Number can be entered. This section may also be used to rescind or modify an earlier Blanket Release. All blanket releases must be approved by the Program Office or its designee and concurred with by the Office of Management Systems and Facilities.

VI. Author/Originator Verification. Required for all DAA forms.

VII. Project Officer/Technical Monitor/Division Chief Review. The Project Officer/Technical Monitor/Author or Originator Division Chief or above must sign and date the form. The office code and typed name should be entered.

VIII. Export Control Review/Confirmation. This section is to be completed by the authorized NASA Headquarters or Center Export Control Administrator for all documents.

IX. Program Office or Delegated Authority Review. This section is to be completed by the duly authorized official representing the NASA Headquarters Program Office. Any delegation from NASA Headquarters to a NASA Center in accordance with NPG 2200.2 should be entered here.

X. Disposition. For NASA Center use.

REPORT DOCUMENTATION PAGE

Form Approved

OMB No. 0704-0188

Public reporting burden for this collection of information is estimated to average 1 hour per response, including the time for reviewing instructions, searching existing data sources, gathering and maintaining the data needed, and completing and reviewing the collection of information. Send comments regarding this burden estimate or any other aspect of this collection of information, including suggestions for reducing this burden, to Washington Headquarters Services, Directorate for Information Operations and Reports, 1215 Jefferson Davis Highway, Suite 1204, Arlington, VA 22202-4302, and to the Office of Management and Budget, Paperwork Reduction Project (0704-0188), Washington, DC 20503.

1. AGENCY USE ONLY (Leave blank)**2. REPORT DATE**

April 1998

3. REPORT TYPE AND DATES COVERED

Contractor Report

4. TITLE AND SUBTITLE

Linkages Between Global Vegetation and Climate—An Analysis Based on NOAA Advanced Very High Resolution Radiometer Data

5. FUNDING NUMBERS

Code 923

NAS5-31752

6. AUTHOR(S)

Sietse Oene Los

7. PERFORMING ORGANIZATION NAME(S) AND ADDRESS (ES)

Biospheric Science Branch
Laboratory for Terrestrial Physics
Goddard Space Flight Center
Greenbelt, Maryland 20771

8. PERFORMING ORGANIZATION REPORT NUMBER

98B00021

9. SPONSORING / MONITORING AGENCY NAME(S) AND ADDRESS (ES)

National Aeronautics and Space Administration
Washington, DC 20546-0001

10. SPONSORING / MONITORING AGENCY REPORT NUMBER

GSFC/CR-1998-206852

11. SUPPLEMENTARY NOTES

S. Los: Science Systems and Applications, Inc., Lanham, Maryland 20706

12a. DISTRIBUTION / AVAILABILITY STATEMENT

Unclassified-Unlimited
Subject Category: 47
Report available from the NASA Center for AeroSpace Information,
7121 Standard Drive, Hanover, MD 21076-1320. (301) 621-0390.

12b. DISTRIBUTION CODE**13. ABSTRACT (Maximum 200 words)**

A monthly global 1 degree by 1 degree data set from 1982 until 1990 was derived from data collected by the Advanced Very High Resolution Radiometer on board the NOAA 7, 9, and 11 satellites. This data set was used to study the interactions between variations in climate and variations in the "greenness" of vegetation. Studies with the Colorado State University atmospheric general circulation model coupled to the Simple Biosphere model showed a large sensitivity of the hydrological balance to changes in vegetation at low latitudes. The depletion of soil moisture as a result of increased vegetation density provided a negative feedback in an otherwise positive association between increased vegetation, increased evaporation, and increased precipitation proposed by Charney and coworkers. Analysis of climate data showed, at temperate to high latitudes, a positive association between variation in land surface temperature, sea surface temperature and vegetation greenness. At low latitudes the data indicated a positive association between variations in sea surface temperature, rainfall and vegetation greenness. The variations in mid- to high latitude temperatures affected the global average greenness and this could provide an explanation for the increased carbon uptake by the terrestrial surface over the past couple of decades.

14. SUBJECT TERMS

Global vegetation, climate, AVHRR

15. NUMBER OF PAGES

199

16. PRICE CODE**17. SECURITY CLASSIFICATION OF REPORT**

Unclassified

18. SECURITY CLASSIFICATION OF THIS PAGE

Unclassified

19. SECURITY CLASSIFICATION OF ABSTRACT

Unclassified

20. LIMITATION OF ABSTRACT

UL

Acknowledgments

The work presented in this dissertation was funded by a National Aeronautics and Space Administration (NASA) Earth Observing System - Interdisciplinary Science (EOS-IDS) grant (Biosphere-Atmosphere Interactions project) contract NAS-531732. I thank Professor Dr. J.J. de Vries for taking on the task of being my "promotor" and for encouraging my work. I thank Dr. A.A. van de Griend, "copromotor", and Drs P.J. Sellers and C.J. Tucker, referents and members of the "leescommissie," for supervising the current research, for many supportive discussions and for useful advice. It is a great privilege to work with Piers Sellers and I am grateful for his interest in the current research. Dr. G.J. Collatz, also a member of the "leescommissie," went through several revisions of this manuscript and I value the many useful discussions with him and his attempts to "straighten me out" on the interpretation of results from the biosphere and general circulation models. I thank the other members of the "leescommissie", Professor Dr. A. Skidmore, Professor Dr. I. Simmers and Dr. R. Leemands, for reviewing this dissertation and for their supportive comments. I also found Dr. J. Privette's comments on an early draft of this manuscript very useful.

Many others have contributed to this research in one way or another. The discussions over the years with Drs. S.D. Prince, C.J. Tucker, C.O. Justice, B.N. Holben, and S.N. Goward helped to shape my views expressed in Chapters 2 and 3 on the potential and limitations to use remote sensing for vegetation monitoring.

The datasets discussed in Chapter 4 were generously provided by Dr. C.J. Tucker. The data were produced by R. Rank, J. Rosenfelder, D. Rosenfelder and W.W. Newcomb of the Global Inventory Modeling and Monitoring System (GIMMS) group at NASA/Goddard Space Flight Center.

Chapter 5 is in many respects central to the research in this dissertation. The discussions with Dr. Sellers were essential in developing ideas to correct the satellite data and in deriving biophysical parameters from these. Dr. E.F. Vermote provided the aerosol optical thickness data, Dr. R.S. DeFries provided the global landcover classification, Dr. D. Strauss advised on the use of Fourier series, and H. Zhang assisted with porting the computer code to a Unix workstation.

N. Pollack assisted with the analysis presented in Chapter 6. The First ISLSCP¹ Field Experiment (FIFE) surface reflectance data used in Chapters 3 and 6 were collected by Dr. D.W. Deering as part of the FIFE Surface Radiance and Biology (SRB3) study. The biophysical properties of the vegetation at the FIFE study area were collected for FIFE by the staff of the Evapotranspiration Laboratory at Kansas State University under the direction of E.T. Kanemasu, and by the staff at the University of Nebraska, Lincoln, under the direction of B. Blad. The dedicated efforts of A. Nelson, J. Killeen, L. Ballou, T. Shah, and C. Hays in collecting and preparing these data are particularly appreciated. The Surface Reflectance Measured with a Mast-borne Modular Multiband Radiometer (MMR) data were collected by B.L. Blad, E.A. Walter-Shea, C.J. Hays, and M.A. Mesarch of the University of Nebraska. Their contribution of these data is particularly appreciated. The Boreal Ecosystem-Atmosphere Study (BOREAS) surface reflectance and fraction of photosynthetically active radiation absorbed by the green part of the vegetation (FPAR) data were collected by Drs P. Rich (FPAR), C. Walthall, and the BOREAS helicopter crew (reflectance), J.M. Chen and J. Cihlar (data in figure 6.3.g and figure 6.5.c), and were made available through the BOREAS information system. Data from the Oregon Transect Ecosystem Research (OTTER) field campaign were obtained from the Oregon Transect Ecosystem Research Project Compact Disk, Vol. 1 (Angelici *et al.* 1991). I thank Dr. K.F. Huemmrich for his comments on the FIFE, OTTER, and BOREAS data. D.A. Dazlich provided the Simple Biosphere model (SiB2) snow-free surface albedo data and Dr. B.R. Barkstrom provided the Earth Radiation Budget Experiment (ERBE) albedo data.

The runs with the Colorado State University Atmospheric General Circulation Model in Chapter 7 were carried out by Dr. L. Bounoua. The discussions with Drs. G.J. Collatz and L. Bounoua were very helpful to interpret the model results.

In Chapter 8 my contribution was limited to providing the land surface biosphere data. I did include this chapter, formerly published as a letter to Science, because it provides an excellent example of the type of modeling that can be

¹ISLSCP: International Satellite Land Surface Climatology Project

done with the coupled Simple Biosphere-general circulation model that runs off satellite derived biospheric parameters. I gratefully acknowledge permission from Drs. P.J. Sellers, L. Bounoua, G.J. Collatz, D.A. Randall, D.A. Dazlich, J.A. Berry, I. Fung, C.J. Tucker, C.B. Field and T.G. Jensen to include this chapter.

I gratefully acknowledge the contributions that Drs G.J. Collatz, P.J. Sellers, C.J. Tucker and L. Bounoua made to Chapter 9. Drs. A.A. van de Griend and M.B.M. van den Bree helped with useful advice and discussions. The U.S. Department of Energy provided the precipitation anomaly data (Eischeid *et al.* 1991) and land surface air temperature anomaly data (Jones *et al.* 1985).

The appendices have been published as peer-reviewed articles. I would like to thank Drs. P.J. Sellers, C.O. Justice, C.J. Tucker, D.A. Dazlich, G.J. Collatz, and D.A. Randall for their contributions and Drs. S.N. Goward, C.O. Justice, S.D. Prince, and A.A. van de Griend for their useful comments on several of the papers.

I thank the management and staff of Science Systems and Applications Inc. for their support and competent administration.

I thank Dr. G. Asrar of NASA/Headquarters for funding this research and for encouraging our work.

Foreword

The defendant, Mr. Sietse Los, joined our Interdisciplinary Science team at the end of 1991. At that point we had adapted the Simple Biosphere (SiB) model to make it suitable for accepting input from satellite data. The new SiB model, referred to as SiB2, had an improved photosynthesis model, an improved way to handle partial snow cover, and the most important parameter related to photosynthesis—the fraction of photosynthetically active radiation absorbed by vegetation (FPAR)—could in principle be derived from satellite data (Sellers *et al.* 1996a, 1996b). The critical issue to be resolved was to obtain spatially and temporally consistent fields of biophysical parameters from satellite data. We assigned this task to the defendant.

The defendant at first derived two prototype datasets. The second of these prototype datasets, a one year dataset for 1987, was refined and published in Sellers *et al.* 1994 and 1996b. The defendant's role in this research was to identify errors in the satellite derived normalized difference vegetation index (NDVI) data (Chapters 2, 3 and 4, Appendix C), develop corrections for the NDVI data (sensor degradation (Appendices A and B), the Fourier Adjustment, Solar zenith angle correction, Interpolation and Reconstruction (FASIR-corrections; see appendix D)) and the derivation of biophysical parameters (Appendix D).

The one-year FASIR-NDVI and biophysical datasets turned out to be very useful and much of the success of our team can be attributed to the quality of these data. This is evidenced by several publications on novel aspects of the global carbon cycle using these data that have since appeared (*e.g.*, Denning *et al.* 1995; Ciais *et al.* 1995; Sellers *et al.* 1996c, Field *et al.* 1995b and 1996b). On the Sellers *et al.* 1996c paper (Chapter 7), the defendant was a supporting author.

Since publication of the Sellers *et al.* (1994) paper, Mr. Los has taken the lead on developing a multi-year FASIR-NDVI and land surface dataset (1982-1990). He developed several new corrections, described in Chapter 5 of this dissertation, validated algorithms and datasets in Chapter 6, and tested the sensitivity of the SiB model towards variations in the satellite data (Chapter 8). The validation and sensitivity analysis showed large improvements in the way the biosphere was modeled compared to previous studies and also identified ways in which further improvements could be made. The research of the defendant in Chapter 9 shows important interannual variation in the satellite-derived vegetation index that should provide important clues on the spatial and temporal distribution of carbon sources and sinks.

We believe that the largest progress in the field of climate research is currently made by teams, rather than by individuals, as was traditionally the case. The interaction among scientists has contributed greatly to the success of our Interdisciplinary Science (IDS) team. As such the defendant has benefited greatly from the expertise of our team, and our team has greatly benefited from several unique and original research contributions produced solely by the defendant.

Piers J. Sellers
Johnson Space Center
Houston, Texas

Compton J. Tucker
Goddard Space Flight Center
Greenbelt, Maryland

Preface

The research presented in this dissertation is the result of a collaboration among many individuals within the Earth Observation System Interdisciplinary Science (EOS-IDS) Biosphere-Atmosphere Interactions project. The defendant, as a leading or supporting author, has contributed to several articles published in the peer-reviewed literature. The most important publications resulting from the research of the defendant are:

- Los, S.O., 1993, Calibration adjustment of the NOAA-AVHRR normalized difference vegetation index without recourse to component channels. *Int. J. Remote Sens.*, **14**, 1907-1917. (Appendix A),
- Los, S.O., 1998, Estimation of the ratio of sensor degradation between NOAA-AVHRR channels 1 and 2 from monthly NDVI composites. *IEEE Trans. GeoSci and Remote Sens.*, in press. (Appendix B),
- Los, S.O., C.O. Justice, and C.J. Tucker, 1994, A global 1° by 1° NDVI dataset for climate studies derived from the GIMMS continental NDVI. *Int. J. Remote Sens.*, **15**, 3493-3518. (Appendix C),
- Sellers, P.J., S.O. Los, C.J. Tucker, C.O. Justice, D.A. Dazlich, G.J. Collatz, and D.A. Randall, 1996b, A revised land surface parameterization (SiB-2) for atmospheric GCMs. Part 2: The generation of global fields of terrestrial biophysical parameters from satellite data. *J. Climate*, **9**, 706-737. (Appendix D),
- Sellers, P.J., L. Bounoua, G.J. Collatz, D.A. Randall, D.A. Dazlich, S.O. Los, J.A. Berry, I. Fung, C.J. Tucker, C.B. Field, and T.G. Jensen, 1996c, Comparison of radiative and physiological effects of doubled atmospheric CO₂ on climate. *Science*, **271**, 1402-1406. (Chapter 8).

Several datasets resulting from the current research were made available by the International Satellite Land Surface Climatology Project (ISLSCP) through the Goddard Distributed Active Archive Center (for more information visit the Goddard DAAC webpage at http://daac.gsfc.nasa.gov/CAMPAIGN_DOCS/ISLSCP/islscp_i1.html).

- Los, S.O., C.J. Tucker and C.O. Justice, 1995, Normalized difference vegetation index (NDVI) 1 by 1 degree global dataset. On: ISLSCP Initiative I-Global Datasets for Land-Atmosphere models, 1987-1988, Vol-1, Publ. on CD by NASA (USA_NASA_GDAAC_ISLSCP_001).
- Los, S.O., P.J. Sellers, C.J. Tucker, and C.O. Justice, 1995, FASIR-NDVI 1 by 1 degree global dataset. On: ISLSCP Initiative I-Global Datasets for Land-Atmosphere models, 1987-1988, Vol-1, Publ. on CD by NASA (USA_NASA_GDAAC_ISLSCP_001).
- Los, S.O., and P.J. Sellers, 1995, FPAR, LAI, Greenness, and roughness length 1 by 1 degree global datasets. On: ISLSCP Initiative I-Global Datasets for Land-Atmosphere models, 1987-1988, Vol-1, Publ. on CD by NASA (USA_NASA_GDAAC_ISLSCP_001).

List of Abbreviations

6S	second simulation of satellite signal in the solar spectrum
AU	Astronomical Unit (1 times the mean Earth-Sun distance)
AVHRR	Advanced Very High Resolution Radiometer
BATS	Biosphere Atmosphere Transfer Scheme
BOREAS	Boreal Ecosystem-Atmosphere Study
BRDF	Bidirectional Reflectance Distribution Function
CIA	Central Intelligence Agency
COLA	Center for Ocean-Land Atmosphere Studies
EOS	Earth Observing System
ERBE	Earth Radiation Budget Experiment
ENSO	El Niño-Southern Oscillation
FAO	United Nations Food and Agricultural Organization
FASIR	Fourier Adjustment, Solar zenith angle correction, Interpolation and Reconstruction of NDVI
FEWS	Famine Early Warning System
FIFE	First ISLSCP Field Experiment
FPAR	Fraction of PAR absorbed by the green part of the vegetation
GAC	Global Area Coverage
GCM	General Circulation Model
GIMMS	Global Inventory, Monitoring and Modeling System
GISS	Goddard Institute for Space Sciences
GSFC	Goddard Space Flight Center
GVI	Global Vegetation Index
HRPT	High Resolution Picture Transmission
IDS	Interdisciplinary Science
ISLSCP	International Satellite Land Surface Climatology Project
ITCZ	Intertropical Convergence Zone
KSU	Kansas State University
LAC	Local Area Coverage
LAI	Leaf Area Index
LOWTRAN	LOW resolution TRANsmittance
LSP	Landsurface Parameterization
MMR	Modular Multiband Radiometer
MODIS	Moderate Resolution Imaging Spectrometer
MSAVI	Modified SAVI
NASA	National Aeronautics and Space Administration
NDVI	Normalized Difference Vegetation Index
NESDIS	National Environmental Satellite Data and Information Service
NIR	Near Infrared
NOAA	National Oceanic and Atmospheric Administration
NPP	Net Primary Production
OTTER	Oregon Transect Ecosystem Research
PAR	Photosynthetically Active Radiation
POES	Polar-orbiting Operational Environmental Satellite
RMS	Root Mean Square

SAIL	Scattering from Arbitrarily Inclined Leaves
SAVI	Soil Adjusted Vegetation Index
SBUV	Solar Backscatter Ultraviolet
SMMR	Scanning Multichannel (or Multifrequency) Microwave Radiometer
SPOT	Satellite pour l'Observation de la Terre
SR	Simple Ratio
SRB	Surface Radiance and Biology study (FIFE)
SST	Sea Surface Temperature
SVI	Spectral Vegetation Index
SiB	Simple Biosphere model
TIROS-N	Television and InfraRed Observational Satellite
TOMS	Total Ozone Mapping Spectrometer
TOVS	TIROS Operational vertical sounder
USGS	United States Geological Survey
UV	Ultra Violet
WDB	world data bank

Contents

1	Introduction	1
1.1	Scope of Current Research	1
1.2	Organization	3
2	Vegetation Monitoring With AVHRR Data	5
2.1	Introduction	5
2.2	The NOAA-AVHRR	7
2.3	History	8
2.4	Relationships Between NDVI and Biophysical Parameters	9
2.5	Desert Margin Studies	10
2.6	Conclusion	12
3	Interferences With AVHRR Landsurface Observations	13
3.1	Image Navigation	13
3.2	Viewing Geometry	13
3.2.1	Solar Zenith Angles	13
3.2.2	Viewing Angles	14
3.3	Sensor Degradation	14
3.4	Clouds	14
3.5	Atmospheric Constituents	14
3.6	Terminator Effect	17
3.7	Bidirectional Reflectance	17
3.8	Topography	18
3.9	Soil Background Effects	18
3.10	Bad Scans	18
3.11	Conclusion	18
4	The GIMMS NDVI Dataset	19
4.1	Introduction	19
4.2	Processing	19
4.3	Discussion	20
5	Estimation of Biophysical Landsurface Parameters	23
5.1	Correction of the AVHRR NDVI Data	24
5.1.1	Sensor Degradation	24
5.1.2	Volcanic Aerosols	24
5.1.3	FASIR Corrections	25
5.2	Landcover Classification	27
5.3	Derivation of Biophysical Parameter Fields	29
5.4	Discussion	31

CONTENTS

6	Evaluation of FASIR-NDVI and Biophysical Landsurface Parameters	33
6.1	Evaluation of FASIR	34
6.1.1	Fourier Adjustment	34
6.1.2	Solar Zenith Angle Correction	35
6.2	Evaluation of Relationships Between NDVI, FPAR, and LAI	37
6.2.1	FPAR	37
6.2.2	Leaf Area Index	39
6.3	Comparison of SiB2 Albedo Fields With ERBE Data	40
6.4	Discussion	41
7	Sensitivity of Landsurface Fluxes to Vegetation Changes	45
7.1	Design of the Experiment	45
7.2	Assimilation	45
7.2.1	SiB2 Photosynthesis Submodel	45
7.2.2	Sensitivity Analysis	47
7.3	Energy Balance	47
7.3.1	SiB2 Energy Submodel	47
7.3.2	Sensitivity Analysis	49
7.4	Water Balance	49
7.4.1	SiB2 Hydrological Submodel	49
7.4.2	Sensitivity Analysis	50
7.5	Feedback Between Vegetation and Climate	53
7.6	Conclusion	56
8	Radiative and Physiological Effects of Doubled Atmospheric CO₂ on Climate	57
8.1	Introduction	57
8.2	Design of Experiment	58
8.3	Results and Discussion	59
8.4	Conclusion	62
9	Linkages Between Climate, Vegetation, and Atmospheric CO₂ During the 1980s	63
9.1	Introduction	63
9.2	Data	63
9.3	Analysis	64
9.4	Discussion	70
10	Summary and Conclusions in English and Dutch	73
	Bibliography	81
A	Calibration Adjustment of the NDVI Without Recourse to Component Channels 1 and 2 Data	91
A.1	Introduction	91
A.2	Data	92
A.3	Theory	92
A.3.1	Effect of Sensor Degradation on NDVI	93
A.4	Verification	94
A.5	Discussion	95
A.6	Conclusion	96
A.7	Appendix	96
B	Estimation of Sensor Degradation From Monthly NDVI Composites	99
B.1	Introduction	99
B.2	Data	100
B.3	Theory	100
B.4	Analysis	101
B.5	Discussion	104

B.6 Conclusion	106
C A Global 1° by 1° NDVI Dataset for Climate Studies	109
C.1 Introduction	109
C.2 The GIMMS Continental NDVI Dataset	110
C.2.1 The NOAA-AVHRR Remote Sensing System	110
C.2.2 Cloud Contamination	111
C.2.3 Atmospheric Perturbations	111
C.2.4 Illumination and Viewing Geometry-Dependent Effects	112
C.2.5 Soil Background Effect	113
C.3 Steps in Processing GIMMS Continental NDVI Data	113
C.3.1 Organization of Level 1B Data	113
C.3.2 Mapping the Daily Global Area Coverage (GAC) Data	113
C.3.3 The Monthly NDVI Composites	115
C.3.4 Correction for Sensor Degradation	116
C.4 Formation of the Continental Data Into a Global Dataset	116
C.4.1 Discussion of the Global 1° by 1° NDVI Data	117
C.5 Spatial Degradation	118
C.6 Discussion	119
C.7 Conclusion	120
D The Generation of Global Fields of Terrestrial Biophysical Parameters From Satellite Data	123
D.1 Introduction	123
D.2 Theoretical Background	124
D.2.1 Albedo	125
D.2.2 Surface Roughness	126
D.2.3 Photosynthesis and Evapotranspiration	127
D.2.4 Deriving Surface Parameters From Satellite Data	128
D.3 Datasets	129
D.3.1 The Global 1° by 1° NDVI Dataset	129
D.3.2 Stratification of the NDVI Data Into Landcover Types	132
D.4 An Adjusted NDVI Product: FASIR-NDVI	132
D.4.1 FASIR: Fourier Wave Adjustment of NDVI Time-Series	132
D.4.2 FASIR: Solar Zenith Angle Correction	134
D.4.3 FASIR: Interpolation of Missing Data	135
D.4.4 FASIR: Reconstruction of NDVI Time-Series Over Tropical Regions	137
D.5 Calculation of FPAR, L_T , and Canopy Greenness Fraction (N) From FASIR-NDVI	137
D.5.1 Calculation of FPAR from FASIR-NDVI	137
D.5.2 Calculation of Green Leaf Area Index From FPAR	137
D.5.3 Canopy Greenness Fraction and Total Leaf Area Index	138
D.6 Generating the Global Parameter Fields From the Core Datasets	139
D.6.1 Soil Physical Properties and Reflectance Properties	140
D.6.2 Radiative Transfer Properties	141
D.7 Turbulent Transfer Properties	141
D.8 Vegetation Biophysical Parameters	141
D.9 Discussion	142
D.10 Conclusion	145
E Color Figures	147
E.1 Figures With Chapter 2	149
E.2 Figures With Chapter 9	151
E.3 Figures With Appendix C	155
E.4 Figures With Appendix D	161

List of Figures

1.1	Components of the Earth Observing System (EOS) Interdisciplinary Science (IDS) Biosphere-Atmosphere Interactions project	2
2.1	Mean global 1° by 1° NDVI for 1982–1990	6
2.2	Seasonally-summed NDVI versus accumulated aboveground biomass	8
2.3	Leaf and soil spectra	10
2.4	Seasonally summed NDVI versus annual rainfall	10
2.5	Mean annual NDVI in the Sahel from 1982–1995	11
3.1	Solar zenith angle values at local overpass times of the NOAA-7, -9, and -11 satellites	15
3.2	Sources of interference in the NDVI	16
5.1	Variation in the NDVI as a function of aerosol optical thickness	24
5.2	FASIR adjustments	26
5.3	Confusion in landcover classifications based on NDVI time-series	28
5.4	Mean Annual NDVI versus the seasonal range in NDVI	28
5.5	Estimation of FPAR and LAI from NDVI	30
6.1	Evaluation of the Fourier Adjustment	34
6.2	Evaluation of the Solar Zenith Angle correction	34
6.3	Evaluation of NDVI FPAR relationships	36
6.4	Relationship between NDVI corrected for Rayleigh scattering and ozone absorption, and uncorrected NDVI	37
6.5	Evaluation of FPAR LAI relationships	39
6.6	Evaluation of albedo fields	40
6.7	Comparison of SiB2 and ERBE albedo fields with FASIR-NDVI	42
7.1	Sensitivity of carbon assimilation to changes in FPAR	46
7.2	Sensitivity of the energy balance to changes in FPAR	48
7.3	Hydrological sub-model in SiB2	50
7.4	Sensitivity of the water balance to changes in FPAR as a function of latitude	51
7.5	Sensitivity of the water balance components to changes in FPAR	52
7.6	Feedbacks in the local climate as a result of changes in FPAR	55
8.1	Leaf photosynthesis and conductance responses to local increases in atmospheric CO ₂ for light-saturated conditions	58
8.2	Sequence and type of numerical CO ₂ experiments	59
8.3	Zonal mean surface air temperature (°C) of numerical CO ₂ experiments	61
8.4	Changes in assimilation rate, A , ($\mu\text{mol m}^{-2} \text{s}^{-1}$) versus changes in surface temperature, T , as projected by the numerical CO ₂ experiments	62
9.1	Monthly mean global and Northern Hemisphere sea surface temperature, NDVI, landsurface air temperature, and precipitation anomalies	64
9.2	Factor loadings from a weighted factor analysis of global NDVI anomaly-, and Sea Surface Temperature anomaly data	66

LIST OF FIGURES

9.3	Pixel-by-pixel covariances of NDVI and SST anomalies with the synthetic factor loadings for 1982-1983, 1984-1985, and 1988-1990	67
9.4	Pixel-by-pixel correlations between NDVI and temperature anomalies, and NDVI and precipitation anomalies.	68
9.5	Examples of time-series with positive correlations ($r > 0.3$) between NDVI and landsurface air temperature anomalies	69
9.6	Relationships between landsurface air temperature anomalies and NDVI anomalies for different parts of the growing season	71
A.1	Relationship between the reciprocal of visible reflectance and the simple ratio	93
A.2	Difference between preflight calibrated NDVI and desert calibrated "true" NDVI as a function of preflight calibrated NDVI	94
A.3	Comparison of models to approximate the rate of sensor degradation in the preflight calibrated NDVI	95
B.1	Apparent ratio of sensor degradation for NOAA-7, -9, and -11	101
B.2	Cross validation of estimated ratio of sensor degradation in AVHRR channels 1 and 2	102
B.3	Comparison of sensor degradation estimated in this study with estimates from published literature	102
B.4	Ratios of sensor degradation from this study versus those from Vermote and Kaufman (1995)	105
B.5	Time-series of monthly NDVI anomalies from 1982-1990 for four arid regions	107
C.1	Sources of interference in the NDVI	112
C.2	Main steps in processing the NOAA-AVHRR level 1B data	114
C.3	Non-linear scaling effects on the NDVI	116
C.4	Time-series from 1982-1990 of average and the range of NDVI values	117
C.5	NDVI time-series for the SiB2 landcover types	120
D.1	Visible and near-infrared reflectance, simple ratio, and FPAR as a function of leaf area index	124
D.2	Dependence of unstressed surface conductance on green leaf area index	126
D.3	Relationship between the simple ratio and FPAR	127
D.4	Schematic of Fourier Adjustment	130
D.5	Dependency of roughness length on leaf area index	132
D.6	Schematic of the analysis to extract the dependence of NDVI on solar zenith angle	134
D.7	Illustration of solar zenith angle correction on a NDVI time-series	135
D.8	Interpolation of missing data in a NDVI time-series	135
D.9	Schematic of procedures used to generate global fields of soil properties for use in SiB2	138
D.10	Schematic of procedures used to generate global surface reflectance and other radiative transfer properties for SiB2	140
D.11	Schematic of procedures used to generate global fields of turbulent transfer properties for SiB2	141
D.12	Generation of global biophysical landsurface parameter fields for SiB2	143
D.13	Average effect of FASIR adjustments on the NDVI by latitude for July 1987	144
D.14	Effect of FASIR corrections on the NDVI for each of the SiB2 landcover classes	145
E.1	Global 1° by 1° NDVI	149
E.2	Pixel-by-pixel covariances of NDVI and sea surface temperature (SST) anomalies with the synthetic factor loadings for 1982-1983, 1984-1985, and 1988-1990	151
E.3	Pixel-by-pixel correlations between NDVI and temperature anomalies, and NDVI and precipitation anomalies.	153
E.4	Normalized difference vegetation index images for February and August 1987	155
E.5	Average NDVI and coefficient of variation for 1982-1990	157
E.6	Spatial variation of each 1° by 1° grid cell	159
E.7	SiB2 global landcover classification	161
E.8	FASIR-NDVI for January and July 1987	163
E.9	Global FPAR fields for January and July 1987	165
E.10	Global SiB1 fields of total leaf area index for January and July 1987	167
E.11	Global SiB2 fields of total leaf area index for January and July 1987	169
E.12	Food and Agricultural Organization soil texture map	171

List of Tables

3.1	Effects of atmospheric constituents on the NDVI	17
5.1	Vegetation cover types with examples of associated biophysical properties	27
6.1	Coefficients to correct the NDVI for solar zenith angle effects	35
6.2	Analysis of variance of alternative models to estimate FPAR from NDVI	39
8.1	Summary of results from six double CO ₂ experiments	60
9.1	Factor loadings from a promax analysis of global and Northern Hemisphere NDVI, SST, precipitation, and landsurface air temperature mean anomaly time-series	65
A.1	Calibration coefficients from Holben <i>et al.</i> (1990) and Kaufman and Holben (1993)	92
A.2	Preflight calibration gain and solar flux	96
A.3	Calibration coefficients as a function of time and satellite	97
B.1	AVHRR channels 1 and 2 preflight calibration coefficients for NOAA-7, -9, and -11	103
B.2	Analysis of variance for sensor degradation as a function of time and satellite	103
B.3	Ratios of sensor degradation between AVHRR channels 1 and 2 for 1982–1993	105
C.1	Effects of atmospheric constituents on the NDVI	113
C.2	Organization of the GIMMS dataset by continent	114
C.3	Estimated magnitude of error in the GIMMS NDVI dataset	116
D.1	Summary of parameters used by SiB1 and SiB2 sub-models	125
D.2	Derivation of SiB2 vegetation classes from the Matthews (1983) and Kuchler (1983) classifications	131
D.3	Vegetation cover types with examples of associated biophysical properties	135
D.4	Biome-dependent time-invariant land-surface properties	136
D.5	Biome independent morphological and physiological parameter	139
D.6	Soil texture types and soil physical parameters	140
D.7	Parameter fields used by SiB2 within the GCM	142

LIST OF FIGURES

E.13 Global fields of snow-free soil background reflectance	173
E.14 Global snow-free albedo values for January and July 1987	175
E.15 Global roughness length values for January and July 1987	177
E.16 Global canopy PAR use parameter fields for January and July 1987	179

Chapter 1

Introduction

A strong interest has emerged during the past decades in both human induced and natural variations in the global climate. Human activities potentially leading to variations in the global climate are increased emissions of greenhouse gases— CO_2 , N_2O , chlorofluorocarbons, methane, and tropospheric ozone—, the clearing of large areas of forests, and desertification (Glantz and Krenz 1992). At the same time, large variations of natural origin occurred in the global climate. These variations occurred at very different time-scales: examples of variations over time periods in the order of four to seven years are the El Niño-Southern Oscillation and the Atlantic Oscillation phenomena; over time-periods in the order of thousands of years are the alternations of glacial and interglacials; and over time-periods in the order of ten to hundred millions of years are periods with and without these alternations of glacial and interglacials. Making the distinction between natural climate variations occurring at these different time scales and human induced climate variations is difficult, but it is necessary in order to understand the global climate and the climate impact of human activities.

The global climate has been divided into five major components (Peixoto and Oort 1992): the atmosphere, the hydrosphere (oceans, lakes, and rivers), the cryosphere (snow and ice), the lithosphere, and the biosphere. The atmosphere is the central component of the climate system. It is highly dynamic and redistributes large portions of water, heat, and momentum over the globe. The oceans, because of their volume and capacity to absorb heat, serve as large heat reservoirs that dampen short-term fluctuations in the global energy balance and regulate the global distribution of temperature. The cryosphere affects the Earth's energy balance in that it reflects high amounts of incoming solar radiation, reduces the amount of heat absorbed by the Earth surface, and insulates the underlying land and oceans. It is important in a different aspect as the largest body of fresh water on the globe. The lithosphere interacts with the atmosphere through the transfer of mass (mainly water vapor), energy, and momentum and fixes carbon over large periods of time. Movements in the lithosphere over time

periods of millions of years explain some of the climate variations during the geologic past as well as variations in sea level on time-scales the length of millions of years (Van Straaten 1973). The biosphere is most important in its ability to sustain life, in regulating the land surface water and carbon balance, and in its effect on the atmospheric composition thereby indirectly affecting the radiative processes in the atmosphere. The direct contribution of the biosphere to the energy balance is modest compared to the contributions of the oceans and atmosphere.

The climate system is complicated because of interactions between and within its components. A disturbance of one component can affect another component and either enhance the initial disturbance (positive feedback) or dampen it (negative feedback). A positive feedback occurs, for example, if the temperature decreases at high latitudes. Provided that precipitation is sufficient, the aerial extent of snow and ice expands, leading to a further reduction of temperature because of an increase in land surface albedo and reflected solar radiation and a decrease in the amount of energy available to heat the atmosphere. This process is reversed if the amount of precipitation diminishes because of decreased convection as a result of decreased temperatures.

Another example of a feedback between climate components is the warming of the eastern equatorial Pacific Ocean known as El Niño. This warming of the eastern equatorial Pacific Ocean has been associated with changes in atmospheric circulation, Southern Oscillation, that in turn affect the oceanic circulations, thus reinforcing the initial warming. The El Niño Southern Oscillation (ENSO) is an important climatic phenomena that has been associated with the occurrence of droughts in some areas and torrential rains in others (Philander 1990, Glantz *et al.* 1991).

1.1 Scope of Current Research

To learn more about climate variations and the effects of human induced changes in the environment, the National Aeronautics and Space Administration (NASA) started the Mission to Planet Earth (MPTE) Earth Ob-

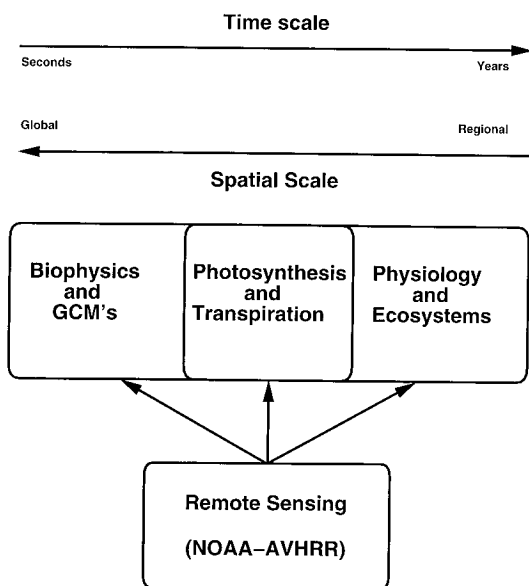


Figure 1.1: *Relationship between biophysical, ecological and remote sensing components of the Interdisciplinary Biosphere-Atmosphere Interactions project (Courtesy Dr. P.J. Sellers, NASA Johnson Space Center).*

serving System (EOS) program. One of the projects funded by EOS is the Interdisciplinary Science Biosphere-Atmosphere Interactions project, of which the current study is part. The objective of the Biosphere-Atmosphere Interaction project is to improve the understanding of the biophysical and ecological processes governing the exchange of energy, water, carbon, and trace gases between the land surface biosphere and the atmosphere. The ultimate goal is to model changes in the physical climate system and carbon cycle over the next 50 to 100 years in response to changes in atmospheric composition and landuse. The Biosphere-Atmosphere Interactions project covers both short-term interactions between the land biosphere and the atmosphere, studied with an atmospheric general circulation model coupled to a biosphere model, and long-term (ecology) interactions, studied with a carbon allocation model (figure 1.1). These two processes overlap in the areas of primary production (photosynthesis) and water exchange (transpiration). Vegetation datasets derived from remote sensing directly feed into these models, and in addition provide observational evidence for climate-vegetation interactions.

This dissertation deals with observational aspects of the land surface biosphere component of the climate system. Traditionally, data on the land surface biosphere have been sparse and have not been collected with the same frequency and spatial coverage as other climate data, *e.g.*, rainfall and temperature data. The lack of available data on the land surface biosphere is potentially a serious limitation to the study of the biosphere as a

component of the global climate. To study the linkages between the biosphere and the global climate with models and from observations, a vegetation dataset was compiled from measurements collected by the Advanced Very High Resolution Radiometer (AVHRR) aboard the National Oceanographic and Atmospheric Administration (NOAA) polar orbiting satellite.

Several methods have been developed to obtain estimates of the biosphere from satellite observations. These methods are based on the unique spectral behavior of vegetation, *i.e.*, vigorous vegetation, in particular leaf material, strongly absorbs radiation in the visible, and strongly reflects radiation in the near-infrared parts of the solar spectrum. Over the past two decades observations in these spectral bands have become available from polar orbiting satellites for the entire globe. With these observations it is possible to obtain realistic estimates of the temporal and spatial variability of vegetation with sufficient resolution for regional and global studies of the biosphere. These satellite data are therefore an attractive means to estimate biospheric parameters for use in general circulation models of the atmosphere and to analyze interactions between the biosphere and variations in the global climate, *e.g.*, temperature and precipitation.

The observation of the land surface from space is not without problems. Sources of inconsistencies in the measurements include a lack of intercalibration of the AVHRRs on successive NOAA platforms, clouds obscuring a substantial part of the Earth from the satellite sensor at any given time, and atmospheric constituents absorbing and scattering the incoming solar radiation and radiation reflected by the Earth surface. To ensure data consistency, both in space and time, a large part of this dissertation is devoted to the correction of the satellite data.

To assess the effect of the biosphere on the global climate, several experiments were conducted with a general circulation model of the atmosphere. The land surface vegetation boundary conditions for these experiments were derived from the corrected satellite observations. In one set of experiments the sensitivity of fluxes between the Earth surface and the atmosphere to changes in vegetation was estimated. In another set of experiments the effect of the biosphere on land surface temperature was estimated under a doubling of atmospheric carbon dioxide from current conditions.

The satellite-derived vegetation data were also used to detect linkages between observed interannual variations in vegetation and in the global climate, in this case precipitation, land surface air temperature, and sea surface temperature. The results have important implications for the global carbon balance.

Qualitative aspects of vegetation change, for example, changes in species composition or changes in ecosystems as a result of changes in climate, were not studied.

1.2 Organization

This dissertation is composed of two parts. The first part is the main body of text that provides a complete overview of the current research. It is a compilation of earlier published research, research that has since been updated and new research. The second part is an appendix consisting of articles published in the peer-reviewed literature. These articles provide background information at a higher level of detail than the main text. There is some repetition of material discussed in the appendices and in some cases parts of the research have been updated since publication. References of these updates are given in the main text. The main part of this dissertation is, besides the current chapter, organized in nine chapters. Chapters 2, 3, and 4 are for the main part based on a review of the literature and serve as background material for the remainder of the current dissertation. The author was involved in various parts of the research presented in this review (see Appendices A, B, and C). Chapters 5, 6, 7, and 9, discuss new research in which the author had a leading role. Chapter 8 presents research in which the author had a supporting role. This chapter is added to illustrate the usefulness of the datasets described in Chapter 5 for the study of climate and to provide insight into some of the responses of vegetation under doubling of atmospheric CO₂.

Chapter 2 provides an overview of vegetation monitoring with data from the NOAA advanced very high resolution radiometer (AVHRR). This overview includes a discussion of model studies, field measurements and satellite observations to justify vegetation monitoring with these data. Research on desert margin studies is presented to discuss several aspects of climate-related interannual variations in satellite-observed vegetation greenness.

Chapter 3 discusses the limitations of vegetation monitoring with AVHRR data as reported in the literature. Amongst these limitations are the effects of orbital drift and sensor degradation, and the impact of clouds, atmosphere, land surface bidirectional reflectance, topography, and soil background.

Chapter 4 discusses processing of NOAA-AVHRR data by the Global Inventory Monitoring and Modeling System (GIMMS) group into a global Normalized Difference Vegetation Index (NDVI) dataset. Processing of the data is discussed in terms of its effectiveness in dealing with the interferences mentioned in Chapter 3.

Chapter 5 consists of three sections: the first section deals with the correction of the GIMMS NDVI data for sensor degradation, volcanic aerosols, outliers in time-series, solar zenith angle effects, interpolation

of missing data, and correction for severe cloud contamination in tropical forests. In the second section a landcover classification based on AVHRR NDVI time-series is discussed that is used to derive biome dependent corrections and to assign biome dependent biophysical properties. The third section deals with the estimation of global biophysical parameters—leaf area index and fraction of photosynthetically active radiation absorbed by vegetation—from the corrected NDVI data and the landcover classification.

Chapter 6 deals with the unique problems of validating the global biophysical parameter fields. The relationships between the biophysical parameters and NDVI are validated with data from the First ISLSCP¹ Field Experiment (FIFE), the Boreal Ecosystem-Atmosphere Study (BOREAS), and the Oregon Transect Ecosystem Research (OTTER) remote sensing experiments. The global biophysical parameters, leaf area index, and fraction of photosynthetically active radiation absorbed by vegetation, are validated by comparing global fields of albedo derived from these biophysical parameters with observations from the Earth Radiation Budget Experiment (ERBE) instrument.

Chapter 7 discusses the sensitivity of the energy, water, and carbon balances to changes in observed vegetation greenness in a general circulation model of the atmosphere.

Chapter 8 deals with the effect of doubling the concentration of carbon dioxide on the global climate. The contributions to global warming due to the atmosphere (through radiative processes) and due to the biosphere (through changes in the photosynthesis) are estimated.

Chapter 9 discusses associations between observed vegetation, precipitation, air surface temperature and sea surface temperature and the implications of these associations for the global carbon balance.

Chapter 10 highlights the most important findings of this study and evaluates their importance for climate research (with a summary in Dutch).

The appendices provide background information on data processing, correction for sensor degradation and several of the adjustments briefly discussed in Chapters 4 and 5. They are based on articles published in the peer reviewed literature.

¹ISLSCP: International Satellite Land Surface Climatology Project

CHAPTER 1. INTRODUCTION

Appendix A discusses an approximate correction of NDVI data for sensor degradation in the NOAA-AVIIRR without recourse to the component channels 1 and 2 data.

Appendix B uses the technique developed in Appendix A to derive calibration coefficients from desert areas.

Appendix C discusses processing of the GIMMS NDVI dataset, several scaling issues of importance to the coarse resolutions used in general circulation models of the atmosphere, and differences in spatial and temporal information.

Appendix D describes the derivation of land surface datasets for the Simple Biosphere model that is coupled to the Colorado State University General Circulation Model of the atmosphere. A brief description of parts of the Simple Biosphere model is given to explain the links with the land surface datasets. Since the time of publication of this article, the biophysical land surface datasets have been revised as discussed in Chapter 5.

Chapter 2

Vegetation Monitoring With AVHRR Data

An overview is provided of monitoring of land surface vegetation at continental and global scales with data collected by the Advanced Very High Resolution Radiometer (AVHRR) on board the National Oceanic and Atmospheric Administration (NOAA) series of Polar-orbiting Operational Environmental Satellites (POES; see Kidwell 1995). Several early field studies are discussed to show empirical relationships between NOAA-AVHRR observations and the amount of land surface vegetation. An overview of model studies is included to provide physical evidence for these empirical relationships. Also discussed is a study on interannual variations in vegetation in sub-Saharan Africa to illustrate the relationships between variations in rainfall and vegetation and to illustrate that these variations in vegetation can be captured by NOAA-AVHRR data.

2.1 Introduction

The parameter used most frequently for vegetation monitoring with NOAA-AVHRR data is the Normalized Difference Vegetation Index (NDVI), which is derived from the visible and near-infrared channels:

$$\text{NDVI} = \frac{\rho_n - \rho_v}{\rho_n + \rho_v}. \quad (2.1)$$

where ρ_v is the reflectance measured in the visible channel, and ρ_n is the reflectance measured in the near-infrared channel. The AVHRR collects data over the entire globe at 4 km resolution twice daily, once during daytime, and once during nighttime. This frequent global coverage makes AVHRR data suitable for applications that require high temporal resolution and coverage over large areas. Applications based on AVHRR data can be seen as one end of a continuum, with applications based on high spatial resolution data from Landsat, SPOT¹, and aerial photography that are typically acquired only

a few times a year on the other end. The high temporal resolution and spatially continuous coverage over large areas provided by AVHRR data have been exploited for various applications, *e.g.*, the comparison of vegetation density between years, monitoring of snow cover extent, and observation of weather systems and cloud patterns (Kidwell 1995, Gurney *et al.* 1993, Tucker 1996).

Figure 2.1 shows global monthly mean NDVI fields for January (figure 2.1.a) and July (figure 2.1.b) aggregated to 1° by 1° resolution and averaged over the period 1982–1990 (Los *et al.* 1994, Sellers *et al.* 1996b, appendices C and D). The January image (figure 2.1.a) has high NDVI values in the Southern Hemisphere indicating dense green vegetation, and low NDVI values in the Northern Hemisphere indicating either dormant or no vegetation. The July image (figure 2.1.b) shows high NDVI values for most of the Northern Hemisphere with the exception of desert areas. The decrease in NDVI values between January and July in the Southern Hemisphere is smaller than the increase in NDVI values in the Northern Hemisphere for these months, reflecting a smaller seasonality of vegetation in the Southern Hemisphere. The data show various other interesting features. For example, the overall difference in NDVI between the Sahara and the Australian deserts is caused by differences in vegetation density. The Sahara is for the most part barren, whereas the vegetation cover in the Australian deserts is rarely below 10 % (AUSLIG 1990). Several areas with higher NDVI values in winter than in summer are found in California, southern Portugal, southern Spain, and southern Asia. These areas have climates with moderate to high temperatures throughout the year and receive most of their rainfall during winter.

AVHRR observations have been used for various applications such as crop yield modeling (Gray and McCary 1981, Greigor and Norwine 1981, Schneider *et al.* 1981, Townshend and Tucker 1981, Duggin *et al.* 1982, Ormsby 1982, Tucker *et al.* 1981, 1983, 1984, 1986b, Justice 1986, Prince and Justice 1991, Yates *et al.* 1984), vegetation monitoring for famine early warning systems

¹ *Satellite pour l'Observation de la Terre*

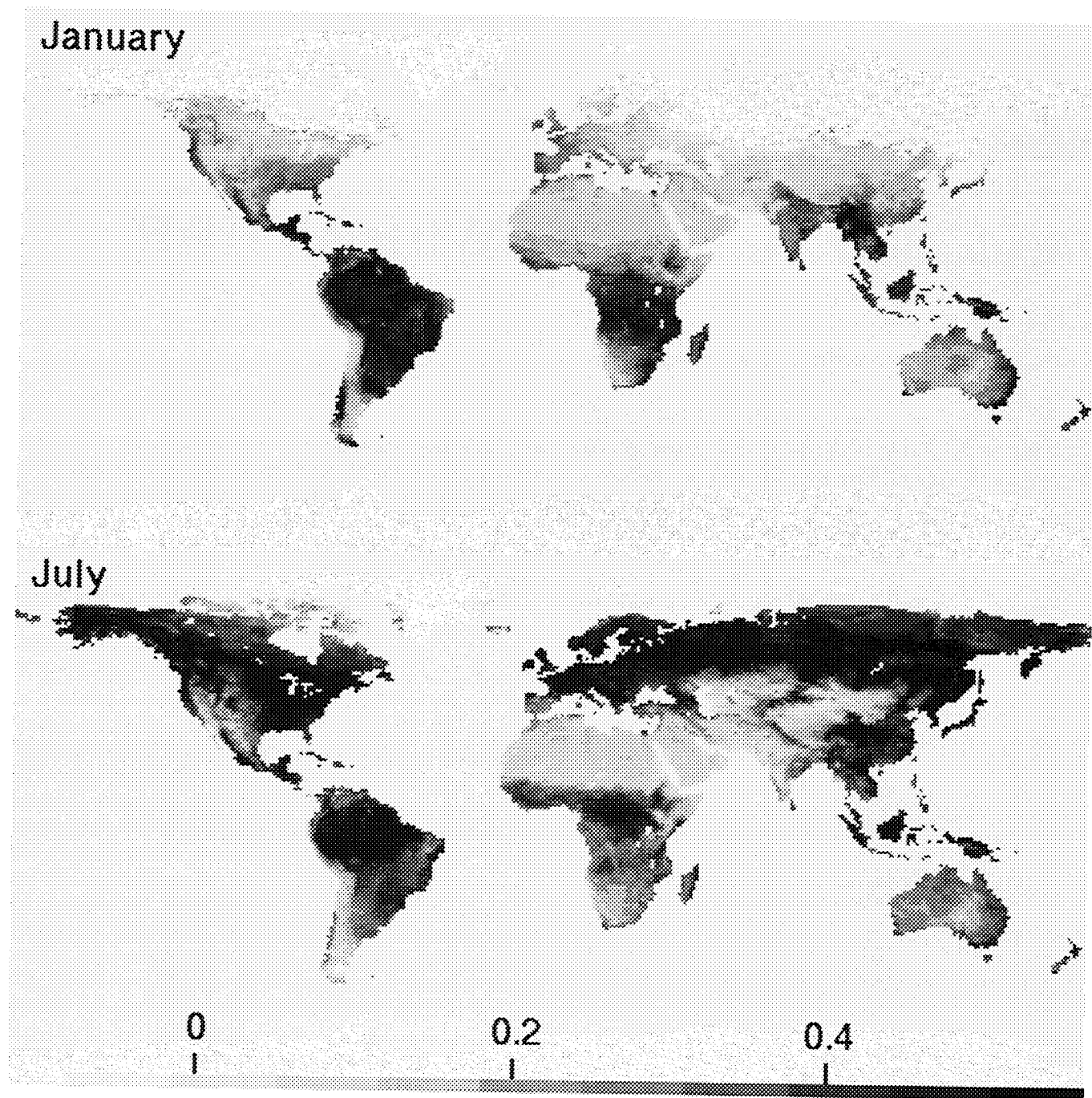


Figure 2.1: Global 1° by 1° monthly mean normalized difference vegetation index (NDVI) for 1982–1990. The two lightest shades of grey indicate missing data, for the most part occurring in the Northern Hemisphere during winter, and oceans, respectively. (top) Global 1° by 1° mean for January, (bottom) Global 1° by 1° mean for July. (For a color version see figure E.1)

(Hielkema 1990, Hutchinson 1991), detection of vegetation conditions favorable for locust breeding (Hielkema *et al.* 1986), landcover classification for large areas (Tucker *et al.* 1985a, Loveland *et al.* 1991, DeFries and Townshend 1994), study of relationships between rainfall and vegetation growth (Nicholson *et al.* 1990), monitoring of desert expansion and contraction (Tucker *et al.* 1991,

1994), and, in synergy with passive microwave observations from the Nimbus Scanning Multichannel Microwave Radiometer (SMMR), for soil moisture monitoring in semi-arid regions (Owe and Van de Griend 1990, Van de Griend and Owe 1994). NDVI data were also used to estimate the global net primary production of vegetation (Potter *et al.* 1993, Field *et al.* 1995b) and to study

the effects of interannual climatic variations in sea surface temperature and precipitation on vegetation (Myneni *et al.* 1995, Anyamba and Eastwood 1996). Recently, biophysical parameters derived from NDVI data were used to provide boundary conditions in a biosphere model coupled to a General Circulation Model of the atmosphere for the calculation of the water, carbon, and energy exchange between the land surface vegetation and the atmosphere (Los *et al.* 1994, Sellers *et al.* 1996a,b,c, Randall *et al.* 1996, Appendices C and D).

2.2 The NOAA-AVHRR

The first AVHRR was mounted on board the polar orbiting Television and InfraRed Observational Satellite (TIROS-N) launched in 1978. This AVHRR was designed to collect data for meteorological applications over the entire globe, *e.g.*, data on clouds, snow cover, wind direction, and sea surface temperature (Kidwell 1995). In its initial design, the AVHRR was equipped with four channels: channel 1 (red to near-infrared) collected data in a spectral band from 0.55-0.90 μm , channel 2 (near-infrared) from 0.73-1.1 μm , channel 3 (mid-infrared) from 3.5-3.9 μm and channel 4 (thermal infrared) from 10.5-11.5 μm . For the NOAA missions that followed the TIROS-N mission, AVHRR channel 1 was confined to the 0.55 - 0.70 μm spectral band. This redesign of the AVHRR, referred to as AVHRR/1, allowed more accurate determination of snow cover extent (Schneider *et al.* 1981). Confining channel 1 to the red part of the solar spectrum also had important implications for vegetation monitoring. The availability of two bands in parts of the solar spectrum where healthy green leaves have a distinct spectral behavior, *i.e.*, strong absorption in the red and strong scattering in the infrared, allowed monitoring of vegetation (section 2.4).

Starting with NOAA-7, a fifth channel (11.5-12.5 μm) was added to the AVHRRs on board the odd numbered NOAA platforms. This 5 channel AVHRR is referred to as AVHRR/2. The even numbered NOAA platforms were equipped with the AVHRR/2 starting with NOAA-12.

The NOAA satellites revolve the Earth in a near-polar sun-synchronous orbit with a period of about 102 minutes. The missions of the NOAA satellites are divided in morning (AM) missions and afternoon (PM) missions (Kidwell 1995). The AM missions, NOAA-6, NOAA-8, NOAA-10, and NOAA-12, passed the equator in descending (North to South) node at local crossing times of around 7:30 AM directly after launch. The PM platforms, TIROS-N, NOAA-7, -9, -11, and -14 passed the equator in ascending (South to North) node at local crossing times between 13:30 to 14:30 PM directly after launch. The equatorial crossing time of the PM platforms, however, drifts about 20 to 40 minutes per year to later times of the day (Price

1991). The scan angle of the AVHRR is approximately 55° and the swath width is about 2800 km.

The AVHRR collects data with a spatial resolution of 1.1 km at nadir. This resolution increases significantly with larger viewing angles. Data at the 1.1 km resolution exist in two formats: High Resolution Picture Transmission (HRPT) format and Local Area Coverage (LAC) format. HRPT data are continuously transmitted to the ground and can be received by a station provided one is in the transmission range of the satellite. LAC data can be recorded on an onboard tape by special request and at a later stage be transmitted to a ground station. Because of the arrangements that need to be made to obtain 1.1 km data, either through NOAA or through a local ground receiving station, the historic record of 1.1 km data is far from complete and has large gaps both in space and time. Efforts were made by NOAA, the United States Geological Survey (USGS), the National Aeronautics and Space Administration (NASA), the European Space Agency and individual receiving stations to obtain a complete global record for several years of observation (Eidenshink and Faundeen 1994).

The 1.1 km data are resampled on board to a 4 km resolution by averaging the first 4 pixels of the first line out of a 5 pixel by 3 line window. The 4 km data are available for the entire globe in global area coverage (GAC) format at daily intervals since August 1981, with only very few interruptions of the record. GAC data from the afternoon platforms are the most generally used for vegetation monitoring.

The launch of a new series of NOAA satellites with redesigned instruments is planned sometime during 1998 (Mandt *et al.* 1996). The AVHRR on board this new series is referred to as AVHRR/3. A near-infrared channel at 1.6 μm , channel 3A, will be added to the AVHRR that will operate during the daylight overpass of the satellite. The channel 3 on the AVHRR/2 will continue as channel 3B on AVHRR/3, and will operate during the nighttime overpass. The solar channels (1, 2, and 3A) will have "split gains" that require two calibration equations per channel, instead of the one equation used for the channels on the current AVHRR/2. This change is implemented to increase the sensitivity of the sensor at low light levels and to improve ice, snow, and aerosol detection. It is possible that as a result of the revised design, incompatibilities will exist between data collected by the AVHRR/2 and the AVHRR/3 instruments.

The NOAA satellites are equipped with various other instruments besides the AVHRR such as the TIROS Operational vertical sounder (TOVS) instruments and the Solar Backscatter ultra-violet (SBUV) instrument. These instruments are used for applications such as cloud detection, estimation of atmospheric precipitable water, sea surface temperatures, windspeed, outgoing longwave radiation, and atmospheric ozone concentration. These in-

struments and the datasets derived from them are not discussed in this chapter. Examples of applications with data collected by these instruments are given in Gurney *et al.* (1993).

2.3 History

Use of NOAA-AVHRR data for vegetation monitoring began in the early eighties (a selection of early papers is referenced by Tucker 1996). The potential of AVHRR data for vegetation monitoring was indicated by Tucker and co-workers (Tucker *et al.* 1981). They concluded that, at that time, the AVHRR was the only sensor system in operation suitable to estimate vegetation primary production from space with a vegetation index approach. They also stated that the AVHRR had several shortcomings such as a large field of view and a broad spectral band width of channels 1 and 2. The time of satellite overpass was thought either too early in the morning (7:30 for NOAA-6) or too late in the afternoon (14:30 for NOAA-7) because of cloud build-up.

The immediate motivation for Tucker and co-workers to start using AVHRR data was a predicted imminent failure of Landsat 3 because of long overdue replacement by Landsat 4 (Tucker 1996). A study was initiated to estimate crop production in the Nile delta with NOAA-AVHRR data and thus determine the potential of the instrument for vegetation monitoring (Tucker *et al.* 1984). Seasonal sums of NDVI were calculated from cloud free 1.1 km AVHRR data and compared with annually accumulated aboveground biomass and crop yield. The relationships between these variables were similar to relationships found in earlier studies where the vegetation index was determined from ground studies with hand-held radiometers (Tucker 1979, figure 2.2). The Nile-delta study was repeated for Senegal with NOAA-7 data (Tucker *et al.* 1983, 1985b) and for other parts of the Sahel with similar results (Justice 1986, Prince and Justice 1991).

During the first year of the Senegal study Tucker and co-workers were fortunate that most of the AVHRR data were cloud free (Tucker *et al.* 1983). This was not the case for the second year of the Senegal study. To obtain spatially continuous fields of NDVI data, several techniques were investigated to fill in missing data as a result of cloud screening and to minimize the effects of the atmosphere and bidirectional reflectance properties of the surface (Kimes *et al.* 1984, Holben 1986). It was decided to form 10-day or monthly NDVI composites by selecting the maximum NDVI for each picture element (pixel) over the period considered. This maximum value compositing technique was implemented by the global inventory, modeling, and monitoring system (GIMMS) group to process AVHRR data into 10-day NDVI composites of Africa in near real-time. These composites were, amongst other

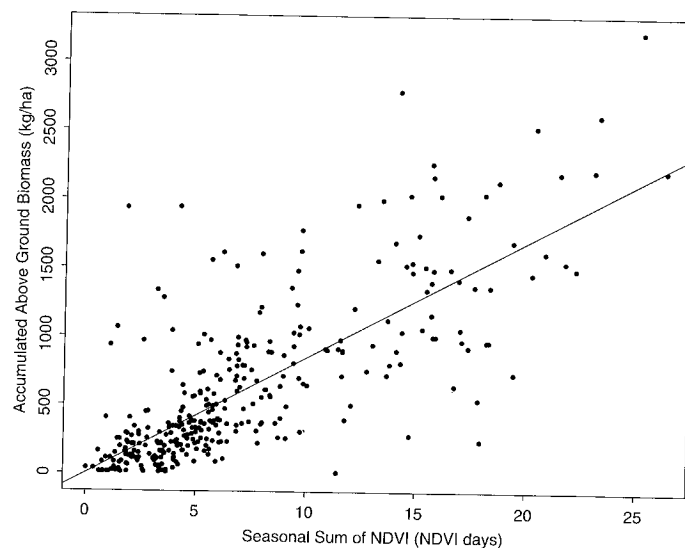


Figure 2.2: *Seasonally summed normalized difference vegetation index (sum of NDVI values over the growing season) versus accumulated aboveground biomass for sites in Senegal, Mali, and Niger (Courtesy Dr. S.D. Prince, University of Maryland at College Park, and Dr. C.J. Tucker, NASA/Goddard Space Flight Center).*

applications, used by the United Nations Food and Agricultural Organization (FAO) for famine early warning and desert locust detection (Hielkema 1990).

In 1983, NOAA started processing the Global Vegetation Index (GVI) dataset (Tarpley *et al.* 1984). The availability of the GVI and GIMMS-NDVI datasets prompted a host of new research on the spatial distribution and temporal dynamics of vegetation over large areas. For example, Tucker *et al.* (1985a) obtained a landcover classification of Africa from NOAA-AVHRR data based on the phenology (seasonality) of vegetation, Goward and Dye (1987) studied net primary production in North America, Malingreau *et al.* (1985) used AVHRR derived NDVI and brightness temperature data to detect forest fires in southeast Asia during the 1982 El Niño drought, Malingreau and Tucker (1988) investigated deforestation in South America, and Tucker *et al.* (1986a) studied the relationship between the annual cycles of NDVI and the seasonal drawdown of atmospheric CO₂ by vegetation.

When multi-year NOAA-AVHRR datasets became available, several shortcomings were noticed. These shortcomings are caused by changes in the sensitivity of the visible and infrared sensors (Price 1987, Holben *et al.* 1990), scattering and absorption by atmospheric constituents, soil background effects, cloud contamination, and errors in navigation of the satellite. In particular, the change in the data receiving protocol from one NOAA platform to the next revealed large discontinuities in the AVHRR data. Several techniques were developed to account for these inconsistencies. Sensor degradation and instrument calibration were estimated from statistical analysis

of global data (Brest and Rossow 1992); from calibrated sensors flown on aircraft over invariant desert targets at the same time as the satellite overpass (Smith *et al.* 1988, Abel *et al.* 1993); from year-to-year changes over desert targets (Staylor 1990, Kaufman and Holben 1993, Los 1994, Los 1998, Appendices A and B); and from ocean glint, cloud tops, and radiative properties of the atmosphere (Vermote and Kaufman 1995).

Improved algorithms for the navigation of imagery from NOAA satellite were developed using more accurate orbital models (Rosborough *et al.* 1994). Corrections were developed for atmospheric effects (Holben *et al.* 1991, 1992, Soufflet *et al.* 1991, Justice *et al.* 1991a, Tanré *et al.* 1992), cloud contamination (Eck and Kalb 1991, Stowe *et al.* 1991, Gutman *et al.* 1994), dependence of surface reflectance on viewing and solar angles (Roujean *et al.* 1992, Privette *et al.* 1995), and reflection from soil background (Qi *et al.* 1994). The implementation of some of these corrections is straightforward, others require data from additional sources that cannot be obtained with sufficient accuracy (Chapter 3).

With the availability of longer, multi-year NOAA-AVHRR data records, it became possible to study the effects of interannual variations in climate on vegetation. One example is the El Niño phenomenon—a warming of the eastern equatorial Pacific Ocean that has been associated with disruptions in convection patterns over large areas around the globe leading to changes in rainfall distribution and drought occurrences. Myneni *et al.* (1995) studied the occurrence of anomalies in NDVI during an El Niño for South America and Australia; and Anyamba and Eastman (1996) found evidence for El Niño related NDVI anomalies in Africa.

To improve modeling of the exchange of water, energy, and momentum between the terrestrial biosphere and the lower atmospheric boundary layer, Dickinson (1984) developed the Biosphere Atmosphere Transmission Scheme (BATS) for climate studies with general circulation models of the atmosphere (GCMs) and Sellers *et al.* (1986) developed in parallel the Simple Biosphere (SiB) model. These models described the water, energy, and momentum fluxes as interdependent processes regulated by the vegetation instead of independent processes as was previously done in “bucket” models (Budyko 1974). In an updated version of SiB, referred to as SiB2, improved photosynthesis and stomatal conductance models (Collatz *et al.* 1991, 1992) and an improved canopy model (Sellers *et al.* 1992) were implemented (Sellers *et al.* 1996a). In SiB2 biophysical parameters were estimated from NOAA-AVHRR NDVI data (Los *et al.* 1994, Sellers *et al.* 1996b), which led to a more realistic spatial and temporal distribution of vegetation compared to the previous version of SiB (Sellers *et al.* 1996b, Randall *et al.* 1996, Appendix D), and allowed modeling of carbon exchange between the atmosphere and biosphere (Sellers *et al.* 1996c, Den-

ning *et al.* 1995, Chapter 8). The SiB2-GCM driven by satellite derived biophysical parameters will aid our understanding of the global carbon cycle and the effects of increasing atmospheric CO₂ on the global climate (Sellers *et al.* 1996a, b, c, Randall *et al.* 1996, Denning *et al.* 1995), the interactions between vegetation and climate, and the role of vegetation as a net terrestrial carbon sink (Tans *et al.* 1990, Keeling *et al.* 1995).

2.4 Relationships Between NDVI and Biophysical Parameters

The results of the initial AVHRR-based vegetation studies were based on empirical relationships between NDVI and biophysical parameters such as above-ground biomass, leaf area index, and fraction of vegetation cover. Physically-based models and field measurements of light transport in a vegetation canopy revealed similar relationships and thus provided a physical explanation for the correlations between biomass and AVHRR observations (Kumar and Monteith 1982, Daughtry *et al.* 1983, Asrar *et al.* 1984, 1985, 1986, Sellers 1985, Tucker and Sellers 1986).

Underlying the relationships between NDVI and various biophysical parameters such as biomass and leaf area index are the unique reflective properties of green leaves. Figure 2.3 shows the reflectance as a function of wavelength for a grass (solid line) and a soil (dotted line). The leaves strongly absorb solar radiation in the visible band between 0.4 and 0.7 μm and at the same time strongly reflect in the near-infrared between 0.7 and 1.3 μm . Because of the strong absorption in the spectral region from 0.4 to 0.7 μm , the radiation in this band is referred to as Photosynthetically Active Radiation or PAR. The absorption of PAR within the leaves is for the most part caused by the leaf pigments chlorophyll a, chlorophyll b, and carotenoids (Salisbury and Ross 1969). The reflection by leaves of near-infrared radiation is due to differences in refractive indices between intercellular spaces, hydrated cells and the irregular facets of cell exteriors, and to a smaller extent by leaf material smaller than 1 μm , (Gates *et al.* 1965).

Compared to the reflectance of leaves, the reflectance of the soil in the infrared is only moderately higher than the reflectance in the visible. Although leaf spectra vary, the large differences between red and infrared reflectance occur for all photosynthetically active leaves and this allows us to distinguish leaves from other remotely sensed objects such as water, soils, and clouds. Besides the leaf and soil spectra, figure 2.3 also shows the band widths of AVHRR channels 1 and 2. Channel 1 coincides with a spectral region of maximum leaf absorption (red) and channel 2 with a spectral region of maximum leaf reflectance (near-infrared).

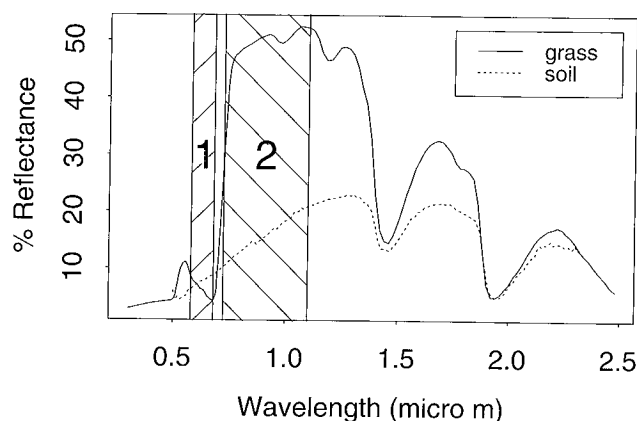


Figure 2.3: Plot of leaf reflectance (continuous line) and soil reflectance (dotted line) as a function of wavelength (μm). The bars indicate the spectral bandwidths of NOAA-AVHRR channels 1 and 2. AVHRR channel 1 collects data from a spectral region where healthy leaves strongly absorb solar radiation (reflectance is small), and channel 2 collects data from a spectral window where leaves strongly reflect solar radiation (absorption is low).

The NDVI is a function of the difference between channel 2 and channel 1 reflectance (equation 2.1) and is therefore a measure of the slope around $0.7 \mu\text{m}$ indicative of photosynthetically active leaves. Several authors have investigated the relationship between the fraction of photosynthetically active radiation (FPAR) absorbed by vegetation and NDVI or functionally equivalent vegetation indices: Hall *et al.* (1990) found a near linear relationship between FPAR and spectral vegetation indices for clumped vegetation; Asrar *et al.* (1992) found that while the relationship between FPAR and NDVI was fairly independent of model formulation, the relationship between leaf area index (LAI) and NDVI did change between models of various degrees of complexity; and Sellers *et al.* (1992a) showed that relationships between NDVI and total leaf area index (green and dead leaves plus branches and stems) vary widely between vegetation morphologies but that the relationships between vegetation indices, FPAR, photosynthesis, and albedo are more consistent. Moreover, Sellers *et al.* (1992a) posited that because the relationships $\text{NDVI} \rightarrow \text{FPAR} \rightarrow \text{photosynthesis}$ were approximately linear, they should be largely scale-invariant. These relationships apply to the live green material in the canopy, rather than the total of live and dead leaves and woody biomass. The NDVI has been associated with other parameters related to vegetation such as transpiration (Box *et al.* 1989), CO_2 fluxes between the atmosphere and the land surface (Tucker *et al.* 1986a, Fung *et al.* 1987), Net Primary Production of vegetation (NPP, see Goward and Dye 1987, Prince 1991, Potter *et al.* 1993), moisture availability to plants (Nicholson *et al.* 1990; figure 2.4), and biomass accumulated over the

growing season (Tucker *et al.* 1984; figure 2.2).

2.5 Desert Margin Studies

A strong relationship between changes in vegetation and changes in climate was first proposed as an important mechanism for desertification. The term desertification is most often used to describe the advance of desert-like conditions (United Nations Conference on Desertification 1977). Poor land management coupled with increased population are often blamed for catastrophic desertification. In the mid-seventies several authors reported an expansion of the Sahara estimated at a rate of 5.5 km per year (Lamprey 1975). This desert encroachment had direct consequences for humans, animals, and plants, and it was suggested that it could trigger a positive feedback loop on the (local) climate that would further increase the desert expansion.

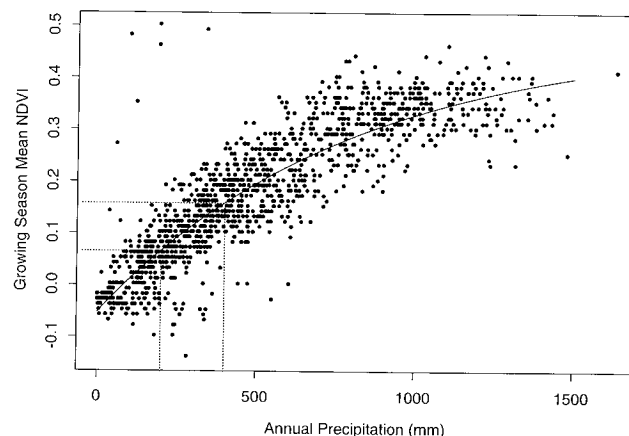


Figure 2.4: Relationship between annual precipitation rates and NDVI values averaged over the growing season. The relationship saturates at annual rainfall rates of 1000 mm (Courtesy Dr. C.J. Tucker, NASA/Goddard Space Flight Center).

Charney *et al.* (1975) proposed a feedback mechanism by which changes in vegetation would affect rainfall. A decrease in vegetation would result in an increase in ground surface albedo because albedo values of vegetation are typically lower than values of bare soil. The decrease of ground surface albedo leads to a reduction in the total (latent and sensible) heat absorbed by the ground surface and results in radiative cooling of the overlying air. This either enhances large area subsidence or suppresses convection and thus reduces the amount of associated rainfall. Charney *et al.* (1975) posited that this mechanism would be especially important for regions like the Sahara because (1) large area subsidence already occurs in this region, (2) most of the rainfall is from cumulus (convective) clouds, and (3) the transport of heat by

winds is too weak to counteract the effect of changes in the albedo. To take into account other non-local meteorological effects, especially the effects of monsoon circulation, Charney *et al.* (1975) tested their feedback mechanism in an atmospheric general circulation model and found that the changes that they imposed on the land surface albedo were sufficiently strong to overcome these other non-local effects.

Charney *et al.* (1975, 1977) made a similar argument for the reversed mode of the feedback loop, *i.e.*, more vegetation leads to lower albedo, which leads to more heat absorption by the land surface, higher evaporation rates, higher rainfall amounts and more vegetation. They thus established a link between variations in land surface vegetation and (local) climate. Since the report of Charney *et al.* (1977), studies were done with improved landsurface models in which interdependent vegetation related parameters (*e.g.*, leaf area index, roughness length, initial soil wetness) were altered at the same time. These studies showed that the local evaporation rate had a larger feedback on precipitation than the albedo (*e.g.*, Xue and Shukla 1991).

A positive feedback is by its very nature highly unstable, it results in a runaway effect when left by itself, and it is therefore obvious that the positive feedback between climate and vegetation is not the only mechanism at work in the Sahel. Large weather systems such as the seasonal movements of the intertropical convergence zone (ITCZ) that are driven by warming and cooling of the oceans dominate the Sahelian rainfall. Nevertheless, the mechanism is likely to enhance variations in the local climate near desert margins, and for this reason, expansions and contraction of desert margins are thought to be an important indicator of global climate change.

The rate of desertification of 5.5 km per year estimated by Lamprey (1975) was questioned by Helldén and co-workers (Helldén 1984, 1988, Olsson 1985). They showed that the high rates of desertification were derived from local areas and were not valid for the entire Sahel. Moreover, the climate in the Sahel is characterized by cycles of increasing and decreasing wet and dry conditions (Nicholson *et al.* 1988, Nicholson 1993). The study of Lamprey (1975) compared data from a wet and a drought cycle and thus overestimated the rate of desert encroachment.

Tucker *et al.* (1991a, 1994) studied the interannual variation of AVHRR-based NDVI data to investigate the rate of desertification for the entire Sahel. The study of Tucker *et al.* (1991a) used monthly GIMMS NDVI composites for Africa (section 4.2). To determine more accurately the interannual variations in NDVI, the data were corrected for sensor degradation and soil background effects. The correction for sensor degradation was done by adding monthly offsets, ΔNDVI , to the NDVI

$$\text{NDVI}_d = \text{NDVI}_p + \Delta\text{NDVI}, \quad (2.2)$$

where NDVI_p stands for preflight-, and NDVI_d for desert-calibrated NDVI. Equation 2.2 is an adequate approximation for sensor degradation between NDVI values of 0 and 0.3 (Kaufman and Holben 1993, Los 1993, Appendix A). The soil background effect was estimated from areas with a standard deviation over the growing season smaller than 0.04 NDVI. For these areas NDVI values corresponding to the highest channel 5 brightness temperatures during the end of the dry period (1 to 21 March) of 1989 were subtracted from the annual time-series. NDVI data were then summed over the growing season and a relationship was derived with annual rainfall using linear regression (figure 2.4). By defining the Sahelian zone as the region with an average annual precipitation between 200 and 400 mm and relating this number to a seasonally-summed NDVI, it became possible to detect year-to-year changes in the aerial extent of vegetation in the Sahel. These variations imply an expansion of desert-like conditions in the Sahel from 1981 to 1984 (figure 2.5), which was a year of severe drought. After 1984, annual precipitation increased in the region which resulted in a gradual increase in the amount of vegetation in the Sahel. Superposed on this long-term trend are interannual variations in vegetation extent caused by interannual variations in rainfall. Ellis and Swift (1988) reported that these areas are in non-equilibrium by nature, *i.e.*, they are always perturbed by abiotic forces, usually droughts.

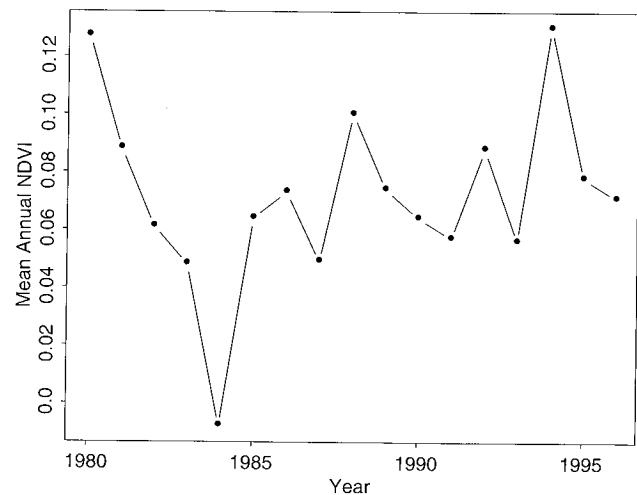


Figure 2.5: Spatially-averaged NDVI of the Sahel (defined as the region south of the Sahara with average annual precipitation between 200 and 400 mm; see Tucker *et al.* 1991a, 1994) for the period of 1981–1995 (Courtesy Dr. C.J. Tucker NASA/Goddard Space Flight Center).

The results from the study by Tucker clearly demonstrate that in order to assess desertification in the Sahel, data must be interpreted in relation to long-term climatic cycles of drought and wetness. It is then possible to estimate the effects of localized degradation and erosion

as deviations from the long-term trend. Several authors (Helldén 1984, 1988, Olsson 1985, Prince 1986, 1991) concluded that increased rangeland activity and intensified agricultural practices have led to, for example, a shift in vegetation composition to species not favored by cattle, shorter periods between fallow and cultivated cycles, increased erosion, and decreased infiltration capacity of the soil, rather than a rapid expansion of the desert. A similar shift from palatable grasses to less palatable shrubs and trees as a result of intensified grazing by livestock was noticed in Botswana (Tolsma 1989, Veenendaal 1991).

2.6 Conclusion

A review is provided of studies reporting relationships between NDVI and vegetation parameters such as net primary production (NPP), crop yield, aboveground biomass accumulated over the growing season, the fraction of photosynthetically active radiation absorbed by the green parts of vegetation (FPAR) and leaf area index. Theoretical studies and field experiments indicate that NDVI is closest related to FPAR: thus the capacity to assess the amount of land surface vegetation with AVHRR data is based primarily on the relationship between NDVI and FPAR, *i.e.*, the NDVI is related to the ability of plants to capture solar radiation in the visible part of the spectrum.

The usefulness of AVHRR data for the assessment of interannual variations in vegetation related to interannual variations in climate (in this case precipitation) was illustrated in the Sahel boundary study. This study also indicates that AVHRR data must be adjusted for variations in the sensitivity of the sensor to obtain meaningful results. The effect of other sources of interference in AVHRR data, such as variations in atmospheric composition, cloud occurrence, and variations in solar zenith angle and viewing angle geometry are also of importance. These effects are discussed in the next chapter.

Chapter 3

Interferences With AVHRR Landsurface Observations

Interferences with Advanced Very High Resolution Radiometer (AVHRR) land surface observations are either related to the design of the National Oceanic and Atmospheric Administration (NOAA)-AVHRR and therefore unique to this satellite-sensor system or they are related to external sources and therefore affect observations by other satellite sensor systems as well. Amongst interferences resulting from the design of the NOAA-AVHRR are inaccuracies in the navigation of the satellite data (Emery *et al.* 1989), the method of onboard data re-sampling (Kidwell 1995), the lack of onboard calibration to correct for sensor degradation in the AVHRR (Price 1987, Kaufman and Holben 1993), and the selection of an early afternoon crossing time, which more-or-less coincides with the time of maximum cloud development around the globe (Sellers and Schimel 1993). Interference caused by external factors are caused by clouds, atmospheric constituents, variations in viewing and solar angles in combination with surface bidirectional reflectance properties of the land surface, topography, and soil background reflectance. These effects often enhance or counteract each other and must be viewed in concert.

3.1 Image Navigation

Image navigation is the registration of pixels to a geographic grid. Accurate navigation requires an accurate model of the satellite orbit. Such a model has two components (Baldwin and Emery 1993): one relates to the gravitational effects of the geode on the satellite's orbit (Brush 1988) and the other to deviations in the satellite's position, timing, and altitude, and the orientation of the sensor (Ho and Asem 1986, Emery *et al.* 1989, Baldwin and Emery 1993). Baldwin and Emery (1993) discuss several image navigation models for the NOAA-AVHRR. The simplest model describes the NOAA orbit as a circular motion around the Earth. This model leads to errors of 35 km or more in the registration of picture elements (Baldwin and Emery 1993). The most advanced models

use an elliptical model, which has corrections for short term orbital oscillations that are obtained from ephemeris data (Kidwell 1995), and corrections for errors in the orientation of the sensor that are determined from ground control points. These models locate data to a geographic grid with an accuracy of 1 km or better. A model of intermediate complexity based on the level 1B orbital parameters from NOAA results in an average error of 6 km (Baldwin and Emery 1993). For the same model, NOAA claims an error of similar magnitude (approximately 5 km) and Holben (1986) found average along-track errors of 4.8 km and across-track errors of 3.6 km, but also documented deviations as large as 17 km.

3.2 Viewing Geometry

The viewing geometry—solar zenith angle, viewing angle, and azimuth angle between the Sun and the sensor—is determined by latitude, time of year, scan angle, and local crossing time of the satellite. The land surface signal measured by the satellite changes as a function of viewing geometry because of the bidirectional reflectance properties of the land surface and the atmosphere. We discuss variations in viewing geometry with the overpass time of the satellite in the next two subsections and the bidirectional reflectance properties of the land surface and atmosphere in section 3.7.

3.2.1 Solar Zenith Angles

Solar zenith angles are a function of the local crossing time of the satellite and the viewing angle. For a particular area, the near sun-synchronous polar orbit of the NOAA satellite allows the AVHRR to collect data from day to day at almost the same local crossing time and range of solar zenith angles. However, solar zenith angles at time of observation vary as a function of latitude, time of year, and the time since launch of the satellite (figure 3.1). Variations in solar zenith angle as a func-

tion of time since launch are caused by a gradual drift from the original target equatorial crossing time of approximately 14:30 to crossing times of 16:00 or even later (Price 1991). The effect of orbital drift is largest for low latitudes and smaller at high latitudes. The AVHRR data reflect differences due to an altered illumination geometry, the bidirectional reflectance distribution function of the land surface and atmospheric effects. These effects are larger on the measured radiance values and partially compensate for each other in the Normalized Difference Vegetation Index (NDVI): the normalization by the sum of channels 1 and 2 reflectance values in the calculation of the NDVI provides a first order correction for solar zenith angle variations and associated effects (Kimes *et al.* 1984).

3.2.2 Viewing Angles

Viewing angles are a function of the scan angle of the AVHRR, which can be as large as 55° off-nadir, and the curvature of the Earth. The surface reflectance measured by the satellite varies with solar zenith angle and viewing angle (See below: Bidirectional Reflectance Distribution Function). The pixel size varies also as a function of viewing angle. A pixel of 1.1 by 1.1 km at nadir is approximately 2.4 by 6.9 km (along track and across track respectively) at 55° off-nadir.

3.3 Sensor Degradation

Sensor degradation results in gradual changes in the observed reflectance over the lifetime of the sensor and leads to discontinuities between successive instruments (figure 3.2.a; Holben *et al.* 1990, Kaufman and Holben 1993, Los 1993, Los 1998, Rao and Chen 1994). NOAA provides a preflight calibration for the visible and near-infrared channels, which relates the signal received by the satellite to a pre-launch standard (Kidwell 1995). This preflight calibration is not updated during the operation of the AVHRR, hence it does not take sensor degradation into account. Correction of AVHRR data for sensor degradation is important to do meaningful interannual comparisons. Several coefficients have been estimated for historic AVHRR data (*e.g.*, Vermote and Kaufman 1995). Currently, these coefficients are not available for real-time applications (Teillet and Holben 1994). A technique exists to derive calibration coefficients from NDVI data over desert targets (Los 1998). This technique can be used to obtain a good approximation of the rate of sensor degradation in near-real time in cases where channels 1 and 2 data components of the NDVI are not available.

3.4 Clouds

Clouds hide a significant portion of the land surface from the satellite. The timing of maximum cloud development in the humid regions of the world more-or-less coincides with the afternoon overpass time of the NOAA-7, -9, and -11 satellites (Sellers and Schimel 1993). Clouds appear as very bright objects in channels 1 and 2 (reflectance generally larger than 0.35 in both channels) and have low, negative NDVI values (-0.05 to -0.2 NDVI). Most cloudy data values can be identified by their low surface temperatures and high brightness and can be eliminated. Mixed pixel data of partly clouds and partly land surface are difficult to identify automatically and are therefore unintentionally incorporated in land surface datasets. The effect of sub-pixel clouds is most pronounced for areas with high NDVI values, the effect in this case being largest on the visible reflectance. For example, a cloud with a reflectance of 0.5 in the visible band covering 20 % of a land surface pixel with a reflectance of 0.05 can increase the apparent surface reflectance to 0.13 (Kaufman 1987). The effect of mixed pixel cloud contamination on the NDVI is substantial, although smaller than on channel 1. Assuming a similar cloud effect on a surface near-infrared reflectance value of 0.4, the change in NDVI is $0.29/0.55 - 0.35/0.45 = 0.25$ NDVI. Studies on cloud distributions show that the frequency of cloud occurrence is inversely related to the cloud diameter, therefore sub-pixel size clouds (diameter smaller than 1.1 km) occur the most frequently (Planck 1969, Wielicki and Welch 1986). Given that areas with dense cloud cover occur in general over the most densely vegetated areas, it follows that cloud contamination is a serious problem for vegetation monitoring.

Figure 3.2.b is an example of the effect of cloud contamination on a NDVI time-series over an evergreen forested area in equatorial Africa. The NDVI should be high throughout the year; instead, data are missing during the end of 1989 and heavily cloud contaminated near the end of 1990. Several techniques exist to screen for clouds: Holben (1986) uses a single temperature threshold, Stowe *et al.* (1991) based a cloud identification technique on various combinations of AVHRR channels, Gutman *et al.* (1994) based cloud identification on departures from mean climatic land surface temperature conditions; and Cihlar (1996) identified clouds based on departures in the NDVI from smoothed time-series.

3.5 Atmospheric Constituents

Atmospheric constituents absorb and scatter solar energy radiated to and reflected from the Earth's surface. The physics that describe the scattering and absorption processes are well understood. Given the type and the concentrations of atmospheric constituents, the ef-

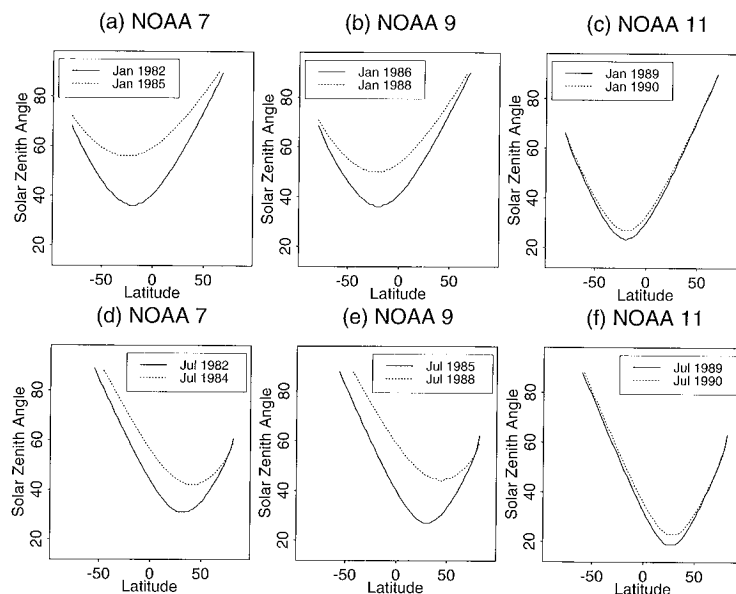


Figure 3.1: Values of solar zenith angle at the local overpass time of the NOAA-7, -9 and -11 satellites. Variations occur as a function of latitude, time of year, satellite, and time in operation. (a, d) start and end of NOAA-7 for January (continuous line) and July (dotted line), (b, e) same for NOAA-9, (c, f) difference between first and second year of operation of NOAA-11. NOAA-7, NOAA-9, and NOAA-11 show differences in solar zenith angle as a function of latitude, time of operation of the NOAA-AVHRR, and time of year. Differences as a function of time of operation are largest for low latitudes and smallest for high latitudes. The differences in solar zenith angle between summer and winter can be as high as 30 degrees. Note that NOAA-11 started at a local crossing time one hour earlier than NOAA-7 and -9; hence solar zenith angles are lower at the start of NOAA-11.

fects of scattering and absorption can be calculated with programs such as the LOW resolution TRANsmittance (LOWTRAN) code (Kneizys *et al.* 1983) or the Second Simulation of Satellite Signal in the Solar Spectrum (6S) model (Tanré *et al.* 1986, Vermote *et al.* 1995). However, since the composition of the atmosphere is generally unknown, these models cannot be used to correct the satellite observations. Atmospheric effects of importance to AVHRR bands 1 and 2 are Rayleigh or molecular scattering (O_2 , N_2 , A), absorption and scattering by gases (principally ozone, CO_2 , and water vapor), and scattering by aerosols (see *e.g.*, Chahine *et al.* 1983, Tanré *et al.* 1992). Table 3.1 from Tanré *et al.* (1992) indicates the effect of atmospheric constituents on land surface observations. In general, atmospheric effects are largest for observations from dark surfaces in the visible band, *e.g.*, water and dense vegetation. Water vapor reduces the land surface reflectance in the near-infrared channel of the AVHRR, because this channel contains a water vapor absorption band (Justice *et al.* 1991a).

The effects of atmospheric scattering and absorption also depend on the spectral properties of the land surface, viewing angle, and solar zenith angle. Examples of atmospheric effects on NDVI time-series are shown in figures 3.2.c and 3.2.d. Figure 3.2.c shows the impact of volcanic dust from the Mt. Pinatubo eruption in July 1991 on a

NDVI time-series of an equatorial forest in Africa. The NDVI decreases sharply after the eruption with about 0.25 and then gradually increases. The effect of the Mt. Pinatubo aerosols on the NDVI was noticeable for about one-and-a-half years after the eruption (Vermote *et al.* 1994). The effect of water vapor is illustrated in a NDVI time-series from an area in the northern part of the Sahel (Figure 3.2.d). During the start of the rainy season around May the intertropical convergence zone (ITCZ) moves into the area. The increased humidity in the atmosphere as a result decreases the reflectance measured in the near-infrared AVHRR channel and thus decrease the NDVI (Justice *et al.* 1991a; Table 3.1).

In some cases the effect of atmospheric constituents on AVHRR measurements can be taken into account. The effects of scattering on molecules, Rayleigh scattering, can be estimated since the distribution of molecules in the atmosphere is known. Variations in atmospheric ozone concentrations can be accounted for by climatic mean ozone concentrations or by satellite observations, *e.g.*, from the Total Ozone Mapping Spectrometer (TOMS) on board the Nimbus-7 satellite (Herman *et al.* 1991, Stolarski *et al.* 1991) and the Solar Backscatter ultraviolet (SBUV)/2 instrument on board the NOAA satellites (Hollandsworth *et al.* 1995). Water vapor and atmospheric aerosols vary highly in concentration over space

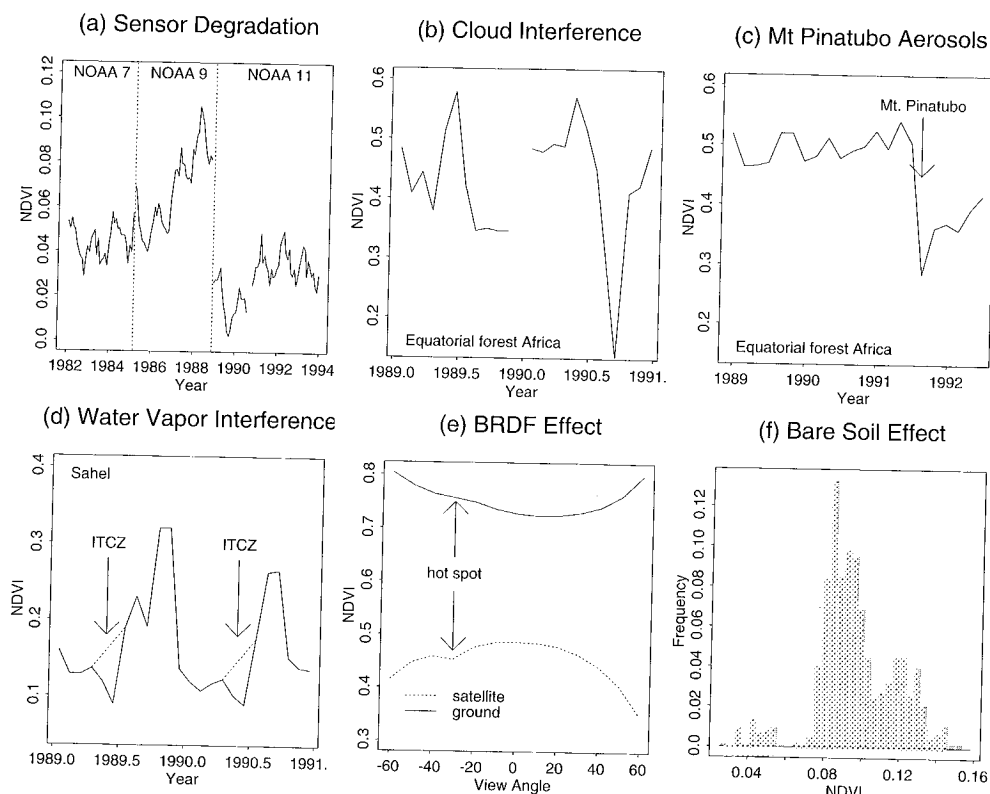


Figure 3.2: Variations in the NDVI as a function of (a) sensor degradation: the NDVI from desert sites is assumed to exhibit only small variations over time. The trends in the NDVI data (c.g., for NOAA-9) are the result of sensor degradation, the discontinuities between satellites (compare data for NOAA-9 and NOAA-11) are caused by differences in calibration between satellites. (b) clouds: NDVI data from an equatorial forest should exhibit low seasonal variation. The strong temporal changes in the NDVI and the missing data are caused by cloud contamination. (c) effect of aerosols from the Mt. Pinatubo eruption (July 1991) on the NDVI. The eruption of Mt. Pinatubo resulted in high concentrations of atmospheric aerosols worldwide. These aerosols strongly increased the reflectance in the visible channel of the AVHRR and decreased the NDVI. Aerosol concentrations gradually diminished over time; the effects were noticeable in the NDVI data for about one-and-a-half years. (d) The near-infrared channel of the AVHRR contains a water vapor absorption band. Increases in atmospheric water vapor at the start of the rainy season in the Sahel related to movements of the Intertropical Convergence Zone (ITCZ), decrease the measured reflectance in the near-infrared channel and decrease the NDVI. (e) Bidirectional effects in the NDVI as a function of viewing angle measured for ground-measured data (top line) and data measured at the top of the atmosphere (bottom line). The ground bidirectional distribution function (BRDF) was simulated with a model from Roujean *et al.* (1992) and the atmospheric effects for a mid-latitude continental atmosphere with fairly high aerosol concentration were simulated with the Second Simulation of Satellite Signal in the Solar Spectrum (6S) program (Vermote *et al.* 1995). The ground-measured NDVI data are higher overall than the data measured at the top of the atmosphere and show an inverse relationship with viewing angle. A small hotspot effect is found at 30° off-nadir in the backscatter direction. This effect occurs when the observer is in the principal plane with the Sun on his/her back and the view zenith angle is equal to the solar zenith angle. In this configuration the amount of shadowing appears at a minimum for the observer (provided the distance between the observer and the target is sufficiently large). (f) Frequency distribution of variations in the NDVI from the Sahara (27.5° N, 1.25° W to 27.4° N, 23.7° E). Most of the variation in the NDVI can be attributed to variations in soil background reflectance, not to variations in vegetation greenness.

and time and it is therefore difficult to correct their effects. It is possible, at least in principle, to obtain their distribution from a ground-based sun-photometer network. Recently, such a network was implemented for selected areas over the globe (Holben *et al.* 1991). At present, satellite-based estimates of atmospheric water vapor (Susskind *et al.* 1984, Holben and Eck 1990, Reuter *et al.* 1988) do not have sufficient accuracy to correct visible

and near-infrared observations from the land (Justice *et al.* 1991a). Aerosol effects from volcanic eruptions such as the eruption of El Chichon in Mexico in 1982 and of Mt. Pinatubo in the Philippines in 1991 have been estimated and accounted for with some degree of success (McCormick and Veiga 1992, Stowe *et al.* 1992, Vermote *et al.* 1994).

Localized aerosol effects over land can be estimated

Table 3.1: Estimates of the effects of atmospheric ozone, molecules, aerosols, and water vapor on the NDVI and the component AVHRR channels 1 and 2 values (modified after Tanré *et al.* 1992).

Atmospheric Effect	Channel 1	Channel 2	NDVI	Largest Effect on
Ozone Absorption	5–15 % <	negligible	0–0.03 >	sparse vegetation
Molecular Scattering	0.02–0.07 >	0.005–0.025 >	0–0.1 <	dense vegetation
Aerosols (Moderate)	0.02–0.08 >	0.02–0.08 >	0–0.1 <	dense vegetation
Aerosols (High)	0.10–0.15 >	0.10–0.15 >	0.1–0.2 <	dense vegetation
Water Vapor	0–5 % <	10–30% <	0.01–0.1 <	sparse vegetation

either from dark surfaces such as lakes and dark dense vegetation, or from areas with high brightness contrast between adjacent pixels (Tanré *et al.* 1992, Holben *et al.* 1992). The spatial coverage of dark or high contrast areas is sparse, and as a result satellite based aerosol corrections have not been implemented for large areas.

3.6 Terminator Effect

High solar zenith angles near the twilight terminator are associated with low light intensities and extremely large atmospheric path lengths for incoming solar radiation. The contribution of the atmosphere to the signal measured by the AVHRR is therefore substantial, to the extent that the signal from the surface is completely obscured. This effect is clearly visible in AVHRR imagery and is referred to as the terminator effect (Holben 1986).

3.7 Bidirectional Reflectance

The AVHRR measures data from a wide range of scan angles (-55° to 55° off-nadir) and solar zenith angles (between 15° and 90°). The illumination and viewing geometry affects the NDVI dependent on the land surface and atmospheric bidirectional reflectance distribution function (BRDF), which describes the reflected radiation from the surface as a function of the angle of incident radiation, the viewing angle, and the azimuth between the illumination source and the measuring device. BRDF effects can be estimated from models that formulate the scattering, transmission, and absorption of solar radiation by green leaves in plant canopies and the soil background (Ross 1981, Goel 1988, Myneni *et al.* 1989, Li and Strahler 1985, Li *et al.* 1995).

In figure 3.2.e an example of variations in the NDVI with viewing angle as a result of BRDF is shown. The BRDF was derived by fitting a simple model (Roujean *et al.* 1992) to data obtained during the First ISLSCP¹ Field Experiment (FIFE) by Deering *et al.* (1992b; see

also Deering and Leone 1986). It shows a BRDF obtained from surface measurements (top curve) and a BRDF obtained from satellite measurements (bottom curve). The satellite-measured BRDF was calculated from the land surface measured BRDF by simulating the effect of a continental mid-latitude atmosphere with 6S (Vermote *et al.* 1995). The difference between ground and satellite-measured BRDF is fairly large because of the high aerosol content used in this simulation. The BRDF from ground measurements shows an increase in NDVI with viewing angle and a small hot-spot effect centered around a view zenith angle of 30° in the backscatter direction (figure 3.2.e).

The BRDF from satellite measurements shows the reverse, *i.e.*, a decrease in NDVI with increasing (off-nadir) viewing angle and maximum NDVI values at near-nadir viewing angles in the forward-scatter direction. The BRDF effect of the atmosphere is generally stronger than the land surface BRDF: compare the upward bowl shape of the relationship between NDVI and viewing angle at the ground with the reversed bowl shape for the relationship between NDVI and viewing angle relationship at the top of the atmosphere.

For ground-measured NDVI, the maximum tends to be at off-nadir viewing angles. This has important implications for maximum NDVI compositing: compositing on atmospherically corrected NDVI data will bias selection of data from off-nadir viewing angles where the change in NDVI as a function of viewing angle is largest, whereas compositing of data that are not corrected for the atmosphere results in selection of data at near-nadir (slight forward-scatter) viewing angles where the change in NDVI as a function of viewing angle is lowest. The large change in NDVI at high viewing angles for atmospherically corrected data causes large viewing angle dependent variations in the NDVI which may be visible in NDVI imagery as striping parallel to the satellite orbit. Implementing a successful correction for atmospheric effects should therefore include a correction for the land surface BRDF.

¹ISLSCP: International Satellite Land Surface Climatology Project

3.8 Topography

Shadowing effects in high relief areas affect the amounts of red and infrared radiation reflected by the land surface. They are dependent on solar zenith angle, viewing angle, and topography. Burgess *et al.* (1995) investigated topographic effects on AVHRR NDVI data with a digital elevation model to simulate the shadowing effects. They found topographic errors, defined as the relative difference between the signal from a variable terrain and the signal from a flat plane, as large as 13.5 % for 50 m resolutions. These errors became smaller with increasing pixel size; for pixels of 1.1 km resolution the error was less than 3 %. Only a small part of the decrease in error with increasing pixel size could be attributed to the resolution of the digital elevation model. Burgess *et al.* (1995) therefore concluded that the fairly strong topographic effects in high resolution data are greatly reduced in low resolution data.

3.9 Soil Background Effects

The reflective properties of a bare soil vary with its type and composition. Differences in the spectral response of channels 1 and 2 manifested by soil color and brightness result from variations in soil properties, such as the amount of iron and organic material present. Figure 3.2.f shows the variation in NDVI values over an area of the Sahara where the contribution of the bare surface to the signal measured by the satellite is large. The standard deviation of this sample is about 0.02 NDVI. A number of vegetation indices have been reported that claim to be less sensitive to the soil background effects than the conventional NDVI, such as the Soil-Adjusted Vegetation Index (SAVI; see Huete 1987, Huete and Tucker 1991). For the calculation of this index a constant is added to channels 1 and 2 reflectances. However, the soil background reflectance usually affects low and intermediate NDVI values more than high NDVI values because the increased vegetation cover tends to mask the soil. Since the correction term in SAVI is not dependent on vegetation cover fraction, it should not be applied to adjust high NDVI values. To accommodate this, Qi *et al.* (1994) developed the Modified SAVI (MSAVI). However, MSAVI has a problem similar to that of SAVI in that the maximum adjustment is applied to the high NDVI values where the adjustment should be small or negligible.

3.10 Bad Scans

At irregular intervals, observations by the AVHRR are subject to extreme errors, resulting in values out of the range of normal observations. These extreme values appear as distinct across-track lines of meaningless NDVI

values in AVHRR imagery. A cause generally mentioned for bad scans is the occurrence of problems at the ground receiving station such as interferences of nearby buildings and trees. Bad scans can easily be identified by visual inspection of the data and can be eliminated.

3.11 Conclusion

NDVI data contain useful information on the temporal and spatial distribution of vegetation. A limitation to the NDVI data is the presence of suspect data, generally with decreased values, that are due to persistent cloud cover, atmospheric attenuation, solar zenith angle variations, missing data, viewing geometry, misregistration, and sensor degradation. The magnitude of inconsistencies in NDVI data, when not accounted for, can be as large as 0.1 to 0.2 NDVI units. How the magnitude of these errors can be reduced by incorporating simple algorithms in the data processing stream is discussed in Chapter 4. The correction of several of the remaining errors in NDVI data after processing is discussed in Chapter 5.

Chapter 4

The GIMMS NDVI Dataset

4.1 Introduction

Several global multi-year landsurface datasets exist that are derived from the National Oceanic and Atmospheric Administration (NOAA) Advanced Very High Resolution Radiometer (AVHRR) data. The most common are: the Global Vegetation Index (GVI) dataset—weekly composites and 0.25° resolution—produced by NOAA (Tarp-ley *et al.* 1984, Gutman 1991, Gutman *et al.* 1995); the Normalized Difference Vegetation Index (NDVI) dataset—10-day, 15-day, or monthly composites, and 8 km resolution—produced by the Global Inventory, Modeling, and Monitoring System (GIMMS) group at the National Aeronautics and Space Administration (NASA) Goddard Space Flight Center (Tucker *et al.* 1994, Los *et al.* 1994, Appendix C) and the Pathfinder AVHRR land dataset—10-day composites and 8 km resolution—produced by a joint effort of NASA and NOAA (James and Kalluri 1994). The Maryland improved GVI was derived from NOAA's GVI dataset (Goward *et al.* 1994). It is important to stress at this point that the GVI, GIMMS, and Pathfinder datasets were derived from the same source and are therefore subject to the same instrument errors and interferences by clouds, atmosphere, illumination, and viewing angles. These datasets differ as a result of their processing protocols, however. Because of the large data volumes handled, the adopted procedures to diminish interferences must be seen as a compromise between effectiveness in terms of removing undesirable effects, and simplicity so as not to overburden the limited computing resources. For the present study the GIMMS NDVI dataset was used. Processing of the GIMMS NDVI is discussed in section 4.2 and the justification to use this dataset is discussed in section 4.3.

4.2 Processing

The GIMMS NDVI first generation dataset was developed by the GIMMS group at the National Aeronautics and Space Administration (NASA) Goddard Space Flight Center (Holben 1986, Tucker *et al.* 1991a, 1991b, 1994, Los *et al.* 1994). The dataset is arranged by con-

tinents. A complete record for Africa exists from August 1981 until the present. The current data record for the other continents is from 1982–1990. Processing of data for the other continents was postponed until a correction for aerosols from the Mt. Pinatubo eruption was implemented in a second generation processing system. Our discussion is limited to the first generation GIMMS data. For this dataset 10-day (Africa), 15-day (other continents), and monthly maximum value NDVI composites were processed.

The processing chain of the first generation GIMMS mapping system contains the following steps:

1. Organization of global NOAA-AVHRR level 1B data by continent. Level 1B data are stored as full global orbits by NOAA and include measurements of the land as well as the oceans. Organization by continent reduces the amount of data that must be processed and allows efficient manipulation of land-surface data in smaller coherent chunks.
2. Ingest of Channels 1, 2 and 5 data. Channels 1 and 2 are used to calculate the NDVI (step 5), and channel 5 is used for cloud screening (step 4).
3. The 45 outer pixels on either side of a scan are discarded to reduce the variation in NDVI as a result of viewing geometry. The threshold of 45 pixels corresponds to a scan angle of approximately 42° off-nadir.
4. Data with a channel 5 brightness temperature below 273 K (288 K for Africa) are assumed from clouds and are eliminated. This cloud screening technique does not identify data from warm clouds or partially cloud covered “mixed” pixels (Eck and Kalb 1991), and in addition it eliminates landsurface data with a brightness temperature below the threshold which results in missing values at high latitude areas during winter (figure 2.1.a).
5. Channels 1 and 2 digital counts are converted to radiances normalized for incoming solar radiation with the preflight calibration coefficients from

NOAA (Kidwell 1995):

$$L_{i,p}^N = \gamma_{i,p}(C_i - \Delta C_{i,p}) \quad (4.1)$$

with C_i the digital count in channel 1 or 2, $\Delta C_{i,p}$ the preflight offset in channel 1 or 2, $\gamma_{i,p}$ the preflight calibration coefficient which converts counts to reflectance values in case of an overhead Sun, $L_{i,p}^N$ the preflight calibrated radiance normalized for the top-of-the-atmosphere solar flux in channel 1 or 2, i refers to either channel 1 or 2, and p indicates preflight calibration. The cosine of the solar zenith angle is missing in equation 4.1, hence only in the case of an overhead Sun does this normalization provide reflectance values. Calibration coefficients are provided in Appendices A and B.

6. The NDVI is calculated according to

$$\text{NDVI} = \frac{L_{2,p}^N - L_{1,p}^N}{L_{2,p}^N + L_{1,p}^N} \quad (4.2)$$

The calculation of the NDVI from normalized radiance values (equation 4.2) is equivalent to the calculation of the NDVI from reflectance values (equation 2.1). The division by the sum of channels 1 and 2 normalized radiance values in the calculation of the NDVI reduces the impact of varying illumination conditions and shadowing effects caused by variations in solar zenith and viewing angle (Kimes *et al.* 1984).

7. The NDVI data are mapped to a geographic projection (a polyconic equal area projection for Australia and a Hammer Aitoff projection for the other continents) as daily data. The resolution of the global area coverage (GAC) data is reduced to allow display of a continental dataset on a 1280 by 1024 element screen. In cases where pixels overlap, the value of the pixel with the highest NDVI is used. This leads to selection of higher values than if the nearest neighbor of the element were selected.
8. The data are visually inspected for registration errors and bad scans. Registration of the data is verified by comparing the outlines of continents and rivers in the NDVI image with those in the Central Intelligence Agency (CIA) world data bank (WDB) II (Gorny 1977). When a mismatch between features is found, the entire image is shifted over a whole number of pixels which reduces the registration error to approximately 4–8 km. Bad scans are removed interactively.
9. The daily images are merged in 10-day, 15-day, or monthly composites by selecting for each pixel

the maximum NDVI for the period considered. Maximum NDVI compositing fills in the gaps between mapped orbits and missing values from cloud screening. Compositing also reduces the effects of the atmosphere, sub-pixel clouds, and viewing geometry (Holben 1986). The effectiveness of compositing depends on the frequency of occurrence of clouds and atmospheric effects (Kaufman 1987). For example, persistent clouds over tropical and subtropical areas cannot be completely removed with this technique. Linear structures with low NDVI values such as lakes and rivers tend to disappear as a result of errors in registration and maximum value compositing. Maximum value compositing tends to select data from 10° in the forward scatter direction.

The GIMMS NDVI data are not corrected for sensor degradation and atmospheric aerosols and are, to a degree, subject to the effects of clouds, viewing and illumination geometry. An approximate correction for sensor degradation can be applied to the NDVI data without recourse to the component channels 1 and 2 data (Appendices A and B). The root mean square error of this correction is 0.002 NDVI or less (Los 1993). This inaccuracy is smaller than the uncertainty in the estimation of the rate of sensor degradation—about 2 % (Vermote and Kaufman 1995). Adjustments for the effects of volcanic aerosols, clouds, and solar zenith angle are discussed in Chapter 5.

4.3 Discussion

Several AVHRR derived landsurface datasets exist besides the GIMMS NDVI dataset. The most commonly-used are the NOAA-GVI dataset and the NOAA/NASA Pathfinder dataset.

Three generations of the NOAA-GVI dataset exist. The first generation (Tarpley *et al.* 1984) covers the period of April 1982 until March 1985, the second generation covers the period of April 1985 until the present, and the third generation is a revision of the second generation dataset and it covers the same period. Incompatibilities exist between the first and second generation GVI due to differences in data navigating, resampling, and compositing. No cloud screening was applied to either the first or second generation GVI data. The third generation GVI uses second generation GVI data to identify clouds and to correct cloud-affected NDVI values. Compositing of the GVI is based on the maximum difference between channel 2 and channel 1, which favors selection of data from extreme backscatter viewing angles and increases the contribution of the atmosphere in the measured signal. No scan angle cut-off was applied to the data. The GVI contains several data layers besides the NDVI; channels 1 and

2 for the first, second, and third generation, and channels 4 and 5 for the second and third generation. Data in the first and second generation GVI were not calibrated, and no corrections were applied for volcanic aerosols from the El Chichon and Mt. Pinatubo eruptions.

The Pathfinder AVHRR landsurface dataset became available several years after the present study was initiated. The data are available as 10-day composites for the period of August 1981 until December 1992 at two spatial resolutions, one at 8 km resolution and the other at 1° by 1° resolution. The Pathfinder data are corrected for sensor degradation and include several data layers: five AVHRR channels, a cloud mask, a quality control flag, and viewing and solar zenith angles. The data were corrected for Rayleigh scattering and ozone absorption. No corrections were applied for aerosol and water vapor effects. There are some artifacts in the Pathfinder dataset that are not yet well understood. Also, after processing the entire dataset it became apparent that the effects of ozone absorption and Rayleigh scattering were only partially accounted for. In an updated version of the Pathfinder data adjustments were made to account fully for ozone and Rayleigh effects. As a result of the atmospheric correction, landsurface Bidirectional Reflectance Distribution Function (BRDF) effects are expected to be stronger and atmospheric BRDF effects are expected to be diminished compared to the GIMMS NDVI dataset. The global one-degree data were not screened for clouds prior to averaging, despite the availability of a cloud mask in the 8 km dataset.

When the present research was initiated only the first and second generation GVI datasets were available as alternatives for the GIMMS NDVI dataset. The GIMMS NDVI dataset was preferred because of its consistent processing history, which resulted in a long compatible data record, the compositing method, and cloud screening. The Pathfinder dataset could have been an alternative for later stages of the project. The reason we continue to work with the GIMMS NDVI is that the effects of several of the processing errors in the Pathfinder data are not well understood, *e.g.*, the effect of partial atmospheric correction, and corrections already developed for the GIMMS NDVI dataset (Chapter 5) had to be derived again for the Pathfinder dataset. The lack of cloud screening in the 1° by 1° Pathfinder data was also seen as a serious limitation, especially since cloud contamination is more severe in the 10-day composites used in the Pathfinder data than in monthly composites used in the GIMMS NDVI dataset.

In a recent study several AVHRR-derived NDVI datasets—GIMMS NDVI, FASIR¹ NDVI (Chapter 5), the Pathfinder NDVI dataset and a dataset derived from the second generation GVI—were used with precipitation and

temperature data to model crop yield for several large areas around the globe for the period 1982–1990. Although all datasets had common problems to an extent, the most credible results with the fewest problems were obtained in model runs which used the GIMMS NDVI and especially the FASIR-NDVI datasets (Malmström *et al.* 1997).

¹FASIR: a sequence of corrections—Fourier Adjustment, Solar zenith angle correction, Interpolation (of missing data) and Reconstruction (over tropical evergreen forests)—applied to NDVI data

Chapter 5

Estimation of Biophysical Landsurface Parameters

Biophysically realistic models of landsurface-atmosphere interactions for use in general circulation models of the atmosphere (GCMs) were developed during the mid 1980s (Dickinson 1984, Sellers *et al.* 1986). These landsurface parameterizations formulate the processes of radiative transfer (albedo), turbulent transfer (roughness length, and evapotranspiration (surface resistance) between landsurface vegetation, soils, and the lower boundary layer of the atmosphere. Prior to the work of Dickinson (1984) and Sellers *et al.* (1986), these landsurface parameterizations were prescribed as independent boundary conditions, *e.g.*, a change in albedo would not necessarily lead to a change in the roughness length or surface resistance. Other shortcomings in the early landsurface parameterizations were: an unrealistic, generally too low, specification of albedo; use of constant values for the entire land surface of roughness length z_0 and the water-holding capacity of the soil; and an unrealistic description of the evaporation process, leading to excessive estimates of evaporation in humid regions (Sellers 1992).

The Biosphere-Atmosphere Transfer Scheme (BATS) of Dickinson (1984) and the Simple Biosphere model (SiB) of Sellers *et al.* (1986) were the first attempts at a biophysically realistic modeling approach for landsurface parameters. In these models, the emphasis is on modeling the soil-vegetation complex itself and thereby specifying the surface attributes of albedo, roughness length, and surface resistance as mutually consistent surface properties. In the case of SiB, a deliberate effort was made to base the radiation, momentum, and mass transfer properties of the vegetated land surface on a set of directly measurable surface parameters (Appendix D).

In the earliest version of the Simple Biosphere model, referred to as SiB1, landsurface vegetation parameters were derived from landcover classification maps such as those produced by Kuchler (1983) and Matthews (1983). Each vegetation type was assigned morphological, spatial, and physiological properties based on values from the ecological literature (Dorman and Sellers 1989). The use of

static landcover classifications made it particularly hard to quantify the spatial and temporal distribution of phenologically varying variables in a credible way, *e.g.*, fraction of photosynthetic active radiation (FPAR) absorbed by the green fraction of the vegetation canopy, leaf area index (LAI), albedo, and roughness length.

The original version of SiB by Sellers *et al.* (1986) has since been modified to include a more realistic model of leaf photosynthesis and conductance as proposed by Collatz *et al.* (1991, 1992). This leafscale model in the revised version of SiB, referred to as SiB2, describes the canopy conductance and photosynthesis as a function of physiological properties specified for each vegetation type (*e.g.*, leaf area index, leaf angle distribution, and leaf and soil optical properties), environmental conditions (provided by the GCM) and the canopy photosynthetically active radiation (PAR) use parameter Π , which is related to FPAR (Sellers *et al.* 1992a, 1996a) according to

$$\Pi \approx \text{FPAR}/\bar{k}, \quad (5.1)$$

with \bar{k} being the time-mean (radiation-weighted) extinction coefficient for PAR.

In the SiB2 photosynthesis and leaf conductance models the PAR use parameter is related to the potential photosynthetic rate, *i.e.*, the rate of photosynthesis that would occur in the absence of environmental stresses, and it is therefore essential in processes related to photosynthesis such as the exchange of carbon, water, and sensible heat between the leaves and the surrounding atmosphere.

The relationships between the PAR use parameter and FPAR on the one hand and the Normalized Difference Vegetation Index (NDVI) on the other (Chapter 2.4) make satellite data an attractive and logical choice for their estimation. Satellite-based methods have several additional advantages over methods that derive these parameters from static landcover classifications. First, estimation of biophysical parameters from satellite data results in spatial and temporal variation of these parameters within-classes. This is more realistic than prescribing

ing landsurface parameters varying in space and time as a function of class alone as outlined in Dorman and Sellers (1989). Second, model results and field experiments for several broadleaf landcover types have shown a consistent relationship between FPAR and NDVI that is dependent only to a minor extent on model formulation and leaf properties (Asrar *et al.* 1992, Sellers *et al.* 1992a). Third, complete global coverage can be obtained by observations from one type of instrument such as the National Oceanic and Atmospheric Administration (NOAA) Advanced Very High Resolution Radiometer (AVHRR). In addition to FPAR, leaf area index can be estimated from satellite data. The relationship between NDVI and leaf area index is not as strong as the relationship between FPAR and NDVI and it depends on several factors such as the canopy structure and leaf optical properties (Asrar *et al.* 1992, Sellers *et al.* 1992a).

To obtain consistent global landsurface parameters from NOAA-AVHRR NDVI data, two issues need to be addressed. First of all, the NDVI data need to be corrected for the various interferences summarized in Chapter 3: sensor degradation, cloud contamination, absorption and scattering by atmospheric constituents, variations in solar zenith angle, and missing data; and second, relationships must be derived to estimate landsurface parameters from the NDVI (Sellers *et al.* 1996b). This chapter discusses the correction of the monthly NDVI data, and the estimation of biophysical parameters—FPAR and LAI—from these.

5.1 Correction of the AVHRR NDVI Data

The Global Inventory, Modeling, and Monitoring System (GIMMS) monthly continental NDVI data from 1982–1990 (Los *et al.* 1994, Chapter 4, Appendix C) were used for the derivation of the global biophysical parameters. To enhance spatial and temporal consistency of the data, corrections should be applied for sensor degradation, cloud contamination, absorption and scattering by atmospheric constituents, variations in solar zenith angle, and missing data (Chapter 3, Appendix C). Several published corrections require information on component channels 1 and 2 data, *e.g.*, sensor degradation and atmospheric effects, or information from additional data sources, *e.g.*, data on atmosphere optical thickness, cloud frequency and size, and viewing geometry. Because this information was not available, approximate corrections were developed to adjust the NDVI data without recourse to the component bands.

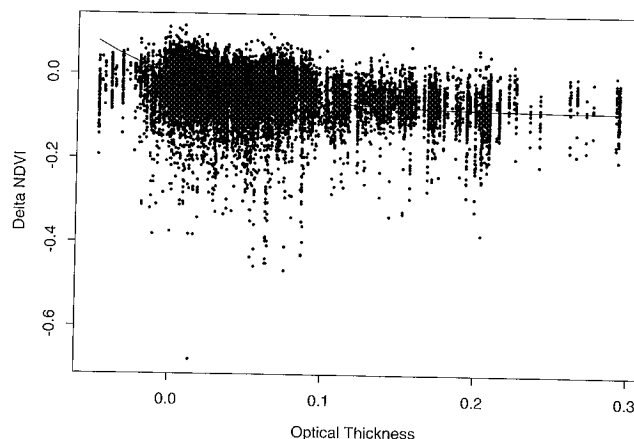


Figure 5.1: Departures in the Normalized Difference Vegetation Index over areas with an average NDVI > 0.5 versus optical thickness data obtained from observations over the Pacific Ocean by Vermote *et al.* (1994). The fitted equation was obtained by a non-linear regression technique (Statistical Sciences 1993, Bates and Watts 1988).

5.1.1 Sensor Degradation

The continental NDVI data were adjusted for sensor degradation and calibration differences between satellites with an approximation developed by Los (1993, 1998, Appendices A and B). First invariant targets were identified by selecting areas with the lowest temporal variation. These areas with the lowest temporal variation were found in the Lybian and Nubian Desert. The NDVI of these areas was assumed to vary as a result of sensor degradation only, not as a result of changes in vegetation density. From the variation in the NDVI the rate of sensor degradation and differences in AVHRR calibration were estimated. The NDVI data were then corrected for sensor degradation without recourse to the component channels 1 and 2 data. The root mean square error of this correction is 0.002 NDVI or less over a range of NDVI values between 0 and 0.6. The error as a result of the approximation is smaller than the error of 2 % in the estimation of sensor degradation (Vermote and Kaufman 1995) and can therefore be neglected.

After the correction for sensor degradation, the continental NDVI data were spatially averaged to a 1° by 1° resolution and merged into a global dataset (Los *et al.* 1994, Appendix C).

5.1.2 Volcanic Aerosols

A correction was applied to the 1982–1984 global NDVI data for aerosols induced in the atmosphere by the eruption of El Chichon in April 1982 located in Chiapas, Mexico. A relationship was derived between the optical thickness data of Vermote *et al.* (1994), obtained over the Pacific Ocean, and deviations in the NDVI values over

the land surface. It was assumed that the aerosol optical thickness was constant with longitude and varied only with latitude and the time since the eruption. Because of the high mixing rates and strong longitudinal component of wind directions in the upper atmosphere, this assumption is reasonable after several months have passed but may not work so well directly after the eruption.

The deviation in NDVI values was estimated by latitudinal band for the period of May 1982 until December 1984 from areas with a monthly average NDVI larger than 0.5. In general, areas with high average NDVI values exhibit low temporal variation in NDVI (see figure 5.4, and Tucker *et al.* 1985a) and it is therefore reasonable to assume that the deviation in the NDVI from these areas was caused by the El Chichon aerosols. A relationship was derived between the deviation in the NDVI, $\Delta\text{NDVI}_{\text{max}}$, and the optical thickness data of Vermote *et al.* (1994; see figure 5.1),

$$\Delta\text{NDVI}_{\text{max}} = \beta_1(1 - e^{\beta_2\tau}), \quad (5.2)$$

with

$$\begin{aligned} \beta_1, \beta_2 &= \text{coefficients estimated with non-linear regression,} \\ \tau &= \text{aerosol optical thickness.} \end{aligned}$$

The deviation in NDVI, ΔNDVI , was assumed largest for high NDVI values, $\Delta\text{NDVI} = \Delta\text{NDVI}_{\text{max}}$, and negligible over bare soils $\Delta\text{NDVI} = 0$. Based on the results of Vermote *et al.* (1994) the deviation in NDVI was assumed to vary linearly with NDVI.

$$\Delta\text{NDVI} = \frac{\Delta\text{NDVI}_{\text{max}}(\text{NDVI} - \text{NDVI}_{\text{min}})}{\text{NDVI}_{\text{max}} - \Delta\text{NDVI}_{\text{max}} - \text{NDVI}_{\text{min}}}, \quad (5.3)$$

with

$$\begin{aligned} \text{NDVI}_{\text{max}} &= 0.54; \text{ the mean NDVI of sites with} \\ &\quad \text{monthly mean NDVI} > 0.5, \\ \text{NDVI}_{\text{min}} &= 0.0339. \end{aligned}$$

The NDVI_{min} value was estimated in Appendix D.4.2. The global NDVI data were adjusted with optical thickness estimates varying as a function of latitude and time.

5.1.3 FASIR Corrections

A sequence of several corrections was applied to the global 1° by 1° NDVI data, collectively referred to as FASIR corrections (Sellers *et al.* 1996b). FASIR stands for Fourier Adjustment of outliers in NDVI time-series, Solar zenith angle correction, Interpolation of missing data, and Reconstruction of NDVI values over tropical rain forests which have almost continuous cloud cover.

Fourier Adjustment

The Fourier-based adjustment of outliers in the NDVI time-series uses two assumptions. The first assumption is that the NDVI varies smoothly over time. This implies that outliers in NDVI time-series are the result of either cloud contamination or sudden changes in the amount of atmospheric constituents. The second assumption is that most sources of error decrease the value of the NDVI. This assumption also justifies the calculation of monthly maximum value composites (Holben 1986). A few exceptions to this assumption exist, but their effects are generally an order of magnitude smaller than the general case and are therefore trivial in this analysis.

Outliers in NDVI time-series are identified in a three-step algorithm that operates on one time-series of a particular grid cell at a time. The first step fits a Fourier series (a summation of sine and cosine functions) through one year of data with ordinary least squares. Weights are calculated from the distance between the original data and the fitted curve. Data points above the curve are assumed reliable and are assigned a weight equal to or larger than unity. Data below the curve are assumed spurious and are assigned a weight between zero and unity (Sellers *et al.* 1996b, Appendix D.4). The second step again fits a Fourier series through the data with ordinary linear least squares. For the second step the least squares solution is altered however; the squared differences between the fitted curve and the data points are multiplied by the weights assigned to the data points. For example, data points far below the fitted curve with zero weighting are eliminated from the second fit. The minimization of the squared differences used in the least squares criterion thus changes, eliminating the influence of bad data from the regression and emphasizing reliable points. In the third and final step the original values and the values from the second fit are compared. This comparison serves to eliminate overestimates. Original values are replaced by the estimates from the second fit if several criteria are fulfilled. The Fourier adjustment technique can identify and restore up to two consecutive outliers in a time-series (compare figure 5.2.a and 5.2.b).

To correct the full 9-year time-series the Fourier Adjustment is repeated on time-series of twelve months with six months of overlap between successive runs. From each run the middle six months of data are used. For example, Fourier Adjustment is applied to a time-series from January 1982 until December 1982, then to a time-series from July 1982 until June 1983 and so on. From the first run, data from January 1982 until September 1982 are saved and from the second run, data from October 1982 until March 1983 are saved. This procedure avoids "wrap-around" effects that may occur when December data influence the correction of January data.

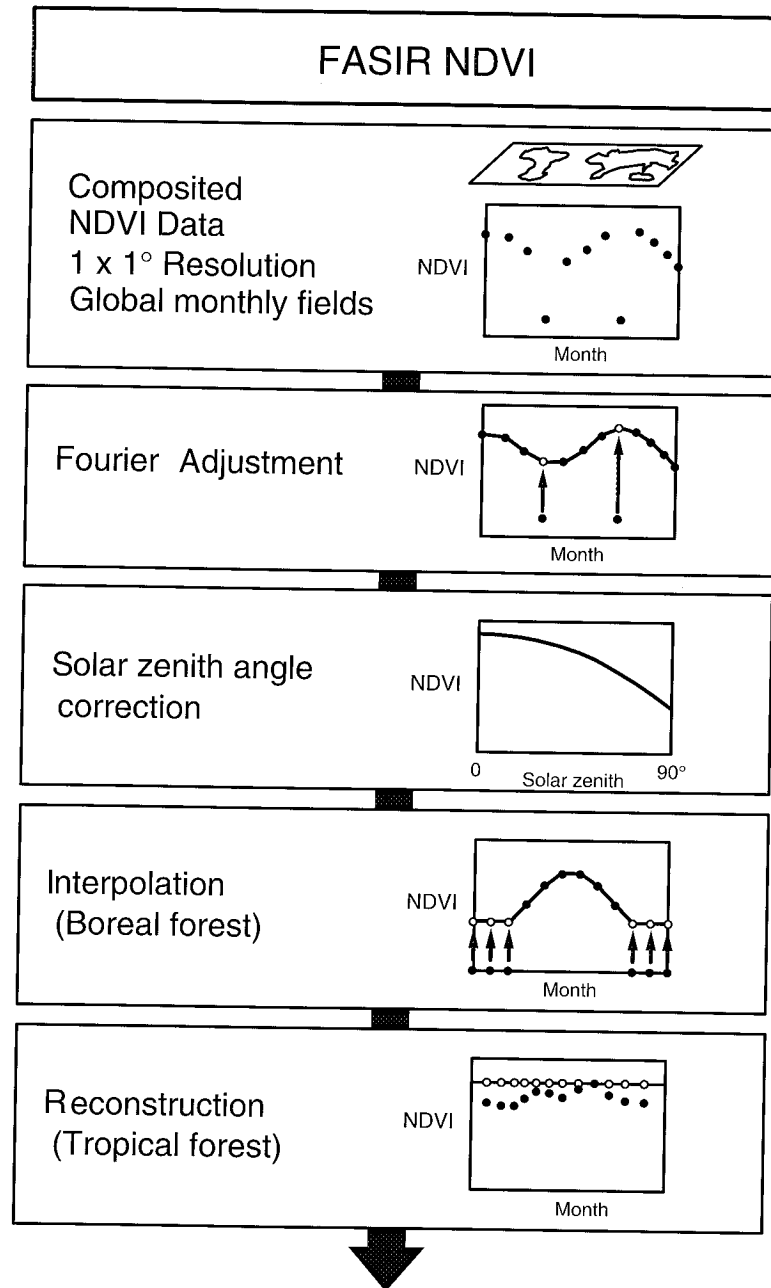


Figure 5.2: Outline of FASIR corrections (Courtesy Dr. P.J. Sellers, Johnson Space Center):
 (a) Original NDVI time-series with outliers (2 lowest NDVI values).
 (b) NDVI time-series after Fourier adjustment (FA of FASIR; open circles are new estimates).
 (c) Relationship between NDVI and solar zenith angle for assumed fully green canopies. For a given solar zenith angle interval, the solar zenith angle effect is assumed linear with NDVI.
 (d) Interpolation of missing data during the winter.
 (e) Reconstruction of NDVI-time-series over tropical forests. The seasonality of tropical forests is removed.

Solar Zenith Angle Correction

The effect of solar zenith angle on the global NDVI data is estimated from a statistical analysis of NDVI distributions. The solar zenith angle effect was established

for two situations where interannual variation in NDVI is low: landcovers with dense vegetation and bare soils (figure 5.4). The analysis of solar zenith angle on dense vegetation was restricted to landcover types with tall veg-

Table 5.1: Vegetation cover types with examples of the associated properties: maximum leaf area index, $L_{T,max}$, stem area index, L_s , NDVI at 5% and 98% of NDVI distributions, parameters for the solar zenith angle correction k_1 through k_4 (see equations D.22 and D.23), and the vegetation cover fraction V (equation D.28). For the solar angle correction only, a distinction is made within SiB2 biome 6 between the old SiB1 biome 6, which is treated as morphologically similar to class 1, and SiB1 biomes 7, 8, and 11, which are treated as morphologically similar to the short vegetation classes.

SiB2 biome	$L_{T,max}$	L_s	NDVI _{98%}	NDVI _{5%}	k_1	k_2	k_3	k_4	V
1	7	0.08	0.618	0.033	0.24	2.82	0	1	0.0
2	7	0.08	0.687	0.033	0.553	2.51	0	1	0.0
3	7.5	0.08	0.687	0.033	0.553	2.51	0	1	0.5
4	8	0.08	0.687	0.033	0.553	2.51	0	1	1.0
5	8	0.08	0.687	0.033	0.553	2.51	0	1	1.0
6-6	5	0.05	0.618	0.033	0.24	2.82	0	1	0.0
6-other	5	0.05	0.630	0.033	0.17	1.61	0	1	0.0
7	5	0.05	0.630	0.033	0.17	1.61	0	1	1.0
8	5	0.05	0.630	0.033	0.17	1.61	0	1	0.0
9	5	0.05	0.630	0.033	0.17	1.61	0	1	0.0

etation (SiB class 1 through 6) and agriculture (SiB class 12). The monthly NDVI data for 1982–1990 were stratified into groups of similar vegetation types (section 5.2) and equal solar zenith angle intervals. For example, data from a deciduous forest at 50° North for July were merged with data from a deciduous forest at 20° South for January (the bias in latitude is caused by the overpass time of the satellite see figure 3.1). The analysis was restricted to areas with noon solar zenith angles smaller than 35° to avoid data from dormant vegetation.

NDVI frequency distributions were calculated for each of the groups with similar vegetation and equal solar zenith angle intervals. The 98 percentiles of these distributions were assumed to correspond to fully green conditions. For each vegetation class, the 98 percentiles were plotted versus the midpoint of the solar zenith angle interval. The 98 percentile values show an apparent decrease in the NDVI with increasing solar zenith angle (figure 5.2.c). The analysis was repeated for NDVI populations from bare soils and deserts (SiB classes 9 and 11) using the 2 instead of the 98 percentiles. No significant effect of solar zenith angle on the NDVI of bare areas was found. A similar conclusion was drawn by Los (1998) from an analysis of sensor degradation effects over desert areas (Appendix B). This conclusion is at odds with the earlier study of Sellers *et al.* (1996b) where, based on the analysis of one year of data, a small solar zenith angle effect was found in NDVI values from deserts. With the solar zenith angle effect estimated for two extremes, intermediate values were corrected assuming a linear effect of solar zenith angle with NDVI. NDVI values of the entire data record were restored to values corresponding to solar zenith angle of 30°.

Interpolation

The cloud screening technique eliminates data from areas with a top-of-the-atmosphere brightness temperature below 273 K (Chapter 4.2, Appendix C.3.2). This re-

sults in data gaps over large parts of the Northern Hemisphere during winter. Missing data are a problem for the SiB2/GCM in situations where evergreen trees protrude through the snow. A zero NDVI value would lead to zero estimates of leaf area index and would overestimate the landsurface albedo and underestimate the roughness length. To avoid these problems the NDVI of needleleaf evergreen landcover types during winter was estimated by extrapolation of the October NDVI value (figure 5.2.d). This assumes that in October most deciduous trees in the boreal forests have shed their leaves and that the greenness of the land surface as measured by the satellite is predominantly from needle trees, which are assumed to exist unchanged through the winter.

Reconstruction

The Fourier adjusted NDVI time-series over the tropics show strong evidence of serious cloud contamination, *e.g.*, low NDVI values coinciding with the climatological occurrence of rainfall and cloud cover. To avoid low values in evergreen broadleaf landcover types, the maximum NDVI value over the year is selected for each pixel to represent the annual time-series (figure 5.2.e). The FASIR corrected NDVI data are taken to be indicative of the amount of green leaves in the vegetation canopy.

5.2 Landcover Classification

A satellite-derived global landcover classification (DeFries and Townshend 1993, 1994) was used for biome dependent adjustments of the NDVI data and biome dependent estimation of landsurface parameters. In a previous study described in Appendix D a landsurface classification derived from conventional ground surveys (Matthews 1983, Kuchler 1984) was used for this purpose. The satellite derived landcover classification of DeFries and Townshend (1983, 1994) was based on Fourier adjusted NDVI time-series (section 5.1). Using one data source to derive a

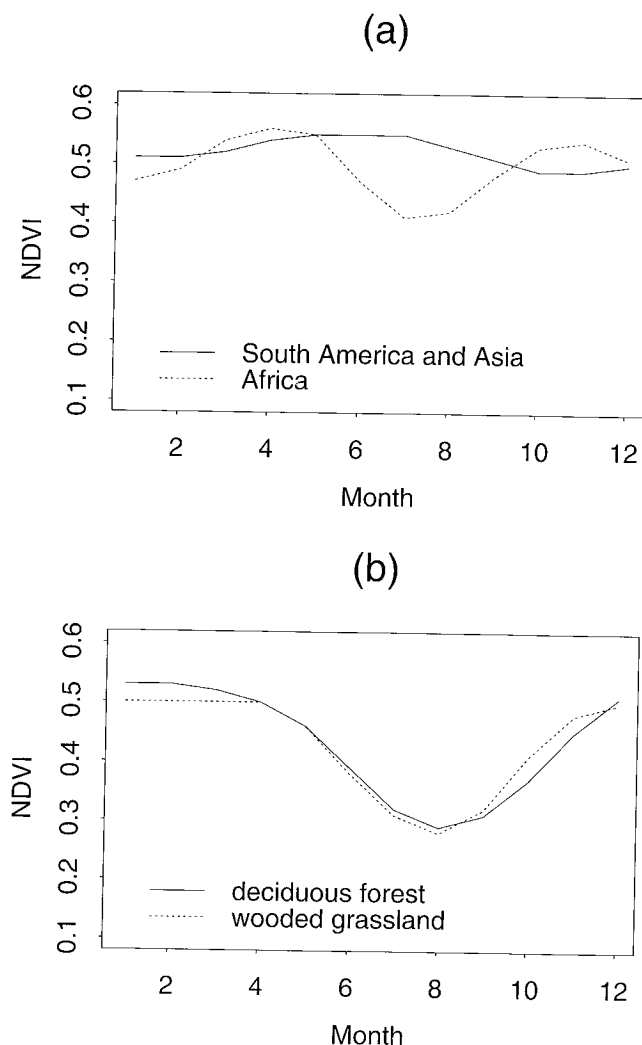


Figure 5.3: (a) NDVI time-series for tropical forests of Africa, South America and Asia, indicating different time-series for similar biome types. (b) NDVI time-series for a deciduous forest and wooded grassland indicating similar time-series for different biome types (Courtesy Dr. R.S. DeFries, University of Maryland at College Park).

classification and landsurface parameters has the potential advantage of a greater consistency between them—data are taken from the same timeperiod by the same instrument—and easier implementation in models since only one source of data is required (DeFries and Townshend 1993, 1994). The classification by DeFries and Townshend (1993, 1994) consisted of four stages

1. The first stage of the classification was the identification of training sites. This was done by comparing the landcover classification from Matthews (1983), Olson *et al.* (1983) and Wilson and Henderson-Sellers (1985). Considerable lack of agreement was found among these three landcover classifications. Where they agreed the accuracy of the classifica-

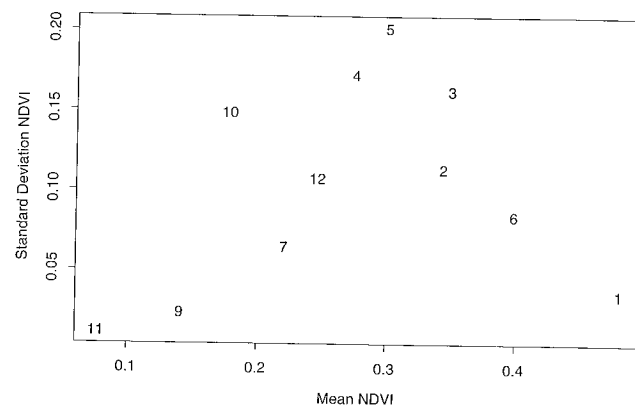


Figure 5.4: x-axis: Mean annual NDVI averaged per biome type, y-axis: standard deviation of annual NDVI time-series, representing the seasonality of vegetation, averaged per biome type. Numbers indicate the SiB 2 landcover types (Sellers *et al.* 1996b; Appendix D.3.2). 1 = broadleaf evergreen (tropical rain forest), 2 = broadleaf deciduous (temperate forest), 3 = mix broadleaf deciduous and evergreen needleleaf (temperate and boreal forests), 4 = evergreen needleleaf (boreal forest), 5 = deciduous needleleaf (larix), 6 = drought deciduous woodland or savannah, 7 = grassland, 9 = shrubs and bare soil, 10 = tundra, 11 = bare soil (desert), 12 = agriculture.

tions was assumed high and these locations were selected as training sites. The uncertainties in the classification are of secondary importance for the derivation of biophysical parameters in section 5.3 and Appendix D.

2. Fourier adjusted, monthly NDVI time-series for 1987 were extracted for the selected training sites. The amount of data was reduced by selecting data from every other month. The dataset was analyzed separately for the Northern and Southern Hemispheres.
3. The feature space was visually examined for each of the classes. Outliers were removed and the spatial distribution of data falling in the same clusters was examined. If data from the same cluster were in distinctly different climate zones, the training sets were subdivided. For example, subdivision was required for agricultural crops because spectral signatures varied widely between continents.
4. The Bhattacharyya distances (Swain and Davis 1978) between the clusters were calculated to assess the separability of the classes. Landcover classes were combined in several cases where separability was poor. For example, the SiB2 landcover classes 6 (savannah, trees with ground cover) and 8 (shrubs with ground cover) had similar temporal profiles and were therefore combined.

Examples of separability problems in the NDVI time-series of training sites are shown in figure 5.3. Figure 5.3.a is an example of two similar landcover types with different temporal profiles and figure 5.3.b is an example of different landcover types with similar profiles. The confusion between classes can be reduced by incorporating additional data sources. For example, Loveland *et al.* (1991) improved a landcover classification from NDVI time-series by incorporating data on climate (mean precipitation and temperature), elevation, ecoregions, and land resources. The classification could also be expanded by using data from additional AVHRR channels, and by incorporating the landsurface Bidirectional Reflectance Distribution Function (BRDF) properties. These improvements are planned for future updates of the current classification.

Figure 5.4 compares the mean annual NDVI and the seasonal range, expressed as the standard deviation in NDVI over the growing season, for each of the SiB2 classes. Similar results were obtained in a landcover classification study of Africa by Tucker *et al.* (1985a). Deserts (class 9) and tropical evergreen broadleaf cover types (class 1) both exhibit small seasonal variation, with deserts having low NDVI values throughout the year and tropical forests high values (figure 5.4). The largest seasonal range is found in high latitude biomes (classes 3, 4, and 5 consist of needleleaf and broadleaf trees). Savannah (classes 6 and 8, both are represented by 6) has larger seasonal variations and smaller mean annual NDVI values than tropical forests. Semi-arid seasonal grasslands (class 7) have a seasonal range similar to the savannah, but lower annual means. The tundra stands out as a unique class with low mean annual NDVI values and high seasonal variation, indicative of a short growing season.

An alternative way to obtain landcover classifications, not used for the present study, is from climate observations such as done in the Köppen and Holdridge classifications (Prentice 1990), and more recently by ecologically functional models (Woodward 1987a, Prentice *et al.* 1992, Haxeltine and Prentice 1996, Cramer and Lee-mans 1993, Neilson *et al.* 1992, Woodward *et al.* 1995). These classifications are based on the interrelationships between vegetation, climate—the latter defined by long-term averages of rainfall, temperature, and evaporation—and environmental variables such as soil indices and topography. Most climate-based landsurface classifications implicitly assume landcover classes to be in balance with their surrounding climate and are generally seen as an identification of naturally occurring, or potential vegetation.

5.3 Derivation of Biophysical Parameter Fields

Biophysical parameters, *e.g.*, leaf area index and FPAR, are inferred from the NDVI using simple relationships. For horizontally homogeneous, closed canopy composed almost exclusively of green material, both theory and measurements have confirmed that FPAR increases almost linearly with Simple Ratio (SR), which is a transform of the NDVI; $SR = (1+NDVI)/(1-NDVI)$. The linearity of this relationship is at least valid for homogeneous vegetation cover with a dark soil background.

Assuming linearity, the equation for SR and FPAR can be derived when two end points are known. These two points can be established with some reliability from the NDVI distributions of a particular landcover class in a way similar to that discussed in the derivation of the solar zenith angle correction (figures 5.5.a, 5.2.c). The 98% NDVI is assumed to represent vegetation with a maximum FPAR value— $FPAR_{max}$, here assumed to be 0.95—and the 2% desert value is assumed to represent no vegetation cover and is assumed to correspond to a FPAR value close to 0— $FPAR_{min}$, here assumed to be 0.001. The relation between FPAR and SR is then given by (Sellers *et al.* 1996b; figure 5.5.b):

$$FPAR = \frac{(SR - SR_{min})(FPAR_{max} - FPAR_{min})}{SR_{max} - SR_{min}} + FPAR_{min}, \quad (5.4)$$

where SR_{max} and SR_{min} are landcover dependent values of the simple ratio corresponding to the 98% and 2% of the NDVI frequency distributions (Table 5.1). The 2% and 98% values are the same values used for the solar zenith angle correction, and are tied to the same vegetation classification.

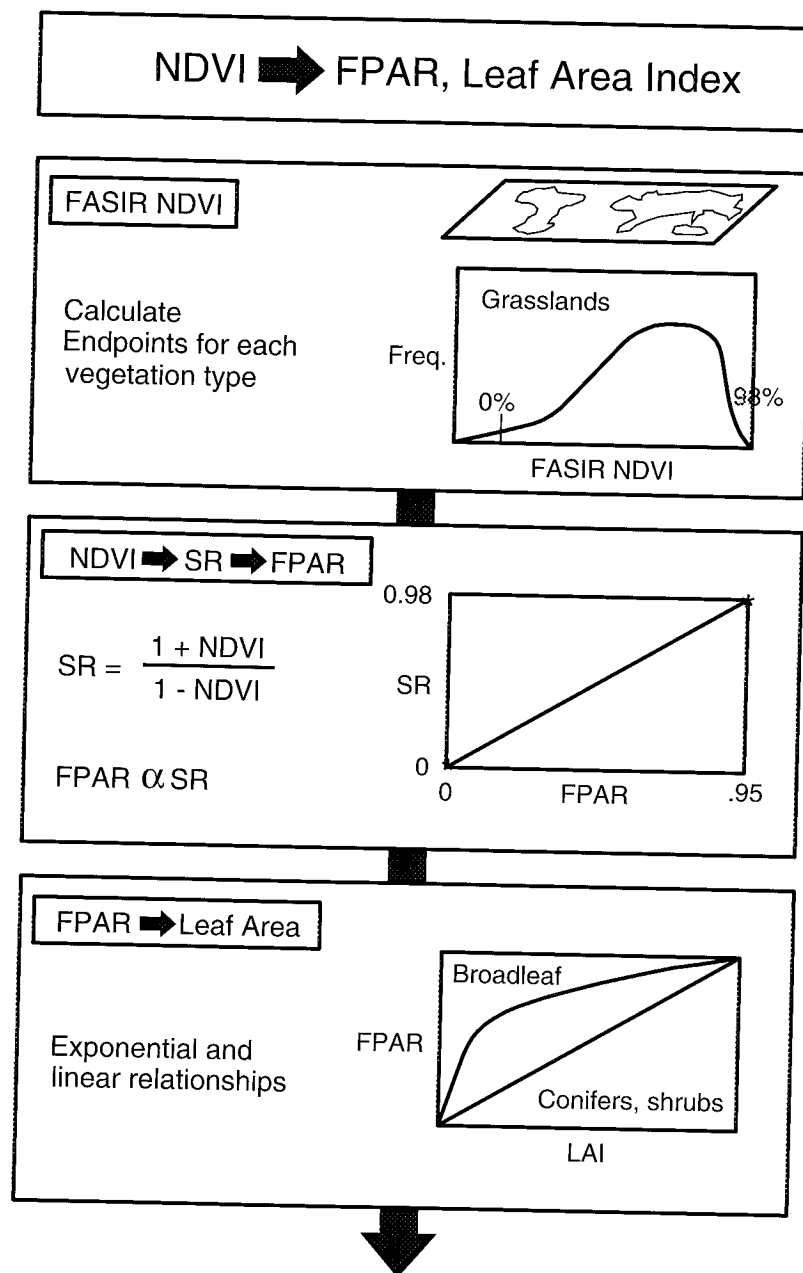
The general relationship between FPAR and green leaf area index L_g can be described by an exponential equation (Monteith and Unsworth 1990; figure 5.5.c),

$$L_g = L_g \frac{\log(1 - FPAR)}{\log(1 - FPAR_{max})}. \quad (5.5)$$

The FPAR and green leaf area index values described above refer only to the green portions of the vegetation canopy.

For clumped vegetation L_g can be described with a linear relationship,

$$L_g = \frac{L_{g,max}(FPAR - 0.001)}{FPAR_{max} - 0.001}. \quad (5.6)$$



F616.003

Figure 5.5: Derivation of the fraction of photosynthetically active radiation (FPAR) absorbed by the vegetation canopy and leaf area index from the normalized difference vegetation index (Courtesy Dr. P.J. Sellers, NASA Johnson Space Center).

(a) calculation of 2% and 98% values from NDVI frequency distributions per vegetation class. The 98% values were derived from tall vegetation class (assumed fully green) and the 2% values were derived from desert and bare soil and shrub classes (assumed bare).

(b) calculation of FPAR from NDVI assuming a linear relationship between FPAR and simple ratio, $SR = (1 + NDVI)/(1 - NDVI)$, with the 98% SR values corresponding to $FPAR = 0.95$ and the 2% SR values corresponding to $FPAR = 0.001$.

(c) calculation of leaf area index from FPAR. An exponential relationship between these two variables is used for broadleaf vegetation classes (equation 5.5). For vegetation classes 4, 5, and 9 a linear relationship, equation 5.6, between maximum leaf area index and vegetation cover fraction is assumed.

Landcover classes 4, 5 (evergreen needleleaf, and deciduous needleleaf), and 9 (shrubland with bare soil) are treated as clustered vegetation types as defined in Sellers *et al.* (1992a). In cases where there is a combination of clustered and evenly distributed vegetation, L_g can be calculated by a combination of equations 5.5 and 5.6.

Several other parameters were derived from FPAR and leaf area index such as the fraction green leaves of total leaves, the roughness length, and hemispheric albedo calculated within the GCM, (Appendix D, Sellers *et al.* 1996b).

5.4 Discussion

The derivation of biophysical parameters from satellite data presented in the current chapter has several advantages over the derivation of biophysical parameters from landcover classifications and look-up tables, as was previously done (see Dorman and Sellers 1987).

- Satellite derived biophysical parameters show realistic variations within and between classes similar to the variation in the NDVI data, whereas landcover-based parameters show between class variation only (Appendix C).
- The cycles of vegetation greening and senescing are realistic, *e.g.*, greening starts at a later time in the northern edge than in the southern edge of the boreal forests. These timing differences were not captured in the parameter estimation by Dorman and Sellers (1987).
- Satellite-derived biophysical parameters show realistic interannual variations (Chapter 9) whereas landcover-derived parameters show none.
- Satellite-derived biophysical parameters are less sensitive to errors in the landcover classification than landcover-derived parameters because they have only second order dependency on landcover type (see also DeFries *et al.* 1997). For example, the NDVI value corresponding to a FPAR of 0.95 varies between 0.618 and 0.687 (table 5.1), hence landcover type accounts for at most 10 % of the variation in FPAR; the variation in LAI with landcover type is larger, between 6% and 35 %.
- Satellite-derived parameters are estimated from observations by one type of instrument and as a result have fewer compatibility problems than landcover-derived parameters.

Validation of biophysical parameters from satellite data is complicated because few spatially extensive ground measurements exist on which to test the derived

parameters. There are several ways in which the FASIR-NDVI and biophysical parameter fields can be evaluated and serious shortcomings can be identified and eliminated. This is the topic of Chapter 6.

Chapter 6

Evaluation of FASIR-NDVI and Biophysical Landsurface Parameters

In Chapter 5 the correction of Normalized Difference Vegetation Index (NDVI) data and the estimation of biophysical parameters were discussed. NDVI data were corrected for:

1. sensor degradation,
2. effects of volcanic aerosols,
3. interferences over one or two consecutive months caused by clouds, atmospheric effects, or both (Fourier Adjustment, FA of FASIR),
4. solar zenith angle effects (Solar zenith angle correction, S of FASIR),
5. missing data during winter in the Northern Hemisphere (Interpolation, I of FASIR),
6. and persistent cloud effects over the tropics (Reconstruction, R of FASIR).

The corrected NDVI, referred to as FASIR-NDVI, was used to estimate landsurface biophysical parameters: the Fraction of Photosynthetically Active Radiation absorbed by the green parts of the vegetation canopy (FPAR), and leaf area index (LAI). The FASIR-NDVI data were converted to the simple ratio ($SR = (NDVI + 1)/(NDVI - 1)$).

1. FPAR was then estimated from SR with a linear relationship,
2. LAI was calculated from FPAR with either an exponential relationship (landcover classes 1, 2, 6, 7, 8, 10, 11, and 12; see section 5.2 for a legend), a linear relationship (classes 4, 5, and 9) or a combination (class 3).

Validation of both the FASIR adjusted NDVI values and of the biophysical parameters, FPAR and LAI, is complicated by a lack of spatially and temporally extensive datasets from other sources. Lacking these datasets,

the validation of the global FASIR-NDVI, FPAR, and LAI fields has to be based on circumstantial evidence:

1. The FASIR-corrected NDVI data and biophysical parameters are checked for consistency in the temporal and spatial domain. This step is not an absolute validation but is useful to identify obvious problems. For example, trends in the data that are correlated with the time of operation of subsequent National Oceanic and Atmospheric Administration (NOAA) satellites, such as sensor degradation in the Advanced Very High Resolution Radiometer (AVHRR) (figure 3.2, Appendices A and B), are a clear indication of problems.
2. The biophysical *parameters* for a 1° by 1° grid cell can be compared with measurements from large remote sensing campaigns, *e.g.*, the First ISLSCP¹ Field Experiment (FIFE; see Sellers *et al.* 1988), the Oregon Transect Ecosystem Research (OTTER; see Angelici *et al.* 1991, Peterson and Waring 1994), and the Boreal Ecosystem-Atmosphere Study (BOREAS; see Hall *et al.* 1993). However, the areal extent of these sites covers only a statistically insignificant fraction of the global land surface. A direct comparison of the FASIR-adjusted NDVI and of the derived biophysical parameter fields with site averages may identify problems but will in general provide inconclusive results. This type of verification was therefore not pursued.
3. The *relationships* between NDVI, FPAR, and LAI can be verified with *relationships* established from large remote sensing campaigns. This comparison is useful for two reasons. First, relationships were derived from the global data without *a priori* knowledge of results from several of the remote sensing campaigns. Second, since relationships can be verified over a wider range of values than parameters

¹ISLSCP: International Satellite Land Surface Climatology Project

averaged over 1° by 1° , the results will be more valid than a comparison of parameters.

4. Parameters derived from the global biophysical NDVI data can be compared with other global observations. For example, the Simple Biosphere model (SiB2) coupled to a General Circulation Model of the atmosphere (GCM) uses leaf area index with leaf and soil optical properties to calculate global fields of snow-free albedo. These can be compared with albedo data derived from a different source such as the Earth Radiation Budget Experiment (ERBE) instrument.

At present a complete validation of the FASIR-NDVI data and of the biophysical parameters derived from these is not possible. The consistency tests are useful to identify problems with the data. However, a test taken by itself will yield inconclusive results. It is only when no serious inconsistencies are revealed in the results of the combined tests that the level of confidence in the data increases.

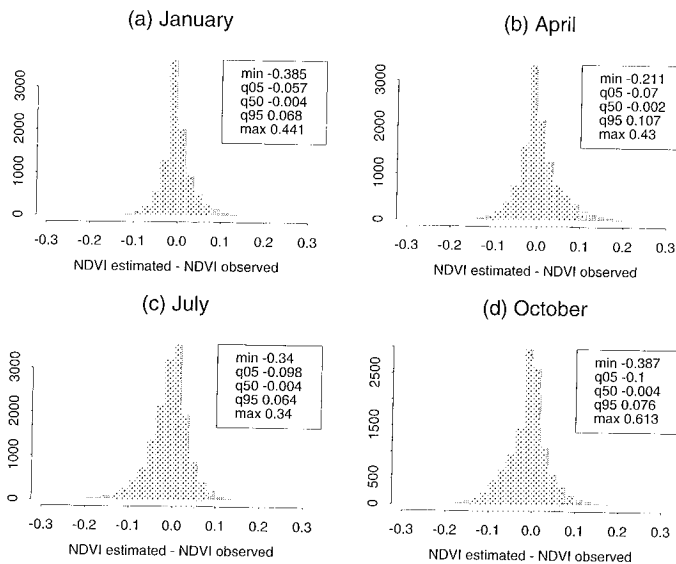


Figure 6.1: Evaluation of the Fourier Adjustment. The months of January, April, July, and October were removed from a sequence of 12 months and their NDVI values were estimated with the Fourier Adjustment technique. The figure shows the frequency distributions of the difference between the estimated and the observed NDVI data with several of the statistics of the distributions (minimum, 5 percentile, median, 95 percentile, maximum). No comparison was made for missing values in the observed NDVI data.

6.1 Evaluation of FASIR

6.1.1 Fourier Adjustment

The Fourier Adjustment (FA of FASIR) technique was developed to remove cloud interferences and atmospheric effects by identifying outliers in NDVI time-series (Chapter 5, Appendix D, Sellers *et al* 1996b). To test the Fourier Adjustment, one month of global NDVI data was removed from a sequence of twelve months. Values for the missing month were estimated with the Fourier Adjustment technique, and the estimates were compared with the original values. To see if errors were dependent on the progression of the growing season, this test was applied leaving out data from January, April, July, and October of 1987.

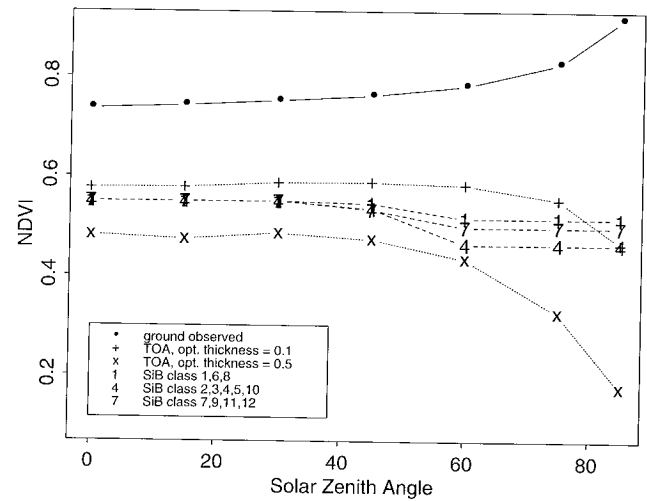


Figure 6.2: Evaluation of the Solar Zenith Angle Correction. The effect of solar zenith angle on NDVI ($\Delta\text{NDVI}/\Delta\theta$) estimated from the global dataset (lines marked 1, 4, and 7, see Chapter 5 and Appendix D) is compared with the effect of solar zenith angle on ground-measured NDVI (top curve) and on ground-measured NDVI with the effects of a clear (optical thickness = 0.1) and hazy (optical thickness = 0.5) atmosphere simulated. The solar zenith angle effect for dashed lines marked "1" and "7" (vegetation types 1, 6, 7, 8, 9, 11, 12) is within the simulations for a clear and hazy atmosphere. The solar zenith angle effect for temperate broadleaf and needleleaf vegetation classes 2, 3, 4, 5, and 10 (dashed line marked "4") is somewhat stronger.

In general, close agreement between the estimated and observed NDVI values was found (figure 6.1). Both the median and the spread of the difference distributions are small, the median is between -0.002 and -0.004 NDVI, and the spread, expressed as the difference between the 5 and 95 percentiles of the difference distribution, is 0.1 NDVI or smaller. A slight skewness exists in the difference distributions of April, July, and October; in April the skewness of the difference distributions is to positive deviations, in July and October to negative deviations.

The standard error of all estimates combined was 0.05 NDVI.

Based on the results of the analysis presented in figure 6.1 it is concluded that the Fourier Adjustment is capable of estimating severely affected NDVI values without introducing gross errors. The estimates of missing values by the Fourier Adjustment are in general conservative: this is evidenced by the slight skewness to negative values in the July and October data and the lack of skewness in the January data. The skewness in positive departures in the estimates for April, the start of the growing season for most of the Northern Hemisphere, indicates that the Fourier Adjustment may overestimate NDVI when large seasonal changes occur in vegetation. This introduces inaccuracies on the order of 0.1 NDVI for specific sites, but the errors are much smaller for the general case. For certain applications, mainly local and regional, the maximum error may be unacceptably large. For implementing the FASIR-NDVI data in a global general circulation model, typically running at resolutions of 4° by 5° or larger, the bias (average error) in the estimates is more important than the white noise (spread). The average error is small and well-behaved and therefore no particular problems associated with the Fourier Adjustment are expected in the atmospheric General Circulation Model (GCM).

6.1.2 Solar Zenith Angle Correction

The solar zenith angle correction adjusts NDVI values for effects related to variations in time of overpass of the NOAA satellite. Validation of the solar zenith angle adjustment (S of FASIR) is complicated because it depends on several factors, such as the landsurface bidirectional reflectance distribution function (BRDF), the composition of the atmosphere, and the viewing angle. Global data on these factors are not available and a thorough validation is therefore not possible. The solar zenith angle correction derived from the global data was evaluated by comparing it with solar zenith angle effects obtained from a model study and by checking time-series of corrected NDVI data for consistency.

The variations in NDVI with solar zenith angle at the top of the atmosphere are explained by contributions from the landsurface BRDF and the atmospheric BRDF. The landsurface BRDF for a FIFE site was estimated by fitting the Roujean model (Roujean *et al.* 1992) through ground-measured NDVI data measured from multiple viewing and solar zenith angles (Deering and Leone 1986, Deering *et al.* 1992b). The atmospheric effects were superposed on the landsurface BRDF by running two simulations with the Second Simulation of Satellite Signal in the Solar Spectrum 6S (Vermote *et al.* 1995): one for a continental mid-latitude atmosphere with a high aerosol optical thickness of 0.5, and the other for a continental

mid-latitude atmosphere with a low aerosol optical thickness of 0.1 (figure 6.2). The ground NDVI from the Roujean model, upper line in figure 6.2, is high and increases with solar zenith angle. The top-of-the-atmosphere NDVI predicted by 6S is lower and decreases with solar zenith angle (lines marked “x” and “+” in figure 6.2).

Table 6.1: *Coefficients to correct the NDVI for solar zenith angle effects with equation D.24. The coefficients in this study were derived from global NDVI observations and are class dependent (Chapter 5, Appendix D), Privette et al. 1995 derived coefficients from a model study using a physically based BRDF model and an atmospheric model, and Singh (1988) derived coefficients with a cone model and an atmospheric model. Both the Privette et al. (1995) and the Singh (1988) coefficients are independent of landcover type.*

This study		
SiB class	k_1	k_2
1,6,8	0.240297	2.821580
2,3	0.552917	2.506860
4,5,10	0.552917	2.506860
7,9,11,12	0.170176	1.609080
Privette <i>et al.</i> 1995		
Atmosphere	k_1	k_2
clear	0.2921	3.751
hazy	0.6014	2.687
Singh 1988		
	k_1	k_2
	0.739	1.602

The statistical analysis of global NDVI data (Chapter 5, Appendix D) shows a dependency of NDVI on solar zenith angle for SiB2 classes 1, 6, 7, 8, 9, 11, and 12 between the two scenarios for different atmospheres simulated with 6S (figure 6.2), indicating that the top-of-the-atmosphere solar zenith angle effect is dominated by the radiative properties of the atmosphere. The solar zenith angle effect estimated for classes 2, 3, 4, 5, and 10 is slightly stronger. The solar zenith angle correction was held constant for solar zenith angles larger than 60° (figure 6.2) because its estimation was deemed unreliable for these angles. Overcorrecting NDVI values as a result of overestimating the solar zenith angle effect is therefore likely to be a minor problem.

Comparison of solar zenith angle effects estimated in the current study with the studies of Privette *et al.* (1995) and Singh (1988) (Table 6.1, Appendix D.4.2) show that the current estimates for all SiB2 classes are between the estimates of Privette *et al.* (1995) for a clear and hazy sky. Singh (1988) estimates a much stronger solar zenith angle effect. Application of the Singh correction results in a shift in the timing of the peak of the growing season to later months of the year (Appendix D). This shift in seasonality is not realistic and is not observed when the

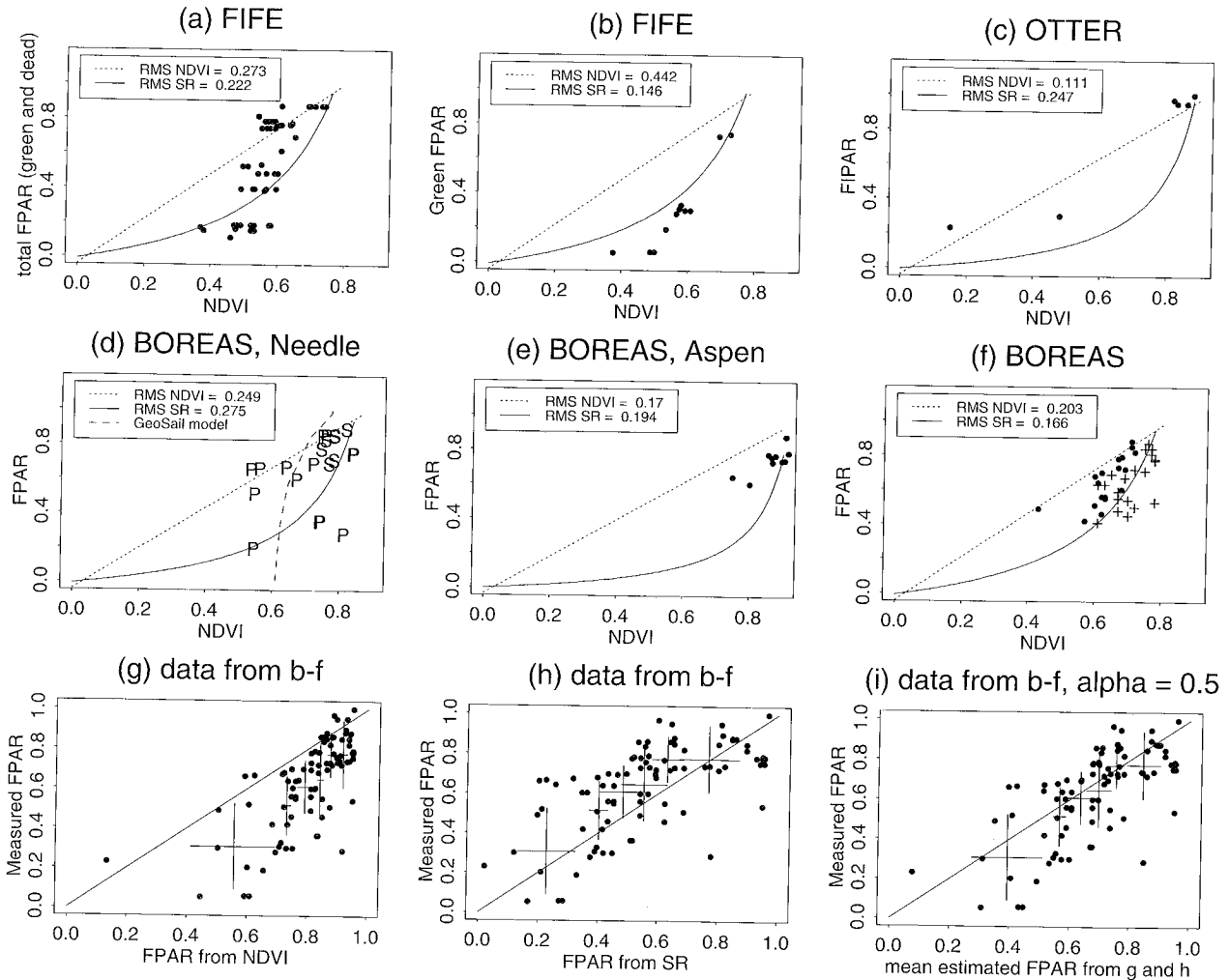


Figure 6.3: Evaluation of NDVI FPAR relationships. The dots indicate ground-measured NDVI versus FPAR. The dotted lines assume a linear relationship between FPAR and the NDVI. The solid lines assume a linear relationship between FPAR and the Simple Ratio ($SR = (1+NDVI) / (1-NDVI)$), and are shown as a curve-linear function of NDVI. (a) NDVI versus total FPAR (from both live and dead vegetation) measured at the FIFE field campaign (Blad and Walter-Shea 1994; see also Hall et al. 1992). (b) NDVI versus FPAR from the green fraction of the leaves (Blad and Walter-Shea 1994; see also Hall et al. 1992). (c) NDVI versus FPAR from the OTTER field campaign (Anglicci et al. 1991). (d) NDVI versus FPAR from a BOREAS black spruce site and a BOREAS pine site (data provided by Drs. C. Walthall, P. Rich, K.F. Huemmrich and the BOREAS information system). (e) NDVI versus FPAR from a BOREAS Aspen site (data provided by Drs. C. Walthall, P. Rich, K.F. Huemmrich, and the BOREAS information system). (f) NDVI versus FPAR from a BOREAS site (see Chen 1996). (g) Measured FPAR versus estimated FPAR from datasets in b-f combined. Solid line is 1 to 1 relationship between estimated and measured FPAR. Crosshairs indicate mean and spread in estimated (horizontal) and measured (vertical) FPAR for seven intervals of estimated FPAR. (h) Same as (g) but for FPAR estimated from SR-FPAR model. (i) Same as g and h, but with FPAR estimated from the mean FPAR estimates in g and h. Comparison of the solid 1 to 1 line with the crosshairs indicates a large bias in the estimates of FPAR from NDVI, a smaller bias in the estimates of FPAR from SR, and the smallest bias in the estimates of FPAR from the mean FPAR estimated by the SR-FPAR and NDVI-FPAR models.

correction obtained in the current study, or the study by Privette *et al.* (1995), is applied. tainty remains.

Based on the analysis in the current study and other studies, the solar zenith angle effect from the statistical analysis of global data seems plausible. Given that additional data on viewing geometry, landsurface BRDF, and atmospheric composition are lacking, a margin of uncer-

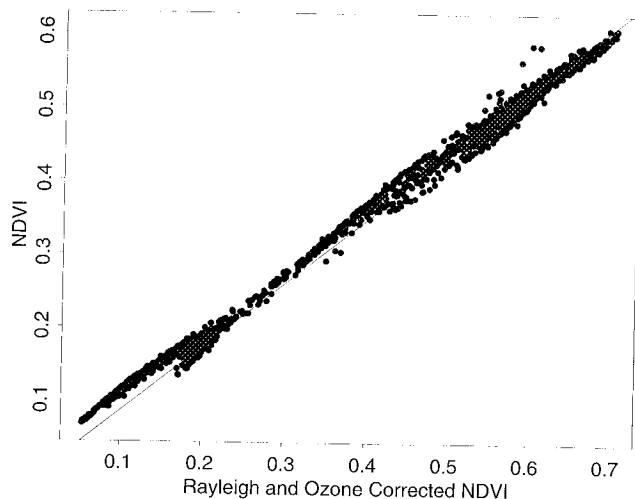


Figure 6.4: Relationship between NDVI corrected for Rayleigh scattering and ozone absorption, and uncorrected NDVI. Data were taken from a N-S transect through Africa from the Sahara, through the equatorial forest and into southern Africa. Data are from NOAA-9 maximum NDVI composites of March 1995.

6.2 Evaluation of Relationships Between NDVI, FPAR, and LAI

In Chapter 5 an outline was given of the relationships between the global 1° by 1° NDVI, FPAR, and LAI fields. NDVI was converted into Simple Ratio (SR), FPAR was estimated from SR with a linear relationship, and LAI was estimated from FPAR with an exponential relationship. The relationship derived from the global data are verified with observations from FIFE, OTTER, and BOREAS. Validation of *relationships* is preferred over validation of *parameters* averaged over 1° by 1° , because the relationships can be evaluated over a wider range of values and the results therefore have more validity.

6.2.1 FPAR

Relationships between FPAR and NDVI were derived by relating the maximum and minimum NDVI for a land-cover class to an assumed maximum and minimum FPAR (Chapter 5 and Appendix D). Intermediate FPAR values were estimated assuming a linear relationship with SR which can be expressed as a transformation of the NDVI ($SR = (1 + NDVI) / (1 - NDVI)$; see Chapter 5, Appendix D). An issue of some debate is whether FPAR is linearly related to the NDVI (this model is referred to as the NDVI-FPAR model) or to the simple ratio (this model is referred to as the SR-FPAR model). To see if one model is to be preferred over the other, FPAR was estimated with both models using the same minimum and

maximum NDVI values.

The comparison of relationships derived from satellite data with relationships derived from ground-measured data is complicated because the top-of-the-atmosphere measured NDVI values are between 0.1 and 0.2 NDVI lower than ground-measured NDVI values (sections 3.5 and 3.7). Thus the NDVI-FPAR and SR-FPAR models derived from the global NDVI data will overestimate FPAR values when applied to ground-measured NDVI data. To circumvent this problem, NDVI-FPAR and SR-FPAR models were derived from the ground data similar to the analysis of the global data (Chapter 5, Appendix D). A maximum FPAR value of 0.95 was assumed to correspond to the 98 percentile of the distribution of NDVI values for a site. This assumption can only hold true if one or more values of the distribution have FPAR values of 0.95 or higher. This was the case for the BOREAS and OTTER data, but not for the FIFE data. For the FIFE data the NDVI corresponding to a FPAR of 0.95 was estimated from the Scattering from Arbitrarily Inclined Leaves (SAIL) model (Verhoef 1984; see Figure D.3). The minimum FPAR value of 0.001 was related to the bare soil NDVI value from the global dataset. This was necessary because the FIFE, OTTER, and BOREAS data were taken from vegetated areas and estimates of bare soil NDVI were lacking. For the SR-FPAR model the minimum and maximum NDVI values were converted to minimum and maximum SR values. Note that comparison of ground-measured relationships between FPAR and NDVI and FPAR and SR with satellite-derived relationships implicitly assumes a near-linear effect of the atmosphere on the NDVI.

The FPAR-NDVI model and the FPAR-SR model were evaluated with data from FIFE (figure 6.3.a, b), OTTER (figure 6.3.c), and the BOREAS campaign (figure 6.3.d, e, f). The relationship between FPAR and NDVI from the FIFE data was derived for a mixture of green and dead leaves (figure 6.3.a) and for the fraction of green leaves only (figure 6.3.b; see Hall *et al.* 1992). The relationship between FPAR and NDVI for the mixture of green and dead leaves shows a larger scatter and has a larger root mean square (RMS) than the relationship for the green fraction. Based on the data of figure 6.3.a and 6.3.b, Hall *et al.* (1992) concluded that NDVI was related to FPAR absorbed by the green part of the canopy.

Of the two alternative models to estimate FPAR, the SR-FPAR model results in better estimates for the FIFE data (compare solid (SR-FPAR model) and dashed (NDVI-FPAR model) lines in figures 6.3.a and 6.3.b). The margin of error, given by the RMS, is fairly large: between 0.15 (figure 6.3.b) and 0.22 (figure 6.3.a) for the SR-FPAR relationships and between 0.27 (figure 6.3.b) and 0.44 (figure 6.3.a) for the NDVI-FPAR relationships.

For OTTER the fraction of intercepted photosynthetically active radiation absorbed by the canopy (FIPAR)

was measured instead of the FPAR (figure 6.3.c). For this discussion FIPAR and FPAR are equivalent; in reality they differ by a small fraction—the amount of upwelling radiation from the canopy in the photosynthetically active radiation (PAR) band. For the OTTER campaign, the FIPAR values from simple ratio are underestimated at the mid range of NDVI ($NDVI = 0.4$). The estimates of FIPAR from NDVI do not show this bias. Because of the small number of data, a definitive conclusion cannot be drawn from the OTTER data as to which model is preferable.

The BOREAS data show mixed results for the SR-FPAR and NDVI-FPAR estimates. In figures 6.3.d and 6.3.e the NDVI-FPAR model results in slightly lower errors in the FPAR estimates than the SR-FPAR model, whereas in figure 6.3.f the reverse is seen. Note that figures 6.3.d and 6.3.e show a large spread in the data. This spread could be the result of inconsistencies in measuring FPAR and NDVI. FPAR was estimated from hemispheric photographs taken in upward direction from 1 m above the ground and therefore ignore the contribution of the first meter of vegetation (understory, lichens, and lower parts of the canopy). NDVI was measured downward from a point above the canopy and is therefore an integral measure of all vegetation in the vertical and is also affected by the soil background reflectance. As a result, the FPAR measurements could be low compared to the NDVI measurements. Data collected from a different BOREAS site (Chen 1996) show a closer fit for the SR-FPAR model than for the NDVI-FPAR model. The BOREAS data cover only part of the entire range of NDVI and FPAR values.

To establish which model performed best, the NDVI-FPAR or the SR-FPAR model, the data of figures 6.3.b–f were combined in figures 6.3.g and h; figure 6.3.i shows the results of a third, intermediate model. For this intermediate model the estimates of FPAR from the NDVI-FPAR and SR-FPAR models were averaged. The reason to incorporate an intermediate model is that the other two models seem either to overestimate FPAR (NDVI-FPAR model) or to underestimate FPAR (SR-FPAR model). We discuss these three models with an analysis of variance (ANOVA; Table 6.2).

In terms of the RMS, the estimates of FPAR from the Simple Ratio ($RMS = 0.20$) are slightly better than the estimates of FPAR from the NDVI ($RMS = 0.24$). The performance of a model should not be evaluated only in terms of its total residual error but should also for its systematic deviations. The scatter plots suggest overestimated FPAR values from the NDVI-FPAR model and underestimated FPAR values from the SR-FPAR model. The bias is seen more clearly when data are divided into groups and the means of estimated FPAR and measured FPAR plotted. To investigate the bias in each of the

models the results were tested for a lack of fit (Draper and Smith 1981).

In figure 6.3.g the x-axis, indicating the FPAR values estimated from NDVI, is divided into 7 groups with approximately the same number of data. For each of the groups the average estimated FPAR and average measured FPAR were calculated. The vertical lines indicate the spread, the mean plus or minus $1 \times$ the standard deviation, in the measured FPAR for each group, and the horizontal lines indicate the spread in the estimated FPAR values for each group. If the model were to predict unbiased FPAR values, the means of each group should be sufficiently close to the 1-to-1 line. A bias in the model estimates can be tested quantitatively by splitting the residual sum of squares—the sum of squares of the differences between the model estimates and the measurements—into a sum of squares attributable to lack of fit and a sum of squares attributable to pure error (Draper and Smith 1981, Table 6.2). An F-value is calculated by dividing the lack of fit mean squares (sum of squares divided by the degrees of freedom) by the pure error mean squares.

The F-values indicate the largest lack of fit for the NDVI-FPAR model and a smaller but still significant lack of fit at the 5% confidence level for the SR-FPAR model. The F-value for the intermediate model indicates no lack of fit. The intermediate model is given by

$$FPAR = \alpha FPAR_{NDVI} + (1 - \alpha) FPAR_{SR}. \quad (6.1)$$

With α arbitrarily set to 0.5, $FPAR_{NDVI}$ is the FPAR estimated with the NDVI-FPAR model and $FPAR_{SR}$ the FPAR estimated with the SR-FPAR model. Given a situation without *a priori* information from which to choose, the NDVI-FPAR or the SR-FPAR model, the intermediate model may be an alternative.

Two issues remain to be discussed. The first is the effect of scaling and the second the effect of the atmosphere. Scaling from high resolution data, the FIFE, OTTER, and BOREAS measurements, to low resolution data, 8 km AVHRR data or global 1° by 1° data, will reduce the noise and both FPAR and NDVI values will regress towards a line through the center of the scatter. The RMS will have values closer to the centers of the cross-hairs in figure (6.3). Thus the error in the NDVI-FPAR model will be close to 0.2 FPAR, the error in the SR-FPAR model will be close to 0.1 FPAR, and the error in FPAR with the intermediate model will be close to 0.09 FPAR.

In our analysis of FPAR-NDVI relationships the effect of the atmosphere was ignored. Figure 6.4 shows the relationship between uncorrected NDVI and the NDVI corrected for Rayleigh scattering and ozone absorption in the atmosphere. The atmospherically corrected NDVI can be estimated from the uncorrected NDVI by multiplying with a constant factor. The root mean square error of this simple model is about 0.01. This error is one order of magnitude smaller than the error in the SR-FPAR

6.2. EVALUATION OF RELATIONSHIPS BETWEEN NDVI, FPAR, AND LAI

Table 6.2: Analysis of variance of alternative models to estimate FPAR from NDVI. *df* is degrees of freedom, *SS* = Sum of Squares, *MS* is Mean Squares. Model Sum of Squares and degrees of freedom and Residual Sum of Squares and degrees of freedom (rows 1 and 2 of table) add up to Total Sum of Squares and Degrees of Freedom (row 5). Lack of Fit Sum of Squares and degrees of freedom (row 3) and Pure Error Sum of Squares and degrees of freedom (row 4) add up to Residual Sum of Squares (row 2). Mean of Squares are calculated as the Sum of Squares divided by the degrees of freedom. *F*-ratio is the ratio between the mean of squares (see text for discussion).

	NDVI-FPAR model				SR-FPAR model				(SR, NDVI)-FPAR model			
Source	df	SS	MS	F-ratio	df	SS	MS	F-ratio	df	SS	MS	F-ratio
Model	1	34	34	583	1	36	36	898	1	37	37	1195
Residual	88	5.1	0.058		88	3.5	0.04		88	2.7	0.03	
Lack of fit	16	3.2	0.2	7.5	16	1.6	0.099	3.6	16	0.76	0.05	1.76
Pure error	72	1.9	0.027		72	1.9	0.026		72	1.93	0.027	
Total Model + Residual	89	39.2			89	39.2			89	39.2		

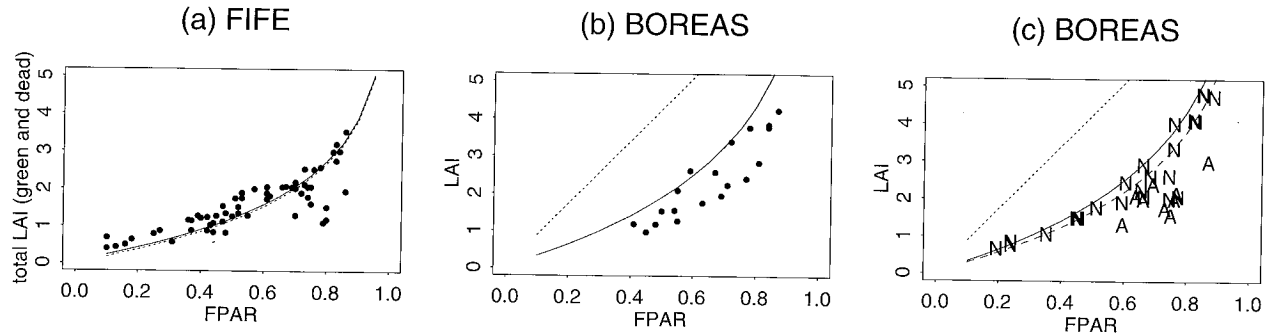


Figure 6.5: Evaluation of FPAR LAI relationships. The dots indicate ground-measured FPAR versus LAI. The solid lines show the exponential model and the dotted line the linear model used to estimate LAI from FPAR. (a) Total (from both live and dead vegetation) FPAR versus total LAI measured at the FIFE field campaign (Shah and Kanemasu 1994). (b) FPAR versus LAI from a BOREAS site (Chen and Cihlar 1996). The solid line shows the exponential model and the dotted line the linear model used to estimate LAI from FPAR. (c) FPAR versus LAI from a BOREAS site (data provided by P. Rich, K.F. Huemmrich, and the BOREAS information system). The data marked "N" indicate measurements from needle leaf vegetation (either black spruce or jack pine) and the data marked "A" indicate measurements from an Aspen site. The solid line shows the exponential model to estimate LAI from FPAR for needleleaf vegetation, the dotted line the linear model for needleleaf vegetation, and the dashed line the exponential model for deciduous broadleaf vegetation. Note that the fit of the linear model is inadequate for both (b) and (c).

model. Thus by ignoring the effects of the atmosphere a negligible error is introduced in the estimation of FPAR.

6.2.2 Leaf Area Index

The relationship between leaf area index (LAI) and FPAR was evaluated with data from the FIFE and BOREAS experiments. The FIFE data show close agreement between the model and the measured FPAR versus total (live and dead) leaf area index (6.5.a).

Figure 6.5.b compares the FPAR versus LAI relationship for needleleaf evergreen vegetation type (black spruce) with BOREAS data. These data indicate that the assumption of linearity between FPAR and LAI for clumped vegetation that was used to derive LAI from satellite observations (Chapter 5, Appendix D) does not hold at the canopy level. Thus equation 5.6 should be modified to vary the leaf area index both as a linear func-

tion of the fraction of vegetation cover to include the effect of clumped structure of vegetation and as an exponential function of FPAR to represent the exponential relationship at the canopy level.

Figure 6.5.c confirms the results in figure 6.5.b. Both the needleleaf vegetation (marked "N" in figure 6.5.c) and the deciduous broadleaf vegetation (Aspen, marked "A" in figure 6.5.c) show an exponential relationship. The model used to estimate LAI for broadleaf vegetation tends to overestimate the LAI of Aspen trees by about 50%.

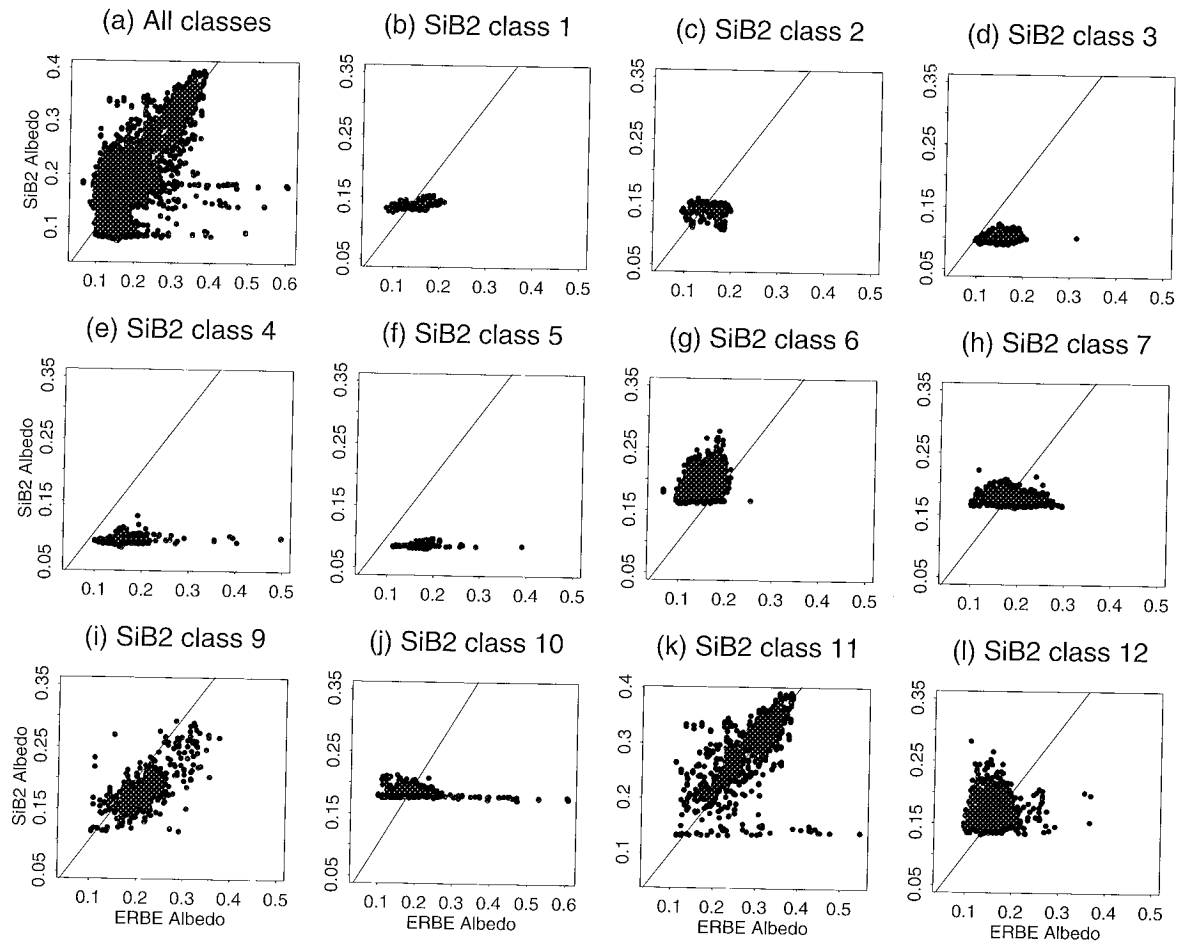


Figure 6.6: Evaluation of albedo fields. Comparison of albedo derived from the Simple Biosphere model (SiB2; see Sellers *et al.* 1996a, 1996b) with albedo derived from the Earth Radiation Budget Experiment (ERBE; see Barkstrom *et al.* 1990, Harrison *et al.* 1990) by landcover class for July 1987. The one-to-one line is drawn for comparison.

(a) All landcover classes combined. (b) Broadleaf evergreen vegetation. (c) Broadleaf deciduous vegetation. (d) Mixed needleleaf and broadleaf vegetation. (e) Needleleaf evergreen vegetation. (f) Needleleaf deciduous vegetation. (g) Drought deciduous woodland and savannah (h) Grassland (i) Shrubs and bare soil. (j) Tundra. (k) Desert (bare soil). (l) Agriculture. (see text for discussion).

6.3 Comparison of SiB2 Albedo Fields With ERBE Data

The Simple Biosphere model combines the estimates of leaf area index with landcover class-dependent leaf and soil optical properties in a two-stream canopy radiative transfer model to calculate snow-free albedo fields (Appendix D.6.2). These fields were generated in an off-line mode at 1° by 1° resolution (Dazlich 1995) similar to the way the SiB2-GCM generates these fields (Sellers *et al.* 1996b, 1996c, Randall *et al.* 1996, Appendix D.6.2). Estimates of global fields of landsurface albedo are also available from observations by the Earth Radiation Budget Experiment (ERBE) instrument (Barkstrom *et al.* 1990, Harrison *et al.* 1990). The ERBE albedo estimates were compared with the SiB2 albedo estimates by landcover

type for July 1987 (figure 6.6).

1. The SiB2 and ERBE albedo estimates for all classes combined show reasonable agreement for a large cluster of data. (figure 6.6). However, in several cases ERBE shows high albedo values (> 0.5) where SiB2 has low albedo values (< 0.2). This discrepancy between SiB2 and ERBE albedo estimates occurs in high latitude biomes (figure 6.6.e (evergreen needleleaf), 6.6.f (deciduous needleleaf), 6.6.j (tundra) and 6.6.l (bare soil)) and can be explained by effects of residual snow in the ERBE data that are not present in the SiB2 snow-free albedo estimates.
2. The SiB2 estimates show a much smaller spread in their estimates than the ERBE albedo for most classes (figures 6.6.b-f, 6.6.h, 6.6.j). This is due to

the specification of SiB2 soil and leaf optical properties which vary as a function of landcover class.

3. The SiB2 estimates are lower for needleleaf landcover types (class 4 and 5, figure 6.6.e-f). Measurements from the BOREAS field campaign indicate albedo values between 0.07 and 0.11 for needleleaf vegetation (the dominant cover type in landcover class 4), between 0.19 and 0.26 for grasslands, and values in between for broadleaf deciduous trees (Betts, personal communication, Sellers *et al.* 1995). For the entire boreal forest the albedo was in the upper range of needleleaf albedo values (close to 0.11). Thus for needleleaf vegetation the SiB2 albedo estimates seem more realistic than the ERBE albedo estimates.

The SiB2 and ERBE albedo data can also be evaluated by comparing them with the FASIR-NDVI data. Albedo values are expected to decrease with increasing NDVI because bare soils tend to be brighter and have lower NDVI values than dense vegetation. The relationships between the SiB2 and ERBE albedo estimates were compared with the FASIR-NDVI data for SiB2 biome types 1 (evergreen broadleaf), 6 (drought-deciduous woodland, or savannah) and 7 (grassland; see figure 6.7). This comparison reveals three differences. First, the ERBE albedo versus NDVI scatter shows a continuous cluster, whereas the SiB2 albedo versus NDVI scatter shows two distinct clusters: one for biome type 1 (center at albedo = 0.12 and NDVI = 0.4) and one for biome type 6 and 7 combined (center at albedo = 0.2 and NDVI = 0.4). Second, the ERBE albedo values have a negative relationship with NDVI whereas the *separate* SiB2 albedo clusters have a positive relationship with NDVI. Third, with decreasing NDVI the ERBE albedo converges to a value around 0.3 whereas the SiB2 albedo converges to a value around 0.17.

The differences between the SiB2 albedo versus NDVI scatter and the ERBE albedo versus NDVI scatter can be explained by the soil optical properties and leaf optical properties assigned to each landcover class in SiB2. They are not the result of the formulation of the radiative submodel in SiB2.

1. The clustering in the SiB2 albedo versus NDVI scatter plot (figure 6.7.b and d) can be explained by the fixed soil and leaf optical properties. In reality, the leaf and especially the soil optical properties vary gradually within and between biomes.
2. The use of a constant, dark reflectance soil background reflectance value relative to the leaf reflectance explains why the SiB2 albedo estimates converge to a value of around 0.17 at low NDVI values.
3. The specification of low soil background albedo values relative to higher leaf albedo values explains

why in these cases the SiB2 albedo increases with NDVI. Over bare soil the SiB2 albedo will be close to the initial soil albedo. When the amount of vegetation increases, SiB2 predicts a change in albedo towards albedo values specified for leaves. The ERBE albedo estimates show a decrease with increasing NDVI and converge to values more typical of dry bare soil and are therefore more realistic in this respect.

6.4 Discussion

Significant changes were made in the SiB2 landsurface parameterization with respect to the previous SiB1 version. Most importantly, vegetation-related parameters for the land surface were directly derived from satellite observations, *i.e.*, the 1° by 1° NDVI dataset discussed by Los *et al.* (1994), rather than inferred from ground cover classes. For the calculation of the vegetation related parameter fields, two major issues had to be addressed: inconsistencies in the source NDVI data had to be accounted for, and relationships between the NDVI and the landsurface parameters had to be established. Correction of the NDVI was hampered by the absence of component channels 1 and 2 data and the lack of information on viewing geometry in the source global dataset. Adjustment procedures were developed based on assumptions about the properties of NDVI datasets associated with different landcover classes. Some of these assumptions, such as the supposition that most of the major sources of error tend to lower the value of the NDVI, have been largely validated by research and can be used with a high level of confidence (*e.g.*, Holben 1986, Los *et al.* 1994, Appendix C). Other assumptions have not been as thoroughly investigated.

The NDVI data were adjusted with a series of corrections, collectively referred to as FASIR (Fourier-Adjustment, Solar zenith angle correction, Interpolation and Reconstruction). These corrections were applied in a predefined sequence, such that corrections which are less dependent on additional non-NDVI data sources were applied first, and corrections which depended more heavily on additional data were applied last. Specifically, the Fourier-adjustment uses only the NDVI data, and does not require input from an additional data source. For the solar zenith angle correction a landcover classification and estimates for the solar zenith angle were used. However, the solar zenith angle correction is not seriously affected by changes in the classification. The interpolation and reconstruction were done specifically for GCM purposes and depend heavily on the landcover classification.

The Fourier-Adjustment (FA of FASIR) provides a conservative correction to the data, *i.e.*, suspect values are adjusted relative to the position of more reliable data. The procedure may lead to some small overestimates in

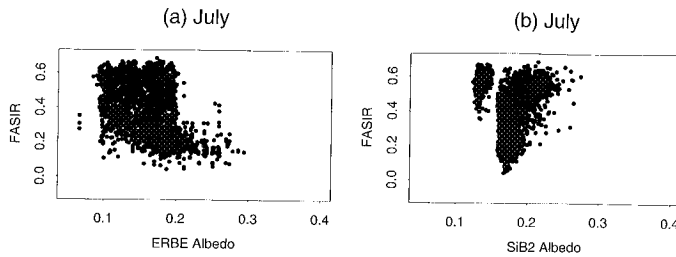


Figure 6.7: Comparison of albedo derived from the Simple Biosphere model (SiB2; see Sellers *et al.* 1996a, 1996b) and from the Earth Radiation Budget Experiment (ERBE; see Barkstrom *et al.* 1990, Harrison *et al.* 1990) with FASIR-NDVI for July 1987. (a) ERBE albedo versus FASIR-NDVI for biome type 1, 6, and 7. (b) SiB2 albedo versus FASIR-NDVI for same biome types. The SiB2 albedo has two distinct clusters that show a positive relationship between albedo and NDVI; one for biome type 1 (center at albedo = 0.12 and NDVI = 0.4) and one for biome types 6 and 7. The ERBE albedo shows one cluster and a continuous, negative relationship with NDVI (see text for discussion).

specific cases, *e.g.*, when a large, sudden change in the amount of vegetation occurs, such as in climates with large seasonality. For these biomes, overestimation could be a problem at the start and end of the growing season. For photosynthesis calculations in the SiB2-GCM, overestimating NDVI at the start and end of the growing season should have only a minor impact, because low ambient temperatures will inhibit assimilation rates (see for example Chapter 7).

The solar zenith angle adjustment (S of FASIR) incorporates a number of assumptions which have yet to be validated against *in situ* observations. The effect of this correction is largest for vegetation types at high latitudes and solar zenith angles (tundra, needleleaf evergreen, and deciduous) and temperate regions (broadleaf deciduous, mixed needleleaf, and deciduous; see Appendix D). The solar zenith angle correction is more conservative than the one derived from first principles by Singh (1988) (Appendix D) and comparable to the one derived by Privette *et al.* (1995).

Although there is some uncertainty about the solar zenith angle correction, overall it should improve the data and it is likely that overcorrections are small. View angle effects in the source 1° by 1° NDVI data are expected to be small: the compositing technique favors selection of maximum NDVI values which should be grouped around an average view angle of 10° in the off-nadir forward-scatter direction (Gutman 1991, figure 3.2.e). Remnants of view angle effects in the 1° by 1° data are confounded with and partially accounted for by the solar zenith angle correction: the correction is derived from the dataset itself, and should partially correct for systematic higher

or lower deviations due to biases in viewing angle when confounded with solar angle. Other residual variations in the NDVI are not accounted for.

The assumption that the solar zenith angle effect is linear with NDVI does not necessarily hold true. Several studies based on ground-measured data found stronger solar zenith angle effects for sparse to intermediate vegetation cover than for dense vegetation cover (Deering *et al.* 1992a, 1992b, 1994). Currently there are no reliable ways to estimate the solar zenith angle effect for intermediate NDVI values because the assumption of low interannual variation—used to derive the solar zenith angle effect for low and high NDVI values—does not hold for intermediate values (figure 5.4, section 5.2). A recent study by Malmström *et al.* (1997) indicates that the FASIR corrections did improve the consistency of the NDVI.

The Interpolation (I in FASIR) of missing data for the Northern Hemisphere evergreen needleleaf vegetation in winter is necessary to obtain realistic estimates of several landsurface parameters in SiB2, in particular those derived from the leaf area index fields such as snow-free albedo and roughness length. Failure to provide NDVI estimates for the winter period would effectively set the leaf area index values to zero and result in near-zero roughness lengths and high albedo values. This would remove the effects of the boreal forests on the physical climate system during winter. For lack of an alternative, a best guess of the minimum NDVI value is made by selecting the value at the end of the growing season before any snowfall is likely to have occurred. Overestimating of the NDVI for these higher latitudes outside the growing season is unlikely to lead to excessive evapotranspiration or assimilation rates in SiB2, because of the physiological effects of low ambient temperatures.

The Reconstruction (R in FASIR) of NDVI time-series for the tropical evergreen broadleaf vegetation is necessary to correct for the effect of persistent cloud cover and atmospheric water vapor effects associated with tropical forests. Low NDVI values would result in low FPAR and leaf area index estimates. A side effect of the procedure is that all seasonality in the data is eliminated and that areas incorrectly classified as evergreen broadleaf will have high NDVI values throughout the year. The procedure does provide an overall improvement in that it diminishes the number of outliers, especially in very cloudy areas. We have no real alternative approach until higher resolution, multi-year datasets become available in which cloud-contaminated data can be identified and discarded and water vapor corrections applied.

Errors at the low end of the NDVI, *e.g.*, as a result of variations in the reflective properties of the soil background, are diminished when transforming the NDVI into SR. This is because the transformation tends to compress the lower values of the NDVI, whereas the higher values become stretched. Errors in the NDVI at the low end

will therefore have little impact on SR and hence FPAR values.

Relationships between the NDVI and biophysical parameters have been established mainly from *in situ* studies involving individual plant species and high resolution radiometric data. Recently, a number of studies have focused on the extrapolation of the relationship between FPAR and SR from the plot-scale (a few meters) to intermediate spatial scales on the order of 100 m² to 15 km² (Sellers *et al.* 1992b). The results support a near-linear relationship between SR and biophysical properties, and by inference FPAR, over this range of spatial scales (Hall *et al.* 1992). These findings were confirmed in the analysis of FPAR versus NDVI and FPAR versus SR relationships in section 6.3.

The near-linear properties of the SR-FPAR relationship combined with assumptions on the occurrence of minimum and maximum vegetation activity has encouraged us to calculate global fields of FPAR and total leaf area index from the satellite data. It is still doubtful that the near-linearity of the FPAR-SR relationship holds for all landcover classes and soil backgrounds; it has been suggested that for some cases, *e.g.*, bright soil backgrounds, the relation between FPAR and NDVI may be more linear than the relationship between FPAR and SR (Choudhury 1987, Goward and Huemmrich 1992). This assertion has not been confirmed by the analysis of FIFE and BOREAS data. The results from the OTTER experiment were inconclusive because of the low number of measurements. Because of the dark soil background assumption, we expect our FPAR estimates to be less reliable for intermediate NDVI values over areas with a bright soil background. For high and low NDVI values we still expect our estimates to be reasonable since the effect of non-linearities should be small close to the end points to which the SR-FPAR relationship was tied. The verification of the SR-FPAR model indicated that satellite based large-area estimates of FPAR can be obtained with a root mean square error around 0.1. Moreover, the estimates with the SR-FPAR model were more accurate than with the NDVI-FPAR model. Because FPAR is critical to calculations of vegetation activity, further research is needed to establish a more accurate relationship between FPAR and vegetation indices.

We have more confidence in the estimates of FPAR than in those of LAI. However, we have seen that the essential surface properties are near-linearly related to FPAR rather than to LAI, which is only used as an intermediate variable. Therefore our uncertainties in albedo, surface roughness, canopy conductance, and photosynthesis seem to scale directly with the errors in the NDVI (SR) and FPAR rather than with the errors in the estimation of LAI.

Analysis of relationships between leaf area index and FPAR indicates a problem with the formulation of this

relationship for clustered vegetation types (SiB2 biomes 4, 5, and 9). This formulation describes the LAI as a linear function of FPAR, which is realistic when different areas with different vegetation densities are considered, but it is not a correct description of the relationship at the canopy level. A future version of SiB is planned that will deal with inhomogeneous grid cells and fractional landcover type within a grid cell. This version of SiB is better suited to model both the linear relationship between FPAR and LAI with cover fraction, and the exponential relationship between FPAR and LAI at the canopy level.

The comparison of SiB2 albedo estimates, ERBE albedo estimates, and measurements from BOREAS showed that the lower SiB2 albedo estimates for boreal vegetation are probably more realistic than the high ERBE estimates. For short, semi-arid landcover types (classes 6, 7 and 9) the ERBE albedo estimates seemed more realistic because they better described the variation within and between landcover types: the ERBE albedos showed gradual changes between landcover classes and a negative relationship with NDVI whereas the SiB2 albedos showed discrete changes between landcover classes and, for several classes, positive relationships between albedo and NDVI. These problems in the SiB2 albedo estimates are related to the landcover-dependent specification of the soil background and leaf reflectance values. The soil background reflectance is generally lower than the leaf reflectance and is specified as one number for each vegetation class. A landcover-independent, spatially varying specification of soil reflectance, *e.g.*, from low reflectance values over densely vegetated areas and high reflectance value over sparsely vegetated areas, would resolve many of the problems in the current specification.

To obtain improved parameter fields over the ones described in Chapter 5, section 6.2, and Appendix D, a number of items need to be addressed.

- In the first place, the source satellite dataset could be improved by incorporating individual channel data that are corrected for atmospheric effects, cloud contamination, and landsurface BRDF. These corrections should be applied in conjunction. For example, a correction for atmospheric effects without a correction for landsurface BRDF will result in large variations in the landsurface NDVI with satellite viewing angle that are clearly undesirable.
- A second area for improvement is in the specification of landsurface parameters such as roughness length, leaf optical properties, and soil background reflectance. These should vary as a function of space and time within a biome type as is now the case with the estimates of FPAR and leaf area index.
- Finally, improvements can be made in the specification of landcover classes as a fractional cover of a

grid cell. This would address the problem of land-cover dependent relationships, *e.g.*, calculation of leaf area index within a grid cell, and is important for a correct description of landsurface processes, *e.g.*, the modeling of vegetation assimilation in C₃ and C₄ plant species.

Chapter 7

Sensitivity of Landsurface Fluxes to Vegetation Changes

The sensitivity of fluxes between the land surface and the atmosphere (water, carbon, and energy) to changes in vegetation was established. Two different landsurface scenarios, a scenario with minimum and maximum fraction of photosynthetically active radiation absorbed by the green part of the vegetation (FPAR), were run with the Simple Biosphere model (SiB2) coupled to the Colorado State University General Circulation Model (CSU GCM) of the atmosphere. The minimum and maximum FPAR scenarios were derived from the 9-year global Normalized Difference Vegetation Index (NDVI) dataset discussed in Chapter 5.

The sensitivity test with the minimum and maximum FPAR runs has two objectives. The first is to establish which parameters are most sensitive to changes in vegetation and thus require the most accurate vegetation boundary conditions; the second is to explore the mechanisms behind the sensitivity of water, carbon, and energy fluxes to changes in vegetation.

7.1 Design of the Experiment

For the minimum and maximum vegetation scenarios a 1-year, monthly, minimum NDVI dataset and a 1-year, monthly, maximum NDVI dataset were calculated. These datasets were created by selecting the minimum (or maximum) NDVI by grid cell and month from the 9-year 1982–1990 Fourier Adjusted, Solar zenith angle corrected, Interpolated, and Reconstructed (FASIR)-NDVI data discussed in Chapter 5 and Appendix D. For example, to obtain a grid cell value for the minimum NDVI dataset in January, the minimum NDVI was selected for that particular grid cell from all 9 Januaries from 1982–1990. The minimum NDVI and maximum NDVI datasets were used to obtain biophysical parameters (FPAR, Leaf Area Index (LAI), roughness length). Because the SiB2-GCM runs off biophysical parameter fields, the datasets produced from the minimum and maximum NDVI are referred to as minimum and maximum FPAR scenarios, respectively.

The SiB2-GCM was run for thirty years to obtain initial sea surface temperature and soil moisture conditions. The minimum and maximum FPAR scenarios were then run over 15 years from these initial conditions. The averages calculated over the last five years of the runs were used for the analysis.

Since the landsurface boundary conditions for the maximum and minimum FPAR scenarios were calculated from satellite observations, they represent realistic, *i.e.*, observed, bounds of interannual variations in vegetation. The water, carbon, and energy fluxes calculated with these minimum and maximum scenarios are likely to represent realistic bounds of interannual variation as well. Within the 9-year period of satellite observations, no year was similar to either the minimum or maximum scenario. For a particular year, occurrence of low NDVI values in one area was concurrent with high values in another. Over a longer period of observation the likelihood of concurrence of same-sign departures in different areas increases, and years will occur that are closer to either the minimum or maximum scenario from the 9-year dataset. In other words: it is plausible that, *e.g.*, 1 year in 100 looks like a minimum or maximum scenario derived from the 9-year data. Thus the variability between the minimum and maximum scenario may not be a gross overestimate of interdecadal variability.

7.2 Assimilation

7.2.1 SiB2 Photosynthesis Submodel

The SiB2 canopy assimilation submodel of Sellers *et al.* (1996a) uses the C₃ photosynthesis model of Collatz *et al.* (1991) and the C₄ photosynthesis model of Collatz *et al.* (1992). The C₃ photosynthesis model of Collatz *et al.* (1991) is modified from the model of Farquhar *et al.* (1980) and coupled to the stomatal model of Ball *et al.* (1987). The model calculates canopy photosynthesis, A_c ,

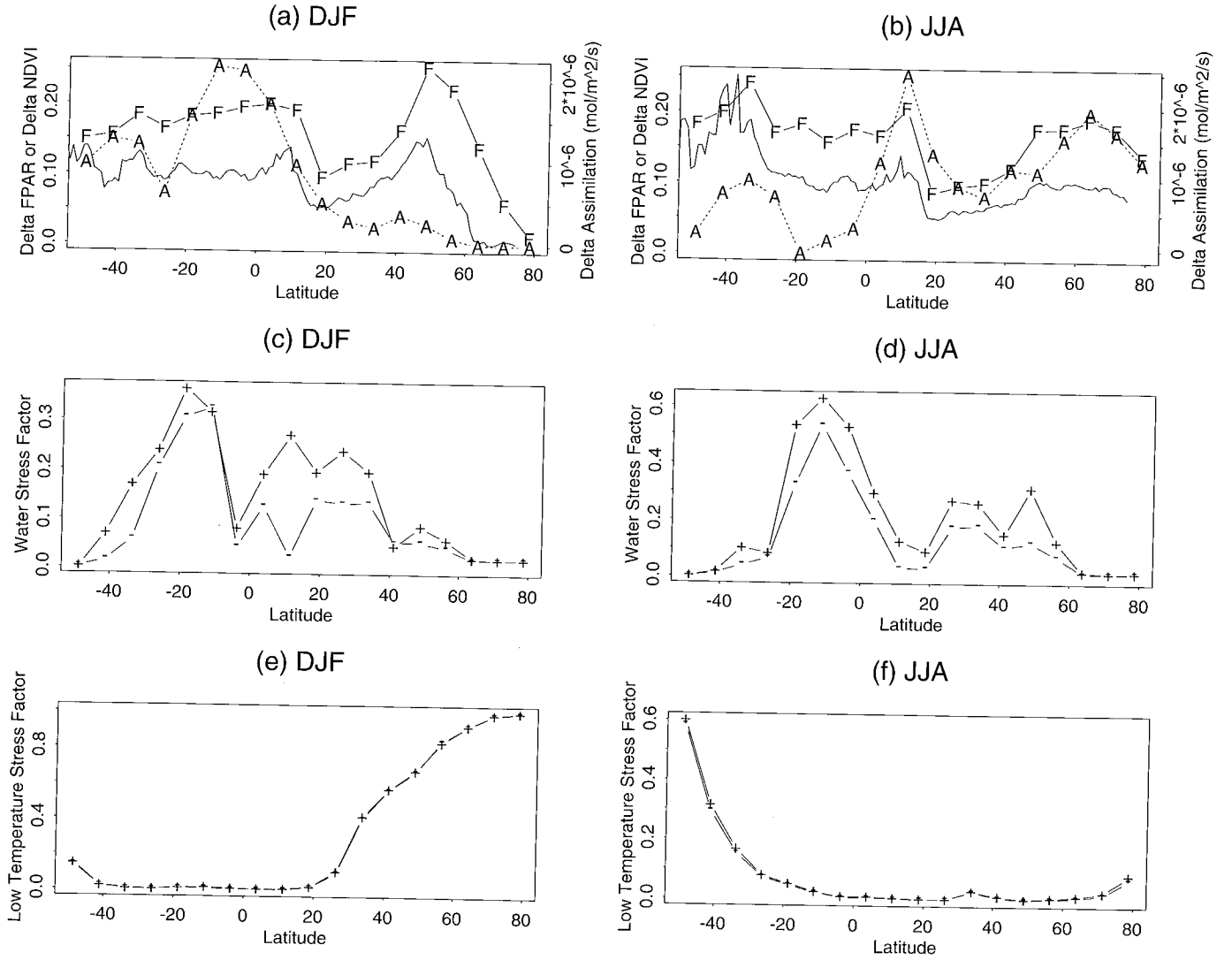


Figure 7.1: Sensitivity of carbon assimilation to changes in FPAR derived from the maximum and minimum FPAR runs with the SiB2-GCM. Delta values are expressed as the difference between the maximum run minus the minimum run. Results are averaged by latitude for December until February (DJF) and June until August (JJA). (a) Delta NDVI (solid line marked F), and Delta carbon assimilation (dotted line marked A) during DJF. (b) Same but for JJA. (c) Water stress factor for maximum run (+) and minimum run (-) during DJF. (d) same but for JJA. (e) Low temperature stress factor for maximum run (+) and minimum run (-) during DJF. (f) Same but for JJA.

and conductance, g_c , as the product of three terms,

$$A_c, g_c = [V_{\max_0}, F_{\pi_0} \downarrow] [B_1 \cdots B_6] [\Pi], (7.1)$$

with

$$\begin{aligned} A_c &= \text{canopy photosynthetic rate, mol m}^{-2}\text{s}^{-1}, \\ g_c &= \text{canopy conductance (m s}^{-1}), \\ V_{\max_0} &= \text{maximum leaf catalytic (Rubisco) capacity for green sun leaves, mol m}^{-2}\text{s}^{-1}, \\ F_{\pi_0} \downarrow &= \text{incident radiant flux of photosynthetically active (visible, 0.4-0.7 } \mu\text{m) radiation, Wm}^{-2}, \end{aligned}$$

$$\begin{aligned} B_1 \cdots B_6 &= \text{environmental forcings including CO}_2, \\ &\quad \text{temperature, relative humidity, and soil moisture,} \\ \Pi &= \text{canopy PAR use parameter.} \end{aligned}$$

The first two terms of equation (7.1) are dependent on the vegetation physiology (V_{\max_0}), the incident flux of photosynthetically active radiation (PAR) (F_{π_0}), and local environmental conditions ($B_1 \cdots B_6$); see Sellers *et al.* (1992a, 1996a). The vegetation physiological parameters and the coefficients governing B_1 and B_6 have been assigned from published values (Appendix D, Sellers *et al.* 1996a). The crucial surface parameter in equation (7.1) is the canopy PAR use parameter, Π , which specifies the

amount of green vegetation present; it varies from 0 (no vegetation) to around 1.5 (dense, green vegetation) (Sellers *et al.* 1992a),

$$\Pi \simeq \frac{\text{FPAR}}{\bar{k}}, \quad (7.2)$$

where

FPAR = fraction of PAR absorbed by the green vegetation canopy,
 \bar{k} = time-mean (radiation-weighted) extinction coefficient for PAR.

FPAR can be approximated by

$$\text{FPAR} = VN(1 - e^{-\bar{k}L_T/V}), \quad (7.3)$$

with

V = vegetation cover fraction,
 N = canopy greenness fraction (Appendix D),
 L_T = total leaf area index.

7.2.2 Sensitivity Analysis

The overall increase in FPAR between the minimum and maximum FPAR run is proportional to the increase in NDVI (figure 7.1.a, b). For December until February (figure 7.1.a) the increase in FPAR is large for the entire Southern Hemisphere. For the Northern Hemisphere, this increase is large near the equator and between 40° and 60° (latitudes with an abundance of vegetation), and smaller between 20° and 40° (latitudes with a large proportion of arid and semi-arid regions). The increase in NDVI and FPAR for July until August (figure 7.1.b) shows a similar pattern.

In several cases the increase in FPAR is not matched by a proportional increase in photosynthesis (carbon assimilation); the increase in assimilation rates is lowest for latitudes between 20°-40° in both hemispheres during summer and winter, and for mid-to-high latitudes in the Northern Hemisphere during the winter.

To explain the small increase in assimilation rate relative to the large increase in FPAR, the effects of environmental moisture and low temperature stresses (equation 7.1) on vegetation were investigated. An environmental stress in SiB2 is calculated as a change in assimilation relative to a change in a particular stress weighted by the potential assimilation of vegetation. The weighting emphasizes conditions during the growing season and during daylight hours. The value of an environmental stress is between zero and unity; zero indicates no inhibition of plant assimilation, and unity indicates complete inhibition. This use of an environmental stress is different from what is common in the ecological literature where a stress is generally referred to as an inhibition of plant growth

by the environment. Within this latter context a desert is referred to as an environment with high moisture stress; by contrast, in SiB2 the moisture stress in a desert can be low as long as the amount of vegetation is small and in equilibrium with the limited amount of moisture available.

The areas where the increase in FPAR is not matched by a similar increase in assimilation have either a high water stress value, a large increase in water stress between the minimum and maximum scenario, or a high value for the low temperature stress (figure 7.1.c-f). For both hemispheres the assimilation is inhibited by the low temperature during their respective winters (compare 7.1.a with 7.1.e for the Northern Hemisphere and 7.1.b with 7.1.f for the Southern Hemisphere). Between the minimum and maximum scenarios water stress increased for low latitudes for the Southern Hemisphere during both summer and winter. A slightly smaller increase was found in the subtropics and temperate regions for the Northern Hemisphere during the summer.

A point worth noting is that both minimum and maximum water stress factors for latitudes between 30° and 10° S during January until March and 20° to 0° S during July until September are high. The high water stress factors for the minimum scenario could indicate an imbalance between the prescribed vegetation and the GCM simulated climate largely as a result of insufficient precipitation.

7.3 Energy Balance

7.3.1 SiB2 Energy Submodel

In its most general form, the total surface energy balance is given by

$$R_n - G = \lambda E + H, \quad (7.4)$$

with

R_n = net radiation, W m^{-2} ,
 G = ground heat flux, W m^{-2} ,
 λE = latent heat flux, W m^{-2} ,
 H = sensible heat flux, W m^{-2} .

In SiB2 the energy balance is divided into separate components for the canopy and the soil surface. Energy fluxes in SiB2 are described in electrical analog form,

$$\text{flux} = \frac{\text{potential difference}}{\text{resistance}}. \quad (7.5)$$

The calculation of the energy balance involves several of the submodels of SiB2:

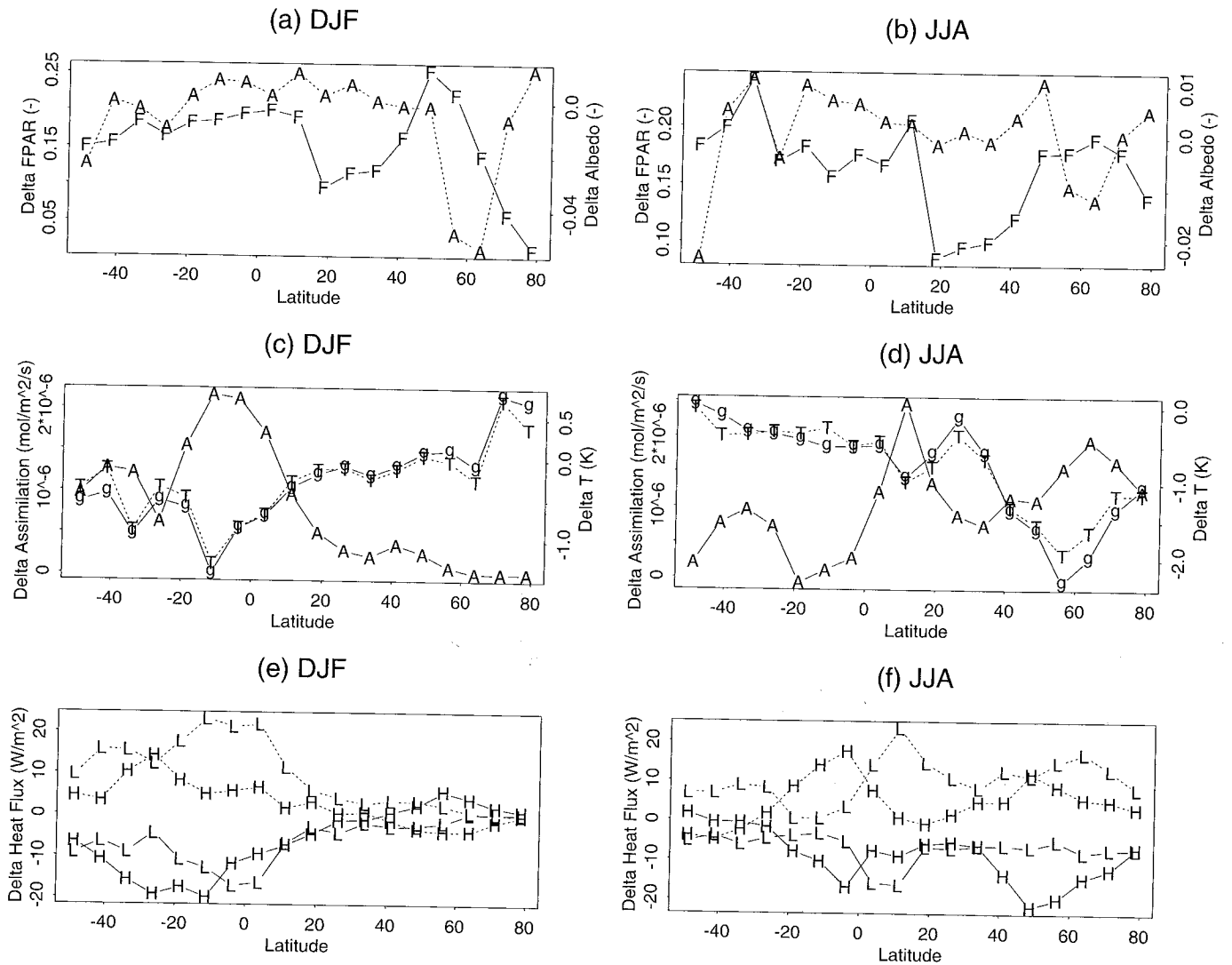


Figure 7.2: Sensitivity of the energy balance to changes in FPAR derived from the maximum and minimum FPAR runs with the SiB2-GCM. Delta values are expressed as the difference between the maximum run minus the minimum run. Results are averaged by latitude for December until February (DJF) and June until August (JJA).

(a) Latitudinal averages of landsurface Δ albedo (A) and Δ FPAR (F) for DJF. The Δ FPAR follows closely the change in NDVI (figure 7.1). Notice that overall changes in albedo are small. (b) Same but for JJA.

(c) Latitudinal averages of landsurface Δ assimilation, Δ ground temperature (g), and Δ landsurface air temperature (T) for DJF. Δ assimilation is inversely related to Δ air temperature and Δ ground temperature because of the close link between assimilation (photosynthesis) and transpiration. (d) Same but for JJA.

(e) Latitudinal averages of latent (L) and sensible (H) heat flux for DJF. (f) Same but for JJA.

1. The net radiation, R_n , is a function of the surface albedo, which in turn is a function of the leaf area index, and the leaf and soil optical properties. The surface albedo is calculated in SiB2 with a two-stream model (Dickinson 1984, Sellers *et al.* 1996a).
2. The total surface latent heat flux consists of a soil and a leaf component. Both the leaf and soil latent heat components are split in a wet and dry fraction. The wet fraction results from interception of water by leaves or the ground surface.

- (a) The latent heat flux from the dry fraction of leaves (transpiration) is calculated analogously to the Penman-Monteith equation and depends amongst other variables on net radiation, aerodynamic resistance for heat and water vapor, and canopy resistance. The aerodynamic resistance is a function of roughness length and canopy resistance is inversely related to the stomatal conductance which is closely related to the assimilation rate (equa-

tion 7.1).

- (b) The latent heat flux from the wet fraction of leaves is a function of the canopy temperature and of the bulk canopy boundary layer resistance.
 - (c) The latent heat flux from the dry soil is a function of the ground temperature, soil water content, windspeed, and the incoming radiation. The incoming radiation for the soil is inversely related to the leaf area index.
 - (d) The latent heat flux from the wet soil is a function of the ground temperature and the aerodynamic resistance between the ground and canopy air-space.
3. The sensible heat flux also consists of a soil and leaf component. The leaf sensible heat flux is related to the difference between the leaf and air temperature, and the soil sensible heat flux is related to the soil and air temperature. The ground and canopy temperatures are calculated in an iterative procedure to balance them with the incoming and outgoing heat fluxes and hence are dependent on the factors under item 2.

7.3.2 Sensitivity Analysis

The albedo directly affects the radiation balance of the land surface. Vegetation in turn affects the albedo, *i.e.*, an increase of green leaves over a bright soil background decreases the albedo and, other things being equal, results in an increase of the amount of radiation absorbed by the land surface. Contrary to the expected mechanism, figure 7.2.a shows that the overall increase in FPAR is matched by only a small decrease in albedo at high latitudes. The lack of relationship between FPAR and albedo was discussed in (section 6.3) and is caused by the specification of a low soil albedo that is close to that of vegetation for most SiB2 landcover types. A change in the amount of leaves therefore leads to a minor change in albedo and, in cases where leaves are brighter than the soil background, to an increase (Chapter 6.3). Because of the small change in albedo no large shifts in the total energy balance, *i.e.*, the total amount of energy absorbed by the sum of land-surface vegetation and soil, are expected.

The change in albedo at northern latitudes around 60° (figure 7.2.a) is most likely the result of an increase in the vegetation cover fraction in the boreal forests and a decrease in the snow cover fraction. The large change in albedo around 60° N during winter has only a small effect on the mean temperature (figure 7.2.c) and the energy balance (figure 7.2.e) because of the low amounts of incoming solar radiation during this time of year. A change in landsurface air temperature is more closely associated with a change in evapotranspiration and assimilation rate

than either a change in albedo or a change in FPAR. When evapotranspiration increases both the ground temperature and landsurface air temperature decrease. The decrease in temperature is large for the tropics (20° S to 20° N) during December until February and for the Northern Hemisphere temperate regions (40° N to 65° N) during June until August. The decrease in temperature in both hemispheres is small throughout the year for arid and semi-arid regions between 20° and 40° N and S and during their respective winters at mid-to-high latitudes.

Although the changes in the total energy balance are small, there is considerable change in the partitioning of energy between its four components: the canopy latent and sensible heat fluxes and the soil latent and sensible heat fluxes. The increase in FPAR caused the canopy latent and sensible heat to increase and the soil latent and sensible heat fluxes to decrease. The increase in canopy latent heat flux closely follows the increase in assimilation due to a direct link between photosynthesis and transpiration. At latitudes where an increase in FPAR is not matched by an increase in assimilation an increase is seen in the sensible heat flux (for example, between 20° and 40° S during DJF and 0° to 20° S during JJA). The decrease in the soil sensible and latent heat flux is the direct result of increased leaf area leading to increased shadowing (reduction of radiation reaching the soil), increased interception of rainfall (increased evaporation from the leaf surface), and increased stomatal conductance (increased plant transpiration).

7.4 Water Balance

7.4.1 SiB2 Hydrological Submodel

The SiB2 hydrological submodel consists of a canopy liquid water storage compartment, a ground liquid water storage compartment, and a three-layer soil model (figure 7.3). Incoming precipitation is divided in a component intercepted by the canopy liquid water storage compartment and a throughfall component. Water intercepted by the canopy can either evaporate or, when the capacity of the canopy liquid water store is exceeded, contribute to the throughfall. The throughfall component, the precipitation that falls through gaps in the canopy, is calculated as a function of leaf area index and of the fraction of vegetation cover in a grid cell. The sum of the direct throughfall and of the water dripping from the leaves reaching the ground is intercepted by the ground liquid water storage compartment.

Water in the ground liquid store either evaporates, infiltrates into the surface layer when the capacity of the ground liquid water store is exceeded, or contributes to the overland flow if the infiltration is in excess of the infiltration capacity of the soil. Overland flow contributes to the surface runoff.

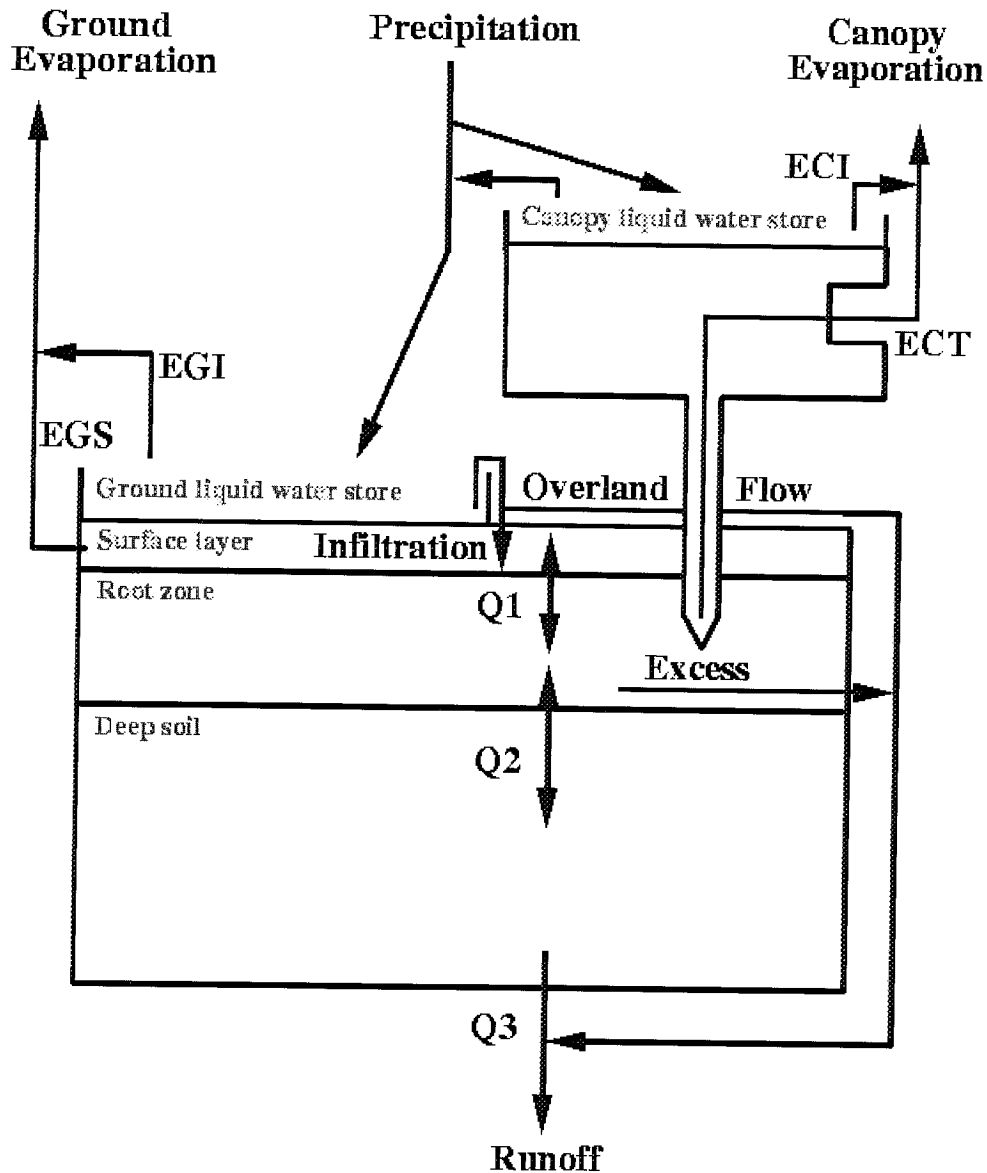


Figure 7.3: *Hydrological sub-model in SiB2* (See text for description). *ECI* is the evaporation of water intercepted by the canopy, *ECT* is the transpiration by plants, *EGI* is the evaporation of water intercepted by the ground surface, *EGS* is evaporation of water in the soil surface layer. *Q1* is the flux from the surface layer to the root zone, *Q2* is the flux from the root zone to the deep soil layer, and *Q3* is the drainage from the deep soil contributing to the runoff. *Q1* and *Q2* can both be incoming and outgoing fluxes, *Q3* can only be an outgoing flux (or zero).

The surface layer is a shallow layer of 2 cm thickness that is held constant for the entire land surface (Appendix D). Water can either evaporate from this layer or infiltrate into the root zone. Water from the root zone can flow up into the surface layer, flow down into the deep soil, contribute to the runoff if the root zone saturates, or can be used by vegetation for transpiration. Note that the root zone is the only layer that can be accessed by vegetation to fulfill its water demand.

Water in the deep soil flows out as drainage where it contributes to the runoff or it flows back into the root

zone. Water in excess of the volume of the deep soil layer also contributes to the runoff. The hydraulic conductance for the upward flow of water, *e.g.*, from the deep layer to the root layer, is many times smaller than the hydraulic conductance for the downward flow of water to avoid depletion of water in the deep layers.

7.4.2 Sensitivity Analysis

Figure 7.5 shows how a change in FPAR affects the components of the water balance in the SiB2-GCM.

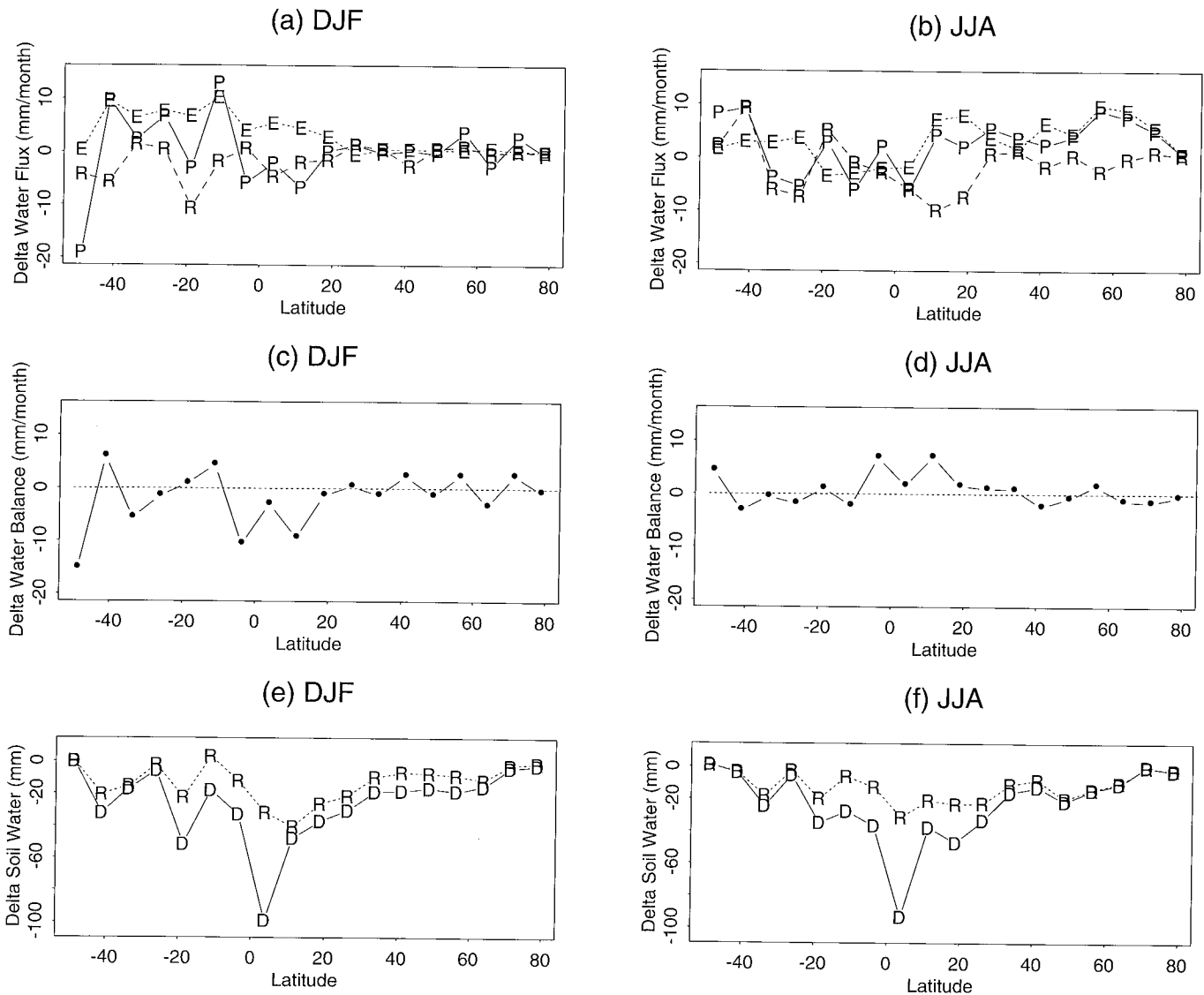


Figure 7.4: Sensitivity of the water balance to changes in FPAR derived from the maximum and minimum FPAR runs with the SiB2-GCM. Delta values are expressed as the difference between the maximum run minus the minimum run. Results are averaged by latitude for December until February (DJF) and June until August (JJA).

(a) Changes in Precipitation (P), Evapotranspiration (E) and Runoff (R) for DJF. (b) Same but for JJA. (c) Net change in water balance (Precipitation - Evapotranspiration - Runoff) for DJF. (d) Same as (c) but for JJA. (e) Change in water contents of the root layer (R) and deep soil layer (D) for DJF. (f) Same as (e) but for JJA.

1. Input fluxes

- (a) Convective precipitation has a large land surface component and increases as a result of increased evapotranspiration,
- (b) Large area (stable) precipitation, for the main part originating over oceans, does not change.

2. Output Fluxes

- (a) Ground evaporation decreases because of reduced absorption of solar radiation by the ground as a result of increased shading by leaves,

- (b) Canopy evaporation increases as a result of both an increase in canopy liquid water store and in transpiration,

- (c) Runoff decreases as a result of decreased flow from the deep soil. The contribution from the overland flow increases somewhat due to a reduction in ground evaporation.

3. Storage Terms

- (a) Canopy liquid water store increases because of increased leaf area index ($\approx 0.1 \text{ mm/LAI}$),

- (b) Ground liquid water store increases because of reduced evaporation,
- (c) Water in the shallow surface layer increases because of reduced evaporation,
- (d) Water in the root zone decreases because of increased transpiration. The other fluxes from and into the root zone in part compensate this increased outflow; water flowing from the root zone into the deep soil (Q2) is reduced and water flowing from the surface into the root zone (Q1) is increased,
- (e) Water in the deep soil layer decreases because of a decreased flux from the root zone (Q2). This decrease is in part compensated by a decrease in the outgoing flux (Q3).

contents in the root zone and deep soil layers; the decrease in the amount of water is larger during December until February compared to the decrease during June until August.

Of all the storage components in the model, the deep soil layer is the most affected. This is counterintuitive because as a general rule the fluctuations in water level decrease with increasing depth (Engelen and Jones 1986). The high fluctuations in the deep soil could be dampened by increasing the drainage resistance and thus diminish the outflow from the deep layer. The other parts of the hydrological submodel behave in a way that is consistent with general knowledge of the working of its components.

One aspect not incorporated in the SiB2 hydrological model is the change in infiltration capacity of the soil that can be expected from changes in the amount of vegetation. Increased amounts of vegetation are related to increased amount of leaves and increased litterfall. A thicker litter layer protects the soil from erosion and has a higher infiltration capacity which leads to a reduction of overland flow and surface runoff immediately after rainfall. The higher infiltration capacity also leads to a higher amount of water stored in the soil and to a prolonged contribution of the deep soil to the base flow component of surface runoff. Thus the association between higher vegetation amount and increased infiltration capacity of the soil is due to an increase of the litter layer depth (Bruijnzeel 1983). The increased infiltration capacity, if incorporated in SiB2, would counteract the increased overland flow found in the current results.

The latitudinal plots of changes in the water balance as a result of changes in FPAR (figure 7.4) show that during summer in both the Northern and Southern Hemispheres the evapotranspiration increases and with it the convective precipitation (see also figure 7.5). The change in runoff closely follows the change in precipitation with the exception of latitudes where a large increase in evapotranspiration relative to the increase in precipitation occurs. The net water balance (precipitation minus the sum of evapotranspiration and runoff) shows the largest fluctuations in the tropics. During December until February a deficit occurs, during June until August a surplus. The impact of the deficit is reflected by the change of water

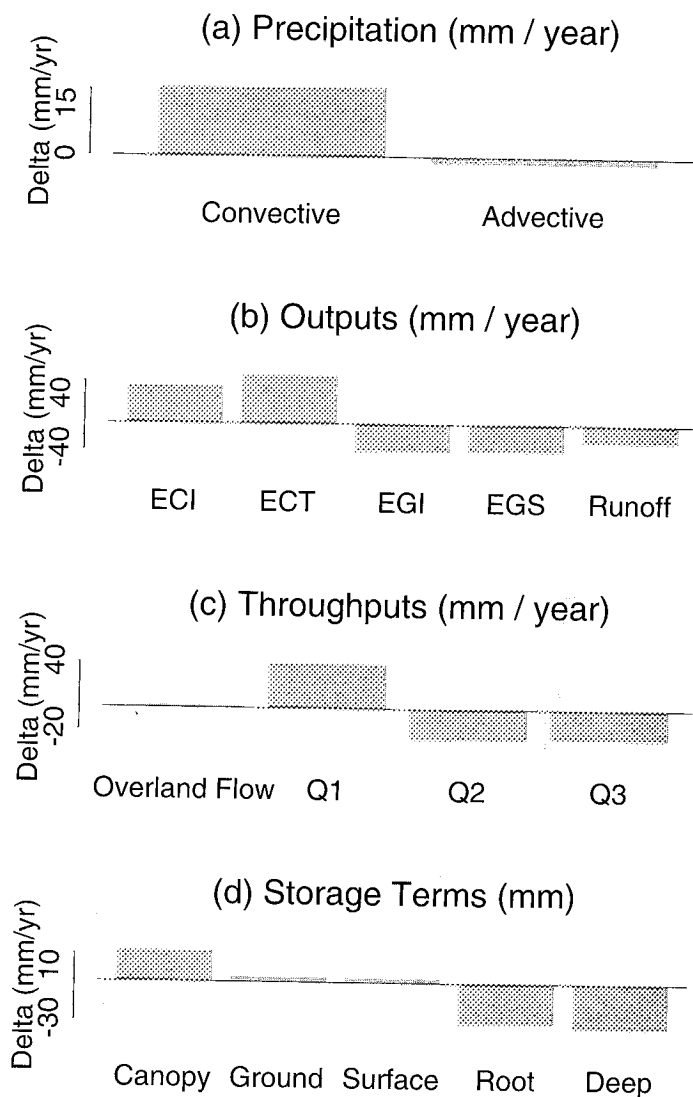


Figure 7.5: Sensitivity of the water balance to changes in FPAR derived from the maximum and minimum FPAR runs with the SiB2-GCM. Delta values are expressed as the difference between the maximum run minus the minimum run. Results are averaged over the global land surface. ECI is the delta in evaporation of water intercepted by the canopy, ECT is the delta in transpiration by plants, EGI is the delta in evaporation of water intercepted by the ground surface, EGS is the delta in evaporation of water in the soil surface layer. Q1 is the delta in the flux from the surface layer to the root zone, Q2 is the delta in the flux from the root zone to the deep soil layer, and Q3 is the delta in the drainage from the deep soil contributing to the runoff. Q1 and Q2 can both be incoming and outgoing fluxes, Q3 can only be an outgoing flux (or zero).

The decrease in the amount of soil water in the deep layer is very large at the equator in part because a large depth is specified in the tropics, about 2 times the deep soil depth elsewhere.

7.5 Feedback Between Vegetation and Climate

One of the first studies to investigate a feedback mechanism between the biosphere and climate with an atmospheric general circulation model was a study by Charney *et al.* (1975). Charney *et al.* (1975, 1977) posited that in desert margins such as the Sahel, a decrease in vegetation cover would lead to a decrease in albedo. As a result, the land surface would absorb less solar radiation and this would decrease the total energy (sum of latent and sensible heat) emitted by the land surface. The reduced radiation by the land surface cools the lower atmosphere and this would either enhance the sinking motion of air over deserts, or decrease the amount of convection. Precipitation rates would diminish leading to a decrease in the moisture available for plant growth, thus enforcing or sustaining the initial decrease in vegetation. Charney *et al.* (1975, 1977) stated that the same logic should apply to the reversed situation, *i.e.*, a situation in which vegetation was increased would lead to an increase in precipitation which would sustain the increased vegetation.

To test if the effects of the increased albedo would be sufficiently strong to affect large circulation patterns, *e.g.*, monsoon circulation, Charney *et al.* (1975, 1977) compared two scenarios with a GCM, a high albedo scenario representing conditions with low vegetation cover in the Sahel and a low albedo scenario representing conditions with high vegetation cover in the Sahel. The GCM results predicted that the induced changes in albedo were sufficiently strong to overcome the monsoon circulation from the south and that an increase in albedo in the initial conditions did result in decrease of precipitation in the Sahel and an increase in precipitation over the tropical forest south of it.

Xue and Shukla (1991) investigated how changes in vegetation affected the climate in the Sahel with a much improved landsurface model, a simplified version of SiB1, coupled to a GCM. They stated that a change in vegetation cover would not only affect the landsurface albedo but also parameters such as the roughness length, initial soil wetness conditions, leaf area index, soil depth, the hydraulic conductivity of the soil, and the fraction of vegetation cover. They obtained estimates of simultaneous changes in these parameters in sub-Saharan Africa by changing landcover types (and associated parameters) from predominantly woodland and shrubland types (SiB classes 6 and 8) to a bare soil with shrubs type (class 9). As in the Charney *et al.* (1975, 1977) study they found

a decrease in the precipitation over the Sahel and an increase in the precipitation over the tropical forest. However, Xue and Shukla (1991) concluded that the major impact of vegetation changes on precipitation in desert margins was related to changes in the latent heat flux rather than to albedo.

The sensitivity analyses with the minimum and maximum FPAR scenarios in the SiB2-GCM also provide an opportunity to test a positive feedback between vegetation and climate. Contrary to the approaches by Xue and Shukla (1991) and Charney *et al.* (1975, 1977), boundary conditions for the minimum and maximum vegetation scenarios were obtained from (satellite) observations rather than being arbitrarily imposed, either by an assumed change in albedo (Charney *et al.* 1975, 1977) or an assumed change in vegetation cover type and associated parameters (Xue and Shukla 1991). Moreover, the parameter changed in this study, FPAR, is more directly linked to vegetation than either albedo or landcover type. The current experiment differs in other aspects from the experiments by Charney *et al.* (1975, 1977), and Xue and Shukla (1991), as well:

1. Compared to the maximum FPAR scenario, the minimum FPAR scenario has decreased values for all vegetated regions (figure 7.1.a, .b), not just in the Sahel.
2. Because of the specification of soil optical properties and leaf optical properties, changes in albedo as a function of FPAR are small (compare a change in the albedo smaller than +1% (figure 7.2.a, b) compared to a change around -8% (Xue and Shukla 1991), or -17% (Charney *et al.* 1975). Thus in this sensitivity analysis we primarily test how a change in FPAR and associated parameters (leaf area index, assimilation, transpiration) affects the climate.
3. Use of a more elaborate landsurface model: the main differences with the simple SiB model used by Xue and Shukla (1991) are the incorporation of a photosynthesis and stomatal conductance model (Collatz *et al.* 1991, 1992) and the use of satellite data to derive biophysical parameters (Chapter 5, Appendix D, Sellers *et al.* 1996b). The Simple Biosphere model uses interdependent relationships to describe the exchange of water, energy, and momentum between the atmosphere and the land surface. For example, evaporation rates are not only a function of soil moisture, atmospheric humidity, and temperature; they are also regulated by the stomatal conductance and photosynthetic rates of vegetation.
4. Differences in initial soil moisture: soil moisture is not prescribed as in the Charney model but is al-

lowed to vary based on the interaction between climate and vegetation.

The analysis of the current model runs was restricted to areas between 40° S and 40° N. Annual pixel-by-pixel averages were used to reduce potential lag effects, *e.g.*, between changes in net precipitation leading to changes in soil water storage.

Figures 7.6.a through c show the relationships between the components of the feedback mechanism proposed by Charney *et al.* (1977), *i.e.*, the relationships between delta FPAR and delta albedo (figure 7.6.a), delta albedo and the delta of the net energy emitted by the land surface, the delta of the net energy emitted by the land surface and delta precipitation (figure 7.6.b), and the delta of the net energy emitted by the land surface and the delta in soil water contents (figure 7.6.c).

Delta FPAR and delta albedo show a weak, positive relationship for tall vegetation ($r = 0.2$) and a stronger positive relationship for short vegetation ($r = 0.67$; figure 7.6.a). Close inspection of the relationship between delta FPAR and delta albedo for short vegetation reveals that this relationship is more complex than a simple one-to-one relationship; in the data, a second, negative relationship can be seen that branches off from the positive relationship at zero delta FPAR and delta albedo values. In Chapter 6.3 it was found that the sign of the relationship between FPAR (or NDVI) and albedo depends on the specification of the soil background reflectance relative to the leaf reflectance. If the soil background is assigned a lower reflectance value than the leaves, the landsurface albedo increases when more leaves are added to a bare soil; if the soil has a higher reflectance than the leaves, the reverse occurs.

The delta albedo, both for tall and short vegetation, has a negative relationship with the delta of the net energy (sum of soil latent and sensible heat and canopy latent and sensible heat) emitted by the land surface. The scatter in the relationship is explained by variations in incoming radiation as a result of variations in cloud cover and radiative transfer properties of the atmosphere. The relationship between delta albedo and delta net energy is strongest for short vegetation ($r = -0.61$) and less strong for tall vegetation ($r = -0.31$). Notice that contrary to the model proposed by Charney *et al.* (1977), the net energy emitted by the land surface decreases with increasing vegetation because of an increase in albedo with increasing FPAR.

The relationship between the delta net energy and the delta precipitation is fairly weak for both short and tall vegetation types. Moreover, when predicting the mean delta precipitation from the mean change in net energy (-12 W/m^2), using the regression line, a decrease in precipitation of about 5 mm per month is found whereas the average change in precipitation is positive and has a value of about 1 mm per month.

The sensitivity analysis with the SiB2-GCM indicates inconsistencies between the relationships of the components of the positive feedback model proposed by Charney *et al.* (1977). The most notable differences are the positive relationship between FPAR and albedo for several vegetation classes and the discrepancy in the delta precipitation versus delta net energy. Delta precipitation shows a negative relationship with the delta net energy but the mean deviations have a reverse sign; the mean delta in net energy is -12 W/m^2 and the mean delta precipitation is +1 mm. Alternative feedback mechanisms more closely linked to the functioning of the biosphere are therefore investigated.

In figures 7.6.e-h an alternative, biophysically-based feedback mechanism is suggested. Figure 7.6 suggests that a positive change in FPAR leads to a positive change in assimilation by the biosphere, which in turn leads to increased evapotranspiration and (convective) rainfall. Contrary to the Charney *et al.* (1975, 1977) model we see a negative feedback because the effective precipitation, the difference between precipitation and evapotranspiration, decreases. This reduces the amount of soil moisture, increases moisture stress on vegetation and thus impacts vegetation growth in a negative way. Compared to the components of the model by Charney *et al.* (1977), the relationships between the components of the biospheric model are consistent between vegetation types, are stronger overall, and are consistent with mean deviations in the components. Compare the association between FPAR and albedo (figure 7.6.a) with the association between FPAR and plant assimilation (figure 7.6.e); the association between albedo and net energy (figure 7.6.b) with assimilation and evapotranspiration (figure 7.6.f); and the association between net energy and precipitation (figure 7.6.c) with evapotranspiration and precipitation (figure 7.6.g); and finally compare the association between the change in net energy and soil water content (figure 7.6.d) with the change in effective precipitation and the change in soil water content (figure 7.6.h).

An aspect not considered by the Charney model, which appears from the biophysical model, is the depletion of soil moisture with increasing evapotranspiration. The increased moisture stress on vegetation leads to increased stomatal resistance and reduced transpiration. To introduce a negative feedback between vegetation and precipitation Charney *et al.* (1977) proposed that increased cloudiness (as a result of increased convection) would decrease the amount of solar radiation available to heat the land surface. In figure 7.6.b a fair amount of variation in the delta albedo versus delta net energy is seen, possibly as a result of variations in cloudiness, but the overall relationship is preserved. Thus the SiB2-GCM does predict variations in net solar radiation, but not to the extent that they provide a negative feedback between increased vegetation and increased precipitation.

7.5. FEEDBACK BETWEEN VEGETATION AND CLIMATE

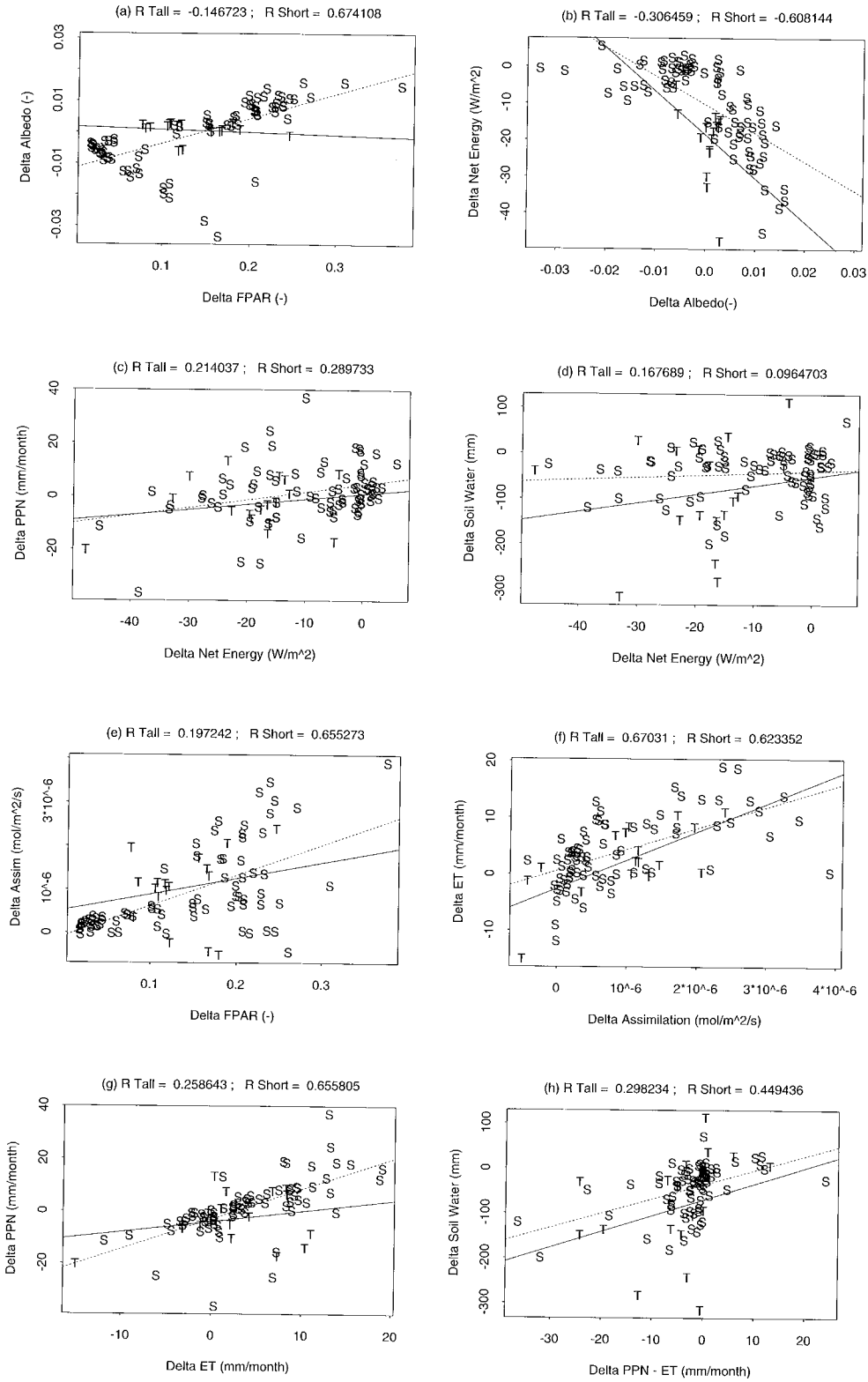


Figure 7.6: Feedbacks in the local climate as a result of changes in FPAR (s = short vegetation, T = tall vegetation; see text for discussion).

7.6 Conclusion

The sensitivity analysis of carbon, energy, and water fluxes between the land surface and atmosphere with the minimum and maximum FPAR runs in the SiB2-GCM revealed several interesting aspects. A change in FPAR first of all affects the photosynthesis, but only if limiting factors (increased stresses by reduced soil moisture and low temperatures) do not significantly increase. Changes in the total energy balance were small because the albedo changed only slightly between the minimum and maximum FPAR run. By contrast, the partitioning between the soil and canopy components of the energy balance changed considerably because the increased leaf area index resulted in increased shadowing (more sensible heat from the canopy, less from the soil) and evaporation (more latent heat from the canopy, less latent heat from the soil). Projected changes in surface air temperature and ground temperature were closely linked to changes in assimilation and were between -2 and 0 °C.

Of the investigated landsurface processes, water balance is the most seriously affected. Increased FPAR leads to increased assimilation, increased evapotranspiration, and a depletion of soil moisture, especially at low latitudes.

The use of a biosphere model in the landsurface parameterization revealed novel aspects in a feedback loop between vegetation and precipitation proposed by Charney *et al.* (1975, 1977). The current results indicate that transpiration by vegetation is a more important driver of convective precipitation than the overall changes in the energy balance (see also Xue and Shukla 1991). In addition, observations of the water balance showed that depletion of soil moisture produces a negative feedback on the increased vegetation → increased precipitation feedback loop, especially at low latitudes.

Chapter 8

Radiative and Physiological Effects of Doubled Atmospheric CO₂ on Climate

Slightly revised from publication by P.J. Sellers, L. Bounoua, G.J. Collatz, D.A. Randall, D.A. Dazlich, S.O. Los, J.A. Berry, I. Fung, C.J. Tucker, C.B. Field, and T.G. Jensen, 1996, *Science*, **271**, 1402-1406.

Abstract

The physiological response of terrestrial vegetation when directly exposed to an increase in atmospheric CO₂ concentration could result in additional warming over the continents above that due to the conventional CO₂ greenhouse effect. Results from a coupled biosphere-atmosphere model (SiB2-GCM) indicate that, for doubled CO₂ conditions, evapotranspiration will drop and air temperature will increase over the tropical continents, amplifying the changes resulting from atmospheric radiative effects. The range of responses in surface air temperature and terrestrial carbon uptake due to increased CO₂ are projected to be inversely related in the tropics year-round, and during the growing season elsewhere.

8.1 Introduction

A number of simulation studies have investigated the impact of increasing atmospheric CO₂ concentration on the energy balance, precipitation, and surface air temperature of the Earth. A recent assessment of the results produced by different atmospheric general circulation models (AGCMs) indicates that the globally-averaged surface air temperature could increase by 1.5 °C to 4.5 °C in response to a doubling of atmospheric CO₂ (Houghton *et al.* 1990). In almost all cases, the impacts of increasing CO₂ are conventionally associated with changes in the radiation and energy balances; physiologically-induced effects on climate are ignored. In this paper we investigate the potential for additional warming over the continents as a result of the physiological response of terrestrial vegetation when exposed to an equilibrium doubling in atmospheric CO₂ concentration.

Terrestrial vegetation takes up CO₂ for photosynthe-

sis through small pores in the leaf surface called stomates. At the same time, water vapor from the leaf interior diffuses out through the stomates to the atmosphere (transpiration). Plants continuously adjust the widths of their stomatal apertures, apparently to enhance CO₂ uptake for a given evaporative loss of leaf water (Cowan 1977). Leaf stomatal conductance to water vapor transfer appears to be sensitive to variations in net photosynthetic rate, and hence to light intensity, temperature, soil moisture, and atmospheric CO₂ concentration, as well as to changes in humidity and CO₂ concentration at the leaf surface. Leaf-scale models of net photosynthetic assimilation, A , and stomatal conductance, g_s , have been formulated to describe these relations (for example, Collatz *et al.* 1991, 1992).

The physiological effects on climate due to increasing atmospheric CO₂ result from the dependence of photosynthesis and stomatal conductance on CO₂ partial pressure (Figure 8.1). Short-term exposure of C₃ plants to 2 × CO₂ (a doubling of the atmospheric CO₂ concentration) stimulates photosynthesis (figure 8.1.a, b) and decreases stomatal conductance (figure 8.1.c) from C (control) to P (physiological response to 2 × CO₂). After long-term exposure to increased atmospheric CO₂, plants may reduce their biochemical capacity for photosynthesis, V_{max} . This response is represented by PV (physiological effects due to 2 × CO₂ with “down-regulated” V_{max}) in figure 8.1.b and c. The PV case in figure 8.1 depicts a large down-regulation response where photosynthesis at 2 × CO₂ is adjusted to maintain about the same rate as under normal (1 × CO₂) conditions. Down-regulation has been observed in some, but not all, experiments with plants grown at elevated CO₂ (Field *et al.* 1992, Tissue *et al.* 1993). The extent of down-regulation apparently depends on species, nutritional status, and environmental stresses (Gunderson and Wullschleger 1994, Field 1991). Our calculations indicate an associated decrease in stomatal conductance in the range of 25% (P) to 50% (PV) which is consistent with the range of experimental ob-

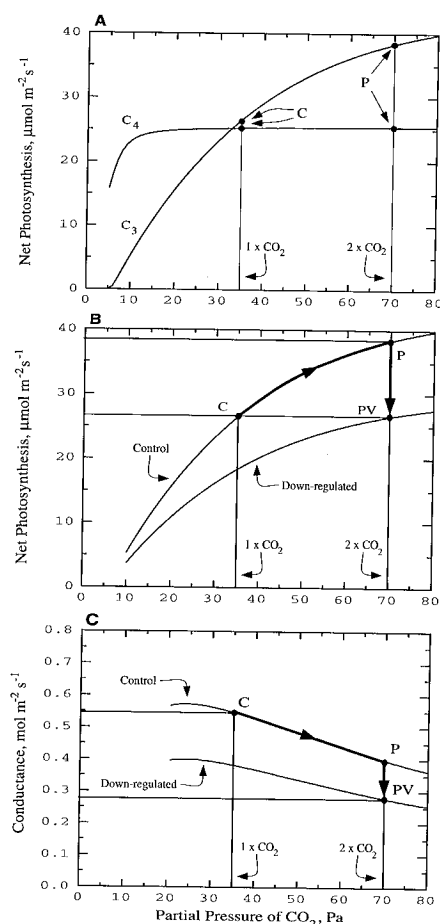


Figure 8.1: Leaf photosynthesis and conductance responses to local increases in atmospheric CO₂ for light-saturated conditions, based on leaf-scale model results. (a) Dependence of leaf photosynthesis for C₃ and C₄ vegetation on exterior air CO₂ concentration. (b) C₃ photosynthesis curves for unadjusted (C, P) and down-regulated (PV) physiology. Note that the "down-regulated" photosynthetic rate at 2 × CO₂ is the same as the control case (1 × CO₂) photosynthetic rate. (c) Effects on stomatal conductance. Curves show the dependence of stomatal conductance with increasing CO₂ for unadjusted vegetation (P) and down-regulated physiology (PV).

servations on trees (Field *et al.* 1995a) and herbaceous species (Morison 1985). Analyses of stomatal densities on fossil or otherwise preserved leaf surfaces (Beerling and Chaloner 1994, Penuelas and Matamala 1990, Woodward 1987b) also imply that g_s has decreased in response to historical increases in atmospheric CO₂ partial pressure.

The lines linking the P and PV points in figure 8.1.b, c thus describe the likely range of physiological responses of vegetation to increased CO₂ in the absence of other climatic effects. Photosynthesis could increase significantly, with a small reduction in stomatal conductance (the P

case); photosynthesis might remain more or less constant and g_s and transpiration significantly reduced (the PV case); or something in between could occur.

The improved simple biosphere model (SiB2) incorporates a coupled photosynthesis-conductance submodel into its vegetation canopy model (Collatz *et al.* 1991, 1992, Sellers *et al.* 1992a, Sellers *et al.* 1996a) so that the exchanges of energy, water, and carbon between the land and atmosphere are modeled as tightly linked processes. SiB2 has been linked to an AGCM (Randall *et al.* 1996) which also incorporates simple ocean and sea-ice models (Jensen *et al.* 1995). Global satellite data for 1987 were used to define the type, density, and greenness of the vegetation worldwide at monthly intervals (Sellers *et al.* 1996b, Chapter 5, Appendix D). The use of these data should correct many biases in previous survey-based descriptions; for example, overestimation of vegetation density in the boreal forest (Dorman and Sellers 1989, Sellers *et al.* 1996b, Appendix D). The satellite data form the basis for specifying monthly fields of albedo, surface roughness, and a canopy light-use parameter which is used to scale up the leaf physiological model to the canopy scale—*i.e.*, to integrate leaf photosynthesis to canopy photosynthesis—and leaf conductance, g_s , to canopy conductance, g_c (Sellers *et al.* 1992a). The model also calculates the contributions of canopy interception loss and soil evaporation to the total evapotranspiration flux. The results from large-area field experiments have been used to test scaling assumptions involved in the use of area-averaged satellite data to describe the vegetation state (Sellers *et al.* 1992a, Sellers *et al.* 1995). The combined SiB2-GCM produces plausible fields of evapotranspiration, carbon assimilation, and surface energy balance components in addition to reasonable climate simulations (Randall *et al.* 1996). Simulations produced by the SiB2-GCM have been used in other biosphere-atmosphere studies (Ciais *et al.* 1995, Denning *et al.* 1995).

8.2 Design of Experiment

Model runs were conducted at 7.2° by 9.0° spatial resolution and 9 layers in the vertical. First, the model was run using observed climatological sea surface temperatures and the current 1 × CO₂ concentration (350 ppm) for 10 years to obtain the implied ocean heat transports (Jensen *et al.* 1995, Hansen *et al.* 1984) and initial conditions for the experiment runs. This was followed by six 30-year integrations (runs) in which sea surface temperatures and sea ice were permitted to evolve with time (figure 8.2).

1. The control (C) run. This consisted of an integration from the initial conditions out to 30 years using 1 × CO₂ (350 ppm) for both the radiative transfer

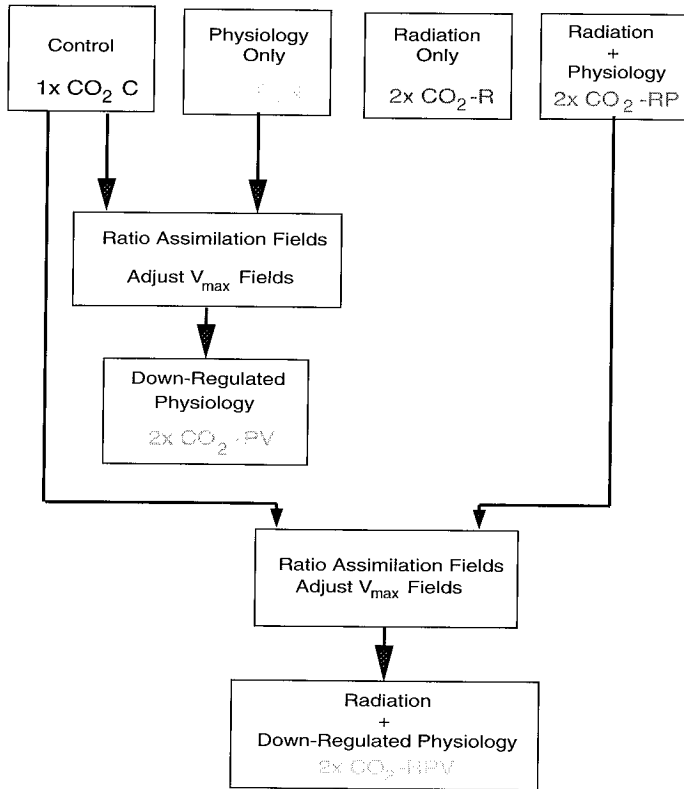


Figure 8.2: Sequence and type of numerical CO_2 experiments performed with the biosphere-atmosphere model, SiB2-GCM. The explanation of each case is described in the text.

code in the AGCM and the vegetation physiological model.

2. The physiology-only (P) run. The CO_2 concentration in the AGCM boundary layer was maintained at $2 \times \text{CO}_2$ (700 ppm) and thus directly influenced the photosynthesis-conductance model, (figure 8.1). In this run, the biome-dependent physiological parameter that limits the maximum photosynthetic rate V_{\max} was the same “unadjusted” as in the control run. The radiation code operated on a $1 \times \text{CO}_2$ (350 ppm) CO_2 atmosphere.
3. The down-regulated physiology (PV) run. The assimilation rates calculated for each grid point for the last 10 years of the C and P integrations were time-averaged and ratios were calculated (C/P). These ratios were used to reduce proportionally the V_{\max} values at every grid point to simulate a large down-regulation effect. The result is that, at doubled CO_2 , the assimilation rates calculated by the vegetation model in the PV run should approach those produced by the C case (figure 8.1.b).

4. The radiation-only (R) run. This is a conventional $2 \times \text{CO}_2$ integration in which only the AGCM radiative transfer code responds to $2 \times \text{CO}_2$; the vegetation “sees” only $1 \times \text{CO}_2$.
5. The radiation plus physiology (RP) run. This is a combination of the R and P treatments; the atmospheric radiation code works with $2 \times \text{CO}_2$ as does the (unadjusted) physiology.
6. The radiation plus down-regulated physiology (RPV) run. The assimilation fields of the last 10 years of the C and RP runs were averaged and their ratios applied to the V_{\max} fields in the same way as for PV. The RPV case was then run forward using these adjusted fields and $2 \times \text{CO}_2$ values for both the AGCM radiation code and the atmospheric boundary layer in contact with the vegetation.

Table 8.1 shows assimilation rate (A), canopy conductance (g_c), evapotranspiration rate (E), precipitation (P), and surface air temperature (T) values for each run and also changes relative to the control run.

8.3 Results and Discussion

The impact of the radiation-only (R-case) treatment on assimilation (A) was very small; the assimilation fields generated by the C and R cases were almost identical everywhere. The P and RP runs had significantly higher A values than their $1 \times \text{CO}_2$ (physiology) counterparts, C and R, respectively. These results were anticipated from an inspection of figure 8.1. The down-regulated A values (PV and RPV) are slightly increased, about 10%, over the control case (C). This difference indicates that the down-regulation of A in the PV and RPV treatments was not complete; largely because A is enhanced at elevated CO_2 concentrations in C_3 plants at lower light intensities; i.e., when V_{\max} is not limiting.

The overall effect of down-regulation (PV and RPV) was to reduce g_c values by 35% relative to the control (C) or radiation-only (R) cases while the unadjusted physiology treatments (P and RP) gave reductions of about 25%. This range of responses falls within that observed in laboratory and field $2 \times \text{CO}_2$ manipulation experiments (Morison 1985, Field 1991, Field *et al.* 1992, 1995a, Tissue *et al.* 1993, Gunderson and Wullschlegel 1994). There is little difference between the radiation-only (R) and control (C) case g_c values, which is consistent with the assimilation results discussed above. Canopy conductance generally decreases away from the equator, following the environmental and vegetation density gradients. We therefore expect to see the largest physiological impacts of $2 \times \text{CO}_2$ on the evapotranspiration rates in the tropics, and smaller effects in the high latitudes.

Table 8.1: Summary of results from six double CO₂ experiments described in the text. C = control, 1×CO₂ for radiation and physiology; P = 1×CO₂ for radiation and 2×CO₂ for physiology; PV = 1×CO₂ for radiation and 2×CO₂ for down-regulated physiology; R = 2×CO₂ for radiation and 1×CO₂ for physiology; RP = 2×CO₂ for radiation and physiology; and RPV = 2×CO₂ for radiation and down-regulated physiology. Values are means over the last 10 years of the 30-year simulations. Values in parenthesis are the percent differences from C, except in the case of surface air temperature where the values are the differences from C. Dashes indicate not applicable.

Experiment	Tropics 14.4° S – 14.4° N		Mid latitudes 28.8° N – 50.4° N		Northern latitudes 50.4° N – 72.0° N		All land points		Global (land and ocean)	
A (μ mol m ⁻² s ⁻¹)										
C	6.0	(-)	1.8	(-)	1.7	(-)	2.7	(-)		
P	8.0	(32)	2.6	(48)	2.3	(36)	3.6	(36)		
PV	6.9	(14)	2.0	(11)	1.8	(6)	2.9	(11)		
R	6.1	(1)	1.7	(-3)	1.6	(-2)	2.7	(0)		
RP	8.1	(35)	2.5	(43)	2.3	(35)	3.6	(36)		
RPV	6.7	(11)	2.0	(14)	1.8	(9)	2.9	(11)		
g_s (mm s ⁻¹)										
C	2.8	(-)	0.8	(-)	0.9	(-)	1.2	(-)		
P	2.1	(-26)	0.6	(-23)	0.7	(-26)	0.9	(25)		
PV	1.8	(-35)	0.5	(-38)	0.6	(-36)	0.8	(-35)		
R	2.8	(1)	0.8	(-1)	0.9	(-1)	1.2	(0)		
RP	2.1	(-24)	0.61	(-24)	0.7	(-25)	0.9	(-24)		
RPV	1.8	(-36)	0.5	(-36)	0.6	(-32)	0.8	(-34)		
E (W m ⁻²)										
C	101	(-)	50	(-)	39	(-)	59	(-)	96	(-)
P	97	(-4)	49	(-1)	38	(-2)	58	(-2)	96	(0)
PV	97	(-4)	48	(-3)	37	(-4)	57	(-4)	96	(0)
R	106	(5)	52	(5)	41	(7)	62	(6)	100	(4)
RP	103	(2)	52	(4)	40	(3)	61	(3)	100	(4)
RPV	100	(-1)	50	(2)	39	(1)	59	(0)	99	(3)
P (mm day ⁻¹)										
C	4.36	(-)	2.7	(-)	2.35	(-)	2.9	(-)	3.29	(-)
P	4.34	(-0.4)	2.69	(-0.2)	2.33	(-1)	2.9	(-0.2)	3.28	(-0.2)
PV	4.35	(-0.2)	2.78	(3)	2.34	(-1)	2.94	(1.3)	3.29	(0.1)
R	4.58	(5)	2.91	(8)	2.54	(8)	3.10	(7)	3.43	(4.2)
RP	4.58	(5)	2.89	(7)	2.49	(6)	3.09	(7)	3.42	(4.0)
RPV	4.45	(2)	2.79	(3)	2.43	(3)	2.99	(3)	3.40	(3.3)
$T(K)$										
C	28.1	(-)	17.4	(-)	4.8	(-)	19.6	(-)	18.5	(-)
P	28.5	(0.4)	17.7	(0.3)	5.1	(0.3)	19.8	(0.3)	18.7	(0.1)
PV	28.8	(0.7)	17.9	(0.5)	5.9	(1.1)	20.2	(0.7)	18.9	(0.3)
R	29.8	(1.7)	20.0	(2.6)	8.8	(4.0)	22.2	(2.6)	20.4	(1.9)
RP	30.2	(2.1)	20.3	(2.9)	8.7	(3.9)	22.4	(2.8)	20.5	(1.9)
RPV	30.6	(2.6)	20.0	(2.6)	8.1	(3.3)	22.2	(2.7)	20.4	(1.8)

The physiological effects of P and PV act to reduce evapotranspiration (*E*) as the stomatal conductance falls (figure 8.1.c). However, the R runs resulted in an increase in available energy (net radiation) at the Earth's surface and, in the absence of physiological effects, *E* was boosted. When the physiological effects were applied along with the radiative effects, evapotranspiration was progressively reduced (RP and RPV) so that ultimately the global mean value of *E* for land in the RPV case was about the same as it was in the control (C) case. The physiological effects thus largely counteracted the radia-

tive effects on evapotranspiration in the RPV case. However, the additional available energy at the surface (net radiation) resulting from the radiative response to 2 × CO₂ was then released as sensible heat, causing a further increase in surface air temperature, in the absence of non-local effects.

For most places, the effects of the physiological treatments (P, PV, RP, RPV) on precipitation were small compared to those of radiation (R). There were only small changes in the total land precipitation rate in the P and PV cases. Precipitation increased significantly in the R

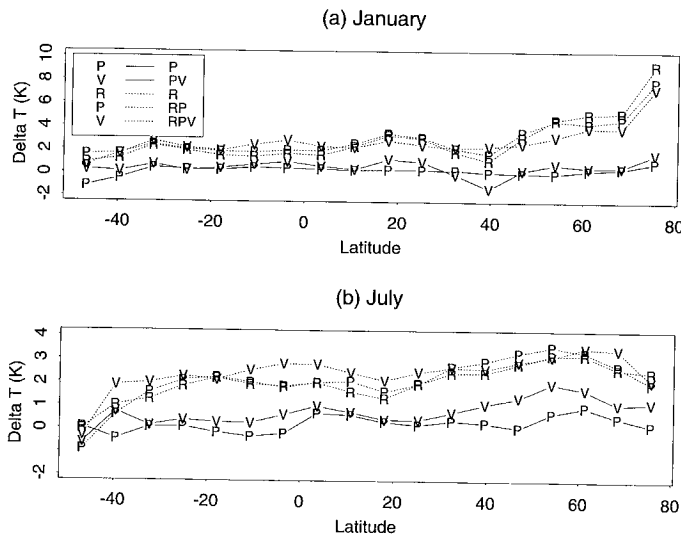


Figure 8.3: Zonal mean surface air temperature ($^{\circ}\text{C}$) for the last 10 years of the simulations for all land points for the experiments discussed in the text, expressed as differences from the control ($1 \times \text{CO}_2$) case. (a) January, (b) July.

case, in line with most other AGCM $2 \times \text{CO}_2$ studies, then fell off slightly with the RP case, and was reduced further in the RPV treatment.

The regional and temporal distributions of the changes in surface air temperature (T) due to physiological effects are striking (figure 8.3). The P and PV effects were generally small compared to those in the R runs, and are consistent with the reductions in evapotranspiration (Table 8.1) and our interpretation of figure 8.1. The increase in temperature in the R run is large in the Northern Hemisphere and relatively small at lower latitudes, in line with results from previous "greenhouse effect" (R-case) studies. In July, the RP and RPV results showed proportionally larger increases in T in the tropics, which reduced the July mean meridional temperature gradient over land in the Northern Hemisphere relative to the R case. Surprisingly, in January, the RP and RPV cases gave rise to a modest reduction in temperature in the land boreal zone relative to the R case (figure 8.3). These results are at odds with those reported by two previous studies (Henderson-Sellers *et al.* 1995, Pollard and Thompson 1995). The landsurface parameterizations used in these two studies were based on highly empirical leaf stomatal conductance formulations which were not linked to photosynthetic processes. Also, the location and state of the global vegetation was based on extrapolations from a relatively small number of ground surveys reported in the ecological literature. Both studies imposed a halving (*i.e.*, 50% reduction) of stomatal conductance everywhere, which may be compared with the reductions of between 25% (P, RP) and 35% (PV, RPV) calculated for g_c in our study. In one of the studies (Pollard and Thompson

1995), evapotranspiration in the tropics was almost unaffected by physiological effects; this may be because the Pollard and Thompson (1995) model distributes convective precipitation evenly over land grid squares resulting in an overestimation of canopy interception loss and a reduction in the importance of canopy transpiration to the total latent heat flux. Both of the previous studies projected significant impacts of physiological effects in the boreal zone in July which led to increases in surface temperature there. For the same area, our results indicate that the combined (radiative plus physiological) responses to $2 \times \text{CO}_2$ yield only a slight warming relative to the R-case in summer and a slight cooling in winter. (figure 8.3). This result implies that non-local effects, generated by the strong year-round physiological responses in the tropics, can affect the high-latitude climate. Thus the radiative and physiological responses to $2 \times \text{CO}_2$ combine in a non-additive way.

The radiation-only (R) results produced by SiB2-GCM give a warming at the low end of the range obtained from other numerical simulations of the equilibrium response to $2 \times \text{CO}_2$ (Houghton *et al.* 1990): the total increase in global surface air temperature in the R case was 1.9°C . The effects of physiological responses to $2 \times \text{CO}_2$ alone, in the absence of radiative effects, were anticipated from a simple consideration of the role of physiological processes in the surface energy budget (P and PV cases). The combination of physiological and radiative effects produced big impacts in the tropics where physiological effects increased the R-case temperature increment from 1.7°C to between 2.1°C (RP case) and 2.6°C (RPV case). The physiologically induced effects are concentrated around midday and so many of the effects generated by the RP and RPV warming scenarios would be greater than those implied by the increases in mean temperatures. The projected tropical temperature increase of 2.6°C (RPV case) is comparable to the results of Amazon deforestation simulation studies, which typically yield increases of $2\text{--}4^{\circ}\text{C}$ in surface air temperature as a result of replacing all of the primary tropical forest with C_4 pasture. It has been suggested that there would be significant ecological impacts as a result of such a climate change (Nobre *et al.* 1991). However, a doubling of atmospheric CO_2 is more likely to occur than the complete deforestation of the Amazon within the next century.

Figure 8.4 compares the changes in global assimilation and surface air temperature resulting from the different treatments; the total response to $2 \times \text{CO}_2$ should lie somewhere along the RP - RPV axes for all cases. The RP and RPV results in figure 8.4 can be compared with the sum of vectors representing the results of separate radiation-only (R) and physiology-only (P, PV) treatments. We have constructed analogues to the RP and RPV cases using (R+P) and (R+PV) vectors, respec-

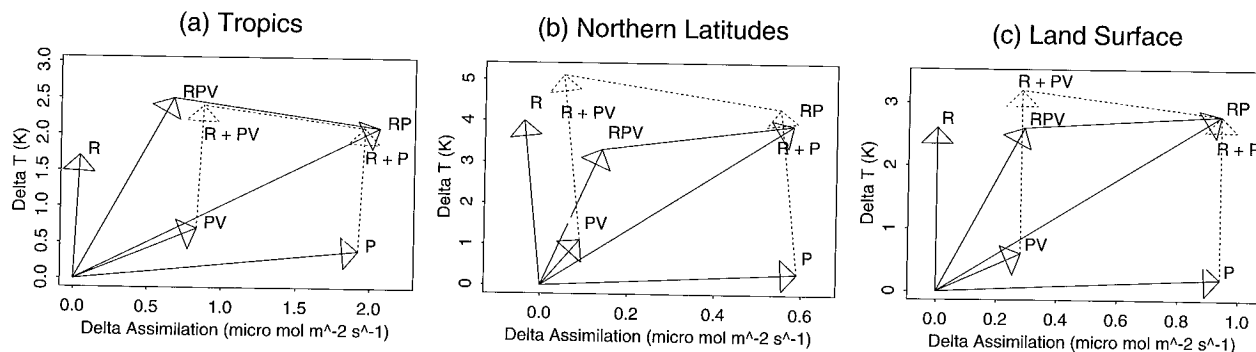


Figure 8.4: Changes in assimilation rate, A , ($\mu\text{mol m}^{-2} \text{s}^{-1}$) plotted against changes in surface temperature, T , ($^{\circ}\text{C}$) for different land areas for all the experiments described in text. All differences are defined relative to the control ($1 \times \text{CO}_2$) case. The vectors (**R**) and (**P**, **PV**) (solid arrows) show the separate effects of radiation and physiology, respectively. (a) tropics, (b) northern latitudes, (c) all land points. The line joining the **RPV** and **RP** points (solid line) is the axis linking the results of the combined radiation and physiology experiments (**RPV**, **RP**). The line joining the “constructed” vectors (**R** + **PV**) and (**R** + **P**) (dotted line) is the analogue of the **RPV**-**RP** axis, created by joining the points generated from the vector sums (**R** + **PV**) and (**R** + **P**) (dotted arrows). If the radiation and physiology responses were completely additive, the two axes, (**RPV** - **RP**) and (**R** + **PV**) - (**R** + **P**), would lie on top of each other. This is almost true for the land tropics (a), but is obviously not true for the northern latitudes (b) or all land points (c). This result indicates that the physiological response of the tropics may play a strong role in determining the climatic response to $2 \times \text{CO}_2$ at higher latitudes.

tively, and have plotted them on figure 8.4.a. A comparison of the **RP** with (**R**+**P**), and the **RPV** with (**R**+**PV**) points indicates that the interactions between the radiation and physiological effects can be non-additive depending on geographical location; that is, the two vectors cannot be treated independently because of non-local influences, particularly in the northern mid and high latitudes (figure 8.4.b). In the tropics, however, the results suggest that these effects are approximately additive, presumably because local processes dominate in this zone (figure 8.4.a). This result is relevant to field studies where vegetation canopies are exposed to enriched CO₂. Figure 8.4 implies that these studies, which generally focus on the carbon budget, should also include energy budget (radiation, water, heat fluxes) measurements. It will be necessary to combine the results from these studies with the anticipated changes in the energy and water balances from AGCM investigations to obtain a complete picture of the total environmental response to increased CO₂.

In the tropics, it is projected that the value of the assimilation rate A for the terrestrial biosphere is inversely related to changes in the surface air temperature under $2 \times \text{CO}_2$ conditions (see the **RPV**-**RP** axis in figure 8.4.a). For the northern latitudes, this is true for the growing season but, because of the lower winter temperatures associated with the **RPV** case, the mean annual assimilation rates and temperatures appear to be correlated (figure 8.4.b). For the globe, the net result is that total assimilation varies widely for little variation in the global mean air temperature (figure 8.4.c).

8.4 Conclusion

We performed six CO₂ simulations using observed vegetation conditions for 1987, as obtained from satellite data. We did not consider morphological responses (that is, changes in leaf area index or greenness) or changes in vegetation type (migration of biomes) in response to altered climate or plant physiology. Human impacts on the distribution of vegetation are likely to be important but are difficult to predict. The potential role of plant physiology on climate is simulated to be substantially larger when physiology is down-regulated than when it is not (**PV** versus **P** and **RPV** versus **RP**). However, there is a large uncertainty as to whether the aggregate terrestrial biospheric response will be closer to the unadjusted (**RP**) or down-regulated (**RPV**) case.

Acknowledgments

This work was supported by NASA Earth Observing System (EOS) funds (Interdisciplinary Science Biosphere-Atmosphere Interactions project). We gratefully acknowledge the encouragement and support from G. Asrar (NASA HQ). We thank NASA Center for Computational Sciences for their cooperation and L. Blasingame and V. McElroy for typing the manuscript.

Chapter 9

Linkages Between Climate, Vegetation, and Atmospheric CO₂ During the 1980s

Publication in preparation by S.O. Los, G.J. Collatz, P.J. Sellers, C.J. Tucker, and L. Bounoua.

Abstract

A monthly global satellite-derived vegetation dataset for the 1980s has recently become available. This dataset allows, for the first time, investigating of linkages between landsurface temperature, sea surface temperature, precipitation and vegetation greenness at a global scale. The results indicate a linkage at mid and high latitudes between climatic variations in sea surface temperature and landsurface temperature that affect landsurface vegetation. A second, more localized linkage was found at low latitudes between sea surface temperature, precipitation, and vegetation greenness. The coupling between sea surface temperature, landsurface temperature, and vegetation greenness suggests that increased photosynthesis was responsible for the terrestrial carbon sink of the past four decades. The increased greenness, and by inference, increased photosynthesis resulting from increased temperatures, was found most important during the start and end of the growing season at mid latitudes and throughout the growing season at high latitudes.

9.1 Introduction

Significant interannual variations were observed in global climate during the 1980s. Two warm El Niño-Southern Oscillation (ENSO) phases occurred during 1982–1983 and 1987–1988 and a cold-ENSO phase occurred during 1988–1989. El Niño is a warming of the eastern equatorial Pacific Ocean that has been related to a reversal of a high and low atmospheric pressure seesaw system over western Australia and the Central Pacific Ocean (the Southern Oscillation; see *e.g.*, Glantz *et al.* 1991, Philander 1990). During ENSO events, large changes in atmospheric and oceanic circulation occur that are associated with droughts in some areas and torrential rains in others (Glantz *et al.* 1991, Philander 1990, Ropelewski and Halpert 1987). Other major climate events during the

1980s were the Sahelian drought of 1984 (Nicholson 1993, Lamb *et al.* 1986), that has been associated with variations in Atlantic sea surface temperatures (Palmer 1986), and an overall, gradual warming of landsurface temperatures from the mid to late 1980s (Jones *et al.* 1990, Jones and Briffa 1992). Keeling *et al.* (1995) suggested that interannual climate variations in landsurface air temperature and possibly precipitation affect the terrestrial biospheric carbon sink-source distribution. This would provide an explanation for the disproportionate rise in atmospheric CO₂ growth rate during the early 1980s and a sharp fall after 1988 and for the large terrestrial carbon sink in the Northern Hemisphere during the past four decades found from atmospheric CO₂ analysis (Keeling *et al.* 1995, Tans *et al.* 1990, Ciais *et al.* 1995, Denning *et al.* 1995). Several authors suggested a lengthening of the growing season as a possible mechanism for an increase in the terrestrial carbon sink (Goulden *et al.* 1996, Keeling *et al.* 1996). In this chapter evidence is presented for linkages between variations in sea surface temperature and vegetation greenness, thus connecting climate variations with variations in atmospheric CO₂.

9.2 Data

Recently a multi-year (1982–1990), monthly, global Normalized Difference Vegetation Index (NDVI) dataset at 1° by 1° resolution has become available (Chapters 4 and 5). The NDVI is a commonly-used index derived from remotely sensed reflectance data in the red and near-infrared spectral regions. The red reflectance is inversely related to the chlorophyll density and the near-infrared reflectance is directly related to scattering within individual leaves and between leaves in the canopy. Combining these two adjacent spectral regions in an index provides a first order correction for differences in irradiance and gives an estimate of the intercepted fraction of the photosynthetically active radiation absorbed by vegetation (see Chapter 2 for references). It is this association of the

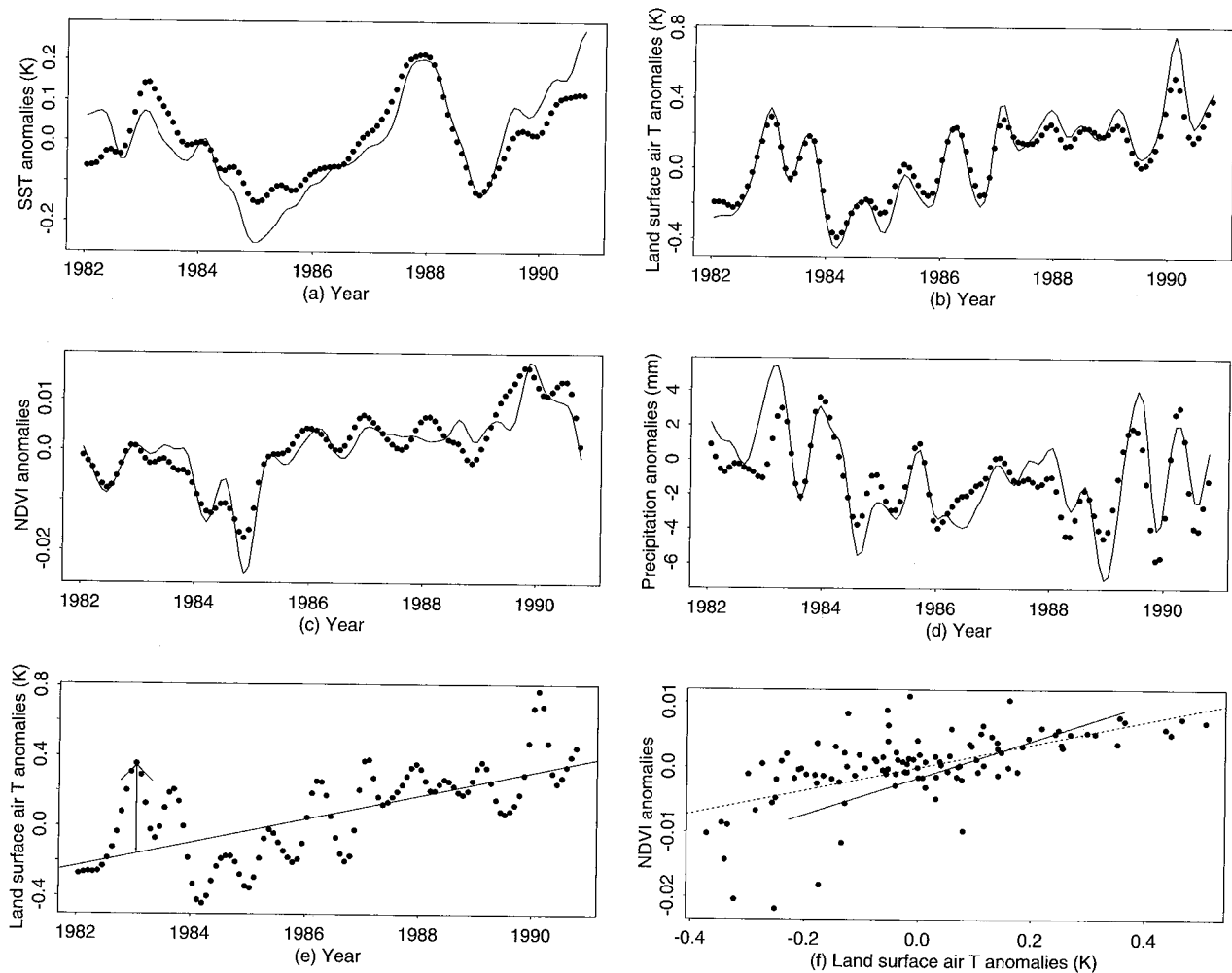


Figure 9.1: (a-d) Monthly mean global anomalies (dots) and monthly mean Northern Hemisphere anomalies (lines). Anomalies were calculated as departures from monthly mean values for 1982–1990. Data above 50 degrees N and below 50 degrees S were eliminated. Time-series of the original datasets were filtered to suppress noise (Tukey 1977).

(a) Sea surface temperature anomalies. (b) Landsurface temperature anomalies. (c) NDVI anomalies. (d) Precipitation anomalies.

Figures e and f show a consistency test of the relationship between landsurface air temperature anomalies and NDVI anomalies for intra- and interannual variations.

(e) Trend (line) and departures from the trend (arrow) in the Northern Hemisphere air temperature anomalies. (f) Plot of departures from the trend in temperature anomalies and departures from the trend in NDVI anomalies (dots). Dashed line shows the least squares fit for the dots. The solid line gives the relationship between the long-term trends of the NDVI and the landsurface air temperature anomalies.

NDVI with vegetation that is exploited to assess interannual variations in vegetation density.

The NDVI data were corrected for sensor degradation and differences in calibration between instruments (Appendices A and B), atmospheric aerosols of the El-Chichon eruption in 1982 (Chapter 5, Vermote *et al.* 1995), and solar zenith angle effects (Chapter 5).

We analyzed associations between interannual variations in vegetation greenness and variations in climate from 1982 through 1990 with the NDVI dataset, the Reynolds sea surface temperature (SST) dataset

(Reynolds *et al.* 1989), and the Department of Energy (DOE) ground-observed landsurface air temperature anomaly (Jones *et al.* 1985) and landsurface precipitation anomaly datasets (Eischeid *et al.* 1991).

9.3 Analysis

Time-series of monthly anomalies—*i.e.*, departures from the monthly means over the period 1982–1990—of SST, NDVI, landsurface air temperature, and landsurface pre-

Table 9.1: *Factor loadings from a promax factor analysis (Reyment and Jöreskog 1993) of globally and Northern Hemisphere averaged monthly NDVI-, SST-, precipitation- and landsurface air temperature anomalies from 1982–1990. High loadings (positive or negative) on a factor indicate high (positive or negative) association between variables.*

	Global		Northern Hemisphere	
	Factor 1	Factor 2	Factor 1	Factor 2
SST	75	42	61	82
T	89	-18	94	20
NDVI	85	-14	92	17
PPN	-11	94	2	92

precipitation data were averaged over the globe and the Northern Hemisphere (figure 9.1). The globally-averaged SST anomalies exhibit a warm phase (1982–1983), a cold phase (1984–1985), a warm phase (1987–1988), and again a cold phase (1988–1989) superposed on a trend over the 1980s. The close resemblance between average Northern Hemisphere and average global landsurface NDVI anomalies reflects the importance of the large Northern Hemisphere landmass for global climate-vegetation interactions. The positive trend in the SST data during the mid to late eighties, and the negative and positive departures during 1984–1985 and 1989–1990, respectively, are reflected in the landsurface air temperature and the NDVI data. The temporal development of precipitation (figure 9.1.d) appears different from the temporal development of the other two landsurface datasets (NDVI and air temperature), although a degree of similarity exists between precipitation and SST anomalies. The similarities and dissimilarities are confirmed by a promax factor analysis (Reyment and Jöreskog 1993) of the global and Northern Hemisphere averaged time-series (Table 9.1). A factor analysis has a similar purpose as a principal component analysis in that it seeks general factors in multivariate datasets. Unlike a principal component analysis, the factors from a promax factor analysis can be rotated at oblique angles to better fit the directions of maximum variance in the data and can therefore have non-zero correlations with each other. A promax factor analysis generally results in a simpler structure than a principal component analysis and thus simplifies the interpretation (Reyment and Jöreskog 1993).

A strong association between SST, NDVI, and air temperature anomalies is indicated by the loadings on the first factor, while precipitation is unique and has little or no relationship with the landsurface variables (Table 9.1). SST anomalies are related to both NDVI and air temperature anomalies in factor 1 and to precipitation anomalies in factor 2. Thus on a global scale, anomalies

in the NDVI are associated with anomalies in landsurface- and sea surface temperatures.

The relationship between Northern Hemisphere NDVI and landsurface air temperature anomalies was tested for consistency within and between years. The relationship between the trend in landsurface air temperature anomalies and the trend in NDVI anomalies is similar to the relationship between the departures from the trend of these two variables (figure 9.1.f). This implies a similar relationship between air temperature and SST anomalies for both short and long time periods, and suggests that the trend in landsurface air temperature over the past four decades has been accompanied by a similar increase in the global photosynthetic capacity.

Temporal phenomena common to both the SST and the NDVI anomaly data were evaluated by a weighted promax factor analysis (Statistical Sciences 1993) of a combined NDVI-, and SST anomaly dataset (figure 9.2). The loadings on the first factor (figure 9.2.a) closely resemble the positive SST departures in the ENSO3 region during the warm ENSO events of 1982–1983 and 1986–1988, and the negative departures during the cold ENSO event of 1988–1989, indicating a strong association between these. The loadings on the fourth factor (figure 9.2.b) are high during the 1984–1985 cold SST phase and close to zero otherwise, indicating a different manifestation of this global event compared to the ENSO events of 1982–1983, 1986–1988 and 1988–1989 visible in the first factor and the ENSO3 anomalies (figure 9.2.a). The globally-averaged SST, temperature, and NDVI anomalies show larger excursions for the 1984–1985 global event than for the 1982–1983, 1986–1988, and 1988–1989 ENSO events. Thus global SST anomalies have a larger immediate impact on global landsurface vegetation processes than SST anomalies in the ENSO3 region.

The factor analysis in figure 9.2 indicated four periods of interest of which three were investigated in more detail: 1982–1983, 1984–1985, and 1988–1990. For these three periods synthetic factors were composed of a zero line with a 24-month half-period sine function superposed (figure 9.2) so that the half period sine function coincided with the occurrence of a particular event. Pixel-by-pixel covariances were calculated between the synthetic factors and the scaled SST and NDVI anomaly dataset (figure 9.3). Negative covariances indicate negative deviations in SST or NDVI associated with a particular event, and positive covariances indicate positive deviations in SST or NDVI.

The covariances show similar spatial patterns with reversed signs for the 1982–1984 warm ENSO event (figure 9.3.a) and the 1988–1990 cold ENSO event (figure 9.3.c). The reversed association between these two periods was also indicated by the loadings on the first factor in the SST and NDVI anomalies (figure 9.2.a). Both the ENSO warm phase (figure 9.3.a) and the ENSO cold phase (fig-

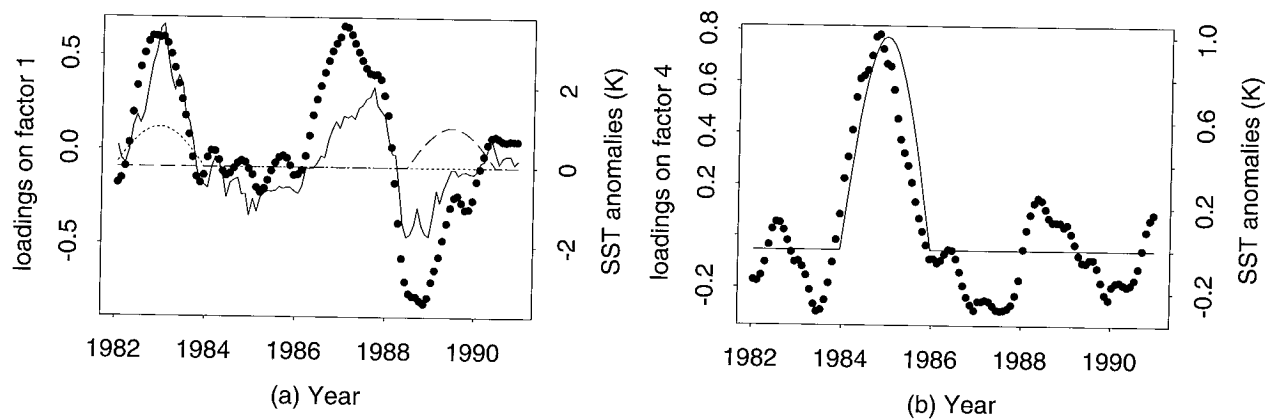


Figure 9.2: Factor loadings (Statistical Sciences 1993) of monthly 1° by 1° NDVI anomaly-, and Sea Surface Temperature anomaly data for 1982–1990. The factor analysis was restricted to data between 50° N and 50° S to avoid gaps associated with high latitude satellite observations during winter. To give equal weighting to landsurface NDVI and SST anomaly data, anomalies were scaled by the standard deviation of their respective total populations and the amount of SST data was reduced by randomly selecting one-third of the data. The NDVI and SST anomaly time-series were filtered to remove high frequency noise from the data (Tukey 1977). (a) Dots: Loadings on the first factor. Continuous line: SST anomaly in the ENSO3 region (5° S to 5° N and 90° W to 150° W). Dotted and dashed lines: synthetic factors composed of a zero line with a half period sine curve of 24 months superposed for the 1982–1983 warm ENSO cycle and the 1988–1990 cold ENSO cycle respectively. (b) Dots: Loadings on the fourth factor. Line: synthetic factor composed of a zero line with a half period sine curve of 24 months superposed for the 1984–1985 period of global cooling of SSTs. The loadings on the first factor (a) coincide with the sea surface temperature anomalies in the ENSO3 region (continuous line). The weak cold cycle during 1984–1985 in the ENSO3 data does not appear in the factor loadings and is therefore different from the other ENSO events (b). The synthetic factors in a and b are used to bring out the association between land-, and sea surface anomaly patterns for the 1982–1983 warm ENSO cycle in figure 9.3.a (dotted line in 9.2.a), the cold global SST event during 1984–1985 in figure 9.3.b (line in 2b) and the cold ENSO cycle of 1988–1990 in figure 9.3.c (dashed line in 2a).

ure 9.3.c) show alternate wedge shaped patterns of positive and negative SST anomalies, respectively, near the equator: warming (cooling) in the eastern Pacific, cooling (warming) in the Atlantic, warming (cooling) over the Indian ocean, and cooling (warming) over the western Pacific. These SST anomaly patterns have been associated with changes in coupled atmospheric and oceanic east-west circulation causing increased convection and rainfall near areas with increased SSTs and decreased convection and rainfall near areas with decreased SSTs (Bjerknes 1969, Trenberth 1991). As a result of the decreased convection we find decreased NDVI values in land areas that are linked to parts of the oceans with decreased SSTs, e.g., northeast Brazil, the Gulf of Guinea in Africa, southeast Africa, and southwest Australia.

At Northern Hemispheric mid-latitudes, the data show a contiguous belt of decreased SSTs and NDVIs for 1982–1983 and increased SSTs and NDVIs for 1988–1989. The departure in NDVIs and SSTs at mid latitudes is opposite in sign from the departures in the western equatorial Pacific, suggesting a teleconnection between these areas.

The 1984–1985 cold SST event (figure 9.3.b), which is uniquely different in its manifestation of spatial patterns from the two events in figures 9.3.a and c, shows a cool-

ing in the western equatorial Pacific Ocean and a belt of negative mid-latitude excursions in the NDVI and SST anomalies resulting in negative values over almost the entire Northern Hemisphere. Thus two dominant features appear in the data, one associated with SST anomalies and vegetation anomalies near the equator, and the other with SST and vegetation anomalies at mid and high latitudes. These two features can have departures of the same sign, which for the 1980s resulted in deviations in SST and vegetation greenness over the entire Northern Hemisphere; or of opposite signs, in which case the mid and high latitude anomalies were stronger than the low latitude anomalies (compare SST and NDVI anomalies in figure 9.1 during 1984 with the anomalies during 1987).

To investigate possible mechanisms between the associations between SST and NDVI anomalies, correlations for each grid cell were calculated between NDVI and landsurface temperature anomalies, and NDVI and precipitation anomalies (figure 9.4). Positive correlations between NDVI and temperature anomalies dominated over mid and high latitude areas in the Northern Hemisphere and positive correlations between precipitation and NDVI anomalies dominated at low latitudes. Notice that areas with positive correlations between NDVI and landsurface temperature anomalies cover a large, contiguous part of

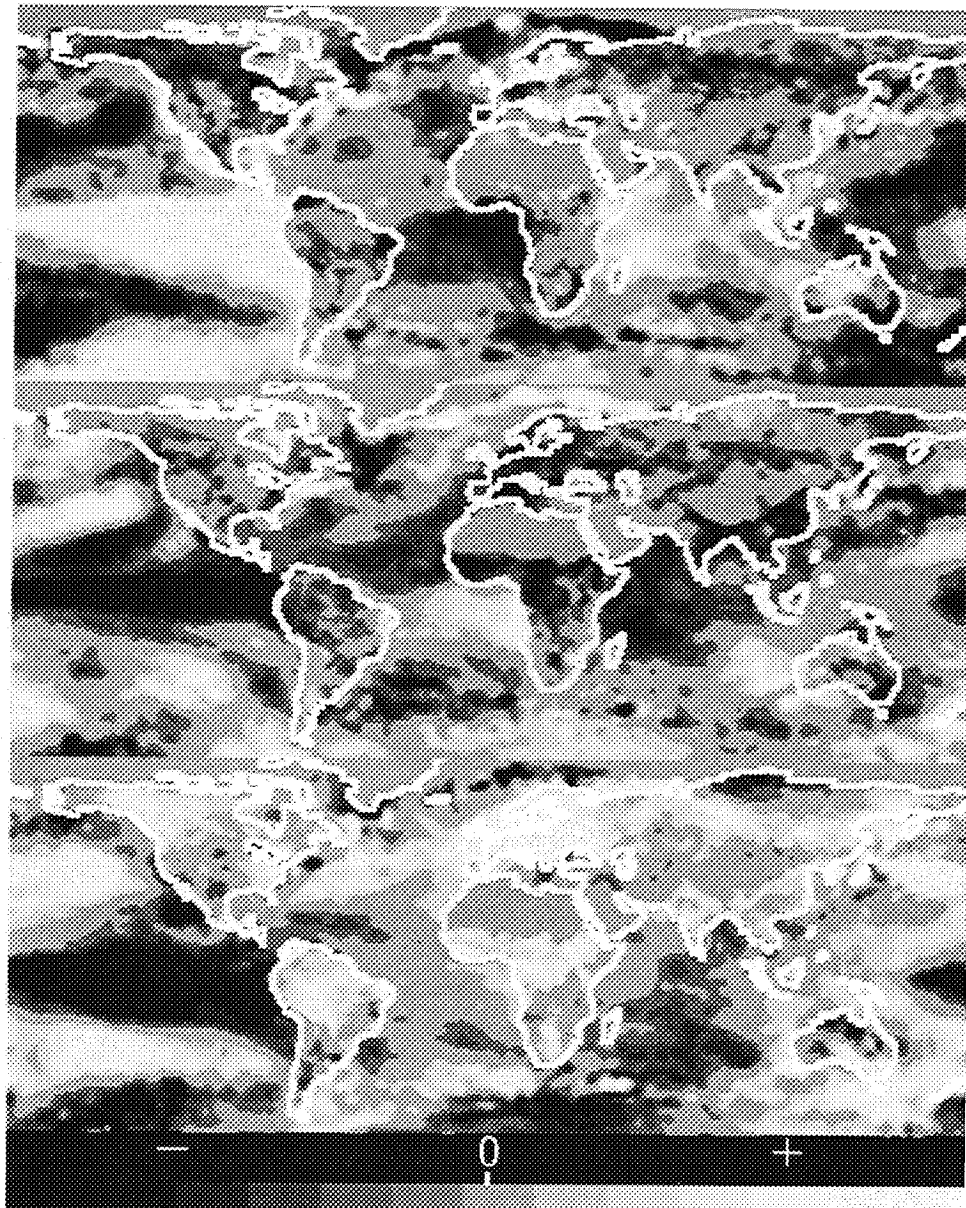


Figure 9.3: Pixel-by-pixel covariances of NDVI and SST anomalies with the synthetic factor loadings of figures 9.2.a and 9.2.c revealing patterns of SST warming and cooling contiguous with land areas of increased and decreased NDVI. NDVI and SST data were scaled by the standard deviation of their respective total populations. Note that for this figure the entire dataset is used. A spatial 3 by 3 median filter was used to suppress noise. For a color version see figure E.2.

(a) Covariances for 1982–1983 with the dotted line in figure 9.2.c reveal (1) strong warming in the eastern equatorial Pacific (El Niño) associated with cooling in the equatorial Atlantic ocean and droughts (decreased NDVI values) in northeast Brazil (Moura and Shukla 1981), the African Gulf of Guinea, and southeast Africa; (2) warming in the Indian ocean and increased NDVI values in northeast Africa and northwest Australia; and (3) cooling of the western Pacific and associated droughts in southwest Australia (Glantz et al. 1991, Philander 1990, Ropelewski and Halpert 1987). Notice the contiguous belt at mid and high northern latitudes of negative SST and NDVI anomalies.

(b) Covariances with synthetic factor loadings for 1984–1985 (figure 9.2.d dotted line) indicate negative anomalies in both SSTs and NDVI over almost the entire globe. A pattern of decreased SST and NDVI values appears over the equatorial Pacific, the Atlantic north of the equator, the Sahel (1984 drought), India, China, Europe, northern Asia, the northern Pacific, and North America.

(c) Covariances with synthetic factor loadings for 1988–1990 (figure 9.2.c, dashed line) show almost the reversed pattern of figure 9.2.a. Cooling is found over the eastern equatorial Pacific and Indian Oceans, warmings over the Atlantic and western equatorial Pacific Oceans. Increased NDVI values occur over northeast Brazil, the Gulf of Guinea, southern and northeastern Africa and southwest Australia. Decreased NDVI values are found over northeast Australia, and the southern part of South America. A belt of increased SSTs and NDVI values is located over mid northern latitudes.

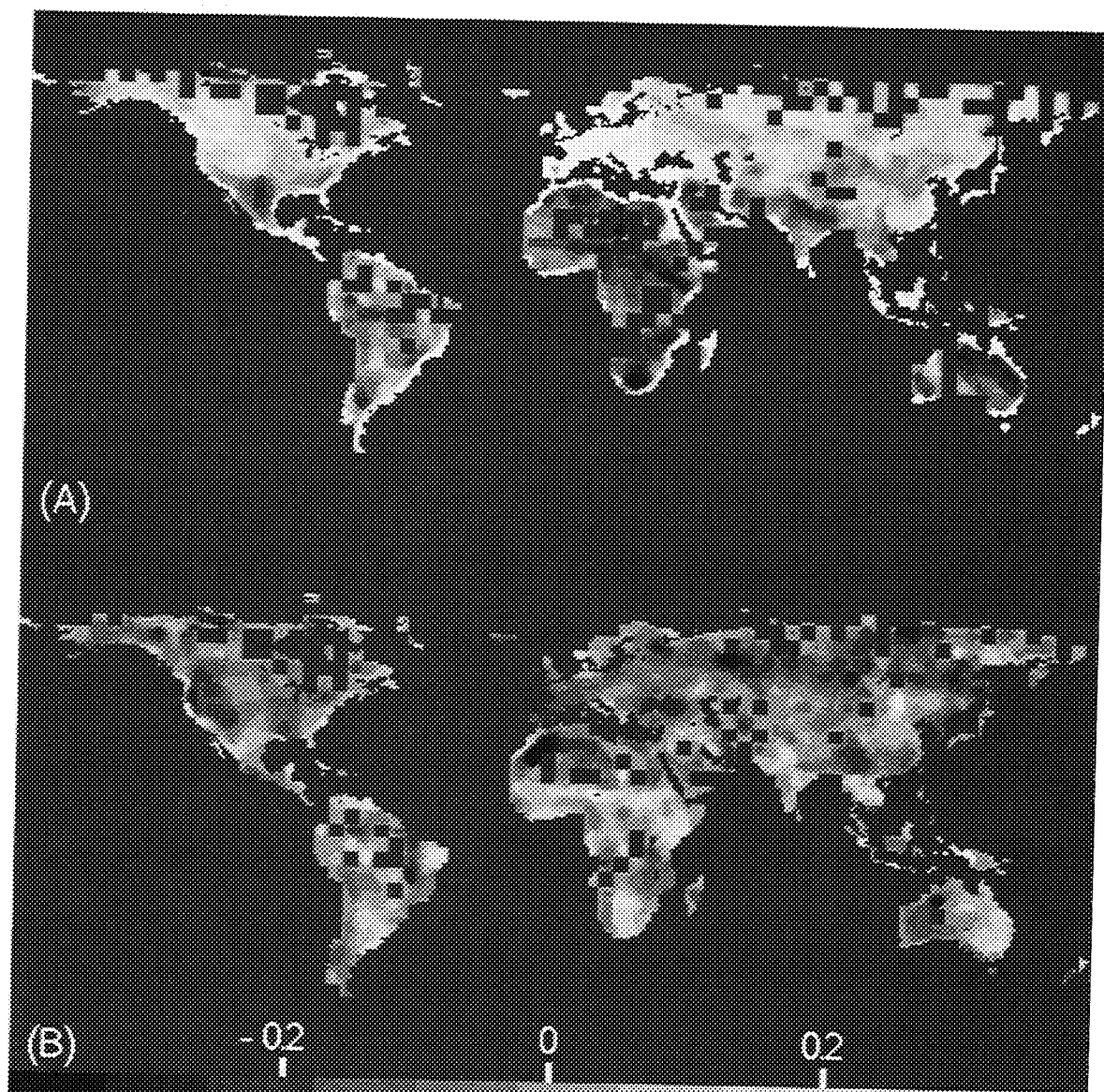


Figure 9.4: (a) pixel-by-pixel correlations between NDVI anomaly-, and landsurface air temperature anomaly time-series. (b) pixel-by-pixel correlations between NDVI and rainfall anomaly time-series. Air temperature and precipitation data were extrapolated to the spatial resolution of the 1° by 1° NDVI data by using one value for each 5° by 5° window. A 3 by 3 median filter was used to suppress noise. For a color version see figure E.3.

the Northern Hemisphere, whereas areas with positive NDVI-precipitation correlations tend to be localized in semi-arid regions. The anomalies in rainfall and NDVI at low latitudes have been associated with changes in convection and SSTs: increased SSTs lead to increased convection, rainfall, and vegetation greenness; and decreased SSTs lead to decreased convection, rainfall, and vegetation greenness (Bjerknes 1969, Ropelewski and Halpert 1987). The data suggest a similar positive linkage at mid and high latitudes between anomalies in SSTs and vegetation greenness but driven by landsurface air temperature anomalies instead of precipitation anomalies (figures 9.3

and 9.4).

It could be argued that the positive correlations between NDVI and landsurface temperature are an artifact resulting from a relationship between increased temperature, decreased cloudiness, and as a result increased NDVI because of a clearer, less cloudy atmosphere. This in itself would be an interesting association but clearly not the one currently investigated. To test this alternative hypothesis correlations between landsurface temperature anomalies and precipitation anomalies were calculated. Areas with a negative correlation between precipitation and air temperature anomalies of $r < -0.2$ and a positive corre-

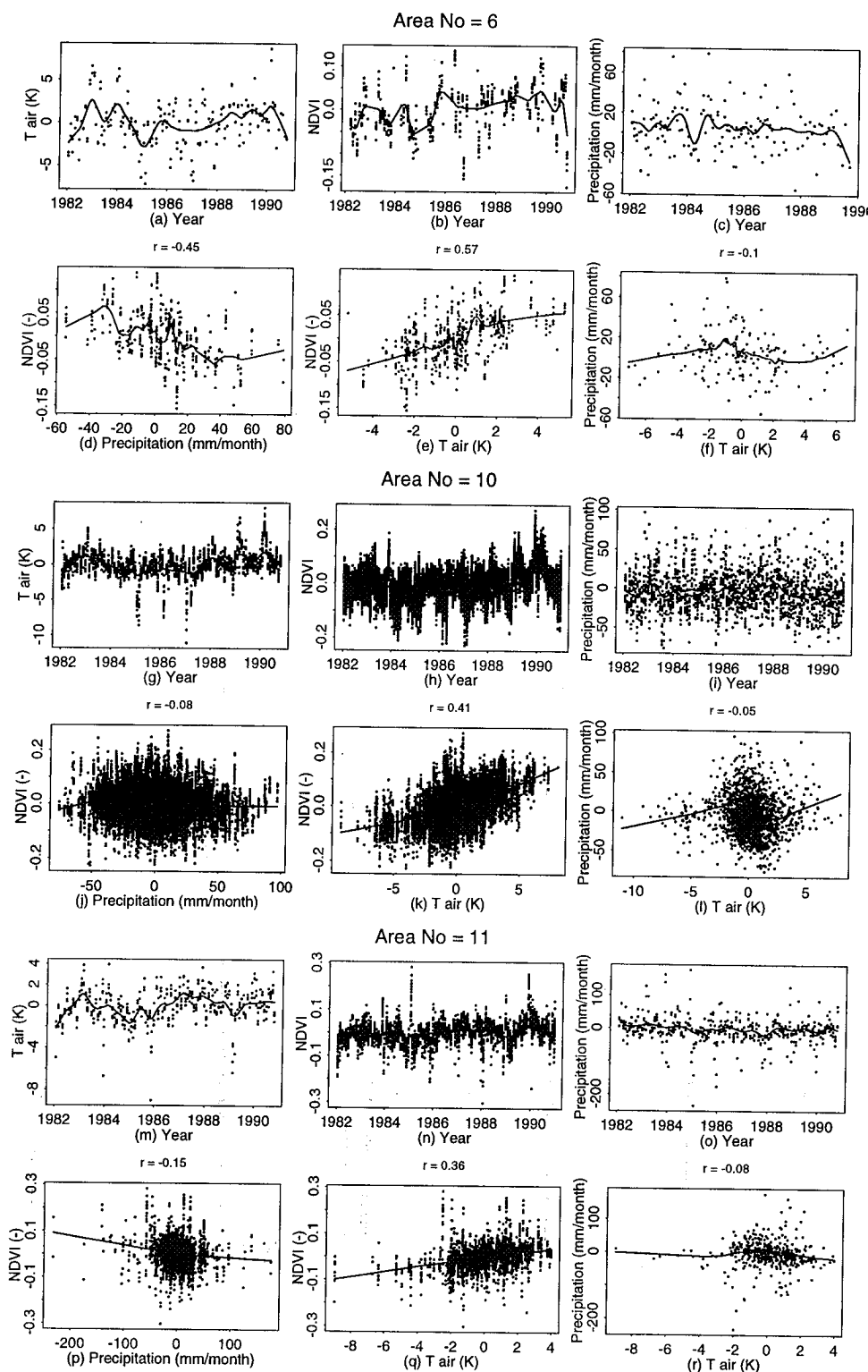


Figure 9.5: Examples of time-series with positive correlations ($r > 0.3$) between NDVI and landsurface air temperature anomalies. Area numbers correspond to numbers in figure E.3.a. (a, g, m) Landsurface air temperature time-series. (b, h, n) NDVI anomaly time-series. (c, i, o) Precipitation anomaly time-series. (d, j, p) Precipitation anomalies versus NDVI anomalies. (e, k, q), Landsurface air temperature anomalies versus NDVI anomalies. (f, l, r) Landsurface air temperature anomalies. Smoothed lines indicate trends in the data. Note that the correlations between landsurface air temperature and NDVI are larger than the correlations between precipitation and NDVI and that their time-series show a larger degree of similarity. For an alternative model to explain the NDVI landsurface air temperature relationship, i.e., higher temperatures lead to less cloudiness (rainfall) and for clearer atmospheres one would expect a negative correlation between landsurface air temperature and precipitation and a positive relationship between landsurface air temperature and NDVI. This is not the case.

lation between NDVI and air temperature anomalies $r > 0.2$ are indicated in figure E.3.a. A small number of these areas were found, mostly located in low to mid-latitudes. In several cases these areas were located next to areas with missing temperature data (figure E.3.a) suggesting that the relationship may be the result of insufficient data coverage.

NDVI, landsurface air temperature, and precipitation anomaly time-series for 1982–1990 are shown in figure 9.5 with the relationships between precipitation and NDVI anomalies; landsurface air temperature and NDVI anomalies; and landsurface air temperature and precipitation anomalies. The relationship between increased temperature and NDVI is especially strong in western Europe. Moreover the NDVI anomalies have no relationship with the precipitation anomalies. For the other two cases, North America and Asia, the correlations between landsurface air temperature and NDVI are larger than the correlations between precipitation and NDVI, and the time-series of NDVI and landsurface air temperature show a larger degree of similarity than the time-series of precipitation and NDVI. The correlation between landsurface air temperature and precipitation anomalies is smaller than the negative correlation between landsurface air temperature and NDVI. Therefore, the relationship between NDVI and landsurface air temperature is most likely not an artifact related to reduced cloudiness, at least not in the majority of cases.

An issue of some debate is whether the largest increase in absorption of atmospheric CO₂ by vegetation occurs during spring, summer, or autumn. Although we do not have direct estimates of CO₂ uptake by vegetation and respiration by the soil, the changes in vegetation greenness as evidenced by the NDVI are useful to indicate the occurrence of largest increase in vegetation, and possibly of the largest increase in carbon assimilation. For three areas in North America, Europe, and Central Asia, a change in temperature was compared with a change in NDVI for the spring (MAM), summer (JJA) and autumn (SON) (figure 9.6). In the selected area in North America the NDVI shows a similar positive relationship for spring, summer, and autumn. In western Europe the relationship between landsurface air temperature and NDVI is stronger positive for the spring than for the summer and autumn. For the selected area in Asia the relationship between NDVI and landsurface air temperature anomalies is similar for spring and autumn, but weaker, if at all existent, for the summer. Thus in all cases increased air surface temperatures lead to increased NDVI values during spring, in two cases increased air surface temperatures lead to increased NDVI values during autumn, and in one case increased air surface temperatures lead to increased NDVI values during summer. This continental scale effect is consistent with the findings of Goulden *et al.* (1996) for a temperate forest; increased temperature during spring

leads to an expansion of the growing season and as a result vegetation greenness increases. The stronger effects during spring or autumn in the selected areas in North America and Europe, which are at a lower latitude than the area in Asia where an effect was found throughout the year, suggest that warming of the land surface results in a reduction of low temperature stress on vegetation. This reduction is important only during the start or end of the growing season in temperate regions, but may be important throughout the growing season in colder, high latitude areas.

9.4 Discussion

The results presented in this study point to a consistent pattern: on a global scale, SST anomalies have a positive correlation with anomalies in vegetation. The data suggest two mechanisms for this association: the first is a link between SST, landsurface temperature, and NDVI anomalies which was found at mid and high latitudes; the second is a link between SST, precipitation, and vegetation which was found in semi-arid regions at low latitudes. For the mid and high latitude areas where water is not a limiting factor (*e.g.* western Europe, and the boreal forests of North America and Asia), negative NDVI anomalies were associated with decreased ocean and landsurface temperatures and shorter growing seasons. The effects are widespread and affect landsurface vegetation over a large part of the Northern Hemisphere. For low latitudes, we see alternating patterns of warming and cooling in the oceans that have been associated with changes in convection and rainfall (Bjerknes 1969, Ropelewski and Halpert 1987) and because of increased drought or wetness, with changes in NDVI. Reduced rainfall over land areas where moisture is a limiting factor causes negative anomalies in NDVI. Decreased NDVI and precipitation are associated with increased landsurface temperatures in these areas. Of the two mechanisms, SST → landsurface temperature → NDVI at mid and high latitudes, and SST → precipitation → NDVI at low latitudes, the effects of sea surface temperature change at mid and high latitudes were found to have a stronger effect on the global mean NDVI values.

Higher NDVI values imply higher photosynthetic rates but not necessarily a higher net drawdown of atmospheric CO₂ as soil respiration may also increase with temperature. Comparing the estimates of Keeling *et al.* (1995) of net terrestrial biospheric carbon exchange for 1984 and 1989 shows that cold years (in terms of landsurface temperatures) are associated with a net carbon source and warm years with a net sink. The NDVI time-series for 1982–1990 are coherent with the overall sink/source inference of Keeling *et al.* (1995), which strongly suggests that large interannual variations in terrestrial CO₂ up-

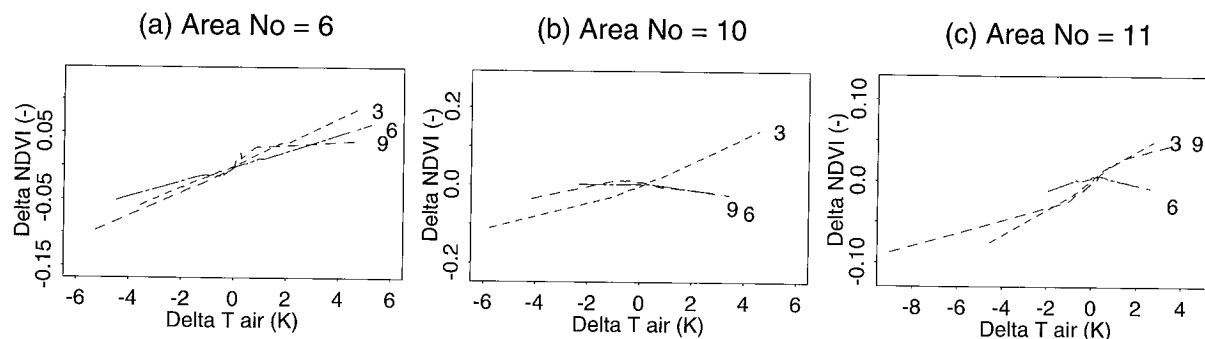


Figure 9.6: Relationships between landsurface air temperature anomalies and NDVI anomalies for different parts of the growing season. Lines marked 3 indicate data for March, April and May. Lines marked 6 indicate data for June, July, and August. Lines marked 9 indicate September, October, and November. (a) Asia, (b) Europe, and (c) North America. Numbers in the figure titles refer to locations indicated in figure E.3.a. In the area in North America the NDVI shows a similar relationship for spring, summer, and autumn. In western Europe the relationship between landsurface air temperature and NDVI is stronger positive for the spring than for the summer and autumn. For the selected area in Asia the relationship between NDVI and landsurface air temperature anomalies is similar for spring and autumn, but weaker, if at all existent, for the summer.

take are most likely caused by an extension of the growing season. Goulden *et al.* (1996) report that annual CO_2 exchange from a deciduous forest in northeastern North America is sensitive to interannual variations in the timing of leaf expansion in the spring and leaf senescence in the fall that are associated with variations in air temperature. Our data suggest a similar mechanism but also suggest that the strongest association between temperature and NDVI may occur during different parts of the growing season because of location- stress.

The interaction between temperature, NDVI, and CO_2 uptake by mid and high latitude vegetation seems to be reflected in the observed interannual variations in the atmospheric CO_2 concentration. This suggests a mechanism for the inferred carbon sink of the 1980s, which was a period of general warming. The trend in temperature over the 1980s has been accompanied by a similar positive trend in vegetation greenness (NDVI); this trend is likely an extension of vegetation activity that followed the warming of the past four decades, since the mechanism responsible for variations within and between years appears similar (figure 9.1). Thus net carbon source/sink patterns which affect the atmospheric CO_2 concentrations are associated with climate-driven variations in vegetation activity as measured by coarse-resolution satellite derived time-series of NDVI. Moreover, the variations in vegetation greenness are linked to variations in sea surface temperature at mid to high latitudes predominantly because of temperature effects over land, not, as was suggested by some, to changes in precipitation rates at low latitudes linked with ENSO events. This is the first directly observed evidence of global scale change in vegetation in response to recent climate variations and is consistent with the inferred terrestrial carbon fluxes from local and global observations.

Acknowledgment

This work was supported by NASA Earth Observing System (EOS) funds (Interdisciplinary Science Biosphere-Atmosphere Interactions project). We gratefully acknowledge encouragement and support from G. Asrar (NASA Headquarters) and thank Drs A.A. van de Griend (Vrije Universiteit, Amsterdam, the Netherlands) and M.B.M. van den Bree (Johns Hopkins Medical Center, Baltimore) for discussions and advice.

Chapter 10

Summary and Conclusions in English and Dutch

Linkages Between Global Vegetation and Climate: An Analysis Based on NOAA Advanced Very High Resolution Radiometer Data

This dissertation deals with temporal and spatial variations in the biosphere observed by satellite and the linkages of these variations with variations in the global climate. The study is part of a larger Earth Observing System (EOS) Interdisciplinary Science (IDS) Biosphere-Atmosphere Interactions project that deals with the implications of these interactions of biosphere-atmosphere interactions for the global carbon cycle. For this dissertation, both model results and observations were used. Six significant goals were achieved:

1. A multi-year, 1982–1990, monthly global vegetation dataset at 1° by 1° resolution was derived from observations by the Advanced Very High Resolution Radiometer (AVHRR) on board the National Oceanic and Atmospheric Administration (NOAA) series of meteorological satellites (Chapter 4, Appendix C). This sensor is widely used for regional and global vegetation monitoring (Chapter 2). NOAA-AVHRR channels 1 and 2 data were converted into a normalized vegetation index, a parameter that is most closely related to the fraction of photosynthetically active radiation absorbed by vegetation. The NDVI data were merged in monthly composites at 1° by 1° resolution providing sufficient temporal and spatial detail to study interannual variations in global vegetation.
2. Potential inconsistencies in the satellite observations of the land surface are caused by sensor degradation, cloud effects, atmospheric interferences, and landsurface bidirectional properties (Chapter 3, Appendix C). A large part of this dissertation is there-

fore devoted to the development of algorithms that correct for these effects. Since individual channel data and data on viewing geometry were not available, the corrections to the NDVI were approximate as a result. Appendices A and B deal with the adjustment of the NDVI for sensor degradation and calibration differences between sensors. Chapter 5 and Appendix D discuss the adjustment of the NDVI for cloud contamination and atmospheric effects, interpolation of missing data, and correction for solar zenith angle effects. An evaluation of these corrections is provided in Chapter 6.

3. Global biophysical parameter fields, the fraction of photosynthetically active radiation absorbed by the green parts of vegetation (FPAR) and leaf area index (LAI), were derived from the corrected NDVI fields (Chapter 5, Appendix D). A linear relationship was established between the NDVI and FPAR, the Simple Ratio (SR, a vegetation index related to NDVI) and FPAR, and an exponential relationship between FPAR and LAI. The NDVI-FPAR, SR-FPAR, and FPAR-LAI relationships were validated with ground data (Chapter 6). Compared to the NDVI-FPAR relationship, better results were obtained with the SR-FPAR relationship. The ground data suggested that a third, intermediate model could be an alternative to estimate FPAR. A fairly high level of noise was found in ground-based estimates of FPAR (Root Mean Square—RMS = 0.2 FPAR) that diminished when data were spatially aggregated (RMS = 0.1). Albedo fields that were derived with the Simple Biosphere model (SiB2)

from LAI and landcover-dependent soil and leaf optical properties were validated with Earth Radiation Budget Experiment (ERBE) data. The SiB2 and ERBE albedo estimates were comparable for most deciduous landcover types and lower but probably more realistic for landcover types with needleleaf vegetation. Comparison of within-class variations of albedo and NDVI showed that inconsistencies in the SiB2 albedo estimates are most likely related to the specification of landcover dependent soil reflectance values, not to errors in the LAI estimates. The within-class variation of albedo in the SiB2 estimates was generally too small and was captured better in the ERBE estimates.

4. The sensitivity of landsurface fluxes—carbon assimilation, water, and energy fluxes—to observed variations in vegetation greenness was investigated with the Colorado State University atmospheric general circulation model (AGCM) coupled to the Simple Biosphere (SiB2) model (Chapter 7). Changes in carbon assimilation as a result of increased greenness only occurred where water or temperature were not limiting. An increase in vegetation greenness strongly reduced the amount of soil moisture at low latitudes. The net energy balance was affected to only a minor extent, however, as a result of increased greenness latent heat increased and sensible heat decreased. A positive feedback loop between landsurface greenness, albedo, total heat flux, and precipitation proposed by Charney *et al.* (1977) appeared stronger when the physiological aspects of vegetation—fraction of photosynthetically active radiation absorbed by vegetation, photosynthetic rates, and evapotranspiration—were considered. At the same time, a negative feedback was found between increased vegetation greenness and a reduced amount of soil moisture available for plant growth.
5. A series of six numerical experiments was performed with the Colorado State University atmospheric general circulation model coupled to the Simple Biosphere model to estimate the physiological response of terrestrial vegetation and its effect on the global climate under a doubling of atmospheric CO₂ (Chapter 8). The results indicate that, for doubled CO₂ conditions, evaporation will drop and air temperature will increase over the tropical land surface, amplifying the changes resulting from atmospheric radiative effects. The range of responses in surface air temperature and terrestrial carbon uptake are projected to be inversely related in the tropics year-round and inversely related during the growing season elsewhere.
6. The linkages between observed variations in vegeta-

tion greenness and observed variations in sea surface temperature, landsurface air temperature and precipitation were studied and the implications for the global carbon balance discussed (Chapter 9). The results suggest two types of linkages: the stronger of the two is a positive link at mid to high latitudes between increased sea surface temperatures, landsurface air temperatures, and photosynthetic rates by terrestrial vegetation that occurs mainly as a result of an extension of the growing season; and the other, weaker link is a localized positive association between sea surface temperature, rainfall, and photosynthetic rates. The changes in sea surface temperature, landsurface air temperature, and inferred photosynthetic rates agree with the terrestrial carbon sink. Three cases investigated in more detail showed that higher temperatures at mid to high latitudes lead to an expansion of the growing season; in two cases no significant increase in vegetation greenness was found during the middle of the growing season. These results indicate that global satellite observations of the land surface are needed for longer periods of time to assess vegetation dynamics and their implications for the global carbon balance.

The doubling of atmospheric CO₂ is projected to occur sometime during the second half of the next century. Most double CO₂ scenarios in atmospheric GCMs predict an increase of the landsurface temperature between 1.5 and 4.5 °C. The biosphere is likely to respond in several ways.

- In mid to high (northern) latitudes increased radiative forcing as a result of increased CO₂ will lead to increased surface temperature at the start and end of the growing season, longer growing seasons, and increased leaf area index and solar radiation captured by plants (Chapter 9). This increase will continue until other factors, most importantly the availability of moisture to plants, become limiting to plant growth. The increased leaf area index at these latitudes will lead to increased evaporation and this will in part counteract the increase in temperature as a result of radiative forcing. The increased stomatal resistance resulting from elevated CO₂ levels and increased temperatures (Chapter 8) tend to reduce evapotranspiration thus counteracting the increase in evapotranspiration as a result of increased leaf area index. The net effect of increased leaf area index (increased evapotranspiration and decrease in temperature) and increased stomatal resistance (decreased evapotranspiration and increased temperature) is yet to be determined. Non-local effects found to be important in the double CO₂ experiments during winter may further complicate this

picture.

- In low latitudes the increased radiative forcing by itself will lead to a somewhat smaller increase in temperatures than at high latitudes. Since moisture availability to plants is a limiting factor in these regions, a reduction in leaf area index and FPAR and an increase in the stomatal resistance are projected. Both effects reduce the evapotranspiration, and this will lead to increased temperatures. Because of the additional effect of reduced leaf area index it is expected that temperatures at low latitudes will increase by a larger amount than was estimated from the double CO₂ runs.

The projected changes in vegetation may sustain the terrestrial carbon sink in mid to high latitudes if moisture availability to plants does not become a limiting factor. The projected warmer temperatures and reduced photosynthetic capacity in lower latitudes are likely to add to the carbon source.

The current study has not investigated the effects of changing climate on the distribution of ecosystems, the changes in land management practices by humans, or the effects of changes in the amount of nutrients available to plant growth. The changes in the spatial distributions of ecosystems occur over longer time periods than the immediate effects of doubling of atmospheric CO₂ on stomatal conductance, leaf area index, and FPAR and are therefore thought to be of secondary importance for the climate in the next couple of decades. Indirect effects of climate change such as a projected increase in frequency of fires and hurricanes could have strong local effects. Land use change over large areas can also cause climatic impacts similar to doubling of CO₂ as illustrated by studies on the effect of deforestation of the Amazon on atmospheric circulation.

The current study has clearly demonstrated the usefulness of satellite data for studying landsurface vegetation in relation to climate and has provided useful insight in the mechanisms underlying the linkages between them. Satellite data will continue to be the only feasible way to obtain comprehensive updates of the state of global vegetation in a timely fashion.

Samenvatting en Conclusies

Verbanden Tussen Globale Vegetatie en Klimaat: Een Analyse Gebaseerd op Data van de NOAA Advanced Very High Resolution Radiometer

Dit proefschrift beschrijft onderzoek naar ruimtelijke en temporele variaties in de biosfeer met behulp van satelliet-data en de samenhang tussen deze variaties en variaties in het klimaat. De studie is onderdeel van een *Earth Observing System (EOS) Interdisciplinary Science (IDS) Biosphere-Atmosphere Interactions* studie dat de interacties tussen de biosfeer en de atmosfeer onderzoekt en nagaat hoe deze de CO₂ kringloop beïnvloeden. Voor dit proefschrift werd een vegetatie dataset samengesteld en werden met deze dataset in een klimaatmodel gekoppeld aan een vegetatiemodel simulaties uitgevoerd waarmee interacties tussen vegetatie en klimaat werden bestudeerd. Ook werden variaties in de vegetatie dataset vergeleken met waargenomen variaties in neerslag over land en variaties in land-, en oceaantemperaturen. De zes belangrijkste resultaten van dit proefschrift zijn:

1. De vervaardiging van een vegetatie dataset met maandelijkse waarnemingen en een oplossend vermogen van 1 bij 1 graad voor het gehele land oppervlak van de aarde over meerdere jaren (1982-1990). Hiervoor werden waarnemingen gebruikt van de *Advanced Very High Resolution Radiometer* (AVHRR), een instrument waarmee de meteorologische satellieten van de *National Oceanic and Atmospheric Administration* (NOAA) zijn toegerust (Hoofdstuk 4, Appendix C). Met dit instrument kan de vegetatie over het gehele landoppervlak worden geobserveerd (Hoofdstuk 2). Observatie van vegetatie berust op het waarnemen van door het landoppervlak gereflecteerde straling in het rode en nabij-infrarode deel van het elektromagnetisch spectrum. Reflectie waarden in het rood en infrarood werden gecombineerd in een genormaliseerde vegetatie-index (NDVI) die gerelateerd is aan de hoeveelheid zonlicht die door vegetatie wordt opgenomen voor fotosynthese. Het ruimtelijk en temporeel oplossend vermogen van de NDVI-

dataset is voldoende om variaties in vegetatie op globaal niveau te onderzoeken.

2. Het verbeteren van de temporele en spatiele samenhang van de vegetatie dataset. Er komen inconsistenties in de satelliet-waarnemingen voor die het gevolg zijn van verloop in de gevoeligheid van het instrument, het ontbreken van gegevens bijvoorbeeld doordat wolken waarneming van het landoppervlak onmogelijk maken, veranderingen in de samenstelling van de atmosfeer, veranderingen in de waarnemings-geometrie in combinatie met de reflectie-eigenschappen van het land-oppervlak en de atmosfeer, en variaties in de reflectie-waarden van de bodem (Hoofdstuk 3, Appendix C). Een groot gedeelte van dit proefschrift is gewijd aan het ontwikkelen van correcties voor deze effecten. Een belangrijk nadeel is dat gegevens die nodig zijn om volledig te corrigeren voor deze effecten niet voor handen zijn. In appendix A en B werden benaderingen uitgewerkt om de vegetatie-index te corrigeren voor het verloop in de gevoeligheid van de AVHRR en om waarnemingen van verschillende instrumenten aan boord van NOAA 7, 9 en 11 te calibreren. In hoofdstuk 5 en appendix D worden technieken besproken om de effecten van wolken en de atmosfeer uit de waarnemingen te filteren, te interpoleren waar waarnemingen ontbreken (voornamelijk op hoge breedtegraden in het noordelijk halfrond tijdens de wintermaanden) en te corrigeren voor variaties in de invalshoeken van de zon. De correcties zijn geëvalueerd in hoofdstuk 6.
3. De schatting van biofysische parameters voor klimaatstudies. Van de gecorrigeerde vegetatie-index gegevens werden biofysische parameters afgeleid: de fractie van het zonlicht opgenomen door de vegetatie voor fotosynthese (FPAR), en de ratio tussen het blad-oppervlak van de vegetatie en het land-

oppervlak (LAI; Hoofdstuk 5, Appendix D). Dit gebeurde door een linear verband tussen de Simple Ratio (SR, een vegetatie index gerelateerd aan de NDVI) en FPAR, en een logaritmisch verband tussen FPAR en LAI te veronderstellen. De modellen (NDVI-FPAR model, SR-FPAR model and FPAR-LAI model) werden getest met waarnemingen van het *First ISLSCP¹ Field Experiment* (FIFE), het *Oregon Transect Ecosystem Research* (OTTER), en de *BOReal Ecosystem-Atmosphere Study* (BOREAS; zie Hoofdstuk 6). Het SR-FPAR model gaf in het algemeen betere, zei het wat te lage, FPAR schattingen dan het NDVI-FPAR model, dat significante overschattingen te zien gaf. Een derde methode waarbij de schattingen van het SR-FPAR model en het NDVI-FPAR model werden gemiddeld gaf de beste resultaten. De ruis in de FPAR schattingen in de locale metingen was hoog (root mean square = 0.2 FPAR). Wanneer de waarnemingen werden gemiddeld over grotere oppervlakten neemt de ruis af (rms = 0.1 FPAR). De biofysische parameters werden verder geëvalueerd door albedo-schattingen van het Simple Biosfeer model (SiB2) te vergelijken met albedo-schattingen van het *Earth Radiation Budget Experiment* (ERBE; zie Hoofdstuk 6). SiB2 albedo werd geschat met behulp van de LAI en met toegekende reflectie waarden voor de vegetatie en de bodem. De SiB2 en ERBE albedo waarden kwamen redelijk overeen voor vegetatie typen bestaande uit loofbomen (SiB2 klas 1 en 2), graslanden (7), toendra (10), woestijn (11) en landbouw (12). De SiB2 albedo-schattingen voor vegetatie typen bestaande uit naaldbomen (4,5) of gemengd bos (3), of schoon aan de lage kant, kwamen beter overeen met waarnemingen van het BOREAS experiment dan de ERBE schattingen. De SiB2 albedo gaf geringe overschattingen te zien voor savannes (6) en geringe onderschattingen voor landschapstypen bestaande uit struiken over een kale ondergrond (9). De ERBE schattingen waren geloofwaardiger voor deze landschapstypen. Vergeleken met de ERBE albedo-schattingen hadden de SiB2 albedo-schattingen een kleine, onrealistische, spreiding binnen een landschapstype. De problemen in de SiB2 albedo-schattingen zijn gerelateerd aan de reflectie waarden die werden toegekend aan de bodem en de vegetatie: in sommige gevallen waren een te donkere bodem en te lichte bladeren gespecificeerd waardoor de albedo toenam met een toename in bladoppervlak. The ERBE waarnemingen daarentegen lieten een neerwaartse trend zien in de albedo als het bladoppervlak toenam.

¹ISLSCP: International Satellite Land Surface Climatology Project

4. De bepaling van de gevoeligheid van fluxen tussen het land oppervlak en de atmosfeer—CO₂ assimilatie, water, en energie fluxen—met betrekking tot waargenomen variaties in de vegetatie-index. De gevoeligheid werd berekend door twee scenario's te draaien met de *Colorado State University Atmospheric General Circulation Model* (AGCM) gekoppeld aan het *Simple Biosphere* (SiB2) model (Hoofdstuk 7). Bij toegenomen vegetatie nam de CO₂ assimilatie alleen toe voor breedtegraden met gematigde temperaturen en voldoende neerslag. De waterbalans veranderde vooral op lage breedtegraden waar een sterke afname in het bodemvocht te zien was. De totale energiebalans gaf slechts een kleine verandering te zien, er was wel een grote verandering in de verdeling tussen voelbare en latente warmte. Door Charney *et al.* (1975, 1977) werd een positieve terugkoppeling verondersteld tussen minder plant materiaal, hogere albedo-waarden, een geringere warmte uitstraling (totaal van voelbare en latente warmte straling) door het aardoppervlak, een afname in convectie en een afname in neerslag. Hierdoor is minder bodemvocht voor vegetatie beschikbaar en dit versterkt of handhaaft de initiële teruggang in de vegetatie. De terugkoppeling werd ook verondersteld in omgekeerde richting te functioneren: meer vegetatie zou tot meer neerslag leiden hetgeen de initiële toename in vegetatie zou versterken. Uit de SiB2-GCM studie bleek dat de fysiologische aspecten van vegetatie belangrijker waren dan de veranderingen in de energie balans die werden verondersteld door Charney *et al.* (1975, 1977). In de SiB2-GCM studie werd een terugkoppeling gevonden tussen meer plant materiaal, meer fotosynthese, meer verdamping, en meer neerslag. Echter, de toename in verdamping was groter dan de toename in neerslag. Hierdoor nam de hoeveelheid bodemvocht af en de stress op de vegetatie toe, waardoor een negatieve terugkoppeling met de initiële toename in vegetatie ontstond.
5. Zes numerieke experimenten werden uitgevoerd met de SiB2-GCM om de gevolgen van een verdubbeling van het atmosferisch CO₂-gehalte op de (huidige) vegetatie te schatten en om de samenhang tussen deze effecten op de vegetatie en klimaatsveranderingen na te gaan (Hoofdstuk 8). Bij een verdubbelde CO₂ concentratie bleek dat de verdamping door vegetatie afneemt waardoor de temperatuur in de tropen toeneemt en de gevolgen van een toegenomen "broeikas-effect" versterkt worden. Volgens de simulaties zijn in de tropen gedurende het gehele jaar en elders alleen gedurende het groeiseizoen de veranderingen in land-temperatuur tegengesteld aan veranderingen in de opname van CO₂ door vege-

tatie.

6. De samenhang tussen variaties in vegetatiedichtheid, oceaan-temperaturen, land-temperaturen en neerslag over land werden onderzocht en de implicaties voor de globale CO₂-kringloop besproken (Hoofdstuk 9). Twee soorten koppelingen tussen vegetatie en klimaat werden gevonden: de sterkste van de twee is een koppeling tussen veranderingen in de oceaan-temperaturen, de land-temperaturen, en de vegetatiedichtheid. Deze koppeling werd gevonden op gematigde tot hoge breedten. Op gematigde breedten zijn hogere temperaturen het sterkst gekoppeld aan een toename van vegetatie gedurende de lente; op hogere breedtegraden gedurende het gehele groeiseizoen. De tweede koppeling is zwakker en bestaat tussen veranderingen in oceaan-temperaturen, neerslag en vegetatie. Deze koppeling werd gevonden op lage breedtegraden. Lagere temperaturen van het oceaan-water zijn gerelateerd aan een afname in convectie en neerslag, en hebben door een afname in bodemvocht een remmend effect op de groei van vegetatie. Het eerste mechanisme (gerelateerde veranderingen in oceaan-temperatuur, land-temperatuur en vegetatiegroei) verschaft mogelijk een verklaring voor de "missing sink"² omdat jaren met hogere temperaturen, en dus meer vegetatie, overeenkomen met een stijging in CO₂ opname door het land en jaren met lagere temperaturen overeenkomen met een daling in CO₂ opname. Indien deze veronderstelling juist is, laten de gegevens zien dat de verdeling van sterkere en minder sterke opname van CO₂ verandert als functie van tijd en plaats.

De verwachting is dat de CO₂ concentratie in de atmosfeer zal verdubbelen tijdens de tweede helft van de volgende eeuw. De meeste klimaatsmodellen voorspellen dat dit zal leiden tot een toename in de land temperatuur van 1.5 tot 4.5 °C. Het is waarschijnlijk dat de biosfeer zich als volgt zal aanpassen.

- Op gematigde tot hoge breedtegraden zal het toegenomen broeikaseffect als gevolg van een verhoogd CO₂ gehalte leiden tot een toename in landtemperaturen met name gedurende het begin en einde van het groeiseizoen. Dit zal tot een langer groeiseizoen leiden, en tot hogere waarden voor biofysische variabelen zoals de hoeveelheid zonlicht geabsorbeerd door planten en het bladoppervlak (Hoofdstuk 9). Deze toename zal doorgaan

²Het verschil tussen het waargenomen atmosferisch CO₂ gehalte en het atmosferisch CO₂ gehalte dat op grond van uitstoot van (fossiele) brandstoffen en opname van CO₂ door oceanen verwacht mag worden.

tot andere factoren, zoals de beschikbaarheid van bodemvocht, de plantengroei beperken. Twee effecten gerelateerd aan de toegenomen vegetatie kunnen de toename in landtemperatuur als gevolg van een sterker broeikas effect beïnvloeden. Het toegenomen bladoppervlak zal leiden tot een toename in de verdamping en dit zal ten dele de toename in temperatuur opheffen (Hoofdstuk 7). De toegenomen stomatale weerstand van de bladeren zal leiden tot een afname in de verdamping en dit zal een toename in temperatuur versterken (Chapter 8). Het netto effect van deze twee mechanismen moet nog bepaald worden. Niet-lokale effecten, zoals de veranderingen in globale circulatie patronen in de winter waarvan het belang bleek uit dubbele CO₂ experimenten, kunnen dit beeld verder compliceren.

- Op lage breedtegraden zal het toegenomen broeikas-effect leiden tot een geringere toename in temperatuur dan op gematigde tot hogere breedtegraden. Omdat water een beperkende factor is in semi-aride en aride gebieden die op deze breedten veel voorkomen, zullen de toegenomen temperaturen leiden tot meer verdamping. Als gevolg daarvan zal de hoeveelheid plantmateriaal afnemen en de stomatale weerstand toenemen. Beide effecten zorgen voor een afname van de verdamping en dit versterkt een toename in de temperatuur. Omdat het bladoppervlak afneemt, een effect waar geen rekening mee werd gehouden in de dubbele CO₂ experimenten, wordt verwacht dat de temperatuur op deze breedtegraden sterker zal toenemen dan de dubbele CO₂ experimenten aangaven.

Op grond van het huidige onderzoek kan worden verwacht dat de vegetatie op gematigde tot hoge breedtegraden als netto effect koolstof zal blijven opnemen mits voldoende bodemvocht beschikbaar is. Op lage breedtegraden zal, als gevolg van afgenomen fotosynthese, een tendens bestaan tot een sterkere afgifte van koolstof in de atmosfeer.

In de huidige studie is het effect van klimaatsveranderingen op de verspreiding van eco-systemen niet onderzocht, noch zijn de effecten van veranderd landgebruik of veranderingen in de hoeveelheid voedingsstoffen voor planten in beschouwing genomen. Het is waarschijnlijk dat veranderingen in de stomatale weerstand en het bladoppervlak over kortere termijn een rol zullen spelen en dat veranderingen in ecosystemen over een langer periode zullen plaatsvinden en voor de korte termijn van minder belang zullen zijn. Indirecte effecten als gevolg van klimaatsveranderingen zoals een veronderstelde toename in het voorkomen van bosbranden, langere perioden van droogte en frequenter voorkomen van orkanen, zijn eveneens niet onderzocht. Klimaatstudies naar het effect

CHAPTER 10 SUMMARY AND CONCLUSIONS

van ontbossing van de Amazone hebben laten zien dat deze verandering in landgebruik een aan een verdubbeling van het atmosferische CO_2 gehalt vergelijkbaar effect kan hebben.

De huidige studie heeft duidelijk de bruikbaarheid van satellietdata voor het onderzoek van verbanden tussen vegetatie en klimaat gedemonstreerd. De observatie van het landoppervlak met satellieten is de enige praktische manier is om tijdig informatie omtrent de vegetatie over de gehele wereld te vergaren.

Opdracht

Ik draag dit proefschrift op aan mijn vrouw, kinderen en ouders.

Bibliography

- Abel, P., B. Guenther, R.N. Galimore, and J.W. Cooper, 1993, Calibration results for NOAA-11 AVHRR channels 1 and 2 congruent path aircraft observations. *J. Atmos. Ocean Tech.*, **10**, 493-508.
- Angelici, G.L., J.W. Skiles, and L.Z. Popovici, 1991, OTTER Pilot Land Data System, Volume 1, Version 1: Satellite, Aircraft, and Ground Measurements. Published on CD-ROM by National Aeronautics and Space Administration. Available on CD-ROM and on-line [<http://www-eosdis.ornl.gov>] from the ORNL Distributed Active Archive Center, Oak Ridge National Laboratory, Oak Ridge, Tennessee, U.S.A.
- Anyamba, A., and R. Eastman, 1996, Interannual variability of NDVI over Africa and its relation to El Niño/Southern Oscillation. *Int. J. Remote Sens.*, **17**, 2533-2548.
- Asrar, G., M. Fuchs, E.T. Kanemasu, and J.L. Hatfield., 1984, Estimating absorbed photosynthetic radiation and leaf area index from spectral reflectance in wheat. *Agron. J.*, **76**, 300-306.
- Asrar, G., E.T. Kanemasu, R.D. Jackson, and P.J. Pinter, 1985, Estimation of total aboveground phytomass production using remotely sensed data. *Remote Sens. Environ.*, **17**, 211-220.
- Asrar, G., E.T. Kanemasu, G.P. Miller, and R.L. Weiser, 1986, Light interception and leaf area estimates from measurements of grass canopy reflectance. *IEEE Trans. Geosci. Remote Sens.*, **24**, 76-82.
- Asrar, G., R.B. Myneni, and B.J. Choudhury, 1992, Spatial heterogeneity in vegetation canopies and remote sensing of Absorbed Photosynthetically Active Radiation: a modeling study. *Remote Sens. Environ.*, **41**, 85-101.
- AUSLIG, 1990, *Atlas of Australian resources*, third series, Vol. 6, Vegetation, Commonwealth of Australia, 63 pp.
- Baldwin, D.G., and W.J. Emery, 1993, Systematized approach to AVHRR navigation. *Ann. Glaciology.*, **17**, 414-420.
- Ball, J.T., 1988, *An analysis of stomatal conductance*. Ph.D. Thesis, Stanford University, Stanford, California, 89 pp.
- Ball, J.T., I.E. Woodrow, and J.A. Berry, 1987, A model predicting stomatal conductance and its contribution to the control of photosynthesis under different environmental conditions. In: J. Briggs, ed., *Progress in Photosynthetic Research*. Vol. IV. Martinus Nijhoff, Dordrecht. 221-224.
- Barkstrom, B.R., E.F. Harrison, and R.B. Lee, 1990, Earth Radiation Budget Experiment, Preliminary seasonal results. *EOS Transactions*, American Geophysical Union, **71** (9), 297 pp.
- Bates, D.M., and D.G. Watts, 1988, *Nonlinear regression analysis and its applications*. John Wiley and Sons, Inc., New York.
- Beerling, D.J. and W.G. Chaloner, 1994, Atmospheric CO₂ changes since the last glacial maximum: Evidence from the stomatal density record of fossil leaves. *Rev. Palaeobot. Palyn.* **81**, 11-17.
- Bjerknes, J., 1969, Atmospheric teleconnections from the equatorial Pacific. *Monthly Weather Review*, **97**, 163-172.
- Blad, B.L., and E.A. Walter-Shea, 1994, First ISLSCP Field Experiment Surface Reflectance Measured with a Mastborne MMR Dataset. In D.E. Strebel, D.R. Landis, K.F. Huemmrich, and B.W. Meeson (1994), *Collected Data of The First ISLSCP Field Experiment*, Vol. 1: Surface Observations and Non-Image Datasets. Published on CD-ROM by National Aeronautics and Space Administration. Available on CD-ROM and on-line [<http://www-eosdis.ornl.gov>] from the ORNL Distributed Active Archive Center, Oak Ridge National Laboratory, Oak Ridge, Tennessee, U.S.A.
- Box, E.O., B.N. Holben, and V. Kalb, 1989, Accuracy of the AVHRR vegetation index as a predictor of biomass, primary production and net CO₂ flux. *Vegetatio*, **80**, 71-89.
- Brest C.L., and W.B. Rossow, 1992, Radiometric calibration and monitoring of NOAA-AVHRR data for ISCCP. *Int. J. Remote Sens.*, **13**, 235-273.
- Bruijnzeel, L.A., 1983, Hydrological and Biogeochemical Aspects of Man-made Forests in South-central Java, Indonesia, Ph.D. dissertation, Vrije Universiteit, Amsterdam.
- Brush, R.J.H., 1988, The navigation of AVHRR imagery. *Int. J. Remote Sens.*, **9**, 1491-1502.
- Budyko, M.I., 1974, *Climate and Life*. Academic Press, 508 pp.
- Burgess, A.W., P. Lewis, and J.P.A.L. Muller, 1995, Topographic effects in AVHRR NDVI data, *Remote Sens. Environ.*, **54**, 223-232.

BIBLIOGRAPHY

- Chahine, M.T., D.J. McCleese, P.W. Rosenkranz, and D.H. Staehlin, 1983, Interaction mechanisms within the atmosphere. In: *Manual of Remote Sensing*, edited by R.N. Collwell, Falls Church, VA, American Soc. of Photogrammetry, 1, 165-230.
- Charney, J., P.H. Stone, and W.J. Quirk, 1975, Drought in the Sahara: A biogeophysical feedback mechanism. *Science*, **187**, 434-435.
- Charney, J., W.J. Quirk, S.H. Chow, and J. Kornfield, 1977, A Comparative Study of the Effects of Albedo Change on Drought in Semi-Arid Regions. *J. Atmos. Sci.*, **34**, 1366-1385.
- Choudhury, B.J., 1987, Relationships between vegetation indices, radiation, absorption, and net photosynthesis evaluated by a sensitivity analysis. *Remote Sens. Environ.*, **22**, 209-233.
- Chen, J. M., 1996, Canopy architecture and remote sensing of the fraction of photosynthetically active radiation absorbed by boreal conifer forests. *IEEE Trans. Geosci. Remote Sens.*, **34**, 1353-1368.
- Chen, J.M., and J. Cihlar, 1996, Retrieving leaf area index of boreal conifer forests using Landsat TM images. *Remote Sens. Environ.*, **55**, 153-162.
- Ciais, P., P.P. Tans, J.W.C. White, M. Troler, R.J. Francey, J.A. Berry, D.A. Randall, P.J. Sellers, G.J. Collatz, and D.S. Schimel, 1995, Partitioning of ocean and land uptake of CO₂ as inferred by $\delta^{13}\text{C}$ measurements from the NOAA/CMDL global air sampling network. *J. Geophys. Res.*, **100**, 5051-5070.
- Cihlar, J., 1996, Identification of contaminated pixels in AVHRR composite images for studies of land biosphere. *Remote Sens. Environ.*, **56**, 149-163.
- Clapp, R.B., and G.M. Hornberger, 1978, Empirical equations for some soil hydraulic properties. *Water Resour. Res.*, **14.4**, 601-604.
- Collatz, G.J., J.T. Ball, C. Grivet, and J.A. Berry, 1991, Physiological and environmental regulation of stomatal conductance, photosynthesis, and transpiration: a model that includes a laminar boundary layer. *Agric. For. Meteorol.*, **54**, 107-136.
- Collatz, G.J., M. Ribas-Carbo, and J.A. Berry, 1992, Coupled photosynthesis stomatal conductance for leaves of C₄ plants. *Aust. J. Plant Physiol.*, **19**, 519-538.
- Collatz, G.J., J.A. Berry and J.S. Clark., 1989, The effect of climate and atmospheric CO₂ partial pressure on the global distribution of C₄ grasses: Present, past, and future. *Oecologia*, (in press).
- Cowan, I.R., 1977, Stomatal behavior and environment. *Adv. Bot. Res.*, **4**, 117-228.
- Cramer, W. and R. Leemans, 1993, Assessing impacts of climate change on vegetation using climate classification systems. In: *Vegetation dynamics modelling and global change*. Chapman-Hall, New York, 190-217.
- Daughtry, C.S.T., K.P. Gallo, and M.E. Bauer, 1983, Spectral estimates of solar radiation intercepted by corn canopies. *Agronomy J.*, **75**, 527-531.
- Dazlich, D.A., 1995, Calculated snow-free albedo. Edited by Meeson *et al.*, ISLSCP Initiative I Global Datasets for Land-Atmosphere Models, 1987-1988, EOS Distributed Active Archive Center, NASA/GSFC, code 902.2, Greenbelt, Maryland 20771.
- Deering, D.W., and P. Leone, 1986, A sphere-scanning radiometer for rapid directional measurements of sky and ground radiance. *Remote Sens. Environ.*, **19**, 1-24.
- Deering, D.W., T.F. Eck, and T. Grier, 1992a, Shinnery oak bidirectional reflectance properties and canopy model inversion. *IEEE Trans. Geosci. Remote Sens.*, **30**, 339-348.
- Deering, D.W., E.M. Middleton, J.R. Irons, B.L. Blad, E.A. Walter-Shea, C.J. Hays, C.W. Walthall, T.F. Eck, S.P. Ahmad, and B.P. Banerjee, 1992b, Prairie grassland bidirectional reflectance measured by different instruments at the FIFE sites. *J. Geophys. Res.*, **97**, 18,887-18,903.
- Deering, D.W., E.M. Middleton, and T.F. Eck, 1994, Reflectance anisotropy for a spruce-hemlock forest canopy. *Remote Sens. Environ.*, **47**, 242-260.
- DeFries, R.S., and J.R.G. Townshend, 1993, Global landcover: Comparison of ground-based datasets to classifications with AVHRR data. In: *Environmental Remote Sensing from Regional to Global Scales*, edited by G. Foody and P. Curran, Chichester, John Wiley and Sons, 84-110.
- DeFries, R.S., and J.R.G. Townshend, 1994, NDVI-derived landcover classifications at global scale. *Int. J. Remote Sens.*, **15**, 3567-3586.
- DeFries, R.S., J.R.G. Townshend and S.O. Los, 1997, Scaling landcover heterogeneity for global atmosphere-biosphere models. In: *Scale in remote sensing and GIS*, edited by D.A. Quattrochi and M.F. Goodchild. Lewis Publishers, New York, 231-246.
- Denning, A.S., I.Y. Fung, and D.A. Randall, 1995, Latitudinal gradient of atmospheric CO₂ due to seasonal exchange with land biota. *Nature*, **376**, 240-243.
- Dickinson, R.E., 1983, Landsurface processes and climate-surface albedos and energy balance. *Adv. Geophys.*, **25**, Academic Press, 305-353.
- Dickinson, R.E., 1984, Modeling evapotranspiration for three-dimensional global climate models. *Climate Processes and Climate Sensitivity*, *Geophysical Monograph*, **29**, J.E. Hansen and T. Takahashi, eds., Amer. Geophys. Union, Washington, D.C., 58-72.

- Dorman, J.L., and P.J. Sellers, 1989, A global climatology of albedo, roughness length and stomatal resistance for atmospheric general circulation models as represented by the simple biosphere model (SiB). *J. Applied Meteor.*, **28**, 833-855.
- Draper, N.R., and H. Smith, 1981, *Applied regression analysis*. John Wiley and Sons, Inc., New York, 709 pp.
- Duggin, M.L., D. Piwinski, V. Whitehead, and G. Tyland, 1982, Evaluation of NOAA-AVHRR data for crop assessment. *Applied Optics*, **21**, 1873-1875.
- Eck, T.F., and V.L. Kalb, 1991, Cloud screening for Africa using geographically and seasonally variable infrared threshold. *Int. J. Remote Sens.*, **12**, 1205-1221.
- Eidenshink, J.C., and J.L. Faundeen, 1994, The 1 km AVHRR global land dataset: first stages in implementation. *Int. J. Remote Sens.*, **15**, 3443-3462.
- Eischeid, J.K., H.F. Diaz, R.S. Bradley, and P.D. Jones, Eds., 1991, A comprehensive precipitation dataset for global land areas. U.S. Dept of Energy, Washington D.C., 82 pp.
- Ellis J.E., and D.M. Swift, 1988, Stability of African pastoral ecosystems: Alternate paradigms and implications for development. *J. Range Management*, **41**, 450-459.
- Emery W.J., J. Brown, and Z.P. Nowak, 1989, AVHRR Image Navigation: Summary and review. *Photogram. Eng. Remote Sens.*, **55**, 1175-1183.
- Engelen, G.B., and C.P. Jones, 1986, *Developments in the Analysis of Groundwater Flow Systems*. IAHS Press, Wallingford, England, 356 pp.
- Farquhar, G.D., S. Von Caemmerer, and J.A. Berry, 1980, A biochemical model of photosynthetic CO₂ fixation in leaves of C₃ species. *Planta*, **149**, 78-90.
- Field, C.B., 1991, Ecological scaling of carbon gain to stress and resource availability. In: H. A. Mooney, W. E. Winner and E. J. Pell, eds., *Integrated Response of Plants to Stress*, Academic Press, San Diego, pp. 35-65.
- Field, C.B., F. S. Chapin III, P.A. Matson and H.A. Mooney, 1992, Responses of terrestrial ecosystems to the changing atmosphere: A resource-based approach. *Annu. Rev. Ecol. Syst.*, **23**, 201-35.
- Field, C.B., R.B. Jackson, and H.A. Mooney, 1995a, Stomatal responses to increased CO₂: implications from the plant to the global scale. *Plant, Cell Environ.*, **18**, 1214-1226.
- Field, C.B., J.T. Randerson and C.M. Malmström, 1995b, Global net primary production: Combining ecology and remote sensing. *Remote Sens. Environ.*, **51**, 74-88.
- Fung, I.Y., C.J. Tucker, K.C. Prentice, 1987, Application of advanced very high resolution radiometer vegetation index to study atmosphere-biosphere exchange of CO₂. *J. Geophys. Res.*, **92**, 2999-3015.
- Gates, D.M., H.J. Keegan, J.C. Schleter, and V.P. Weidner, 1965, Spectral properties of plants, *Appl. Optics*, **4**, 11.
- Glantz, M.H., R.W. Katz, and N. Nicholls, eds., 1991, *Teleconnections Linking Worldwide Climate Anomalies*. Cambridge University Press, New York, 535 pp.
- Glantz, M.H., and J.H. Krenz, 1992, Human components of the climate system. In: *Climate System Modeling*, K.E. Trenberth, ed., Cambridge University Press, New York, pp. 27-49.
- Goel, N.S., 1988, Models of vegetation canopy reflectance and their use in estimation of biophysical parameters from reflectance data, *IEEE Trans. Remote Sens. Rev.*, **4**, 1-222.
- Gorny, A.J., 1977, World Data Bank II, General User Guide. Central Intelligence Agency, Washington D.C..
- Goulden, M.L., J.W. Munger, S.M. Fan, B.C. Daube, and S.C. Wofsy, 1996, Exchange of carbon dioxide by a deciduous forest: Response to interannual climate variability, *Science*, **271**, 1576-1578.
- Goward, S.N., and D.G. Dye, 1987, Evaluating North American net primary productivity with satellite observations. *Adv. Space Res.*, **7**, 165-174.
- Goward, S.N., and K.F. Huemmrich, 1992: Vegetation canopy PAR absorptance and the normalized difference vegetation index: An assessment using the SAIL model. *Remote Sens. Environ.*, **39**, 119-140.
- Goward, S.N., B. Markham, D.G. Dye, W. Dulaney, and J. Yang, 1991, Normalized Difference Vegetation Index measurements from the Advanced Very High Resolution Radiometer. *Remote Sens. Environ.*, **35**, 257-277.
- Goward, S.N., S. Turner, D.G. Dye, and S. Liang, 1994, The University of Maryland improved Global Vegetation Index product. *Int. J. Remote Sens.*, **15**, 3365-3395.
- Gray, T.I., and D.G. McCarty, 1981, Meteorological satellite data—A tool to describe the health of the world's agriculture. AgRISTARS Report EW-NI-04042, Johnson Space Center, Houston, Texas, 7 pp.
- Gregor, D.H., and J. Norwine, 1981, A gradient model of vegetation and climate utilizing NOAA satellite imagery - Phase 1: Texas transect. AgRISTARS Report JSC-27435, FC-J1-04176, Johnson Space Center, Houston, Texas, 58 pp.
- Gunderson, C.A., and S.D. Wullschleger, 1994, Photosynthetic acclimation in trees to rising atmospheric CO₂: A broader perspective. *Photosynthesis Res.*, **39**, 369-388.
- Gurney, R.J., J.L. Foster, and C.L. Parkinson, 1993, *Atlas of satellite observations related to global change*. Cambridge University Press, New York, 470 pp.

BIBLIOGRAPHY

- Gutman, G.G., 1991, Vegetation indices from AVHRR: An update and future prospects. *Remote Sens. Environ.*, **35**, 121-136.
- Gutman, G.G., A. Ignatov, and S. Olson, 1994, Towards better quality of AVHRR composite images over land: reduction of cloud contamination. *Remote Sens. Environ.*, **50**, 134-148.
- Gutman, G.G., D. Tarpley, A. Ignatov, and S. Olson, 1995, The enhanced NOAA Global Land dataset from the Advanced Very High Resolution Radiometer. *Bull. Amer. Meteor. Soc.*, **76**, 1141-1156.
- Hall, F.G., K.F. Huemmrich, and S.N. Goward, 1990, Use of narrow band spectra to estimate the fraction of absorbed photosynthetically active radiation. *Remote Sens. Environ.*, **32**, 47-54.
- Hall, F.G., K.F. Huemmrich, S.J. Goetz, P.J. Sellers, J.E. Nickeson, 1992, Satellite remote sensing of surface energy balance: success, failures, and unresolved issues in FIFE. *J. Geophys. Res.*, **97**, 19,061-19,089.
- Hall, F.G., P.J. Sellers, M. Apps, D. Baldocchi, J. Cihlar, B. Goodison, H. Margolis, 1993, BOREAS: Boreal Ecosystem-Atmosphere Study, *IEEE Geosci. Remote Sens. Soc. Newslet.*, March, 9-17.
- Hansen, J.E., A. Lacis, D. Rind, G. Russell, P. Stone, I.Y. Fung, R. Ruedy, and J. Lerner, 1984, Climate sensitivity: Analysis of feedback mechanisms. In: *Climate process and climate sensitivity*, Maurice Ewing Series (5), J. E. Hansen and T. Takahashi, eds., American Geophysical Union, 130-163.
- Harrison, E.F., P. Minnis, B.R. Barkstrom, V. Ramanathan, R.D. Cess, and G.G. Gibbison, 1990, Seasonal variation of cloud radiative forcing derived from the Earth Radiation Budget Experiment. *J. Geophys. Res.*, **95**, 18,687-18,703.
- Haxeltine, A., and I.C. Prentice, 1996, BIOME3: An equilibrium terrestrial biosphere model based on ecophysiological constraints, resource availability, and competition among plant functional types. *Global Geochem. Cycles*, **10**, 693-709.
- Helldén, U., 1984, Remote sensing for drought impact assessment—A study of land transformation in Kordofan, Sudan. *Adv. Space Res.*, **4**, 165-168.
- Helldén, U., 1988, Desertification monitoring; is the desert encroaching? *Desertification Control Bull.*, **17**, 8-12.
- Henderson-Sellers, A., K. McGuffie, and C. Gross, 1995, Sensitivity of global climate model simulations to increased stomatal resistance and CO₂ increases. *J. Climate*, **8**, 1738-1756.
- Herman, J.R., R. Hudson, R.D. McPeters, R.S. Stolarski, Z. Ahmad, X.Y. Gu, S. Taylor, C. Wellemeyer, 1991, A new self-calibration method applied to TOMS and SBUV backscattered ultraviolet data to determine long-term global ozone change. *J. Geophys. Res.*, **96**, 7531-7545.
- Hielkema, J.U., 1990, Operational environmental satellite remote sensing for food security and locust control by FAO. The ARTEMIS and DIANA systems. In: *Proceedings of the ISPRS, Session: Global Monitoring TP-1*, 18 Sept 1990, Victoria, B.C., Canada.
- Hielkema, J.U., J. Roffey, and C.J. Tucker, 1986, Assessment of ecological conditions associated with the 1980/81 desert locust plague upsurge in West Africa using environmental satellite data. *Int. J. Remote Sens.*, **7**, 1609-1622.
- Ho, D., and A. Asem, 1986, NOAA-AVHRR image referencing. *Int. J. Remote Sens.*, **7**, 895-904.
- Hoaglin, D.C., F. Mosteller, and J.W. Tukey, 1983, *Understanding robust and exploratory data analysis*. John Wiley and Sons, Inc., New York, 447 pp.
- Holben, B.N., 1986, Characteristics of maximum-value composite images for temporal AVHRR data. *Int. J. Remote Sens.*, **7**, 1435-1445.
- Holben, B.N., and R.S. Fraser, 1983, Effects of atmosphere and view and illumination geometry on visible and near-infrared radiance from the Advanced Very High Resolution Radiometer (AVHRR). *Remote Sens. Environ.*, **9**, 115-129.
- Holben, B.N., and R.S. Fraser, 1984, Red and near-infrared response to off-nadir viewing. *Int. J. Remote Sens.*, **5**, 145-160.
- Holben, B.N., D.S. Kimes, and R.S. Fraser, 1986, Directional reflectance response in AVHRR red and near-IR bands for three cover types and varying atmospheric conditions. *Remote Sens. Environ.*, **19**, 213-236.
- Holben, B.N., and T.F. Eck, 1990, Precipitable water in the Sahel measured using Sun photometry. *Agric. Forest Meteor.*, **52**, 95-107.
- Holben, B.N., Y.J. Kaufman, and J. Kendall, 1990, NOAA-11 AVHRR visible and near-IR inflight calibration. *Int. J. Rem. Sens.*, **11**, 1511-1519.
- Holben, B.N., T.F. Eck, and R.S. Fraser, 1991, Temporal and spatial variability of aerosol optical depth in the Sahel Region. *Int. J. Remote Sens.*, **12**, 1147-1163.
- Holben, B.N., E.F. Vermote, Y.J. Kaufman, D. Tanré, V.L. Kalb, 1992, Aerosol retrieval over land from AVHRR data: Application for atmospheric correction. *IEEE Trans. Geosci. Remote Sens.*, **30**, 211-221.
- Hollandsworth, S.M., R.D. McPeters, L.E. Flynn, W. Planet, A.J. Miller, and S. Chandra, 1995, Ozone trends deduced from combined NIMBUS-7 SBUV and NOAA-11 SBUV/2 data. *Geophys. Res. Letters*, **22**, 905-908.

- Houghton, J.T., G.J. Jenkins, and J.J. Ephraums, eds., 1990, Climate Change. The IPCC Scientific Assessment, World Meteorological Organization / United Nations Environment Programme, Cambridge Univ. Press, New York, 365 pp.
- Huemmrich, K.F., and S.N. Goward, 1992, Spectral vegetation indices and the remote sensing of biophysical parameters. Proc. Int. Geosci. Remote Sens. Symposium (IGARSS). Institute of Electrical and Electronics Engineers, Houston, Texas, 1017-1019.
- Huete, A.R., 1987, Soil-dependent spectral response in a developing plant canopy. *Agron. J.*, **79**, 61-68.
- Huete, A.R., and C.J. Tucker, 1991, Investigation of soil influences in AVHRR vegetation imagery. *Int. J. Remote Sens.*, **12**, 1223-1242.
- Hutchinson, C.F., 1991, Uses of data for famine early warning in sub-Saharan Africa. *Int. J. Remote Sens.*, **12**, 1405-1421.
- James, M.E., and S.N.V. Kalluri, 1994, The Pathfinder AVHRR land dataset: An improved coarse resolution dataset for terrestrial monitoring. *Int. J. Remote Sens.*, **15**, 3347-3363.
- Jensen, T.G., D.A. Dazlich and D.A. Randall, 1995, A one-dimensional mixed-layer ocean and sea ice model with prescribed oceanic heat transport. Dept. of Atmospheric Science Paper, **593**, 48 pp.
- Jones, P.D., S.C.B. Raper, B. Santer, B.S.G. Cherry, C. Goodess, P.M. Kelly, T.M.L. Wigley, R.S. Bradley, H.F. Diaz, eds., 1985, A grid point surface air temperature dataset for the Northern Hemisphere. U.S. Dept of Energy, Washington D.C., 251 pp.
- Jones, P.D., T.M.L. Wigley, P.B. Wright, 1990, Global and hemispheric temperature variations between 1861 and 1990. Report No. NDP-022/R1. CDIAC (Oak Ridge National Lab).
- Jones, P.D., and K.R. Briffa, 1992, Global surface air temperature variations over the twentieth century: Part 1 Spatial, temporal and seasonal details. *Holocene*, **2**, 105-179.
- Justice, C.O. (ed.), 1986, Monitoring the grasslands of semi-arid Africa using NOAA-AVHRR data. *Int. J. Remote Sens.*, **7**, 1383-1622.
- Justice, C.O., J.R.G. Townshend, B.N. Holben, and C.J. Tucker, 1985, Analysis of the phenology of global vegetation using meteorological satellite data. *Int. J. Remote Sens.*, **6**, 1271-1318.
- Justice, C.O., T.F. Eck, D. Tanré, and B.N. Holben, 1991a, The effect of water vapor on the normalized difference vegetation index for the Sahelian region from NOAA-AVHRR data. *Int. J. Remote Sens.*, **12**, 1165-1187.
- Justice, C.O., J.R.G. Townshend, and V.L. Kalb, 1991b, Representation of vegetation by continental datasets derived from NOAA-AVHRR data. *Int. J. Remote Sens.*, **12**, 999-1021.
- Kaufman, Y.J., 1987, The effect of subpixel clouds on remote sensing. *Int. J. Remote Sens.*, **8**, 839-857.
- Kaufman, Y.J., and B.N. Holben, 1993, Calibration of the AVHRR visible and near-IR bands by atmospheric scattering, ocean glint, and desert reflection. *Int. J. Remote Sens.*, **14**, 21-52.
- Kaufman, Y.J., D. Tanré, B.N. Holben, B. Markham, A. Gitelson, 1992, Atmospheric effects on the NDVI - Strategies for its removal. Proceedings of the International Geoscience and Remote Sensing Symposium (IGARRS), held in Houston, Texas. Institute of Electrical and Electronics Engineers, 1238-1241.
- Keeling, C.D., T.P. Whorf, M. Wahlen, and J. van der Plicht, 1995, Interannual extremes in the rate of rise of atmospheric carbon dioxide since 1980. *Nature*, **375**, 666-670.
- Keeling, C.D., J.F.S. Chin, and T.P. Whorf, 1996, Increased activity of northern vegetation inferred from atmospheric CO₂ observations. *Nature*, **382**, 146-149.
- Kidwell, K.B., 1995, Polar orbiter data users guide. U.S. Dept. of Commerce, NOAA/National Environmental Satellite Data and Information Service, National Climatic Data Center, Satellite Data Services Division, Washington D.C., 410 pp.
- Kimes, D.S., 1983, Dynamics of directional reflectance factor distributions for vegetation canopies. *Appl. Opt.*, **22**, 1364-1372.
- Kimes, D.S., B.N. Holben, C.J. Tucker, and W.W. Newcomb, 1984, Optimal Directional View Angles for Remote-Sensing Missions. *Int. J. Remote Sens.*, **5**, 887-908.
- Klink, K., and C.J. Wilmott, 1985, Notes on a global vegetation dataset for use in GCMs. Department of Geography, University of Delaware, Newark, Delaware.
- Kneizys, F.X., E.P. Shettle, W.O. Gallexy, J.H. Chetwynd, L. Abreu, J.E.A. Selby, S.A. Clough, and R.W. Fenn, 1983, Atmospheric transmittance / radiance: Computer code LOWTRAN6. Report: AFB MA 01731, Opt. Phys. Div., Air Force Geoph. Lab., Hanscom AFB, MA.
- Kuchler, W.A., 1983, World map of natural vegetation. *Goode's World Atlas*, 16th ed., Rand McNally, 16-17.
- Kumar, M., and J.L. Monteith, 1982, Remote sensing of plant growth. In: *Plants and the Daylight Spectrum*, Academic Press, London.
- Lamb, P.J., R.A. Peppler, and S. Hastenrath, 1986, Interannual variability in the tropical Atlantic. *Nature*, **322**, 238-240.

BIBLIOGRAPHY

- Lamprey, H.F., 1975, Report on the desert encroachment reconnaissance in northern Sudan, 21 October to 10 November 1975. UNESCO/UNEP, Nairobi. Republished in *Desertification Control Bulletin*, **17**, 1-7.
- Li, X., and A.H. Strahler, 1985, Geometric optical modeling of a coniferous forest canopy. *IEEE Trans. Geosci. Remote Sens.*, **23**, 207-221.
- Li, X., A.H. Strahler, and C.E. Woodcock, 1995, A hybrid geometric optical-radiative transfer approach for modeling albedo and directional reflectance of discontinuous canopies. *IEEE Trans. Geosci. Remote Sens.*, **33**, 466-480.
- Los, S.O., 1993, Calibration adjustment of the NOAA-AVHRR normalized difference vegetation index without recourse to component channels. *Int. J. Remote Sens.*, **14**, 1907-1917.
- Los, S.O., 1998, Estimation of the ratio of sensor degradation between NOAA-AVHRR channels 1 and 2 from monthly NDVI composites. *IEEE Trans. GeoSci. Remote Sens.*, **36**, 206-213.
- Los, S.O., C.O. Justice, and C.J. Tucker, 1994, A global 1° by 1° NDVI dataset for climate studies derived from the GIMMS continental NDVI. *Int. J. Remote Sens.*, **15**, 3493-3518.
- Loveland, T.R., J.W. Merchant, D.O. Ohlen, and J.F. Brown, 1991, Development of a landcover-based characteristics database for the conterminous U.S. *Photogram. Eng. Remote Sens.*, **57**, 1453-1463.
- Maling, D.H., 1973, *Coordinate systems and map projections*. George Phillip and Son, Ltd., London.
- Malingreau, J.P., 1986, Global vegetation dynamics: Satellite observations over Asia. *Int. J. Remote Sens.*, **7**, 1121-1146.
- Malingreau, J.P., G. Stevens, and L. Fellows, 1985, Remote sensing of forest fires: Kalimantan and North Borneo in 1982-83. *Ambio*, **14**, 314-321.
- Malingreau, J.P., and C.J. Tucker, 1988, Large-scale deforestation in the southern Amazon Basin of Brazil. *Ambio*, **17**, 49-55.
- Malmström, C.M., M.V. Thompson, G. Juday, S.O. Los, J.T. Randerson, and C.B. Field, 1997, Interannual variation in global-scale primary production: Testing model estimates. *Glob. Biochem. Cycles*, **11**, 367-392.
- Mandt, G., J. O'Neal, P. Taylor, 1996, NOAA Polar-orbiting operational environmental satellite program: Status and plans. POES Users' Symposium, held June 10-12, 1996, Annapolis, Maryland, NOAA, Washington D.C.
- Matthews, E., 1983, Global Vegetation and Land Use: New High-Resolution Data Bases for Climate Studies. *J. Climate App. Meteor.*, **22**, 474-487.
- Matthews, E., 1984, Prescription of landsurface boundary conditions in GISS GCM II: A simple method based on high resolution vegetation data bases. NASA Technical Memorandum 86096, NASA, Washington D.C. 20546, 20 pp.
- McCormick, M.P., and R.E. Veiga, 1992, SAGE II measurements of early Pinatubo aerosols. *Geophys. Res. Letters*, **19**, 155-158.
- Middleton, E. M., 1991, Solar zenith angle effects on vegetation indices in tall grass prairie. *Remote Sens. Environ.*, **38**, 45-62.
- Monteith, J.L., and M.H. Unsworth, 1990, *Principles of Environmental Physics*. Edward Arnold, 291 pp.
- Morison, J.I.L., 1985, Sensitivity of stomata and water use efficiency to high CO₂. *Plant Cell Environ.*, **8**, 467-474.
- Moura, A.D., and J. Shukla, 1981, On the dynamics of droughts in northeast Brazil: Observations, theory and numerical experiments with a general circulation model. *J. Atm. Sciences*, **38**, 2653-2675.
- Mosteller, F., and J.W. Tukey, 1977, *Data analysis and regression*. Addison-Wesley, Reading, Massachusetts, 588 pp.
- Myneni, R.B., J. Ross, and G. Asrar, 1989, A review on the theory of photon transport in leaf canopies. *Agric. Forest Meteor.*, **45**, 1-153.
- Myneni, R.B., G. Asrar, D. Tanré, and B.J. Choudhury, 1992, Remote sensing of solar radiation absorbed and reflected by vegetated land surface. *IEEE Trans. Geosci. Remote Sens.*, **30**, 302-314.
- Myneni, R.B., S.O. Los, and C.J. Tucker, 1995, Satellite-based identification of linked vegetation index and sea surface temperature anomaly areas from 1982-1990 for Africa, Australia and South America. *Geophys. Res. Lett.*, **23**, 729-732.
- Neilson, R.P., G.A. King, and G. Koerper, 1992, Toward a rule-based biome model. *Landscape Ecol.*, **7**, 27-43.
- Nicholson, S.E., 1993, An overview of African rainfall fluctuations of the last decade. *J. Climate*, **6**, 1463-1466.
- Nicholson, S.E., J. Kim, and J. Hoopingarner, 1988, *Atlas of African Rainfall and its Interannual Variability*. Tallahassee, Florida: Department of Meteorology, Florida State University, 237 pp.
- Nicholson, S.E., M.L. Davenport, and A.R. Malo, 1990, A comparison of the vegetation response to rainfall in the Sahel and East Africa, using normalized difference vegetation index from NOAA-AVHRR. *Climate Change*, **17**, 209-242.
- Nobre, C.A., P.J. Sellers, and J. Shukla, 1991, Amazonian deforestation and regional climate change. *J. Climate*, **4**, 957-988.

- Olson, J.S., J. Watts, and L. Allison, 1983, Carbon in live vegetation of major world ecosystems. W-7405-ENG-26, U.S. Dept. of Energy, Oak Ridge National Laboratory.
- Olsson, L., 1985, Desertification or climate? Investigation regarding the relationship between land degradation and climate in the central Sudan. Lund's Studies in Geography XCVIII, Department of Geography, University of Lund, Lund, Sweden.
- Ormsby, J.P., 1982, Classification of simulated and actual NOAA-6 AVHRR data for hydrological land-surface feature definition. *IEEE Trans. Geosci. Remote Sens.*, **20**, 262-268.
- Owe, M., and A.A. van de Griend, 1990, A daily surface moisture model for large area and semi-arid land application with limited climate data. *J. Hydrology*, **121**, 119-132.
- Palmer, T.N., 1986, Influence of the Atlantic, Pacific, and Indian Oceans on Sahel rainfall. *Nature*, **322**, 251-253.
- Patt, F.S., and W. Gregg, 1994, Exact closed-form geolocation algorithm for Earth survey sensors. *Int. J. Rem. Sens.*, **15**, 3719-3724.
- Peixoto, J.P. and A.H. Oort, 1992, *Physics of Climate*. American Institute of Physics, New York, 520 pp.
- Penuelas, J., and R. Matamala, 1990, Changes in N and S leaf content, stomatal density and specific leaf area of 14 plant species during the last three centuries of CO₂ increase. *J. Exp. Bot.*, **41**, 1119-1124.
- Peterson, D. L. and R.H. Waring, 1994, Overview of Oregon transect ecosystem research project, *Ecol. Appl.* **4**, 211-225.
- Philander, S.G.H., 1990, *El Niño, La Niña, and the Southern Oscillation*. Academic Press. 293 pp.
- Planck, V.G., 1969, The size distribution of cumulus clouds in representative Florida populations. *J. Appl. Meteor.*, **8**, 46-67.
- Pollard, D., and S.L. Thompson, 1995, Use of a land-surface-transfer scheme (LSX) in a global climate model: the response to doubling stomatal resistance. *Global Planet. Change*, **10**, 129-161.
- Potter, C.S., J.T. Randerson, and C.B. Field, 1993, Terrestrial ecosystem production: a process model based on global satellite data. *Global Biogeochem. Cycles.*, **7**, 811-841.
- Prentice, K.C., 1990, Bioclimatic distribution of vegetation for general circulation model studies. *J. Geophys. Res.*, **95**, 11,811-11,830.
- Prentice, I.C., W. Cramer S.P. Harrison, R. Leemans, R.A. Monserud, and A.M. Solomon, 1992, A global biome model based on plant physiology and dominance, soil properties, and climate. *J. Biogeography*, **19**, 117-134.
- Price, J.C., 1987, Calibration of satellite radiometers and the comparison of vegetation indices. *Remote Sens. Environ.*, **21**, 15-27.
- Price, J.C., 1991, Timing of NOAA afternoon passes. *Int. J. Rem. Sens.*, **12**, 193-198.
- Prince, S.D., 1986, Monitoring the vegetation of semi arid tropical rangelands with the NOAA-7 Advanced Very High Resolution Radiometer. In: *Remote sensing and tropical land management*, M. J. Eden, and J. T. Parry, Eds., John Wiley and Sons, Inc., New York.
- Prince, S.D., 1991, Satellite remote sensing of primary production: comparison of results for Sahelian grasslands. *Int. J. Remote Sens.*, **12**, 1301-1311.
- Prince, S.D., and C.O. Justice, eds., 1991, Coarse resolution remote sensing of the Sahelian environment. *Int. J. Remote Sens.*, **12**, 1133-1421.
- Privette, J.L., C. Fowler, G.A. Wick, D. Baldwin, and W.J. Emery, 1995, Effects of orbital drift on advanced very high resolution radiometer products: normalized difference vegetation index and sea surface temperature, *Remote Sens. Environ.*, **53**, 164-171.
- Qi, J., A. Chehbouni, A.R. Huete, Y.H. Kerr, and S. Sorooshian, 1994, A modified soil adjusted vegetation index. *Remote Sens. Environ.*, **48**, 119-126.
- Randall, D.A., P.J. Sellers, J.A. Berry, D.A. Dazlich, C. Zhang, G.J. Collatz, A.S. Denning, S.O. Los, C.B. Field, I.Y. Fung, C.O. Justice, and C.J. Tucker, 1996, A revised land-surface parameterization (SiB2) for GCMs. Part 3: The greening of the Colorado State University General Circulation Model. *J. Climate*, **9**, 738-763.
- Rao, C.R., and J. Chen, 1994, Post-launch calibration of the visible and infrared channels of the advanced very high resolution radiometer on NOAA-7, -9, and -11 spacecraft. NOAA Technical Report NESDIS-78, National Oceanic and Atmospheric Administration, Washington D.C. 20233, 22 pp.
- Reyment, R., and K.G. Jöreskog, 1993, *Applied factor analysis in the natural sciences*. Cambridge University Press, New York, 371 pp.
- Reynolds, R.W., C.K. Folland, and D.E. Parker, 1989, Biases in satellite-derived sea surface temperatures. *Nature*, **341**, 728-731.
- Reuter, D., J. Susskind, and A. Pursch, 1988, First guess dependence of a physically based set of temperature humidity retrievals from HIRS2/MSU data. *J. Atmos. Ocean Tech.*, **5**, 70-83.
- Ropelewski, C.F., and M.S. Halpert, 1987, Global and regional scale precipitation patterns associated with the El Niño Southern Oscillation. *Mon. Wea. Rev.*, **115**, 1606-1626.

BIBLIOGRAPHY

- Ross, J., 1981, *The radiation regime and architecture of plant stands*. Dr. W. Junk Publishers, The Hague, 392 pp.
- Rosborough, G.W., D.G. Baldwin, and W.J. Emery, 1994, Precise AVHRR image navigation. *IEEE Trans. Geosci. Remote Sens.* **32**, 654-657.
- Roujean, J.L., M. Leroy, and P.Y. Deschamps, 1992, A bidirectional reflectance model of the Earth's surface for the correction of remote sensing data. *J. Geophys. Res.*, **18**, 20455-20468.
- Salisbury, F.B., and C. Ross, 1969, *Plant physiology*. Belmont, California, Wadsworth Press, 747 pp.
- Sato, N., P.J. Sellers, D.A. Randall, E.K. Schneider, J. Shukla, J.L. Kinter, Y.T. Hou, and E. Albertazzi, 1989, Effects of implementing the Simple Biosphere Model (SiB) in a general circulation model. *J. Atmos. Sci.*, **46**, 2757-2782.
- Schneider, S.R., D.F. McGinnis, Jr., and J.A. Gatlin, 1981, Use of NOAA-AVHRR visible and near-infrared data for land remote sensing. NOAA Technical Report NES84, NOAA National Earth Satellite Service, Washington D.C., pp 48.
- Sellers, P.J., 1985, Canopy reflectance, photosynthesis, and transpiration. *Int. J. Remote Sens.*, **6**, 1335-1372.
- Sellers, P.J., 1987, Canopy reflectance, photosynthesis and transpiration. II. The role of biophysics in the linearity of their interdependence. *Remote Sens. Environ.*, **21**, 143-183.
- Sellers, P.J., 1992, Biophysical models of landsurface processes. In: *Climate System Modeling*, K.E. Trenberth, ed., Cambridge University Press, New York.
- Sellers, P.J., and F.G. Hall, 1992, FIFE in 1992: Results, scientific gains, and future research directions. *J. Geophys. Res.*, **97**, 19,091-19,109.
- Sellers, P.J., and D. Schimel, 1993, Remote sensing of the land biosphere and biochemistry in the EOS era: Science priorities, methods, and implementation — EOS land biosphere and biogeochemical panels. *Global Planet. Change*, **7**, 279-297.
- Sellers, P.J., Y. Mintz, Y.C. Sud, and A. Dalcher, 1986, A simple biosphere model (SiB) for use with general circulation models. *J. Atmos. Sci.*, **43**, 505-531.
- Sellers, P.J., F.G. Hall, G. Asrar, D.E. Strelbel, and R.E. Murphy, 1988, The First ISLSCP Field Experiment (FIFE). *Bull. Amer. Meteor. Soc.*, **69**, 22-27.
- Sellers, P.J., J.W. Shuttleworth, J.L. Dorman, A. Dalcher, and J.M. Roberts, 1989, Calibrating the simple biosphere model (SiB) for Amazonian tropical forest using field and remote sensing data: Part 1, Average calibration with field data. *J. Appl. Meteor.*, **28**, 727-759.
- Sellers, P.J., J.A. Berry, G.J. Collatz, C.B. Field, and F.G. Hall, 1992a, Canopy reflectance, photosynthesis and transpiration. III. A re-analysis using improved leaf models and a new canopy integration scheme. *Remote Sens. Environ.*, **42**, 187-216.
- Sellers, P.J., M.D. Heiser, and F.G. Hall, 1992b, Relations between surface conductance and spectral vegetation indices at intermediate (100 m² to 15 km²) length scales. *J. Geophys. Res.*, **97**, 19,033-19,059.
- Sellers, P.J., M.D. Heiser, F.G. Hall, S.J. Goetz, D.E. Strelbel, S.B. Verma, R.L. Desjardins, P.M. Schuepp, and J.I. MacPherson, 1991, Effects of Spatial variability in topography, vegetation cover, and soil moisture on area-averaged surface fluxes: A case study using the FIFE 1989 data. *J. Geophys. Res.*, **100**, (D12), 25,607-25,629.
- Sellers, P.J., S.O. Los, C.J. Tucker, C.O. Justice, D.A. Dazlich, G.J. Collatz, and D.A. Randall, 1994, A global 1° by 1° NDVI dataset for climate studies. Part 2: The generation of global fields of terrestrial biophysical parameters from the NDVI. *Int. J. Remote Sens.* **15**, 3519-3545.
- Sellers, P.J., F.G. Hall, H. Margolois, B. Kelly, D. Baldocchi, G. den Hartog, J. Cihlar, M.G. Ryan, B. Goodison, P. Crill, K.J. Ranson, D. Lettenmaier, and D.E. Wickland, 1995, The Boreal Ecosystem-Atmosphere Study (BOREAS): An overview and early results from the 1994 year. *Bull. Am. Met. Soc.*, **76**, 1549-1577.
- Sellers, P.J., D.A. Randall, G.J. Collatz, J.A. Berry, C.B. Field, D.A. Dazlich, C. Zhang, and L. Bounoua, 1996a, A revised land-surface parameterization (SiB2) for GCMs. Part 1: Model Formulation. *J. Climate*, **9**, 676-705.
- Sellers, P.J., S.O. Los, C.J. Tucker, C.O. Justice, D.A. Dazlich, G.J. Collatz, and D.A. Randall, 1996b, A revised landsurface parameterization (SiB-2) for atmospheric GCMs. Part 2: The generation of global fields of terrestrial biophysical parameters from satellite data. *J. Climate*, **9**, 706-737.
- Sellers, P.J., L. Bounoua, G.J. Collatz, D.A. Randall, D.A. Dazlich, S.O. Los, J.A. Berry, I. Fung, C.J. Tucker, C.B. Field, and T.G. Jensen, 1996c, Comparison of radiative and physiological effects of doubled atmospheric CO₂ on climate. *Science*, **271**, 1402-1406.
- Shah, T., and E.T. Kanemasu, 1994, First ISLSCP Field Experiment Leaf Area Index and PAR Determined from KSU Light Bar Measurements Dataset. In: D.E. Strelbel, D.R. Landis, K.F. Huemmrich, and B.W. Meeson (1994), *Collected Data of The First ISLSCP Field Experiment*, Vol. 1: Surface Observations and Non-Image Datasets. Published on CD-ROM by National Aeronautics and Space Administration. Available on CD-ROM and on-line [<http://www-eosdis.ornl.gov>] from the ORNL DAAC, Oak Ridge National Laboratory, Oak Ridge, Tennessee, U.S.A.

- Shuttleworth, J.W., J.H.C. Gash, C.R. Loyd, C.J. Moore, J. Roberts, A. De O. Marques Filho, G. Fish, V. De Paula Silva Filho, M. De Nazaré Góes Ribeiro, L.C.B. Molion, L.D. De Abreusa, C.A. Nobre, O.M.R. Cabral, S.R. Patel, and J. Carvalho De Moraes, 1984a, Eddy correlation of energy partition for Amazonian forest. *Quart. J. Roy. Meteor. Soc.*, **110**, 1143-1162.
- Shuttleworth, J.W., J.H.C. Gash, C.R. Loyd, C.J. Moore, J. Roberts, A. De O. Marques Filho, G. Fish, V. De Paula Silva Filho, M. De Nazaré Góes Ribeiro, L.C.B. Molion, L.D. De Abreusa, C.A. Nobre, O.M.R. Cabral, S.R. Patel, and J. Carvalho De Moraes, 1984b, Observations of radiation exchange above and below Amazonian forest. *Quart. J. Roy. Meteor. Soc.*, **110**, 1163-1169.
- Singh, S.M., 1988, Simulation of solar zenith angle effect on global vegetation index (GVI) data. *Int. J. Remote Sens.*, **9**, 237-248.
- Smith, G.R., R.H. Levin, P. Abel, and H. Jacobowitz, 1988, Calibration of the solar channels of the NOAA-9 AVHRR using high altitude aircraft measurements. *J. Atmos. and Ocean. Technol.*, **5**, 631-639.
- Soufflet, V., D. Tanré, A. Begue, A. Podaire, and P.Y. Deschamps, 1991, Atmospheric effects in NOAA-AVHRR imagery over Sahelian regions. *Int. J. Remote Sens.*, **12**, 1189-1203.
- Statistical Sciences, 1993, *S-PLUS Guide to Statistical and Mathematical Analysis, Version 3.3*. Seattle, Statsci/Mathsoft, Inc.
- Staylor, W.F., 1990, Degradation rates of the AVHRR visible channel from the NOAA-6, -7, and -9 Spacecraft. *J. Atmos. Ocean. Tech.*, **7**, 411-423.
- Steven, M.D., P.V. Biscoe, and K.W. Jaggard, 1983, Estimation of sugar beet productivity from reflection in the red and infrared spectral bands. *Int. J. Remote Sens.*, **4**, 325-334.
- Stolarski, R.S., P. Bloomfield, R.D. McPeters, and J.R. Herman, 1991, Total ozone trends deduced from Nimbus-7 TOMS data. *Geophys. Res. Lett.*, **19**, 159-162.
- Stowe, L.L., E.P. McClain, R.M. Carey, P.P. Pellegrino, G.G. Gutman, P. Davis, C. Long, and S. Hart, 1991, Global distribution of cloud cover derived from NOAA-AVHRR operational satellite data. *Adv. Space Res.*, **3**, 51-54.
- Stowe, L.L., R.M. Carey, and P.P. Pellegrino, 1992, Monitoring the Mt. Pinatubo aerosol layer with NOAA-11 AVHRR data. *Geophys. Res. Lett.*, **19**, 159-162.
- Susskind, J., J. Rosenfeld, D. Reuter, and M.T. Chahine, 1984, Remote sensing of weather and climate parameters from HIRS2/MSU on TIROS-N. *J. Geophys. Res.*, **89**, 4677-4697.
- Swain, P.H., and S.M. Davis, 1978, *Remote Sensing: The Quantitative Approach*. McGraw Hill, New York.
- Tanré, D., C. Deroo, P. Duhaut, M. Herman, J.J. Morcette, J. Perbos, and P.Y. Deschamps, 1986, Simulation of the satellite signal in the solar spectrum (5 S), Users Guide. Laboratoire d'Optique Atmosphérique, U.S.T.L., 59655, Villeneuve d'Ascq Cdex, France.
- Tanré D., B.N. Holben, and Y.J. Kaufman, 1992, atmospheric correction algorithms for NOAA-AVHRR products: Theory and application. *IEEE Trans. Geosci. Remote Sens.*, **30**, 231-248.
- Tans, P.P., I.Y. Fung, and T. Takahashi, 1990, Observational constraints on the global atmospheric CO₂ budget. *Science*, **247**, 1431-1438.
- Tarpley, D., Schneider, S.R., and Money, R.L., 1984, Global vegetation indices from the NOAA-7 meteorological satellite. *J. Climate Appl. Meteor.*, **23**, 491-494.
- Teillet, P.M., and B.N. Holben, 1994, Towards operational radiometric calibration of NOAA-AVHRR imagery in the visible and near-infrared channels. *Can. J. Remote Sens.*, **20**, 1-10, 1994.
- Tissue, D.T., R.B. Thomas, and B.R. Strain, 1993, Long-Term Effects of Elevated CO₂ and Nutrients on Photosynthesis and RuBisCO in Loblolly Pine Seedlings. *Plant Cell Environ.*, **16**, 859-865.
- Tolsma, D.J., 1989, On the Ecology of Savanna Ecosystems in Southeastern Botswana. Ph.D. dissertation, Vrije Universiteit, Amsterdam, 243 pp.
- Townshend, J.R.G., and C.J. Tucker, 1981, Utility of AVHRR of NOAA-6 and -7 for vegetation mapping. Matching Remote Sensing Technologies and their Applications. Proceedings of an international conference, London, December 1981, 97 pp.
- Townshend, J.R.G., and C.O. Justice, 1990, The spatial variation of vegetation changes at very coarse scales. *Int. J. Remote Sens.*, **11**, 149-157.
- Townshend, J.R.G., T.E. Goff, and C.J. Tucker, 1985, Multi-temporal dimensionality of meteorological satellite data at continental scales. *IEEE Trans. Geosci. Remote Sens.*, **23**, 881-887.
- Trenberth, K.E., 1991, General characteristics of El Niño Southern Oscillation. In: *Teleconnections Linking Worldwide Climate Anomalies*, M.H. Glantz, R.W. Katz, and N. Nicholls, eds., Cambridge University Press, New York, 13-42.
- Tucker, C.J., 1979, Red and photographic infrared linear combinations monitoring vegetation. *Remote Sens. Environ.*, **8**, 127-150.
- Tucker, C.J., 1996, History of the use of AVHRR data for land applications. In: *Advances in the Use of NOAA-AVHRR Data for Land Applications*. G. D'Souza, A.S. Belward and J.P. Malingreau, eds., ECSC, EEC, EAEC, Brussels and Luxembourg, 1-19.

BIBLIOGRAPHY

- Tucker, C.J., and M. Matson, 1985, Determination of volcanic dust deposition of El Chichon from ground and satellite data. *Int. J. Remote Sens.*, **6**, 619-627.
- Tucker, C.J., and P.J. Sellers, 1986, Satellite remote sensing of primary production. *Int. J. Remote Sens.*, **7**, 1395-1416.
- Tucker, C.J., B.N. Holben, J.H. Elgin, and J.E. McMurtrey, 1981, Remote sensing of total dry matter accumulation in winter wheat. *Remote Sens. Environ.*, **11**, 171-189.
- Tucker, C.J., C.L. VanPraet, E. Boerwinkel, and A. Gaston, 1983, Satellite remote sensing of total dry accumulation in the Senegalese Sahel. *Remote Sens. Environ.*, **13**, 461-474.
- Tucker, C.J., A. Gatlin, and S.R. Schneider, 1984, Monitoring vegetation in the Nile Delta with NOAA-6 and NOAA-7 AVHRR. *Photogram. Eng. Remote Sens.*, **50**, 53.
- Tucker, C.J., J.R.G. Townshend, and T.E. Goff, 1985a, African land-cover classification using satellite data. *Science*, **227**, 369-375.
- Tucker, C.J., C.L. VanPraet, M.J. Sharman, and G. van Iltersum, 1985b, Satellite remote sensing of total herbaceous biomass production in the Senegalese Sahel: 1980-1984. *Remote Sens. Environ.*, **17**, 233-249.
- Tucker, C.J., I.Y. Fung, C.D. Keeling, and R.H. Gammon, 1986a, The relationship of global green leaf biomass to atmospheric CO₂ concentrations. *Nature*, **319**, 159-199.
- Tucker, C.J., C.O. Justice, and S.D. Prince, 1986b, Monitoring the grasslands of the Sahel 1984-1985. *Int. J. Remote Sens.*, **7**, 1571-1582.
- Tucker, C.J., H.E. Dregne, and W.W. Newcomb, 1991a, Expansion and contraction of the Sahara Desert from 1980 to 1990. *Science*, **253**, 299-301.
- Tucker, C.J., W.W. Newcomb, S.O. Los, and S.D. Prince, 1991b, Mean and inter-year variation of growing-season normalized difference vegetation index for the Sahel 1981-1989. *Int. J. Remote Sens.*, **12**, 1133-1135.
- Tucker, C.J., H.E. Dregne, and W.W. Newcomb, 1994, AVHRR datasets for determination of desert spatial extent. *Int. J. Remote Sens.*, **15**, 3547-3565.
- Tukey, J.W., 1977, *Exploratory data analysis*. Addison-Wesley, Reading, Massachusetts, 688 pp.
- United Nations Conference on Desertification (UNCOD), 1977, *Desertification: Its Causes and Consequences*. (Nairobi, Kenya: Secretariat of United Nations Conference on Desertification, Pergamon Press).
- Van de Griend, A.A., and M. Owe, 1994, The influence of polarization on canopy transmission properties at 6.6 GHz and implications for large-scale soil moisture monitoring in semi-arid environments. *IEEE Trans. Geosci. Remote Sens.*, **32**, 409-415.
- Van Straaten, L.M.J.U., 1973, Eustatische zeespiegelbewegingen en verschuiving der continenten. *Kon. Ned. Akad. Wetensch. Versl. gew. verg. Afd. Natuurk.* **82**, (1), 6-8.
- Veenendaal, E.M., 1991, *Adaptive Strategies of Grasses in a Semi-Arid Savanna in Botswana*, Ph.D. dissertation, Vrije Universiteit, Amsterdam, 170 pp.
- Verhoef, W., 1984, Light scattering by leaf layers with application to canopy reflectance modeling: the SAIL model. *Remote Sens. Environ.*, **16**, 125-141.
- Vermote, E.F., and Y.J. Kaufman, 1995, Absolute calibration of AVHRR visible and near-infrared channels using ocean and cloud views. *Int. J. Rem. Sens.*, **16**, 2317-2340.
- Vermote, E.F., D. Tanré, J.L. Seuz, M. Herman, and J.J. Moret, 1995, 6S user guide version 1. Department of geography, University of Maryland at College Park, 216 pp.
- Vermote, E.F., N. El Saleous, Y.J. Kaufman, and E. Dutton, 1994, Data preprocessing: Stratospheric aerosol perturbing effect on the remote sensing of vegetation: Correction method for the composite NDVI after the Pinatubo eruption. *Société Internationale de Photogrammétrie et de télédétection (ISPRS) Sixième Symp. Int.*, Val d'Isere, France, 151-158.
- Wielicki, B. A., and R.M. Welch, 1986, Cumulus cloud properties derived using Landsat satellite data. *J. Clim. Appl. Meteor.*, **25**, 261-276.
- Wilson, M.F., and A. Henderson-Sellers, 1985, A global archive of landcover and soils data for use in general circulation models. *J. Climatology*, **5**, 119-143.
- Woodward, F.I., 1987a, Stomatal numbers are sensitive to increases in CO₂ from pre-industrial levels. *Nature*, **327**, 617-618.
- Woodward, F.I., 1987b, *Climate and Plant Distribution*. Cambridge University Press, New York, 174 pp.
- Woodward, F.I., T.M. Smith, and W.R. Emanuel, 1995, A global land primary productivity and phytogeography model. *Global Biogeochem. Cycles*, **9**, 471-490.
- Xue, Y., and J. Shukla, 1991, The influence of land properties on Sahel Climate. Part I: Desertification. *J. Climate*, **6**, 2232-2245.
- Yates, H.W., J.D. Tarpley, S.R. Schneider, D.F. McGinnis, and R.A. Scofield, 1984, The role of meteorological satellites in agricultural remote sensing. *Remote Sens. Environ.*, **14**, 219-233.
- Zobler, L., 1986, A world soil file for global climate modeling. NASA Technical Memorandum 87802, NASA, Washington D.C. 20546, 35 pp.

Appendix A

Calibration Adjustment of the NDVI Without Recourse to Component Channels 1 and 2 Data

Slightly revised from publication by S.O. Los, 1993, Calibration Adjustment of the NOAA-AVHRR Normalized Difference Vegetation Index without Recourse to Component Channels 1 and 2 Data, *Int. J. Remote Sens.*, **14**, 1907-1917.

Abstract

The effect of sensor degradation in the Advanced Very High Resolution Radiometer (AVHRR) channels 1 and 2 on the Normalized Difference Vegetation Index (NDVI) was established. Three models were developed to adjust the NDVI for sensor degradation without recourse to component channels 1 and 2 data. The models were verified with data obtained by the AVHRR on board NOAA-7, -9, and -11. Two models provide accurate results in some cases, but perform less well in others. A third model is applicable to all cases investigated, and it estimates the effect of sensor degradation with a maximum root mean square error of 0.002 NDVI. The remaining error depends on surface characteristics and the magnitude of the sensor degradation, and cannot be accounted for without the component channels 1 and 2 data.

A.1 Introduction

The Normalized Difference Vegetation Index (NDVI) is based on channel 1 (red) and channel 2 (infrared) data sensed by the Advanced Very High Resolution Radiometer (AVHRR) on board the NOAA-7, -9, and -11 satellites and has been related to photosynthetic active radiation absorbed by vegetation (Kumar and Monteith 1982, Sellers 1985, Tucker and Sellers 1986). Because of this characteristic it is widely used to assess the state of vegetation, both quantitatively and qualitatively (Tucker 1979, Tucker *et al.* 1985b, Justice 1986, Prince and Justice 1991).

The AVHRR is not equipped with onboard calibration which results in a gradual change of the NDVI over time and hampers comparison of data between years. Espe-

cially large discontinuities may occur between successive AVHRR instruments.

Several studies have focused on sensor degradation in individual channels (Kaufman and Holben 1993, Holben *et al.* 1990, Staylor 1990, Teillet and Holben 1994, Brest and Rossow 1991, Smith *et al.* 1988). After establishing the degradation in channels 1 and 2, data can be corrected and the NDVI recalculated. However, in view of the large data quantities that need to be handled to process individual channel data into monthly NDVI composites (Holben 1986), this may not always be a feasible option. In cases where NDVI imagery is used for early warning of disasters by comparison of imagery between years (Hielkema 1990, Hutchinson 1991), no individual channel data are available, and a correction is needed that employs NDVI data only.

A first-order correction to adjust low NDVI values ($0 < \text{NDVI} < 0.3$) was suggested by Holben *et al.* (1990) and was applied in a study on desert margins by Tucker *et al.* (1991a, 1994). The NDVI is adjusted by adding a constant value, which is calculated as the average deviation in NDVI of different pairs of channels 1 and 2 data, or as the difference in NDVI between different periods from assumed invariant targets such as deserts.

In this paper the effect of sensor degradation over a wider range of NDVI ($0 < \text{NDVI} < 0.6$) is studied and the possibility adjusting the NDVI without use of the component channels 1 and 2 data is investigated. In addition to the method proposed by Holben *et al.* (1990), two alternative models were developed, and their ability to describe the effect of sensor degradation on the NDVI investigated.

In addition to sensor degradation, other effects, *e.g.*, atmospheric effects, sub-pixel cloud contamination, and viewing geometry, affect the surface signal, in various cases to a larger extent than sensor degradation (Tanré *et al.* 1992, Soufflet *et al.* 1991, Holben *et al.* 1986, Kimes

1983). This article is mainly concerned with the adjustment for sensor degradation of the signal received by the AVHRR, regardless of the degree of contamination of the signal.

A.2 Data

Three datasets were obtained from different years and sensors, representative for different types of surface cover. Each dataset consists of the maximum NDVI of a 10- to 18-day period, with the corresponding channels 1 and 2 values. No cloud screening was applied.

The first dataset (NOAA-7, 21-30 August 1982, $n = 5185$) covers a transect of approximately 10 pixels wide through southern Africa, ranging from the equatorial zone to the coast (0° N, 30° E – 10° S, 30° E – 15° S, 32° E – 30° S, 32° E). NDVI values vary between -0.1 and 0.5. The data were heavily affected by clouds, part of which still showed after the compositing. Also included in this set were pixels containing surface water and cloud shadows.

The second dataset (NOAA-9, 21-30 August 1985, $n = 3816$) covers a transect of approximately 15 pixels wide through west Africa ranging from the desert into the equatorial zone (20° N, 20° E – 5° N, 20° E). Most of the cloud contamination was removed by the compositing. NDVI values ranged from 0.0 to 0.6.

The third dataset (NOAA-11, 13-30 March 1989, $n = 3200$) covers a transect of 10 pixels wide, almost similar to the second dataset (20° N, 20° E – 0° , 20° E). Most cloud cover was removed by compositing. The NDVI varied between 0.0 and 0.6.

A.3 Theory

AVHRR data are provided by NOAA on level 1B tapes in digital format. Digital data are converted into radiance, normalized radiance, or reflectance value using preflight calibration constants that are on tape. Generally a normalization with respect to the irradiance in the red and infrared parts of the solar spectrum is preferred (Price 1987, Goward *et al.* 1991). The conversion of digital counts into reflectances is given by Kidwell (1995).

$$\rho_{i,p} = \gamma_{i,p}(C_i - C_{0,i,p}) \cos \theta = L_{i,p}^N \cos \theta. \quad (\text{A.1})$$

Where $\rho_{i,p}$ is the preflight calibrated reflectance, $\gamma_{i,p}$ is the preflight calibration coefficient, C_i is the integer count read from the tape, $C_{0,i,p}$ is the preflight calibration offset, θ is the solar zenith angle $L_{i,p}$ is the normalized radiance. Subscript i refers to either channel 1 or channel 2, and subscript p indicates that preflight calibration coefficients are used. Note that $\gamma_{i,p}$ is the slope and $\gamma_{i,p}C_{0,i,p}$ is the offset.

The preflight calibration coefficients are assumed constant over time. However, both in channel 1 and channel 2 the sensitivity has degraded during the lifetime of NOAA-7, -9, and -11 (Smith *et al.* 1988, Holben *et al.* 1990, Staylor 1990, Teillet *et al.* 1990, Brest and Rossow 1991, Kaufman and Holben 1993). Equation A.1 therefore should be expressed as

$$\rho_{i,c} = \gamma_{i,c}(C_i - C_{0,i,c}) \cos \theta = L_{i,c}^N \cos \theta \quad (\text{A.2})$$

with the adjusted calibration coefficient, $\gamma_{i,c}$, and adjusted offset or deep space count, $C_{0,i,c}$, variant over time (Appendix A.7). Equations A.1 and A.2 assume a linear relationship between digital counts and reflectance. This assumption is implicit in the derivation of calibration coefficients.

Table A.1: Calibration coefficients from Holben *et al.* (1990) and Kaufman and Holben (1993) to correct AVHRR channels 1 and 2 reflectances for sensor degradation. r_1 , r_2 are ratios between preflight and true calibration coefficient for channels 1 and 2. $\Delta C_{0,1}$, $\Delta C_{0,2}$ are differences between preflight, and true deep space offset. ΔNDVI is the average error in preflight calibrated NDVI. Table is updated with values from Holben. (personal communication), ΔNDVI values were recalculated from reflectances, using the same conditions as Kaufman and Holben.

Period	r_1	r_2	$\Delta C_{0,1}$	$\Delta C_{0,2}$	ΔNDVI
8 - 1981	0.909	0.872	-3.8	-5.4	0.019
8 - 1982	0.865	0.801	-3.8	-5.1	0.036
8 - 1983	0.839	0.771	-3.6	-4.8	0.043
8 - 1984	0.813	0.753	-3.2	-4.6	0.038
2 - 1985	0.947	0.884			0.032
8 - 1985	0.920	0.858	-1.8	-3.8	0.030
2 - 1986	0.894	0.840			0.028
8 - 1986	0.870	0.819	-1.7	-3.2	0.023
8 - 1987	0.818	0.802	-1.6	-3.0	0.011
2 - 1988	0.784	0.790			0.004
8 - 1988	0.781	0.781	-1.6	-2.9	-0.005
2 - 1989	0.785	0.692	1.2	1.0	0.059
8 - 1989	0.790	0.78	1.2	1.0	0.067
2 - 1990	0.775	0.668	1.2	1.0	0.072
8 - 1990	0.798	0.683	1.2	1.0	0.075
2 - 1991	0.834	0.742	-0.2	0	0.058
8 - 1991	0.833	0.746	-0.2	0	0.054

The corrected normalized radiances can be calculated from preflight calibrated values by combining equations A.1 and A.2:

$$L_{i,c}^N = \frac{1}{r_i}(L_{i,p}^N + \gamma_{i,p}\Delta C_{0,i}) = \frac{1}{r_i}(L_{i,p} + \Delta_i) \quad (\text{A.3})$$

where r_i is the ratio between the preflight and true calibration coefficient, $\gamma_{i,p}/\gamma_{i,c}$, and Δ_i is the difference

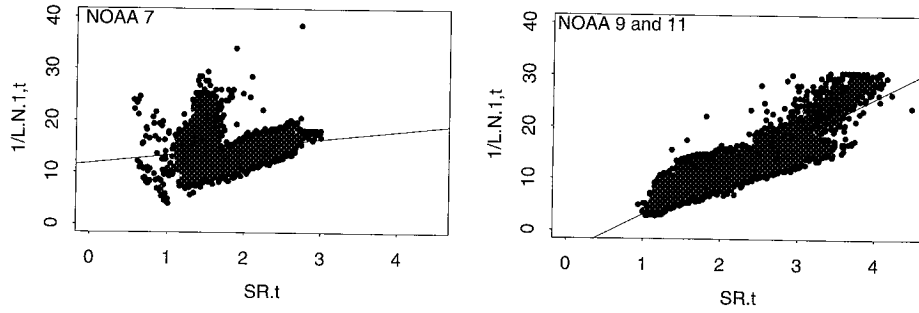


Figure A.1: Relationship between the reciprocal of visible reflectance $1/L_{1,t}^N$ and true Simple Ratio SR_c for the datasets derived from the different transects through Africa (see text). a: Data from transect through southern Africa, August 21-30 1982 NOAA-7, $1/L_{1,t}^N = 11.98 + 1.541 * SR_c$, $R = 0.17$. b: Data from transect through West Africa, August 21-30 1985, NOAA-9, and March 13-30, NOAA-11, $1/L_{1,t}^N = 4.35 + 7.48 * SR_c$, $R = 0.93$

between the preflight and true deep space offset multiplied by the preflight calibration $\Delta_i = \gamma_{i,p} \Delta C_{0,i} = \gamma_{i,p} (C_{0,i,p} - C_{0,i,c})$. For this study values for r_i and $\Delta C_{0,i}$ published by Holben *et al.* (1990), and Kaufman and Holben (1991), were used because these coefficients are available for the entire active period of NOAA-7, -9, and -11 (Tables A.1 and A.2).

A.3.1 Effect of Sensor Degradation on NDVI

The NDVI is given by

$$NDVI = \frac{\rho_2 - \rho_1}{\rho_2 + \rho_1} = \frac{L_2^N - L_1^N}{L_2^N + L_1^N}, \quad (A.4)$$

where ρ_2 is the infrared reflectance, ρ_1 the red reflectance, L_2^N the infrared normalized radiance, and L_1^N the red normalized radiance.

Three methods are discussed that relate the NDVI corrected for sensor degradation, $NDVI_c$, to the preflight calibrated $NDVI_p$ without recourse to component channels 1 and 2 data. The first method assumes the difference in $NDVI_p$ and $NDVI_c$ approximately constant over the entire range of NDVI. The relation between $NDVI_p$ and $NDVI_c$ is then given by

$$NDVI_c \approx NDVI_p + \sum_{i=1}^n \frac{\Delta NDVI_i}{n}, \quad (A.5)$$

with $\Delta NDVI = NDVI_c - NDVI_p$ and n is the number of observations. The $\Delta NDVI$ in equation A.5 can be calculated from the average difference in NDVI between a number of selected, calibrated and preflight calibrated, channels 1 and 2 combinations representing different surfaces (Holben *et al.* 1990, Kaufman and Holben 1993), or as the change in NDVI over time measured from invariant targets such as deserts (Tucker *et al.* 1991, 1994).

The model represented by equation A.5 is referred to as model 1.

Alternative approaches to approximate the calibrated $NDVI_c$ from $NDVI_p$ can be found by reworking equation A.4:

$$L_{2,p}^N = L_{1,p}^N \frac{1 + NDVI_p}{1 - NDVI_p} = L_{1,p}^N SR_p \quad (A.6)$$

where SR is the simple ratio, $SR = L_2^N / L_1^N$. Combining equations A.3 and A.4 yields

$$NDVI_c = \frac{(L_{2,p} + \Delta_2)/r_2 - (L_{1,p} + \Delta_1)/r_1}{(L_{2,p} + \Delta_2)/r_2 + (L_{1,p} + \Delta_1)/r_1}, \quad (A.7)$$

and substituting $L_{2,p}^N$ in equation A.7 with equation A.6 yields

$$NDVI_c = \frac{r_1(SR_p + \Delta_2/L_{1,p}^N) - r_2(SR_p + \Delta_1/L_{1,p})}{r_1(SR_p + \Delta_2/L_{1,p}^N) + r_2(SR_p + \Delta_1/L_{1,p})}. \quad (A.8)$$

Equation A.8 must be written in a form that is independent of $L_{1,p}^N$. This is done in two ways. The first way approximates equation A.8 by neglecting the difference between the preflight calibration offset and the deep space count: $\Delta_1 \approx \Delta_2 \approx 0$. Equation A.8 then becomes

$$NDVI_c \approx \frac{r_1 SR_p - r_2}{r_1 SR_p + r_2}. \quad (A.9)$$

This equation is referred to as model 2.

The second way to approximate equation A.8 is by expressing $L_{1,p}^N$ in terms of NDVI as suggested by figure A.1. This avoids neglecting the difference between the preflight calibration offset and the deep space count. Figure A.1 shows channel 1 normalized radiances $L_{1,p}^N$ as a function of the simple ratio, SR_c , for two cases. The 1982

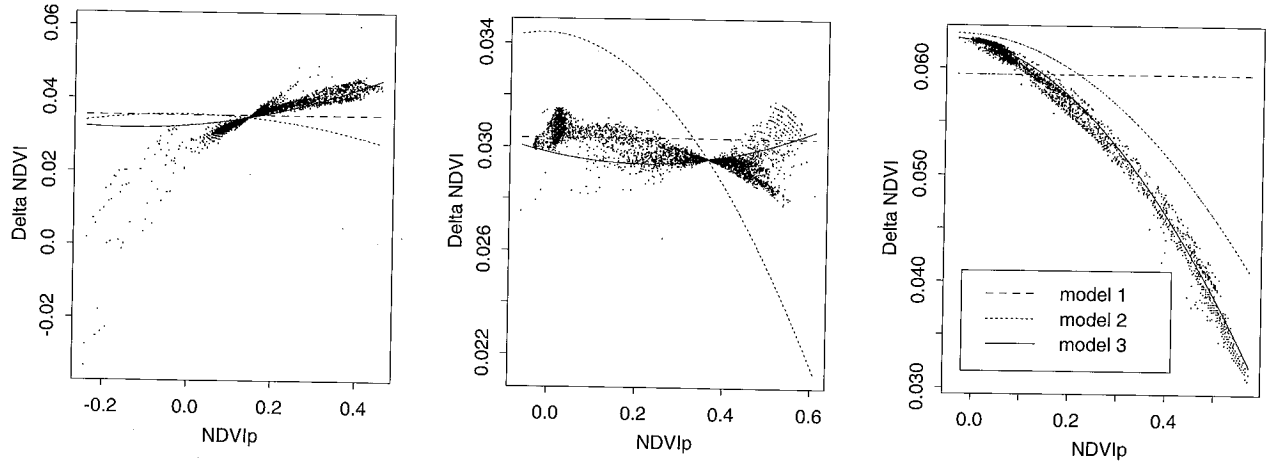


Figure A.2: Deviations of the preflight calibrated NDVI from the desert calibrated “true” NDVI (ΔNDVI) for the three datasets of figure A.1, as well as the approximated deviations from the three models described by equations A.5 (ΔNDVI approximated by a constant), A.9 (ΔNDVI approximated by neglecting differences in the offset) and the combination of A.8 and A.10 (ΔNDVI approximated by use of a relation between SR and $1/L_{1,p}^N$).

(NOAA-7) data show a weak linear relation ($R=0.17$) caused by values deviating from the linear trend at low NDVI. The 1985 (NOAA-9) and 1989 (NOAA-11) data show an identical trend and are combined to obtain a relation between $1/L_{1,p}^N$ and SR using linear regression,

$$\frac{1}{L_{1,c}^N} \approx a + b \times \text{SR}_c, \quad (\text{A.10})$$

with $a = -4.34$ and $b = 7.48$, and the correlation coefficient $R = 0.93$. Using the same constants a and b for the relationship between $L_{1,p}^N$ and SR_p introduces an error smaller than the error in the approximation itself. The combination of equations A.10 and A.8 is referred to as model 3.

A.4 Verification

NDVI values adjusted for sensor degradation by the models derived in the previous section were compared with NDVI values calculated from individually calibrated channels. Data from 1982, 1985, and 1989 were used, as well as a generated dataset for the entire active period of operation of NOAA-7, -9, and 11.

In figure A.2, differences between adjusted and preflight calibrated NDVI values, $\Delta\text{NDVI} = \text{NDVI}_c - \text{NDVI}_p$, are plotted against preflight calibrated NDVI_p for the NOAA-7, -9, and -11 datasets. ΔNDVI values obtained from individually corrected channels appear as a scatter of points along a trend. ΔNDVI values obtained by models 1, 2, and 3 are shown as lines. For all cases, model 3 follows the trend in the scatter closest. In specific cases model 1 (in the case of 1985, NOAA-9) or model 2 (in the case of 1989, NOAA-11) describe this trend al-

most equally well, in other cases large deviations occur especially at high NDVI values.

To establish the accuracy of the methods over the entire period of operation of NOAA-7, -9, and -11, a dataset was generated with calibrated channels 1 and 2 values. This was done by using three end members representing different surface conditions with typical reflectance in channels 1 and 2; vegetation ($L_{v,1}^N = 0.04$, $L_{v,2}^N = 0.23$), dark soil ($L_{d,1}^N = 0.04$, $L_{d,2}^N = 0.05$), and bright soil ($L_{b,1}^N = 0.4$, $L_{b,2}^N = 0.42$). For 60 data pairs the end members were mixed with fractions determined by random numbers (ran) between 0 and 1:

$$L_i^N = \frac{\text{ran}_1^2 L_{v,i} + \text{ran}_2^2 L_{d,i} + \text{ran}_3^2 L_{b,i}}{\text{ran}_1^2 + \text{ran}_2^2 + \text{ran}_3^2}. \quad (\text{A.11})$$

For the 60 data pairs the effect of sensor degradation on preflight calibration was simulated using the inverse of equation A.3. Starting at January 1981 and ending November 1991, sensor degradation was simulated every other month. The NDVI affected by sensor degradation was calculated and the three models were applied to adjust the degraded NDVI values. The adjusted NDVI values were compared to the non-degraded NDVI data. The results are summarized in figure A.3.

Figure A.3.a shows the effect of each of the models on the average of the 5 lowest NDVI values in the dataset, figure A.3.b shows the effect on the average of all data, and figure A.3.c shows the effect on the average of the 5 highest NDVI values. The goodness of fit of the models is shown in figure A.3.d by means of the Root Mean Square (RMS):

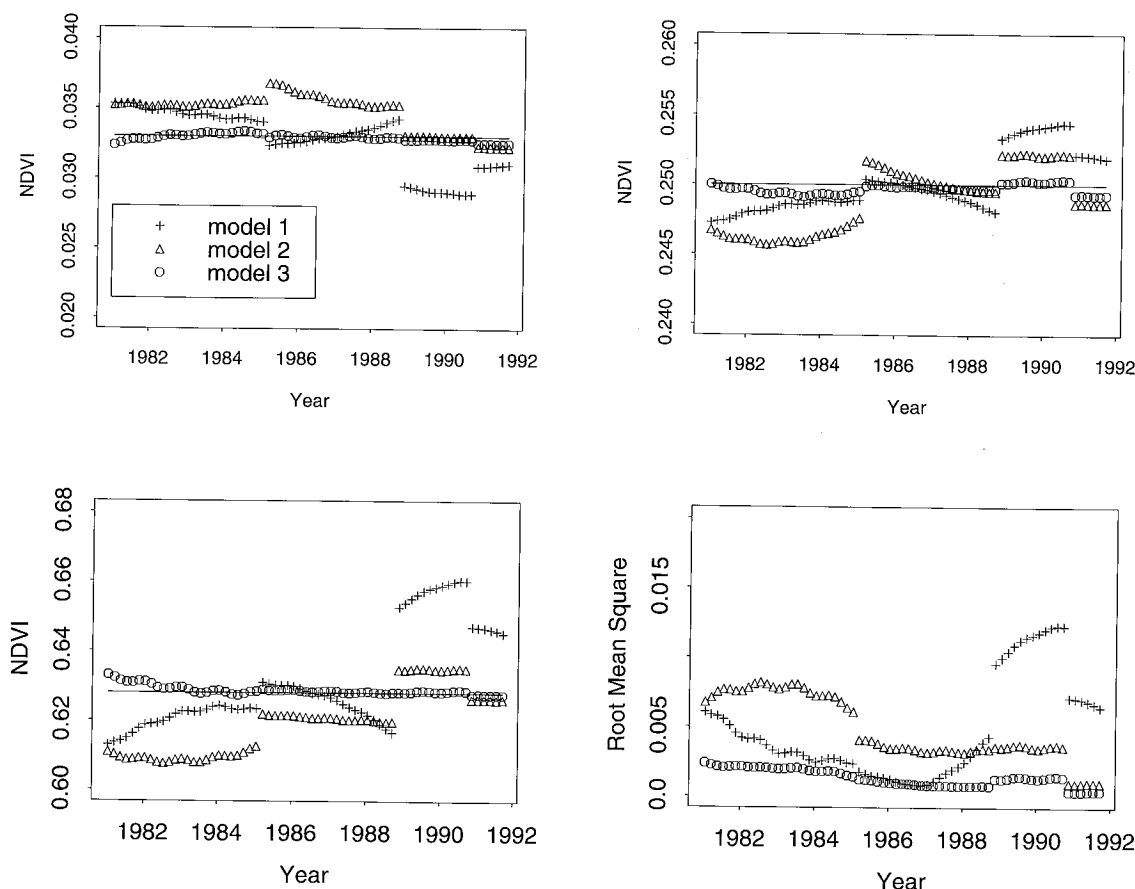


Figure A.3: Comparison of models for the entire active period of NOAA-7, -9 and -11 with generated dataset. Sensor degradation was applied to the generated dataset using equation (A.3), and models 1, 2, and 3 were used to adjust the degraded $NDVI_p$, (a) average NDVI of 5 lowest values in the dataset as a function of time (line is correct NDVI). (b) Average over entire generated dataset (line is correct NDVI). (c) Average NDVI of 5 highest values in the dataset (line is correct NDVI). (d) RMS values to indicate goodness of fit over time. Maximum RMS of model 3 is 0.002 (NOAA-7), minimum RMS = 0.0003 for NOAA-11. A small annual signal is apparent in the data as a result of neglecting the Earth-Sun distance R (equation A.13)

A.5 Discussion

The accuracy of the approximation to adjust the NDVI for sensor degradation without use of component channels 1 and 2 data depends not only on the accuracy of the method used for correction, but also on the accuracy with which sensor degradation can be determined. Holben *et al.* (1990) estimate that sensor degradation in the AVHRR can be estimated with an absolute accuracy of 5–10 percent and a relative accuracy of 0.3–1.0 percent. The order of magnitude of the relative error introduced by model 3 is much smaller, about 0.0003 NDVI to 0.002 NDVI (0.01–0.7 per cent on an average NDVI of 0.3).

Figure A.2.a shows that model 3 applies less well in situations where channels 1 and 2 values are both low and channel 1 > channel 2 ($NDVI < 0$, $SR < 1$). These values are generally associated with dark surfaces such as open water bodies or areas with cloud shadows, and are of minor importance to the study of vegetation.

The results support the conclusions drawn from the verification of the 1982, 1985, and 1989 datasets. Model 3 is generally applicable, and only in specific cases can the same accuracy be obtained by the other two models. The largest deviations tend to occur at high NDVI values. The accuracy of the adjustment of the preflight calibrated NDVI is dependent on the magnitude of the difference in deep space count $\Delta C_{0,i}$. For example, the NDVI from NOAA-7, where the magnitude of $\Delta C_{0,i}$ is largest, cannot be estimated as accurately as the NDVI from NOAA-9 or -11.

$$RMS = \sqrt{\sum_{j=1}^n \frac{(NDVI_p - NDVI_c)^2}{(n-1)}} \quad (A.12)$$

Goward *et al.* (1991) discuss the influence of random errors on the NDVI under different illumination conditions. When these errors are larger than the deviation due to sensor degradation, calibration of the NDVI becomes less meaningful. The magnitude of the random error for AVHRR-Local Area Coverage (LAC) data due to the error contributions of one channel varies between 0.0009 NDVI for high NDVI and high illumination conditions, and 0.01 for low NDVI and low illumination conditions. For AVHRR Global Area Coverage (GAC) data this error is reduced because reflectance values are calculated as the average of 4 LAC pixels. The random error in GAC NDVI will vary between 0.00007 and 0.007. In most cases this value is smaller than the improvement of model 3 over model 1 or 2. Preference of model 3 over model 1 or 2 is therefore justified even in cases of low illumination conditions.

Table A.2: Preflight Calibration gain α ($W \mu m^{-1} sr^{-1} m^{-2}$) and solar flux F_0 ($W \mu m^{-1} m^{-2}$) at Sun-Earth distance of 1 Astronomical Unit (AU) for channels 1 and 2 of the NOAA-AVHRR. Preflight calibration for NOAA-11 was changed on 27 September 1990.

AVHRR	α_1	α_2	$F_{0,1}$	$F_{0,2}$
NOAA-7	0.56	0.35	1649	1040
NOAA-9	0.55	0.36	1629	1043
NOAA-11 (old)	0.47	0.28	1630	1053
NOAA-11 (new)	0.49	0.30	1630	1053

A.6 Conclusion

It is possible to accurately adjust the NDVI for sensor degradation without recourse to component channels 1 and 2 data. The most accurate method is applicable over the entire range of NDVI generally associated with land surfaces ($0 < NDVI < 0.6$). The method was verified with data from the AVHRR on board NOAA-7, -9, and -11. Although the approximation does not result in the same accuracy as a correction applied to data from individual channels, the method provides a quick and easy means to correct the NDVI, and allows for a direct comparison of data from different sensors and periods of time. The method does not provide the same improvement over dark surfaces, such as shaded areas and open water. However, this limitation is of little concern for the study of vegetation dynamics.

Acknowledgments

I would like to thank Brent Holben and Sam Goward for advice and discussions and Steve Prince and Chris Justice

for critical reading of the manuscript and their comments for improvement.

A.7 Appendix

The calibration coefficient $\gamma_{i,p}$ is a function of the gain $\alpha_{i,p}$ ($W \mu m^{-1} sr^{-1} m^{-2}$), which is sensor dependent, and the incoming solar flux $F_{0,i}$ ($W \mu m^{-1} m^{-2}$) at the top of the atmosphere (Table A.2).

$$\gamma_{i,p} = \frac{\alpha_{i,p} \pi}{F_{0,i}} R^2 \quad (A.13)$$

The solar flux changes as a function of the Sun-Earth distance R (in Astronomical Units), as a result of the elliptic path of the Earth around the Sun. The Sun-Earth distance is neglected which causes a small variation, less than 3%, in $\Delta_i = \gamma \Delta C_{0,i}$. Otherwise the Sun-Earth distance cancels in the calculation of NDVI.

The ratio r_i between the preflight calibration coefficient and true calibration coefficient for a given period and sensor can be estimated using the equations from Kaufman and Holben (1991) and Holben *et al.* (1990) which can be found in Table A.3. Equations for the calculation of $\Delta C_{0,i}$ are also given in Table A.3. The coefficients for these equations were determined with ordinary least squares from the values in Table A.1.

Table A.3: Equations for the calculation of r_1 , r_2 , $\Delta C_{0,1}$, and $\Delta C_{0,2}$ (After Kaufman and Holben 1991, including updated values from Holben). Equations were established with least squares. Note that NOAA changed the preflight calibration coefficients on September 27, 1990 for channels 1 and 2 on NOAA-11.

NOAA-7	r_1	$0.9443 - 0.05165(Y - 1981) + 0.00450(Y - 1981)^2$
	r_2	$0.9368 - 0.09832(Y - 1981) + 0.01325(Y - 1981)^2$
	$\Delta C_{0,1}$	$-3.7003 - 0.22295(Y - 1981) + 0.09980(Y - 1981)^2$
	$\Delta C_{0,2}$	$-5.5469 + 0.26995(Y - 1981)^2$
NOAA-9	r_1	$0.9599 - 0.05854(Y - 1985) + 0.002331(Y - 1985)^2$
	r_2	$0.8911 - 0.04870(Y - 1985) + 0.005290(Y - 1985)^2$
	$\Delta C_{0,1}$	$-1.9044 + 0.17611(Y - 1985) - 0.02504(Y - 1985)^2$
	$\Delta C_{0,2}$	$-4.2445 + 0.82006(Y - 1985) - 0.12508(Y - 1985)^2$
NOAA-11 old (until 27 September 1990)	r_1	$0.7837 + 0.00210(Y - 1989) + 0.00094(Y - 1989)^2$
	r_2	$0.6964 - 0.02887(Y - 1989) + 0.00951(Y - 1989)^2$
	$\Delta C_{0,1}$	1.2
	$\Delta C_{0,2}$	-0.2
NOAA-11 new (starting 27 September 1990)	r_1	$r_{1,\text{NOAA-11 old}} * 0.95/0.906$
	r_2	$r_{2,\text{NOAA-11 old}} * 0.90/0.827$
	$\Delta C_{0,1}$	-0.2
	$\Delta C_{0,2}$	0.0

Appendix B

Estimation of Sensor Degradation From Monthly NDVI Composites

Slightly revised from publication by S.O. Los, 1998, Estimation of the ratio of sensor degradation between NOAA-AVHRR channels 1 and 2 from monthly NDVI composites, *IEEE Trans. Geosci. Remote Sens.*, **36**, 206-213.

Abstract

Applications based on Normalized Difference Vegetation Index (NDVI) data calculated from Advanced Very High Resolution Radiometer (AVHRR) channels 1 and 2 require continuous updates of calibration coefficients that correct for the sensor degradation in these channels. A method was developed to estimate calibration coefficients from desert targets in monthly NDVI composites without recourse to the component channels 1 and 2 data. The method was tested on NDVI data from the AVHRR on board the NOAA-7, -9, and -11 satellites for the period 1982 until 1993. The results of the current study correlated highly ($r = 0.95$) with those from studies that estimated sensor degradation for the individual AVHRR bands.

Keywords: AVHRR, sensor degradation, NDVI composites, desert calibration

B.1 Introduction

Normalized Difference Vegetation Index (NDVI) composites, calculated from channel 1 (red) and channel 2 (near-infrared) data collected by the Advanced Very High Resolution Radiometer (AVHRR) on board the National Oceanic and Atmospheric Administration (NOAA)-7, -9, and -11 satellites, are widely used to study vegetation at regional and global scales (*e.g.* Tucker *et al.* 1985b, 1986, 1991a, 1994, Justice 1986, Prince and Justice 1991). Currently, a multi-year NDVI dataset exists that was processed and archived by the Global Inventory Monitoring and Modeling System (GIMMS) group at the National Aeronautics and Space Administration (NASA) Goddard Space Flight Center (Tucker *et al.* 1994, Holben 1986, Los *et al.* 1994). This dataset is updated on an operational basis for the Africa Famine Early Warning System

(FEWS; see Hutchinson 1991). FEWS, which is part of the US Agency for International Development, informs government agencies of potential occurrences of drought and associated crop failures. FEWS compares current NDVI data with NDVI data from the historical GIMMS archive to assess conditions of vegetation on the ground.

To do meaningful interannual comparisons, the historical archive and the present data must be consistent. Differential radiometric sensor degradation in AVHRR channels 1 and 2 affects NDVI values as a function of time and sensor satellite system. GIMMS uses the NOAA preflight calibration coefficients to relate AVHRR channels 1 and 2 reflectances to a preflight calibration standard on the ground (Los *et al.* 1994, Kidwell 1995). The NOAA preflight calibration does not take sensor degradation into account. Therefore, if no corrections for sensor degradation in the AVHRR are made, the validity of conclusions obtained from interannual comparisons with the GIMMS NDVI data, such as on the occurrence of wet and dry years, may be seriously compromised.

Several studies have estimated calibration coefficients that correct for sensor degradation in AVHRR channels 1 and 2, and relate observations of AVHRRs carried on successive NOAA platforms to a common standard. Calibration coefficients can be estimated from desert targets (Holben *et al.* 1990, Kaufman and Holben 1993, Staylor 1990), ocean glint (Vermote and Kaufman 1995), aircraft observations (Abel *et al.* 1993, Smith *et al.* 1988), and statistical analysis of global datasets (Brest and Rossow 1992). Occasionally calibration coefficients obtained with these methods are not available. For example, no calibration coefficients were available for the AVHRR when NOAA switched the data collection protocol from NOAA-11 to NOAA-9 in 1994, and from NOAA-9 to NOAA-14 in 1995. For users who depend on accurate current NDVI data, this is clearly an undesirable situation. A further complication is that often these users do not have access to AVHRR channels 1 and 2 data, yet they do have a clear need for a consistent NDVI dataset from which the

effects of sensor degradation are removed.

Los (1993) developed an approximate method to correct the preflight calibrated NDVI for radiometric sensor degradation without recourse to the component channels 1 and 2 data. The method was validated with calibration coefficients calculated by Kaufman and Holben (Los 1993, Holben *et al.* 1990, Kaufman and Holben 1993). The calibrated NDVI values adjusted with the approximate method were in close agreement with the calibrated NDVI values calculated from individually adjusted channels 1 and 2 data — the root mean square error varied between 0.002 NDVI units for NOAA-7, and 0.0001 NDVI units for NOAA-11 AVHRR data. The results were valid for a range of NDVI values between 0.0 and 0.6.

This paper builds on the method of Los (1993) to obtain estimates for radiometric sensor degradation between AVHRR channels 1 and 2 from monthly NDVI composites. This would allow a user, who has access to only NDVI data, to estimate the effect of sensor degradation from the NDVI and to make adjustments accordingly. The procedure to obtain a correction for sensor degradation from monthly NDVI composites consists of several steps. First, an expression is derived for the ratio of radiometric sensor degradation in AVHRR channels 1 and 2 as a function of the preflight calibrated “uncorrected” NDVI, and a reference “corrected” NDVI. Areas are then identified that are assumed to be time-invariant with respect to the NDVI. The temporal variation in the NDVI of these areas can be attributed to sensor degradation, and ratios of sensor degradation between AVHRR channels 1 and 2 can therefore be estimated. This procedure may lead to inaccurate estimates of radiometric sensor degradation if other effects — *e.g.*, as a result of atmospheric effects and solar zenith angle variations — are confounded with sensor degradation effects. The results of the present analysis are therefore tested for these effects, and comparisons are made with the results of other studies that are based on more in-depth analyses (Vermote and Kaufman 1995, Kaufman and Holben 1993, Holben *et al.* 1990, Rao and Chen 1994). Tests for consistency are made to see if a simplified version of the method can be used for near real-time applications. As a final check, the calibration coefficients are applied to an existing dataset and the results are compared with a NDVI dataset calculated from AVHRR channels 1 and 2 data corrected with calibration coefficients from Rao and Chen (1994).

B.2 Data

For this study, the GIMMS continental NDVI dataset from 1982–1993 for Africa was used. This dataset has a spatial resolution of about 7.6 km and a temporal resolution of a month. Processing of the GIMMS NDVI data is discussed in Holben (1986) and Los *et al.* (1994). A

brief outline is given here.

Preflight calibration was applied to daily NOAA-AVHRR level 1B channels 1 and 2 data. The preflight calibration converts integer counts to radiance values that are normalized for the solar flux in the respective bands (Kidwell 1995)

$$L_{i,p}^N = \gamma_{i,p}(C_i - C_{0,i,p}), \quad (\text{B.1})$$

with

- $L_{i,p}^N$ = radiance in channel i normalized for incoming solar radiation in band i (-),
- $\gamma_{i,p}$ = $\alpha_{i,p}\pi R^2/F_{0,i}$, the preflight calibration coefficient for channel i ,
- $\alpha_{i,p}$ = preflight calibration gain ($\text{W}\mu\text{m}^{-1}\text{sr}^{-1}\text{m}^{-2}$),
- R = the Sun-Earth distance (≈ 1 astronomical unit),
- $F_{0,i}$ = top-of-the-atmosphere solar flux for channel i ($\text{W}\mu\text{m}^{-1}\text{m}^{-2}$),
- C_i = integer count in AVHRR channel i ,
- $C_{0,i,p}$ = preflight calibration offset in channel i (integer count),
- i refers to either AVHRR band 1 or 2,
- p indicates preflight calibrated values,
- N indicates normalization for the solar flux.

NDVI values were calculated from preflight calibrated AVHRR channels 1 and 2 normalized radiance values according to

$$\text{NDVI}_p = \frac{L_{2,p}^N - L_{1,p}^N}{L_{2,p}^N + L_{1,p}^N}. \quad (\text{B.2})$$

Note that calculation of the NDVI from normalized radiance values is equivalent to calculation from reflectance values ($\rho_{i,p} = L_{i,p}^N \cos \theta$ for Lambertian surfaces) because the cosine of the solar zenith angle cancels in equation B.2.

Data from clouds are assumed to have channel 5 brightness temperature values below a threshold of 288 K, and are eliminated. Data are also discarded when the scan angle exceeds approximately 42° off-nadir to avoid extreme viewing angle conditions. The remaining daily NDVI data are merged into monthly composites by selecting the maximum NDVI value for each pixel over the monthly period. This step further minimizes the effects of clouds, atmosphere, and viewing geometry (Holben 1986).

B.3 Theory

The relationship between the NDVI adjusted for sensor degradation, NDVI_c , and the preflight calibrated NDVI— NDVI_p expressed as the simple ratio $\text{SR}_p = (1 + \text{NDVI}_p)/(1 - \text{NDVI}_p)$ —is given by Los (1993):

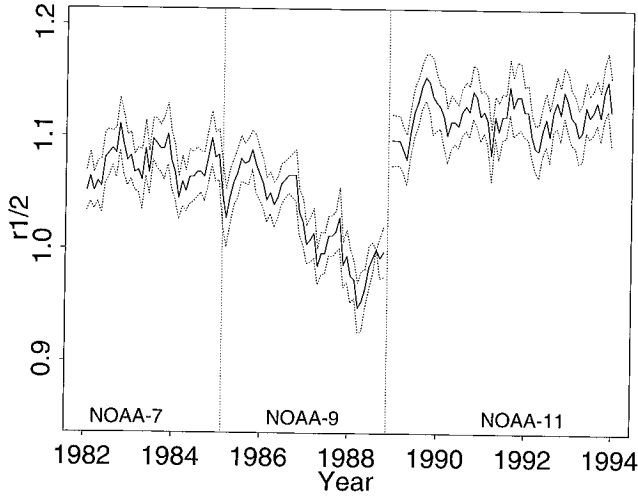


Figure B.1: Apparent ratios of sensor degradation for the NOAA-7, -9, and -11 AVHRR channels 1 and 2 calculated from 100 invariant pixels in the Sahara. Shown are the average (middle line), the average + 1 times the standard deviation (upper line), and the average - 1 times the standard deviation (lower line).

$$\text{NDVI}_c = \frac{r_{1/2}(\text{SR}_p + \Delta_2/L_{1,p}^N) - (1 + \Delta_1/L_{1,p}^N)}{r_{1/2}(\text{SR}_p + \Delta_2/L_{1,p}^N) + (1 + \Delta_1/L_{1,p}^N)}, \quad (\text{B.3})$$

with

- NDVI_c = the desert calibrated NDVI,
- $r_{1/2}$ = the ratio of sensor degradation between channels 1 and 2,
- SR_p = the preflight calibrated simple ratio,
 $= L_{2,p}^N / L_{1,p}^N = (1 + \text{NDVI}_p) / (1 - \text{NDVI}_p)$,
- Δ_i = $\gamma_{i,p} \Delta C_{0,i} = \gamma_{i,p} (C_{0,i,p} - C_{0,i,d})$,
- $C_{0,i,d}$ = the deep space count for channel i .

Values for the difference between the preflight calibration offset and the deep space count $\Delta C_{0,i} = C_{0,i,p} - C_{0,i,d}$ can be found in Table B.1. Equation B.3 is an exact relationship between the preflight and desert-calibrated NDVI, *i.e.*, application of this equation leads to exactly the same NDVI values as NDVI values calculated from individually calibrated bands, provided that the same input parameters are used. If both Δ_1 and Δ_2 are zero in equation B.3, the terms with $\Delta_i/L_{1,p}^N$ cancel from the equation. In cases that either Δ_1 or Δ_2 , or both, are small but non-zero, equation B.3 can be approximated by substituting the following empirical relationship between the preflight calibrated channel 1 and the simple ratio (Los 1993):

$$\frac{1}{L_{1,p}^N} \approx a + b * \text{SR}_p, \quad (\text{B.4})$$

with $a = -4.34$ and $b = 7.48$ (dimensionless) estimated by linear regression. The relationship that is obtained by substituting equation B.4 in equation B.3 has a root mean square error between 0.002 and 0.0001 for NDVI data collected by the NOAA-7 and NOAA-11 AVHRR, respectively (Los 1993). Comparison of the root mean square values with the difference between the deep space count and the preflight calibration offset $\Delta C_{0,i}$ from Table B.1 confirms that the approximation becomes more accurate with smaller $\Delta C_{0,i}$. The maximum root mean square error of 0.002 NDVI translates to an error on an order of magnitude smaller than the 2% error in the estimation of the rate of sensor degradation that was quoted by Vermote and Kaufman (1995).

Solving equation B.3 for the ratio of sensor degradation between AVHRR channels 1 and 2, $r_{1/2}$, and substituting equation B.4 leads to

$$r_{1/2} \approx \frac{1 + \Delta_{1,p}(a + b * \text{SR}_p)}{\text{SR}_p + \Delta_{2,p}(a + b * \text{SR}_p)} \text{SR}_c. \quad (\text{B.5})$$

Thus, with $\Delta_{i,p}$, NDVI_p (here expressed in terms of SR_p) and a reference SR_c known, the ratio of sensor degradation between channels 1 and 2 can be estimated. Given changes in the NDVI time-series from an invariant target, one can obtain absolute calibration coefficients if one or more values of the time-series can be related to a standard. If no calibration standard is available, relative calibration coefficients can be estimated by arbitrarily selecting one NDVI value from the series as the reference SR_c .

B.4 Analysis

Upon obtaining an expression for the ratio of sensor degradation as a function of observed NDVI and a reference NDVI (equation B.5), invariant targets must then be identified. The term “invariant targets” is used in this paper to indicate pixels with NDVI values that change as a function of sensor degradation only. Hence, factors such as changes in vegetation (both within and between years), viewing and illumination angle, atmosphere and clouds can be neglected. To identify invariant targets, it is assumed (1) that the NDVI of each pixel is subject to sensor degradation and (2) that any effect in addition to sensor degradation increases the total variation in a NDVI time-series. The second assumption implies that the effects of vegetation seasonality, atmosphere, illumination, and clouds will not compensate the effects of sensor degradation. For the moment, assumptions 1 and 2

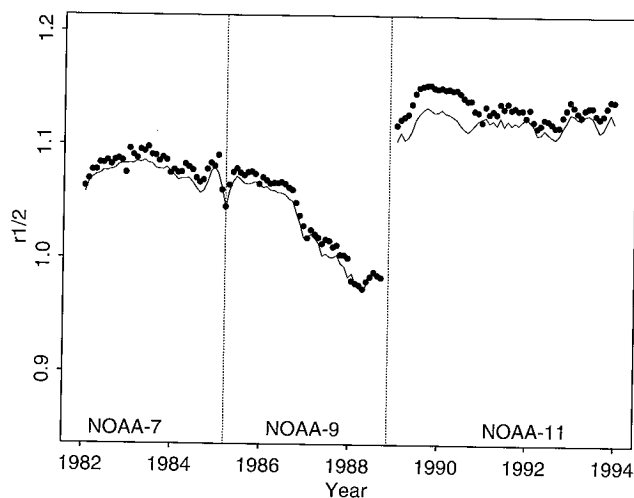


Figure B.2: Cross validation of ratios of sensor degradation between NOAA-7, -9, and 11 AVHRR channels 1 and 2 estimated from a 13 year dataset. To obtain estimates, invariant targets were identified and an annual cycle was removed (see text). Lines—Ratios of sensor degradation estimated from invariant targets and annual cycle calculated from the same 13-year period. Dots—Ratios of sensor degradation calculated for one year at a time with the invariant targets and the annual cycle estimated from the other 12 years of the 13 year data record. The close agreement, correlation $r = 0.99$ and residual standard error = 0.006, shows that the annual cycle is consistent and that the invariant targets are invariant from one year to the next.

will be used as working assumptions. To verify that these assumptions will not lead to gross errors, the results of the analysis will be tested for the effects of changes in solar zenith angle and will be compared with results obtained from other analyses.

An estimate for the temporal variation in NDVI time-series, expressed as V , is given by

$$V = \frac{\sum_{t=1}^{N-1} (NDVI_t - NDVI_{t+1})^2}{n - 2}, \quad (B.6)$$

with V calculated for each pixel, n to the number of months in the dataset, and t to the month. Thus pixels with low month-to-month variations in NDVI have low values for V , and pixels with high month-to-month variations have high values for V . Because large discontinuities may exist in NDVI values when data collection is changed from one satellite-sensor system to the next, values for (V) are calculated for the NOAA-7, -9, and -11 AVHRR sensors separately and then summed. Invariant targets are arbitrarily defined as areas with $V \leq 0.0001$. This results in identification of approximately 8000 pixels, all of which are located in the Sahara. Most of these pixels are located in the Libyan and Nubian Deserts. Of these approximately 8000 pixels, 100 are randomly selected for

further analysis.

The 100 selected NDVI values for the month of August 1988 are used in equation B.5 as reference values $NDVI_c$. The reference values are corrected for sensor degradation, with equations B.3 and B.4 and the calibration coefficients ($r_{1/2}$, Δ_1 , Δ_2) of (Kaufman and Holben 1993, Holben *et al.* 1990). Equation B.5, the values for Δ_i from Table B.1, and the adjusted reference values are used to calculate 100 monthly time-series of ratios of sensor degradation between AVHRR channels 1 and 2 over the period 1982–1990 for each of the 100 selected pixels. The results are summarized in figure B.1. Note that in figure B.1 the ratio of sensor degradation for August 1988 is 1 for all cases, *i.e.*, according to Kaufman and Holben (1993) and Holben *et al.* (1990), the rate of sensor degradation in AVHRR channel 1 is equivalent to the rate of sensor degradation in AVHRR channel 2.

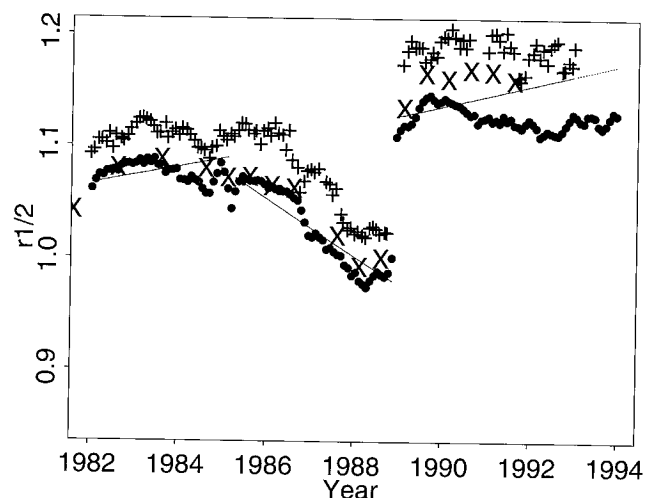


Figure B.3: Comparison of ratios of sensor degradation between the NOAA-7, -9, and -11 AVHRR channels 1 and 2 obtained in this study (dots) and the studies by Vermote and Kaufman (1995) (+-es); Holben *et al.* 1990, Kaufman and Holben (1993) (X-es); and Rao and Chen (1994) (lines).

The ratios of sensor degradation shown in figure B.1 are, for the moment, referred to as apparent ratios of sensor degradation $r'_{1/2}$. The term “apparent” is used because no checks are made for the effects of other variables such as solar zenith angle. If these effects exist, they should be removed to obtain estimates for the “true” ratio of sensor degradation. Inspection of figure B.1 reveals a cyclic signal in the data with a period of a year. A similar signal is apparent in the channel 2 data of Rao and Chen (1994). Potential sources of this signal could be variations in solar zenith angle or an effect with an annual cycle. Solar zenith angle is a function of both the time of year and the age of the satellite (Price 1991). An annual, cyclic effect is defined as a function of the time of year only. Although no assumptions are made about the

Table B.1: Preflight calibration coefficients for NOAA-7, NOAA-9, and NOAA-11. γ is the preflight calibration coefficient that converts integer counts to radiance values normalized for the solar flux. $\Delta C_{0,i} = C_{0,i,p} - C_{0,i,d}$ in integer counts is the difference between the preflight calibration offset and the deep space count. Y is the year with the time of year expressed in decimals, ($Y(15 \text{ January } 1982) = 82.041$). NOAA-7 data were acquired until February 1985, NOAA-9 data were acquired from March 1985 until November 1988, and NOAA-11 data were acquired from November 1988. The preflight calibration parameters for NOAA-11 were changed in September 1990 (in parentheses).

NOAA-7	γ_1	0.1068
	γ_2	0.1069
	$\Delta C_{0,1}$	$-3.7003 - 0.22295 (Y-81) + 0.00450 (Y-81)^2$
	$\Delta C_{0,2}$	$-5.5469 + 0.26995 (Y-81)$
NOAA-9	γ_1	0.1063
	γ_2	0.1075
	$\Delta C_{0,1}$	$-1.9044 + 0.17611 (Y-85) - 0.02504 (Y-85)^2$
	$\Delta C_{0,2}$	$-4.2445 + 0.82006 (Y-85) - 0.12508 (Y-85)^2$
NOAA-11	γ_1	0.0906 (0.95)
	γ_2	0.0835 (0.90)
	$\Delta C_{0,1}$	1.2 (-0.2)
	$\Delta C_{0,2}$	-0.2 (0.0)

Table B.2: Analysis of Variance Table for the terms in equation (B.7). The individual terms are grouped to represent intercalibration, $n_7\beta_0$, $n_9\beta_4$, and $n_{11}\beta_8$; sensor degradation, $n_7P_7(t)$, $n_9P_9(t)$, $n_{11}P_{11}(t)$; solar zenith angle effect, $\beta_{12}\cos\theta + \beta_{13}(\cos\theta)^2$; and an annual cycle $\beta_{14}\sin(2\pi t/12) + \beta_{15}\cos(2\pi t/12)$. Sum of squares indicates the amount of variance explained of the data in figure (B.1) by each of the terms, the F values indicate the statistical significance of each of the terms (see text).

	Df	Sum of Squares	Mean Sq	F Value
$n_7\beta_0$	1	0	0.00	0
$n_7(\beta_1t + \beta_2t^2 + \beta_3t^3)$	3	0.27	0.09	166
$n_9\beta_4$	1	10.30	10.30	18897
$n_9(\beta_5t + \beta_6t^2 + \beta_7t^3)$	3	5.07	1.69	3099
$n_{11}\beta_8$	1	1.70	1.70	3112
$n_{11}(\beta_9t + \beta_{10}t^2 + \beta_{11}t^3)$	3	0.42	0.14	259
$\beta_{12}\cos\theta + \beta_{13}(\cos\theta)^2$	2	3.64E-03	1.82E-03	3
$\beta_{14}\sin(2\pi t/12) + \beta_{15}\cos(2\pi t/12)$	2	1.98	0.99	1812
residuals	14284	7.79	5.45E-04	

origin of this effect, it could be caused by variations in the Earth-Sun distance or seasonal changes in the composition of the atmosphere. A model was fitted with ordinary least squares to estimate the importance of both the solar zenith angle effect and the annual cycle:

$$\begin{aligned}
 P_7(t) &= \beta_0 + \beta_1t + \beta_2t^2 + \beta_3t^3, \\
 P_9(t) &= \beta_4 + \beta_5t + \beta_6t^2 + \beta_7t^3, \\
 P_{11}(t) &= \beta_8 + \beta_9t + \beta_{10}t^2 + \beta_{11}t^3, \\
 t &= \text{month starting with } t = 0 \text{ for January 1982,} \\
 \theta &= \text{solar zenith angle.}
 \end{aligned}$$

$$\begin{aligned}
 r'_{1/2} = & n_7P_7(t) + n_9P_9(t) + n_{11}P_{11}(t) + \\
 & \beta_{12}\cos\theta + \beta_{13}(\cos\theta)^2 + \\
 & \beta_{14}\sin(2\pi t/12) + \beta_{15}\cos(2\pi t/12), \quad (\text{B.7})
 \end{aligned}$$

with

$$\begin{aligned}
 n_7 &= 1 \text{ for NOAA-7, 0 otherwise,} \\
 n_9 &= 1 \text{ for NOAA-9, 0 otherwise,} \\
 n_{11} &= 1 \text{ for NOAA-11, 0 otherwise,} \\
 \beta_{0\dots 15} &= \text{regression coefficients to be estimated,}
 \end{aligned}$$

The term $P_{7,9,11}(t)$ describes the sensor degradation for the AVHRR on board NOAA-7, -9, and -11 as a function of time t . The coefficients $n_{7,9,11}$ serve as a switch to fit sensor degradation for each of the separate satellite-sensor systems. The solar zenith angle effect, $\beta_{12}\cos\theta + \beta_{13}(\cos\theta)^2$, and the annual cycle, $\beta_{14}\sin(2\pi t/12) + \beta_{15}\cos(2\pi t/12)$, should be the same for each of the satellite-sensor systems since they act on the observations, and not on the satellite-sensor system. Since they are a common factor, there is no multiplication

with the switch $n_{7,9,11}$. The annual cycle is modeled by the sum of a sine and cosine function to estimate both the amplitude and phase. Solar zenith angle values are not available in the GIMMS dataset and are therefore estimated. Potential complications in the estimation of solar zenith angle occur as a result of biases introduced by compositing. Compositing introduces a bias to selection of observations later in the month in the case of seasonally increasing NDVI values, and earlier in the month in the case of seasonally decreasing values. Compositing also tends to favor selection of observations from approximately 10 degrees in the forward scatter direction (Holben 1986, Los *et al.* 1994). In figure B.1, higher NDVI values occur during late summer when solar zenith angles are lower, and lower NDVI values occur during early spring when solar zenith angles are higher. To accommodate the biases introduced by compositing, solar zenith angle values were calculated as the minimum solar zenith angle for the 5th, 15th, and 25th day of each month at 10° off-nadir in the forward-scatter direction. Calculations were done with the Pathfinder navigation routines (James and Kalluri 1994, Baldwin and Emery 1993, Patt and Gregg 1994).

The importance of each of the terms of equation B.7 in explaining the variance in the data of figure B.1 is summarized in an analysis of variance table (Table B.2). In this table the individual terms are grouped to represent intercalibration, terms $n_7\beta_0$, $n_9\beta_4$, $n_{11}\beta_8$; sensor degradation, terms $n_7P_7(t)$, $n_9P_9(t)$, $n_{11}P_{11}(t)$; solar zenith angle effect, terms $\beta_{12}\cos\theta + \beta_{13}(\cos\theta)^2$; and the annual cycle, terms $\beta_{14}\sin(2\pi t/12) + \beta_{15}\cos(2\pi t/12)$. The sums of squares for the intercepts, $n_7\beta_0$, $n_9\beta_4$, and $n_{11}\beta_8$, show that lack of intercalibration between instruments from different satellites is a major source of variance in the AVHRR data from NOAA-9. The lack of intercalibration between the NOAA-7 and NOAA-11 AVHRR is much smaller. To show only the effect of intercalibration in Table B.2, the mean ratio of sensor degradation between channels 1 and 2 for the NOAA-7 AVHRR was subtracted from all ratios of sensor degradation (hence the sum of squares for the term $n_7\beta_0$ is zero).

The sums of squares for the sensor degradation, terms $n_7\beta_1t \dots n_7\beta_3t^3$ combined, terms $n_9\beta_5t \dots n_9\beta_7t^3$ combined, and terms $n_{11}\beta_9t \dots n_{11}\beta_{11}t^3$ combined, show the importance of sensor drift during the time of operation of the AVHRR on board NOAA-7, NOAA-9, and NOAA-11, respectively. The contribution to the sums of squares by differential sensor drift in AVHRR channels 1 and 2 is substantial for NOAA-9, and smaller for NOAA-7 and NOAA-11. This is also indicated in figure B.1 by the large decrease in the apparent ratio of sensor degradation for NOAA-9, and the more constant signals for NOAA-7 and -11. The variance explained by solar zenith angle, terms $\beta_{12}\cos\theta + \beta_{13}(\cos\theta)^2$, is smaller than the variance explained by any of the other effects. In fact,

the variance is so small that the F value is below the threshold for the 99% confidence level. It is therefore concluded that solar zenith angle does not have a significant effect on the apparent ratio of sensor degradation and that this effect can conveniently be ignored. The terms $\beta_{14}\sin(2\pi t/12) + \beta_{15}\cos(2\pi t/12)$ that model the annual cycle have a significant effect on apparent ratios of sensor degradation, as evidenced by the large sums of squares and F values. The annual cycle should therefore be removed. The coefficients for the annual cycle are $\beta_{14} = -0.01704$ and $\beta_{15} = 0.00273$. Subtracting the annual cycle and applying a 3 month moving average to the data resulted in the estimated rates of sensor degradation given in figure B.2 and Table B.3.

The estimation of sensor degradation from NDVI composites can be simplified if the identification of the invariant targets and the estimation of the annual cycle can be done once and be used outside the time-period from which they were derived. To see if simplification leads to consistent results, the 13 year data record is split into 13 12-year datasets by leaving out a different year each time. For each of the 13 12-year datasets created, the same procedures discussed in the previous part of this section are followed. The invariant targets are identified and different samples of 100 pixels are then randomly selected. The apparent rate of sensor degradation is calculated, and the annual cycle is estimated. Ratios of sensor degradation are estimated for the year left out from the 100 invariant sites and the annual cycle obtained from the 12-year record. A 3-month moving average was applied to remove the noise from the estimates of sensor degradation for that one year. Rates of sensor degradation were thus obtained for each of the 13 individual years left out from the estimation of the invariant targets and the annual cycle. A comparison with the rates of sensor degradation calculated from the full 13-year data record is shown in figure B.2. This figure shows close agreement between the two results, correlation $r = 0.99$ and residual standard error $= 0.006$, indicating that consistent parameters can be obtained if the invariant targets and the annual cycle are estimated from data of a different timeperiod.

B.5 Discussion

A procedure was developed to estimate the differential rate of sensor degradation in AVHRR channels 1 and 2 on board NOAA-7, -9, and -11 consisting of the following steps: identifying invariant targets in the Sahara, estimating apparent rates of sensor degradation, and estimating and subsequently removing of an annual cycle in the apparent ratios of sensor degradation. It was shown that the effects of solar zenith angle variations on the NDVI from deserts could be ignored. It was further shown that the invariant targets and the annual cycle need to be estimated

Table B.3: Ratios of sensor degradation between the NOAA-7, -9, and -11 AVHRR channels 1 and 2 for every other month between February 1982 and December 1993. Stars indicate change in data collection from one satellite-sensor system to the next.

Year	Feb	Apr	Jun	Aug	Oct	Dec
1982	1.067	1.071	1.075	1.074	1.081	1.081
1983	1.085	1.086	1.086	1.079	1.075	1.077
1984	1.067	1.070	1.065	1.054	1.064	1.082
1985	1.059*	1.056	1.070	1.066	1.066	1.063
1986	1.061	1.060	1.056	1.050	1.040	1.018
1987	1.020	1.014	1.006	1.000	0.991	0.982
1988	0.978	0.972	0.982	0.982	0.980*	1.106
1989	1.117	1.119	1.132	1.141	1.139	1.138
1990	1.139	1.136	1.131	1.139	1.132	1.123
1991	1.121	1.120	1.120	1.116	1.113	1.122
1992	1.116	1.110	1.110	1.107	1.116	1.127
1993	1.121	1.126	1.125	1.113	1.122	1.128

only once and that they can be used outside the timeperiod from which they were derived. Therefore, rates of sensor degradation can be estimated in near real-time by monitoring NDVI changes over the same invariant targets after eliminating the annual cycle.

In the analysis in the previous section, the effects of the atmosphere and viewing angle were not explicitly considered, and the analysis was done on monthly composites instead of daily observations. To see if gross errors were introduced by these simplifications, a comparison was made with the results from several other studies (Holben *et al.* 1990, Kaufman and Holben 1993, Vermote and Kaufman 1995, Rao and Chen 1994). In these studies, sensor degradation was estimated separately for AVHRR channels 1 and 2, and closer attention was paid to the effects of atmosphere, viewing geometry, and solar zenith angle. Figure B.3 summarizes the results for the period 1982 until 1993 obtained in this study (dots) and in the studies of Vermote and Kaufman (1995) (+es), Holben *et al.* 1990, and Kaufman and Holben (1993), (X-es) and Rao and Chen (1994) (lines).

The data of Vermote and Kaufman (1995)(+es) show a fairly large overall difference with the results from the present study. However, this difference is consistent and of equal magnitude over the entire period investigated. Close agreement between the study of Vermote and Kaufman (1995) and the current study is found when the monthly values are plotted against each other. The data then fall in a straight line (figure B.4). The correlation between the two datasets is high, $r = 0.95$. A linear fit between these datasets results in an intercept (0.0104) of equal magnitude as the standard error (0.0114). Because

the intercept term is small and equal in magnitude as the standard error, it can be ignored. Thus one can convert the estimates in this study to those from Vermote and Kaufman by multiplying with a factor of 1.0425. The multiplication factor is explained by the different references used; in this study NDVI values from August 1988 corrected with the calibration coefficients of Kaufman and Holben (1993) served as reference values, whereas Vermote and Kaufman (1995) derived a calibration standard by using the radiative properties of the atmosphere. The otherwise high degree of similarity between the independently derived ratios of sensor degradation for all three AVHRRs in this study and the study of Vermote and Kaufman (1995) gives confidence in the results of this study and justification for the simple assumptions used in the current study.

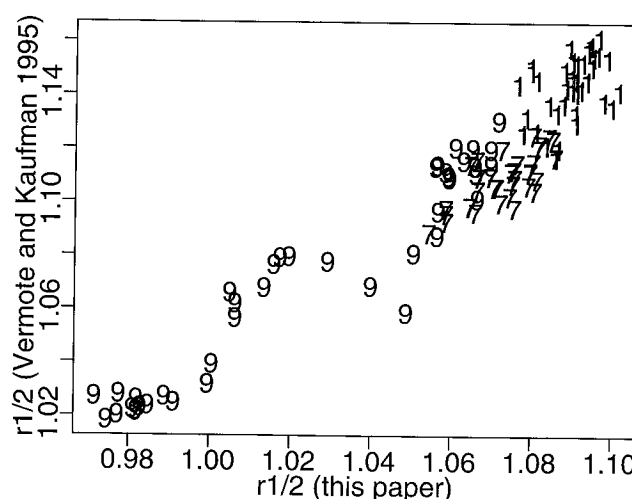


Figure B.4: Scatter plot of monthly ratios of sensor degradation for the NOAA-7, -9, and -11 AVHRR channels 1 and 2 obtained in this study and in the study by Vermote and Kaufman (1995). 7 indicates ratios of sensor degradation for NOAA-7, 9 ratios of sensor degradation for NOAA-9, and 1 ratios of sensor degradation for NOAA-11.

The values found by Holben *et al.* (1990) and Kaufman and Holben (1993) agree well for the AVHRR on board NOAA-7 and -9, but the agreement is not as good for NOAA-11. The ratio of sensor degradation for NOAA-11 is consistently different, and the relative changes over time are similar. Note that the results from the present study and the results from Vermote and Kaufman (1995) are consistent for all three satellites. The differences in estimates of sensor degradation for NOAA-11 by Kaufman and Holben (1993) could be caused by the small number of data points and timeslots used in combination with somewhat higher noise levels in the data from the AVHRR on board NOAA-11 (see figure B.3). Another explanation for inconsistency in the results could be that on several occasions NOAA has sent out preflight cali-

bration coefficients with the data that are different from the official documentation by Kidwell (1995) (Table B.1). Use of different preflight calibration coefficients can easily explain the difference between the results from Kaufman and Holben (1993) and the present study.

The sensor degradation reported by Rao and Chen (1994), which is based on the technique developed by Staylor (1990), describes the sensor degradation in the AVHRR as an exponential decay function. The differences in the ratios of sensor degradation across satellite sensor systems are similar to those found in this study, and the exponential decay functions, though derived from a different data source, closely fit the rates of sensor degradation found in the present study. The one exception is the discrepancy found in 1993. This was caused by extrapolating the exponential decay function beyond the 1988–1992 data record from which it was derived. It clearly demonstrates that relationships obtained by fitting the data of one period cannot be used for extrapolating to another. Therefore, real-time calibration coefficients must be estimated from current data (Teillet and Holben 1994).

As a final test, the calibration coefficients found in this study were applied to the global 1° by 1° NDVI dataset of Los *et al.* (1994) and the results were compared with the global 1° by 1° NDVI Pathfinder dataset (James and Kalluri 1994). The Pathfinder NDVI data were calculated from channels 1 and 2 reflectance values that were corrected for sensor degradation with the coefficients of Rao and Chen (1994). Monthly anomalies — *i.e.*, departures from the monthly median NDVI — over the period of January 1982 until December 1990, were calculated for the two global datasets for four arid regions; the Sahara desert from 25° N 5° W to 20° N 20° E, the Gobi and Taklimakan Deserts from 40° N 80° E to 35° N 100° E, the southwestern United States from 35° N 105° W to 25° N 100° W, and southern Africa from 25° S 20° E to 30° S 25° E (figure B.5). The NDVI anomalies over these arid regions should be small if sensor degradation is appropriately addressed. Figure B.5 shows that the calibration coefficients obtained in this study as applied to the data of Los (1994), with the approximate model of equations B.3 and B.4, lead to comparable if not better results (in terms of stability of time-series) than the calibration coefficients of Rao and Chen (1994) applied to individual channels 1 and 2 data. The monthly estimates of sensor degradation used in this study lead to more consistent NDVI time-series when data collection is changed from the NOAA-9 to the NOAA-11 AVHRR for the Sahara and Gobi Deserts. This finding is especially evident when the anomalies that occur around November 1988 in the Los (1994) dataset are compared to the much larger departures in the Pathfinder data (James and Kalluri 1994). Notice, however, that these departures do not occur consistently in all data (see *e.g.* the time-series

for the southwestern USA in figure B.5).

B.6 Conclusion

It was shown that the ratio of sensor degradation between channels 1 and 2 of the AVHRR can be calculated from monthly maximum NDVI composites with a high degree of accuracy. The ratios of sensor degradation correlate highly with the independently derived results of Vermote and Kaufman (1995; $r = 0.95$), and of Rao and Chen (1994; $r = 0.94$), which gives a high level of confidence in the results of the current study. Failure to extrapolate expressions that describe sensor degradation as a function of time clearly shows the need for a reliable method that uses current data to correct NDVI composites for sensor degradation.

Acknowledgments

Funding was provided by a NASA Earth Observing System - Interdisciplinary Science (EOS-IDS) program (Biosphere-Atmosphere Interactions project; contract NAS-531732). Thanks to Drs. Piers Sellers (NASA Johnson Space Center) and Adriaan van de Griend (Vrije Universiteit, Amsterdam, the Netherlands) for their comments that improved this manuscript and their encouragement of the present study.

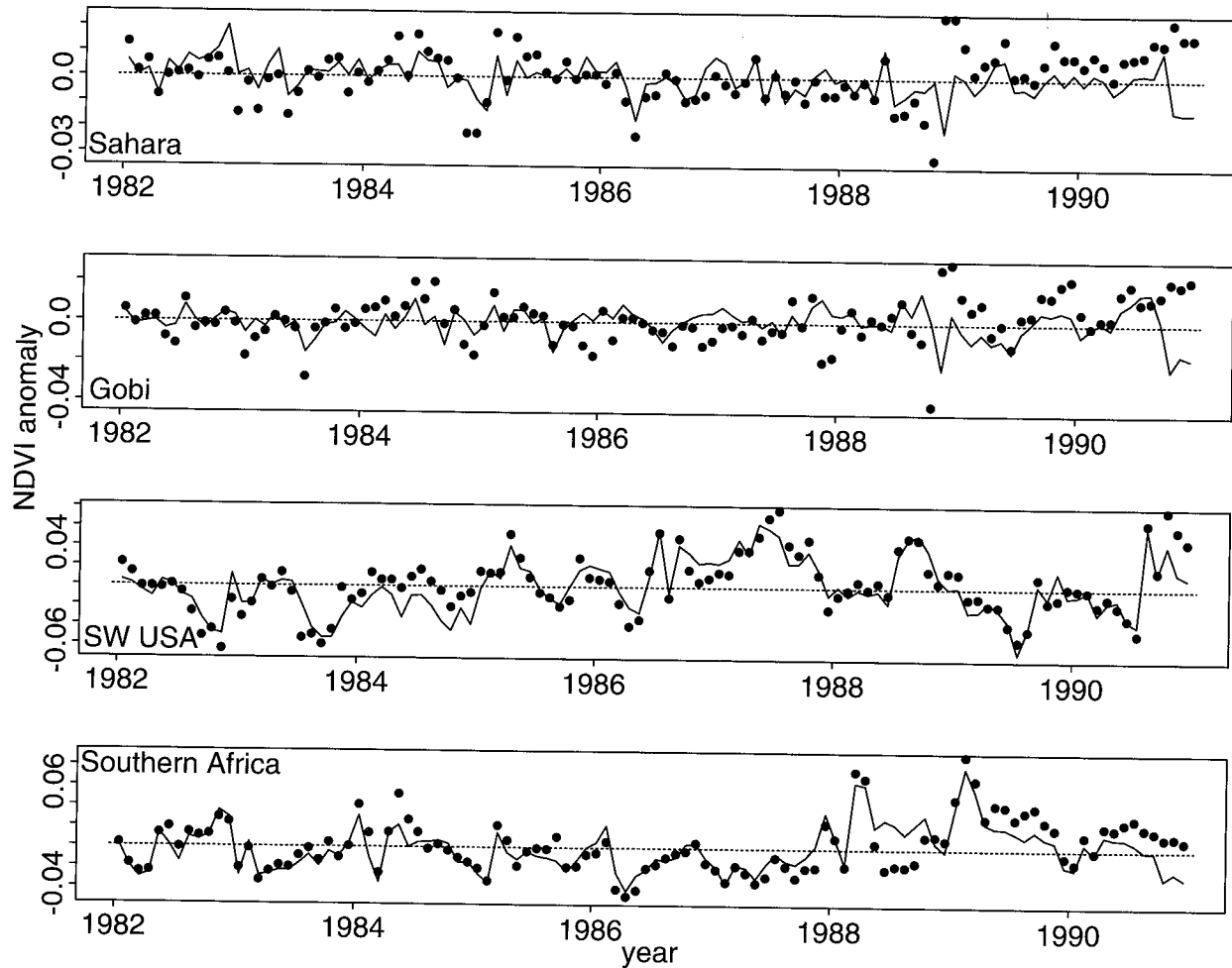


Figure B.5: Monthly anomalies—i.e., departures from the monthly median NDVI—over the period of January 1982 until December 1990 for four arid regions; the Sahara desert from 25° N 5° W to 20° N 20° E, the Gobi and Taklimakan Deserts from 40° N 80° E to 35° N 100° E, the southwestern United States from 35° N 105° W to 25° N 100° W, and southern Africa from 25° S 20° E to 30° S 25° E. Solid line — time-series from the global 1° by 1° NDVI dataset of Los et al. (1994) corrected with calibration coefficients from this study. Dots — time-series from the global 1° by 1° NDVI Pathfinder dataset (James and Kalluri 1994) corrected with the calibration coefficients of Rao and Chen (1994) applied to channels 1 and 2 data. Notice the large jump in the anomalies over the Sahara in the Pathfinder data when data collection is changed from the NOAA-9 to the NOAA-11 AVHRR in November 1988.

Appendix C

A Global 1° by 1° NDVI Dataset for Climate Studies

Slightly revised from the publication by S.O. Los, C.O. Justice, and C.J. Tucker, 1994, A global 1° by 1° NDVI dataset for climate studies derived from the GIMMS continental NDVI data, *Int. J. Remote Sens.*, **15**, 3493-3518.

Abstract

A 9-year (1982–1990) global Normalized Difference Vegetation Index (NDVI) dataset with a spatial resolution of 1° by 1° and a temporal resolution of one month was compiled for use in climate studies. This dataset was derived from higher resolution (5–8 km) monthly continental NDVI datasets that were processed and archived by the Global Inventory Monitoring and Modeling System (GIMMS) group at NASA/Goddard Space Flight Center. The continental GIMMS NDVI datasets were calculated from Global Area Coverage (GAC) data collected at daily intervals by the Advanced Very High Resolution Radiometer (AVHRR) on board the NOAA-7, -9, and -11 satellites.

The global 1° by 1° NDVI dataset was produced to estimate landsurface parameters for use within general circulation models of the atmosphere (GCM). In view of this quantitative application, an evaluation is given of the representation by the NDVI data of the spectral properties of vegetation at the land surface. Errors are defined as deviations from measurements obtained under standard conditions, *i.e.*, conditions at the top of the atmosphere with no clouds, clear atmosphere, near-nadir viewing angles, overhead Sun, and invariant soil background. The discussion includes an assessment of (1) the data collected and processed by the AVHRR on board the NOAA satellites; (2) processing of the AVHRR data into the continental GIMMS NDVI datasets; (3) resampling of the continental datasets to a 1° by 1° dataset; and (4) propagation of inconsistencies and biases from (1), (2), and (3) into the 1° by 1° global NDVI data. Examples are shown of the temporal and spatial variations in spectral properties of vegetation contained in the 1° by 1° NDVI data, and these are compared with the dynamics of biophysical parameters derived from landcover classes that were used in previous climate studies.

C.1 Introduction

Developments in the study of global climate have led to incorporating biosphere models into general circulation models of the atmosphere (GCMs), *e.g.*, the Biosphere-Atmosphere Transfer Scheme (BATS) of Dickinson (1984) and the Simple Biosphere Model (SiB) of Sellers (Sellers *et al.* 1986; see also Sellers *et al.* 1992a, Sellers *et al.* 1996a). These biosphere models differ from prior efforts in that they provide a more realistic treatment of the water, energy, and carbon exchanges between the land surface and the lower boundary layer of the atmosphere (Sato *et al.* 1989). With the development of these models, a need for datasets emerged from which the global distribution of biophysical parameters could be derived. To obtain these datasets, Dorman and Sellers (1989) used look-up tables compiled from datasets assembled by Klink and Willmott (1985) to assign biophysical parameters to the global landcover classifications of Matthews (1983) and Kuchler (1983). This approach is not without problems. First, landcover classes typically contain only rudimentary information on within-class variations and vegetation seasonality. Second, biophysical parameters reflect conditions at selected sites and these may not be representative for an entire class, *e.g.*, if a classification distinguishes only one type of grassland, the parameters derived for grasslands with either C₃ or C₄ based photosynthesis cannot be properly assigned. Third, landcover datasets can be inaccurate, partly because they may be intended for a different purpose, *e.g.*, DeFries and Townshend (1993) found large disagreements among global landcover datasets compiled by different authors.

An alternative way to obtain global distributions of biophysical parameters is by means of satellite data. Solar radiation in the visible and near-infrared wavebands, reflected by the Earth's surface and collected by a remote sensing device, can be combined into a spectral vegetation index such as the normalized difference vegetation index (NDVI) and related to physical properties of vegetation (Tucker 1979, Kumar and Monteith 1982, Sellers

1985, Justice 1986, Prince and Justice 1991). For example, the NDVI has been related to the fraction of absorbed photosynthetic radiation (FPAR), green leaf area index (L_g), and carbon assimilation of vegetation (Sellers 1985, Tucker *et al.* 1986a, Fung *et al.* 1987, Box *et al.* 1989, Sellers 1987, Sellers *et al.* 1992a, Asrar *et al.* 1992). Seasonal integrals of the NDVI have been correlated with the accumulation of aboveground biomass in sub-Saharan Africa and North America (Tucker *et al.* 1981, Tucker *et al.* 1985, Goward and Dye 1987). In an updated version of SiB, referred to as SiB2, similar relationships are employed to calculate from monthly NDVI data, monthly values of FPAR, leaf area index, landsurface albedo, and roughness length. These monthly values are interpolated to obtain values at smaller time steps that are used for calculating photosynthesis and transpiration (Sellers *et al.* 1992a, Sellers *et al.* 1996b, Chapter 5, Appendix D).

To obtain 1° by 1° global fields of NDVI, monthly NDVI datasets with a spatial resolution of around 5 to 8 km were used that were compiled by continent for the period 1982 to 1990 by the Global Inventory Monitoring and Modeling System (GIMMS) group at the National Aeronautics and Space Administration (NASA) Goddard Space Flight Center. These datasets were calculated from data collected by the advanced very high resolution radiometer (AVHRR) on board the National Oceanic and Atmospheric Administration (NOAA)-7, -9, and -11 satellites. In this paper, an assessment is provided of the continental datasets in terms of how consistently the data represent the spectral properties of landsurface vegetation. Errors or inconsistencies in the data are defined as deviations from the top-of-the-atmosphere measurements carried out at the middle of the month under standard conditions, *i.e.*, data collected at near-nadir viewing angles under clear, cloud-free atmospheric conditions, with an overhead Sun and an invariant soil background. For example, a cloud-contaminated pixel is referred to as erroneous, since it does not correlate with the condition of the vegetation at the land surface. An evaluation is given of data collecting and processing by the AVHRR, compiling the GIMMS continental datasets, and resampling of the continental data into a 1° by 1° dataset.

Given the wide range of conditions under which data are collected and the diverse ways the data can be affected, this discussion can be limited in scope only. Major problems in the dataset are highlighted, and a very rough estimate is given of the magnitude of inconsistencies. The spatial and temporal variations in the NDVI are compared with the temporal development of biophysical parameters for the 12 SiB biomes of Dorman and Sellers (1989). An evaluation of the propagation of errors in the NDVI dataset into climate models is beyond the scope of this paper; however, some issues that are of concern to the translation of NDVI into biophysical parameters are addressed in the discussion. A correction of the most

important remaining errors in the dataset and the calculation of biophysical parameter fields are discussed in Sellers *et al.* (1996b), Chapter 5, and Appendix D.

C.2 The GIMMS Continental NDVI Dataset

Spectral vegetation indices derived from NOAA-AVHRR data, such as the GIMMS NDVI (Holben 1986) and the NOAA global vegetation index (GVI) (Tarpley *et al.* 1984), have been employed in various studies around the globe to obtain information on the state of vegetation (Tucker *et al.* 1985, Justice *et al.* 1985, Townshend *et al.* 1985, Malingreau 1986, Justice 1986, Goward and Dye 1987, Fung *et al.* 1987, Malingreau and Tucker 1988, Box *et al.* 1989, Prince and Justice 1991, Tucker *et al.* 1991a, b). As studies became more quantitative and attention was focused on interpreting longer time-series and larger areas, it became apparent that both spatial and temporal inconsistencies were present in the data (Goward *et al.* 1991). These inconsistencies originated from a number of sources: satellite navigation uncertainties, a drift in the satellite's local crossing time, degradation of the AVHRR sensor, onboard resampling of the data, cloud effects, atmospheric attenuation of the signal from the land surface, variations in the viewing and solar zenith angle, surface bidirectional reflectance distribution function (BRDF), and variations in the soil background. A short discussion of each of these effects is provided in this section and the order of magnitude of these effects is summarized in Table C.3. In section C.3, data processing in terms of its ability to remove these inconsistencies is discussed.

C.2.1 The NOAA-AVHRR Remote Sensing System

The NOAA-AVHRR was designed to collect meteorological data on the entire globe. After the satellite became operational, its potential for vegetation monitoring was realized with the launch of NOAA-7 in 1981. The original requirements (meteorological applications) which drove the design of the AVHRR explain some of its shortcomings for monitoring vegetation, such as the limitations in accurately determining the satellite orbit (Emery *et al.* 1989), the method of onboard data resampling (Kidwell 1995), a lack of onboard calibration to correct for decreasing sensitivity of the AVHRR over time (Price 1987, Holben *et al.* 1990, Kaufman and Holben 1993), and the selection of an early afternoon crossing time, which more-or-less coincides with the time of maximum cloud development around the globe (Sellers and Schimel 1993).

An accurate orbital model of the NOAA satellite is important to correctly locate data to a position on the

ground. Emery *et al.* (1989) discuss several orbital models and conclude that with the most advanced models, data can be located with an accuracy of about 1 km. These models use highly accurate orbital parameters, ground control points, and inverse image referencing, *i.e.*, satellite data are registered in a way that minimizes the distance between the location of the satellite data and the elements of the geographic projection onto which the data are mapped. In the navigation software of the GIMMS group, which uses the orbital parameters on the tape that are provided by NOAA, many of the techniques discussed by Emery *et al.* (1989) are not implemented. The navigation accuracy is therefore lower: NOAA cites an error in the surface pixel location of ~ 5 km and Holben (1986) found along- and across-track errors of 4.8 km and 3.6 km, respectively, but also documented deviations of as much as 17 km (Table C.3).

Over their time of operation (3 to 5 years) the NOAA-7, -9, and -11 satellites have experienced a gradual drift from the original target equatorial crossing time of $\sim 14:30$ (solar time) to local solar crossing times of $\sim 16:00$ or later (Price 1991). The AVHRR data can reflect differences due solely to an altered illumination geometry (higher solar zenith angles) as a result (Chapter 3.2.1, Appendix D.4.2).

The AVHRR collects data at 1.1 km resolution at the satellite sub-point. To reduce the amount of data that is stored on board between transmissions to the ground, data are resampled to global area coverage (GAC) resolution. This is done by averaging the four left-most pixels of the first row of a 5 by 3 pixel window. Since only 4/15 of the original window is used, a locale can be inaccurately represented by a GAC pixel, especially in areas with high spatial variability in vegetation cover (Justice *et al.* 1991b).

NOAA provides a preflight calibration for the visible and near-infrared channels, which relates the signal received by the satellite to a pre-launch standard (Kidwell 1995). The preflight calibration does not take into account degradation of the AVHRR that occurs after the launch of the satellite. Sensor degradation results in gradual changes in the NDVI over the lifetime of the sensor and leads to discontinuities between successive instruments (figure C.1.a). The deviations are dependent on the magnitude of the NDVI and are generally between -0.10 and $+0.01$ NDVI compared to the pre-launch standard (Holben *et al.* 1990, Kaufman and Holben 1993, Los 1993).

C.2.2 Cloud Contamination

A significant proportion of the land surface is obscured by clouds, the timing of maximum cloud development in the humid regions of the world more-or-less coinciding with the afternoon overpass time of the NOAA-7, -9,

and -11 satellites. Clouds appear as very bright objects in channels 1 and 2 (reflectances generally larger than 0.35 in both channels) and have low, negative NDVI values (-0.05 to -0.2 NDVI). Most cloudy data values can be identified by their low surface temperatures and high brightness and thus can be eliminated. Mixed pixel data that are part clouds and cloud shadows, and part land surface, are difficult to identify automatically, and are therefore likely to be incorporated in the datasets. The effect of sub-pixel clouds is especially serious for vegetated areas, the effect in this case being largest on the visible reflectance. For example, a cloud with a reflectance of 0.5 in the visible band and a fraction of 20% in a landsurface pixel with a reflectance of 0.05 can increase the apparent surface reflectance by 0.08 (Kaufman 1987). Studies on cloud distributions show that sub-pixel size clouds (< 1.1 km) occur the most frequently (Planck 1969, Wielicki and Welch 1986). Also, given that areas with high cloud cover coincide with densely vegetated areas, it follows that cloud contamination is a serious problem for vegetation monitoring.

C.2.3 Atmospheric Perturbations

The amount of solar energy radiated to and reflected from the Earth's surface is modified by atmospheric constituents. Important to AVHRR bands 1 (visible, 0.55 - 0.68 μm) and 2 (near-infrared, 0.72 - 1.1 μm) are: absorption and scattering by gases (principally ozone, CO_2 and water vapor), Rayleigh or molecular scattering (O_2 , N_2 , A) and scattering by aerosols (*e.g.*, Chahine *et al.* 1983, Tanré *et al.* 1992). Of these, water vapor and atmospheric aerosols vary highly in concentration over space and time and their effect is therefore difficult to account for without knowledge of their distribution in the atmosphere. Atmospheric ozone concentrations also vary over the globe, but to a lesser extent. It is possible to obtain the distribution of atmospheric constituents from a ground-based sun-photometer network (water vapor and aerosols), radiosonde (water vapor) or satellite data (water vapor and ozone and to some extent aerosols) (see *e.g.*, Tanré *et al.* 1988, Holben and Eck 1990, Herman *et al.* 1991, Holben *et al.* 1991, Stolarski *et al.* 1991, Holben *et al.* 1992, McCormick and Veiga 1992, Stowe *et al.* 1992). Rayleigh scattering can be accounted for because molecules are distributed in the atmosphere in an even, predictable way. The impact of atmospheric scattering and absorption on the signal measured by the satellite is also dependent on the spectral properties of the land surface, and is enhanced by viewing angle and illumination geometry effects (section C.2.4). The effects of the atmospheric components on AVHRR channels 1 and 2 data, and on the NDVI, are summarized by Tanré *et al.* (1992). Some of their estimates are given in Table C.1.

Examples of atmospheric effects on NDVI time-series

APPENDIX C. A GLOBAL 1° BY 1° NDVI DATASET FOR CLIMATE STUDIES

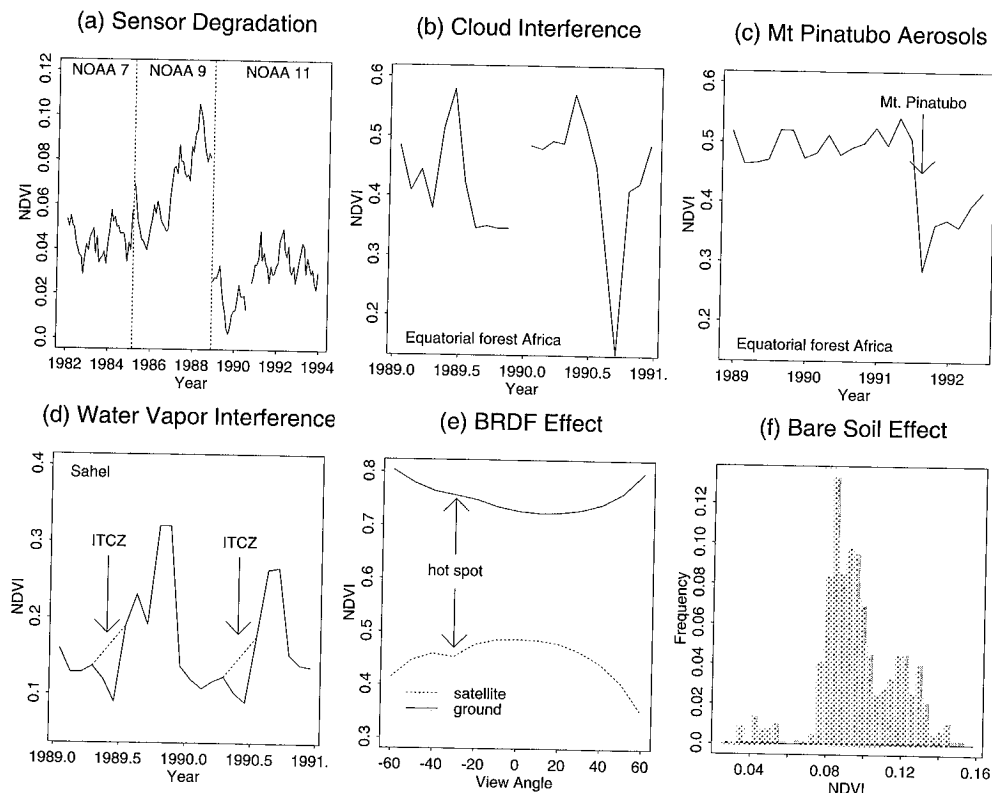


Figure C.1: Variations in the NDVI as a function of (a) sensor degradation: the NDVI from desert sites is assumed to exhibit only small variations over time. The trends in the NDVI data (e.g. for NOAA-9) are the result of sensor degradation, the discontinuities between satellites (compare data for NOAA-9 and NOAA-11) are caused by differences in calibration between satellites. (b) clouds: NDVI data from an equatorial forest should exhibit low seasonal variation. The strong temporal changes in the NDVI and the missing data are caused by cloud contamination. (c) effect of aerosols from the Mt. Pinatubo eruption (July 1991) on the NDVI. The eruption of Mt. Pinatubo resulted in high concentrations of atmospheric aerosols worldwide. These aerosols strongly increased the reflectance in the visible channel of the AVHRR and decreased the NDVI. Aerosol concentrations gradually diminished over time; the effects were noticeable in the NDVI data for about one-and-a-half years. (d) The near-infrared channel of the AVHRR contains a water vapor absorption band. Seasonal increases in atmospheric water vapor, e.g., at the start of the rainy season in the Sahel, decrease the measured reflectance in the near-infrared channel and decrease the NDVI. (e) Bidirectional effects in the NDVI as a function of viewing angle measured for ground-measured data (top line) and data measured at the top of the atmosphere (bottom line). The ground bidirectional distribution function (BRDF) was simulated with a model from Roujean *et al.* (1992) and the atmospheric effects for a mid-latitude continental atmosphere with fairly high aerosol concentration were simulated with the Second Simulation of Satellite Signal in the Solar Spectrum6S (Vermote *et al.* 1995). The ground-measured NDVI data are overall higher than the data measured at the top of the atmosphere and show an inverse relationship with viewing angle. A small hotspot effect is found at 30° off-nadir in the backscatter direction. This effect occurs when the observer is in the principal plane with the Sun in his/her back and the view zenith angle is equal to the solar zenith angle. In this configuration the amount of shadowing appears at a minimum for the observer (provided the distance between the observer and the target is sufficiently large). (f) Frequency distribution of variations in the NDVI from the Sahara (27.5° N, 1.25° W to 27.4° N, 23.7° E). Most of the variation in the NDVI can be attributed to variations in soil background reflectance, not to variations in vegetation greenness.

are shown in figures C.1.c and C.1.d. Figure C.1.e shows the impact of volcanic dust blown into the air after the Mt. Pinatubo volcanic eruption on a NDVI time-series of an equatorial forest (Vermote *et al.* 1995). Figure C.1.d is from an area in the Sahel. At the start of the growing season NDVI values are decreased by the movement of a large humid air mass into the area that is at the boundary of the intertropical convergence zone (ITCZ) (Justice *et al.* 1991a).

C.2.4 Illumination and Viewing Geometry-Dependent Effects

The AVHRR measures data from a wide range of viewing angles (between $\pm 55^\circ$ off-nadir) and illumination conditions (solar zenith angles between 20° and 90°). The variation in illumination and viewing geometry will affect

Table C.1: Values from Tanré *et al.* (1992). The effect on high and low NDVI values (vegetated and bright surfaces respectively) by atmospheric attenuation of ozone ($U_{O_3} = 0.35$ cm.atm), water vapor ($U_{H_2O} = 3.0$ g.cm⁻²), Rayleigh scattering (scattering in the forward principal plane; $\phi_v = 180^\circ$), and aerosols (scattering in the forward principal plane; $\phi_v = 180^\circ$, optical depth $\tau_a = 0.20$) for a solar zenith angle of $\theta_s = 30^\circ$, and a viewing angle of $\theta_v = 30^\circ$.

	Δ NDVI (NDVI = 0, bright)	Δ NDVI (NDVI = 0.9)
ozone	+0.025	+0.01
water vapor	-0.07	-0.02
Rayleigh	0.00	-0.06
aerosol	0.00	-0.10

the NDVI, depending on the surface BRDF and the optical properties of the atmosphere. Ground-based studies on the surface BRDF have revealed a wide variety of responses in the NDVI that are dependent on factors such as vegetation type, the amount of green material, the architecture of plants, and the way plants are distributed (clustered, rows, evenly distributed, etc.; see Myneni *et al.* 1989, Deering *et al.* 1992a). For example, Deering *et al.* (1992b, 1994) found the occurrence of maximum NDVI for a range of viewing angles to be dependent on solar zenith angle. For a spruce-hemlock stand the maximum NDVI was in the forward scatter direction for solar zenith angles smaller than 40° , and for larger angles in the back scatter direction (Deering *et al.* 1994). Middleton (1991) found for grasslands both increasing and decreasing relationships between the NDVI and solar zenith angle.

Several authors have studied the combined effect of atmosphere and surface BRDF on viewing and illumination geometry. Most of these studies used simplified models for the surface BRDF and combined these with radiative transfer models for a limited sample of atmospheric conditions (Kimes 1983, Holben and Fraser 1983, 1984, Holben *et al.* 1986). These studies found maxima in the relation between NDVI and viewing angles in the near-nadir and slight forward scatter directions ($\sim 10^\circ - 20^\circ$; figure C.1.b). Relationships between solar zenith angle and the NDVI were not investigated, but a few examples calculated by these authors showed a slight decrease in NDVI with increasing solar zenith angle.

At very high solar zenith angles near the twilight terminator, light intensities become low and atmospheric path lengths for incoming solar radiation large. The contribution of the atmosphere to the signal measured by the AVHRR will therefore be large, to the extent that the signal from the surface is completely obscured (Holben 1986).

C.2.5 Soil Background Effect

The reflective properties of a bare soil vary with its type and composition. Differences in the spectral response of channels 1 and 2 manifested by soil color and brightness result from variations in soil properties, such as the amount of iron and organic material present. Figure C.1.f shows the variation in NDVI values over an area of the Sahara where the contribution of the bare surface to the signal measured by the satellite is large. The standard deviation of this sample is about 0.02 NDVI. The impact of the soil reflective properties on the NDVI becomes less important when the amount of vegetation cover increases. A number of vegetation indices are reported that are less sensitive to the soil background effects such as the soil-adjusted vegetation index (SAVI) described by Huete and Tucker (1991).

C.3 Steps in Processing GIMMS Continental NDVI Data

In this section processing the continental NDVI dataset is discussed and evaluated in terms of its adequacy to remove the effects summarized in section C.2. An outline of the major steps in the compilation of the dataset is given in figure C.2, and the order of magnitude of remaining effects on the NDVI through various stages of processing is assessed and summarized in Table C.3. Because of the large amount of data, labor, and resources involved in compiling the continental dataset, simple and robust algorithms were employed to reduce the processing time. Constraints in the amount of data storage available in the early stages of the GIMMS program caused datasets from intermediate stages in data processing to be discarded. For example, the individual channel data that are necessary to correct the NDVI for atmospheric scattering and absorption are unavailable in this dataset.

C.3.1 Organization of Level 1B Data

The first stage in data processing merely organizes the NOAA data to facilitate subsequent data processing. In the original level 1B format provided by NOAA/National Environmental Satellite Data and Information Service (NESDIS), global area coverage (GAC) data are stored as full orbits and include measurements of the land surface as well as the oceans. The orbits are divided and organized by continent for efficient manipulation and to reduce data processing (Table C.2).

C.3.2 Mapping the Daily Global Area Coverage (GAC) Data

In the second stage, global area coverage (GAC) data were processed by continent. Simple algorithms were imple-

APPENDIX C. A GLOBAL 1° BY 1° NDVI DATASET FOR CLIMATE STUDIES

Table C.2: Organization of the GIMMS dataset by continent with properties of projections. HA = Hammer Aitoff polyconic equal area, CED = conical equidistant projection with two standard parallels (Maling, 1973).

continent	projection	pixel size (km)	T threshold (K)	upper left corner	lower right corner	center
N-America	HA	8.0*5.5	273	70° N - 157° W	9° N - 65° W	40° N -103° W
S-America	HA	7.0*6.5	273	23° N - 97° W	56° S - 15° W	16° S - 64° W
Europe	HA	7.5*4.5	273	75° N - 82° W	24° N - 58° E	50° N - 25° E
Africa	HA	7.5*8.0	288	45° N - 30° W	43° S - 62° E	1° N - 17° E
Asia	HA	13.5*5.5	273	70° N -76° W	18° N - 150° W	50° N - 90° E
Centr. Asia	HA	5.5*4.5	273	66° N - 17° E	14° N - 114° E	40° N - 82° E
S-Asia	HA	5.5*5.0	273	50° N - 46° E	0° N - 121° E	25° N - 90° E
SE-Asia	HA	5.5*5.0	273	35° N - 84° E	15° S - 152° E	10° N - 120° E
Australia	CED	5.5*5.0	273	4° N - 101° E	44° S - 169° W	25° S - 135° E

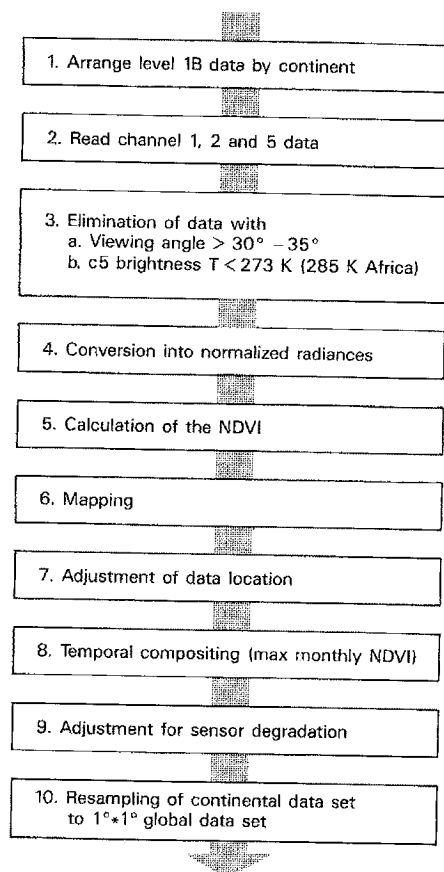


Figure C.2: Main steps in processing the NOAA-AVHRR level 1B data into the continental and global datasets (see section C.3)

mented to eliminate or reduce the impact of data that were affected by cloud contamination, atmospheric scattering and absorption, and viewing geometry. The remaining data were mapped to cartographic projections and stored in image format (Table C.2). The generalized stages of processing are shown in figure C.2 and can be summarized as follows:

1. Organizing level 1B data (previous section)
2. Reading channels 1, 2 and 5 data from the continental dataset tapes.
3. Eliminating spurious data based on the following thresholds:
 - (a) The 45 outer pixels on either side of a scan are discarded. This corresponds to eliminating data from viewing angles larger than 42° off-nadir. This cut-off reduces the variation in ΔNDVI ($\text{NDVI}_\theta - \text{NDVI}_0$), with θ the viewing angle) as a result of viewing geometry, in some cases by as much as 50%. For example, Holben (1986) found for an average aerosol load and a top-of-the-atmosphere NDVI of 0.6 observed at nadir, a ΔNDVI of + 0.02 at 10° to 20° in the forward scatter, and a ΔNDVI of -0.18 and -0.08 for 56° and 42°, respectively, in the backscatter direction (figure C.1.e).
 - (b) Cloud-affected data are detected by low surface brightness temperatures in the AVHRR thermal-infrared channel 5. For Africa, data with a temperature below 288 K are eliminated, for the other continents a temperature threshold of 273 K is used. The cloud screening technique does not eliminate data from warm clouds or from partially cloudy "mixed" pixels. For example, Eck and Kalb (1991) show that only part of the cloud cover in the Gulf of Guinea is removed by the temperature threshold technique. Similar problems are found in other areas with persistent cloud cover, such as north-east India during the monsoon, and the South American, African, and southeast Asian tropical rain forests (figure C.1.b). Cloud cover, with typically low NDVI, will lead to increased spatial variability over tropical areas with high NDVI (areas in the tropics with high spatial variability are identified in section C.5

and figure C.3.a). A problem inherent to the cloud screening technique is the elimination of all data with low brightness temperature, whether they are from clouds or from land surfaces. As a result, the continental dataset does not contain data for high latitude areas during the Northern Hemisphere winter (figure E.4.a). This will cause the disappearance of all vegetation during the winter, even of evergreen needle trees, which will affect estimates of vegetation dependent parameters such as surface roughness and albedo (Sellers *et al.* 1996b, Appendix D).

4. Channels 1 and 2 digital counts are converted to radiances and normalized for the solar flux at the top of the atmosphere in the respective bands using the preflight calibration provided by NOAA (Kidwell 1995). The resulting values correspond to reflectance values in the case of an overhead Sun. The preflight calibration does not take sensor degradation into account (figure C.1.a, Appendix A, B).

5. The NDVI is calculated according to

$$\text{NDVI} = \frac{L_2^N - L_1^N}{L_2^N + L_1^N}, \quad (\text{C.1})$$

with L_1^N and L_2^N the normalized radiance values in channel 1 (visible) and 2 (near-infrared), respectively. Using normalized radiances results in the same NDVI values as if reflectance values were used, because the cosine of the solar zenith angle cancels in equation C.1. The conversion of channels 1 and 2 data into the NDVI strongly reduces the impact of varying illumination conditions and shadowing effects that are, for example, caused by variations in solar and viewing angle (Kimes *et al.* 1984).

6. The NDVI data are mapped to an equal area or equidistant projection (Table C.2), in blocks of 1 to 5 days of data at a time. The resolution of the GAC data is reduced to allow display of a continent on a 1280 by 1024 element screen (Table C.2 lists the resolutions of the projections). In cases where pixels overlap, the value of the pixel with the highest NDVI is used. This procedure will lead to selection of higher values than if the nearest neighbor of the element were selected. An average difference of +0.03 NDVI between maximum value and nearest neighbor sampling was found over a 1° by 1° cell in the African equatorial forest. Some areas on the edges of continents were not mapped in a consistent fashion: most data for New Zealand, and some data from the southern parts of Central America (mainly for 1982) and the southeast coast of the Arabian Peninsula (mainly for 1982) are missing.

7. A visual check of the registration was made by comparing the outlines of continents and rivers in the image with those in the Central Intelligence Agency (CIA) World Data Bank II (Gorny 1977). When a mismatch between features was found, the entire image was shifted over a whole number of pixels to fit the CIA World Data Bank II. This reduces the registration error of the final product to ~4 - 8 km (~1 - 2 pixels).

8. Compositing: The daily images show large areas where data are missing. These areas result from gaps between mapped orbits and from data elimination during the various stages of processing. The amount of useful data is further reduced by the effects of clouds, atmosphere, and viewing and illumination geometry. To obtain almost complete cover of the land surface and to reduce the impact of these effects, a monthly maximum value composite is obtained from the daily images by selecting the maximum NDVI of the month for each pixel. Because most of the cloud, atmosphere and viewing effects decrease the NDVI, compositing will result in monthly NDVI values that for the main part are selected from data collected at near-nadir viewing angles under cloud-free, clear atmospheric conditions (Holben 1986). Changes in NDVI values as a result of sensor degradation, solar zenith angle, and soil background cannot be accounted for by compositing.

C.3.3 The Monthly NDVI Composites

After compositing, evidence of inconsistencies are still present in the NDVI data. Examples of areas where decreased NDVI values are found are in the tropics and subtropics as a result of persistent cloud cover (*e.g.*, Gulf of Guinea during August - September, equatorial Africa, Amazon, Indonesia, northeast India during the monsoon, figure C.1.b); of areas near the ITCZ as a result of prolonged high humidity, (*e.g.*, figure C.1.d, Justice *et al.* 1991a), and after volcanic eruptions as a result of long term presence of atmospheric aerosols (*e.g.*, El Chichon, see Tucker and Matson 1985; and Mount Pinatubo, see figure C.1.c and Vermote *et al.* 1995).

The extent to which errors due to off-nadir viewing geometry are diminished depends on the frequency of occurrence of cloud-free, clear atmosphere data (Kaufman *et al.* 1992). Under favorable conditions, data from slight forward scatter positions (10° - 20°) tend to be selected. For densely vegetated areas this can result in values of ~0.02 higher NDVI as compared to data collected at a nadir viewing angle. When the occurrence of cloud or atmospheric turbidity becomes more frequent, preference for the forward scatter viewing angles is less pronounced,

Table C.3: Estimates of the magnitude of possible errors in the continental and global normalized difference vegetation index datasets.

	8 km data	1°*1°	source
cloud	$-0.7 < e < 0$	$-0.3 < e < 0$	time-series
atmosphere	$-0.3 < e < -0.1$	$-0.2 < e < -0.1$	Holben (1986), Tanré <i>et al.</i> (1992)
solar zenith angle	$-0.2 < e < 0$	$-0.2 < e < 0$	Sellers <i>et al.</i> (this issue)
terminator	$e > \text{signal}$	$e > \text{signal}$	Holben (1986)
soil background	$-0.07 < e < 0.08$	$-0.07 < e < 0.08$	Huete and Tucker (1991)
viewing angle	$-0.1 < e < 0.05$	$-0.02 < e < 0.02$	Holben (1986)
compositing	$0 < e < 0.05$	$0 < e < 0.02$	time-series analysis
registration	$0 < e < 0.03$	$0 < e < 0.01$	equatorial forest
sensor degradation	$-0.1 < e < 0.01$	N/A	Los (1993)
sensor degradation after adjustment	$-0.002 < e < 0.002$	0	Los (1993)
Non-linearities c1, c2 versus NDVI	0	$-0.005 < e < 0.015$	this paper (figure C.3)

and data are selected more randomly over the range of viewing angles.

Forming composites of misregistered data results in increased NDVI values for adjacent areas of different vegetation density. For the study of local phenomena this inaccuracy may be a limitation, but for global studies, with data resampled to a much coarser resolution, the net effect is believed to be small.

For areas where a gradual change of vegetation occurs within the compositing period, a positive bias in the NDVI is likely to be introduced. In the case of growing vegetation, values near the end of the month tend to be selected, for senescing vegetation the bias will be to selection of values collected at the beginning of the month. Assuming a linear change from one month to the next, the error is about $0.5 * (NDVI_{t+1} - NDVI_{t-1}) * (\text{day}_n - \text{day}_{15}) / (\text{ndays})$ with day_{15} indicating the 15th day of the month and day_n the day from which the value was selected. Examples of the diminished magnitude of errors as a result of compositing are given in Table C.3.

C.3.4 Correction for Sensor Degradation

Because the correction for sensor degradation involves both additive and multiplicative terms, it is best applied separately to single channel data. However, information on individual channel data is not retained in the mapped daily data or the maximum value composites. To adjust the monthly NDVI composites for the effect of sensor degradation, an approximation was used that was developed by Los (1993). This approximation uses NDVI as the only input and the parameters of Kaufman and Holben (1993) and Holben *et al.* (1990). Using this approximation, an acceptable accuracy (Root Mean Square—RMS smaller than 0.002 NDVI) can be obtained. This is generally much better than the absolute accuracy with which sensor degradation can be established (~5%–10% in both channels 1 and 2, Holben personal communication), and is of the same order or smaller than the relative

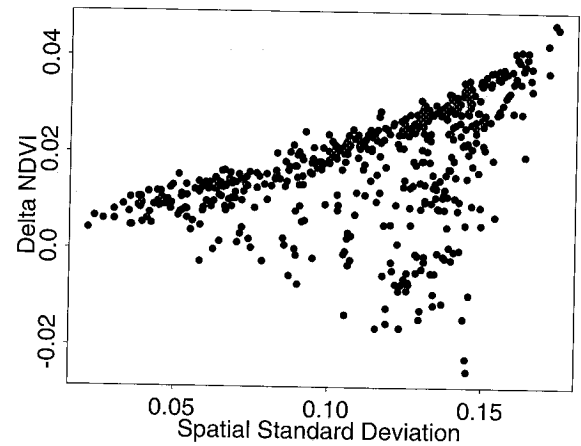


Figure C.3: Effect of non-linearities between channels 1 and 2 normalized radiances versus normalized difference vegetation index (NDVI) as a function of standard deviation. $\Delta NDVI$ is the difference between the NDVI averaged over 128 values and the NDVI calculated from the average of 128 channels 1 and 2 data pairs. Dataset was generated using random mixtures of three end members (dark soil, bright soil and vegetation) with various weights assigned (see text).

accuracy.

C.4 Formation of the Continental Data Into a Global Dataset

To obtain a resolution that is useful to GCM studies, the data were resampled to 1° by 1°. The 1° by 1° grid cell has dimensions of ~110 by 110 km at the equator and represents ~12 by 12 to ~20 by 20 GAC pixels depending on latitude and resolution of the projection. Resampling was done by averaging over 1° by 1°. Missing values, NDVI data from solar zenith angles larger than 85°, and data from water bodies such as oceans, seas, and lakes, were excluded from averaging. NDVI data from rivers were

not excluded, but their impact is believed to be small because the combined effects of compositing and misregistration strongly reduce linear features with low NDVI values. Surface water was identified with a mask based on the outlines of continents and lakes in the CIA World Data Bank II (Gorny 1977). The outlines of the data base were included with the surface water mask. Each 1° by 1° cell was identified as a landsurface cell and assigned a NDVI value if it contained less than 50% surface water. Because New Zealand was not mapped in a consistent fashion, a maximum value composite for all the individual months was made using the 9 years of data. For example, all January data from 1982–1990 were combined to obtain one January dataset. This dataset was then used to represent the NDVI of all the months of January from 1982 until 1990. As a result, the New Zealand data do not show changes from one year to the next.

Averaging over the 1° by 1° grid cells may lead to inaccuracies caused by non-linearities in the relationships between the NDVI and channels 1 and 2 data and between the NDVI and biophysical parameters to be derived. The error in the average resulting from non-linearities in the channels 1 and 2 versus NDVI relationship is depicted in figure C.3 as a function of the spread of NDVI values (standard deviation) within a 1° by 1° cell. Each data point in figure C.3 was calculated from 128 data points generated by

$$\rho_i = \frac{(w_1 r_{1,i,1} + w_2 r_{2,i,2} + w_3 r_{3,i,3})}{(w_1 r_1 + w_2 r_2 + w_3 r_3)}, \quad (C.2)$$

with r_1, r_2, r_3 = random numbers between 0 and 1; w_1, w_2, w_3 weights that were identical for each set of 128 channel pairs, but varied among sets to obtain a wide range of standard deviations (each weight was assigned values 1,2,5,10,17); $(\rho_{v,1}, \rho_{n,1}) = (0.04, 0.23)$; $(\rho_{v,2}, \rho_{n,2}) = (0.04, 0.05)$; $(\rho_{v,3}, \rho_{n,3}) = (0.40, 0.42)$ representing end-members for a vegetated surface, a dark background and a bright background, respectively. For each set, the standard deviation of the NDVI values and the differences between the average NDVI and the NDVI of the averages of the channel pairs were calculated. The relationship between these as depicted in figure C.3 shows that the error introduced by averaging as a result of non-linearities in the NDVI versus channels 1 and 2 relationship is small; a comparison between figures C.3 and E.6.a shows that this error will be between -0.005 and +0.015 NDVI for most cases.

The relationship between the NDVI or simple ratio (SR) and the fraction of photosynthetically active radiation absorbed by the green vegetation canopy (FPAR), which is crucial to calculating other biophysical parameters, was found to be largely scale-invariant in several studies (Sellers *et al.* 1992b, Asrar *et al.* 1992). Selecting the average to represent the NDVI of a 1° by 1° grid cell is

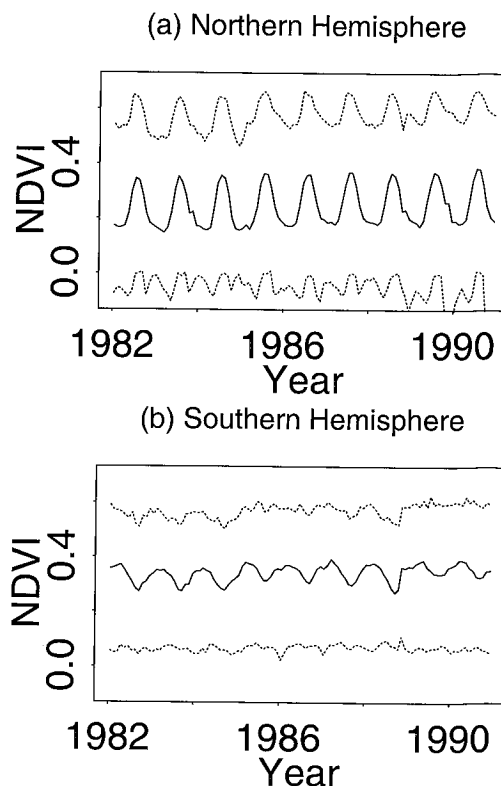


Figure C.4: (a) Temporal development of statistics of the normalized difference vegetation index for the Northern Hemisphere land surface over the period of January 1982 to December 1990 (98 percentile, average, and 2 percentile). (b) same for the Southern Hemisphere.

therefore believed to be an appropriate choice. In highly heterogeneous areas, the assumptions of scale invariance and linearity of relationships may not hold. Areas with high spatial heterogeneity are identified in Appendix C.5.

C.4.1 Discussion of the Global 1° by 1° NDVI Data

Examples of the global dataset are shown in figures E.4, E.5, and C.4. Figures E.4.a and E.4.b (February and August 1987) depict the NDVI for a Northern Hemisphere winter and summer, respectively. In winter, vegetation activity is concentrated in the Southern Hemisphere, whereas in summer the vegetation is active in the Northern Hemisphere and over a much larger area. Also shown in the winter image are the large areas without data at high latitudes. Figure E.5.a shows the average NDVI over the entire period of 9 years, and figure E.5.b the coefficient of variation (standard deviation divided by the mean) over the same period. For calculating the average and the coefficient of variation, missing values over the land surface were set to NDVI = 0. The average NDVI over one season, or multiple seasons as in this case, was found to be an important parameter for calculating

primary production of vegetation (Kumar and Monteith 1982, Steven *et al.* 1983, Goward and Dye 1987). Not surprisingly, the average NDVI is highest in the tropics, and in humid mid-latitude areas such as the East coast and the Pacific Northwest in the United States, western Europe, and eastern Australia. A belt of intermediate values more-or-less coincides with the location of boreal forests in North America and Eurasia. Also notice the differences in the average NDVI between the Sahara and the deserts of Australia and North America, reflecting somewhat higher amounts of vegetation, or possibly differences in the composition of the soil background, in the latter two.

Figure E.5.b shows the coefficient of variation. This value is low over both tropical forests and deserts, indicating that these areas show little seasonal variation. Intermediate to high values are found in areas that exhibit higher seasonality and variation in the amount of vegetation between years (Sahel, India, China). High coefficients of variation are found in high latitude areas, with a belt of local minima roughly coinciding with the extent of the boreal forest. Some of the variation at high latitudes is caused by missing values and the inclusion of aberrant data (*e.g.*, from high solar zenith angles). Figure C.4 shows the temporal development of statistics of the NDVI (average, and 2 and 98 percentiles of the monthly NDVI distributions) over the Northern and Southern Hemisphere land surfaces. Compared to the Northern Hemisphere, the variations in seasonality in the Southern Hemisphere are less pronounced. The very small variations in the 2% values indicate that the data were appropriately corrected for sensor degradation. The anomalies in the 2% values during the Northern Hemisphere winters of 1989 and 1990 are caused by incorporating data from high latitude areas that were not included in the other years. Note that NDVI values are expected to be decreased as a result of the volcanic eruption of El Chichon (middle of 1982 to about the end of 1983) and as a result of higher solar zenith angles at the end of the time of operation of the satellites.

A summary of the magnitude of the errors in the 1° by 1° NDVI data is given in Table C.3. The estimates of cloud and atmospheric effects in the 1° by 1° data were made by analyzing time-series data. Solar zenith angle, soil background, and terminator effects are assumed to be spatially correlated, hence compositing, will not diminish their effect. Viewing angle, compositing and registration errors were calculated assuming a spatially random distribution of errors and 4 clear views per month for each pixel. The largest errors in this dataset are caused by cloud contamination, atmospheric attenuation, and solar zenith angle variations. These errors are systematic and their effect is found over large areas and can persist over time. Errors that are about an order of magnitude smaller are caused by remaining variations in viewing an-

gle, soil background, misregistration, compositing, and resampling. These errors have, in some cases, opposite signs: errors caused by variations in viewing geometry are negative or slightly positive; errors as a result of compositing are positive, errors in misregistration in combination with compositing are positive. Because they are of opposite sign and about equal magnitude, these errors will, to some extent, cancel each other out. The error introduced by resampling as a result of the non-linearity of the NDVI versus channels 1 and 2 relationship can be both positive or negative. The effect of soil background is largest for the low end of the range of NDVI values over the land surface, but is not important for the high end. The errors resulting from sensor degradation that remain in the dataset after the adjustment by Los (1993) and averaging over 1° by 1° are negligible.

C.5 Spatial Degradation

Averaging the high resolution (5 - 8 km) NDVI data to provide one value representative of the entire 1° by 1° cell results in a loss of spatial information within the cell. For areas that exhibit little spatial variability in the NDVI, averaging will lead to little loss in information. However, those areas which exhibit high spatial variability or markedly bimodal distributions in the NDVI are poorly represented by an average value and may require alternative procedures to derive meaningful biophysical parameters.

A study was undertaken to identify those areas of high spatial variability, where resampling to 1° by 1° might result in a misrepresentation of surface state. It is recognized that the 8-km source product for the 1° by 1° dataset is subject to substantial spatial degradation by onboard sampling and mapping of the data. It is also recognized that a considerable amount of spatial variation on the land surface takes place at scales below the 8-km resolution of the global area coverage (GAC) data (Townshend and Justice 1990).

Figure E.6.a shows the sum of the standard deviations from each month for 1987 for each 1° by 1° cell. This annual sum of the standard deviations highlights those cells with consistently high spatial variability throughout the year. Areas with low spatial variability throughout the year correspond to hot and cold desert areas. Cells showing the highest overall variability correspond to the major mountain chains of the world: the Andes, the Himalayas, the Kunlun Mountains, the African Rift Valley, the Rocky Mountains, and the Alps. These areas show a considerable variability in vegetation distribution as a function of elevation and large variations in illumination due to relief, but also have a high incidence of cloud and snow cover which will contribute to the variability in the NDVI. In addition, areas of persistent cloud cover such as

in equatorial Guinea, Venezuela, Guyana, and Kalimantan exhibit a high overall variability in the NDVI. Other areas exhibiting a high overall spatial variability include cells containing major rivers or wetland areas, such as the Nile Valley, the Pantanal and the Indus Valley. A further but minor category of areas of high spatial variability in the NDVI includes areas with a mix of land and water which remain after the coastal masking using the World Data Bank II, for example the fjord coasts of northern Norway and Tierra del Fuego and the islands of the West Indies, Sulawesi, the Philippines, and the Arctic Ocean.

In addition to the overall spatial variability, it is important to recognize that the spatial variability in vegetation distribution has various temporal characteristics. Figure E.6.b shows the standard deviation of the monthly, spatial standard deviations which gives one measure of how the spatial variability changes through the year. Areas exhibiting a high temporal variability in their spatial variability include the semi-arid areas of annual grasslands at the margins of the world's deserts, *e.g.*, the Sahel and Mongolia. In these areas, vegetative activity is restricted to two or three months of the year and is highly variable spatially, being dependent on rainfall, the occurrence of (near) surface water, etc. It is also worth noting that these areas will most likely exhibit large inter-annual variability in the NDVI (Figure E.5.b, Prince 1991, Tucker *et al.* 1986b, 1991a, b). The high latitudes in the Northern Hemisphere also have a very short growing season and show a marked seasonality in the spatial distribution of the NDVI. For example, the 1° by 1° grid cells in western Siberia and Alaska show data only two to three months of the year with a high standard deviation. In South America, the Cerrado in Brazil also shows a high seasonal spatial variability.

The above observations of spatial variability within 1° by 1° cells show those areas where a single average NDVI value may provide a poor representation of the cell. This is particularly the case in areas of rugged relief or those areas exhibiting a strong climatic gradient. It is apparent that an area of $\sim 10,000 \text{ km}^2$ can include a wide range of vegetation types and conditions. If one wishes to monitor such areas in the context of climate change studies, then clearly it is advisable to do so at a much higher spatial resolution than offered by this 1° by 1° dataset. The study also shows that the spatial characteristics of a cell can vary through one year of observations.

Previous research has demonstrated that at 1° by 1° spatial resolution it is possible to capture the broad patterns of global vegetation and that at this scale climate appears to be the major factor in vegetation patterns (Justice *et al.* 1991b). Our 1° by 1° dataset is designed specifically for use at the scale of current global climate models. Future analyses will have to overcome the problems of scaling up over such large areas, possibly through a process of aggregation from higher resolution analyses.

C.6 Discussion

The GIMMS NDVI dataset satisfies the requirements of internal consistency and sufficient spatial and temporal resolution to quantitatively derive biophysical parameters for use in GCMs. Compared to landcover classifications previously used to derive global parameter fields for use in GCMs, much was gained because the spatial and temporal patterns are more closely reflected by the NDVI data. Figures C.5.a–C.5.l illustrate these points. In these figures the temporal development of NDVI statistics in the Northern Hemisphere for 1987 is shown for the 12 landcover classes used by Dorman and Sellers (1989). For two vegetation types (figures C.5.h and i), data for the winter months are not shown because they are few and for the most part suspect. Note that, except for class 12, Dorman and Sellers assigned the same biophysical properties to an entire class. The NDVI statistics for the months of 1987, the 5 and 95 percentiles, the average and the average plus or minus the standard deviation, do reflect within-class variation for all classes in figure C.5, except for the bare soil class. Also shown are variations in the timing of the start of the growing season for low and high ranges of NDVI; see for example the distributions for deciduous forest with evergreens (figure C.5.c), the sub-tropical drought-deciduous woodland (figure C.5.f), and the grasslands with shrub cover (figure C.5.g). Examples of variations in the spatial distribution of the data are found in figures E.4 and E.5 (*e.g.*, the gradient between the Sahara and the equatorial forest, and presence of elevated values along large rivers in semi-arid areas).

Although it seems fair to say that the dataset represents an improvement in the description of global vegetation dynamics, it has problems that need to be addressed to obtain more reliable estimates of biophysical parameters. The most significant inconsistencies in the data are caused by persistent cloud cover, atmospheric perturbations, elimination of data with low surface temperature and solar zenith angle effect. The adjustment of these errors is discussed in a companion paper by Sellers *et al.* (1996b; Chapter 5, Appendix D). Other errors are effectively dealt with by processing the data and they are of minor importance. These are errors that remain after the adjustment for sensor degradation, compositing, off-nadir viewing, and soil background reflective properties, or errors that are introduced by resampling the data over 1° by 1° .

Errors caused by cloud contamination, atmospheric attenuation, and solar zenith angle can be large and may lead to underestimation of biophysical parameter values. For example, if we assume a tropical forest with a top-of-the-atmosphere NDVI of 0.6 throughout the year and the combined effect of clouds and atmosphere to be -0.2 NDVI, and we attempt to calculate primary production (P) using (Kumar and Monteith 1982, Prince 1991),

APPENDIX C. A GLOBAL 1° BY 1° NDVI DATASET FOR CLIMATE STUDIES

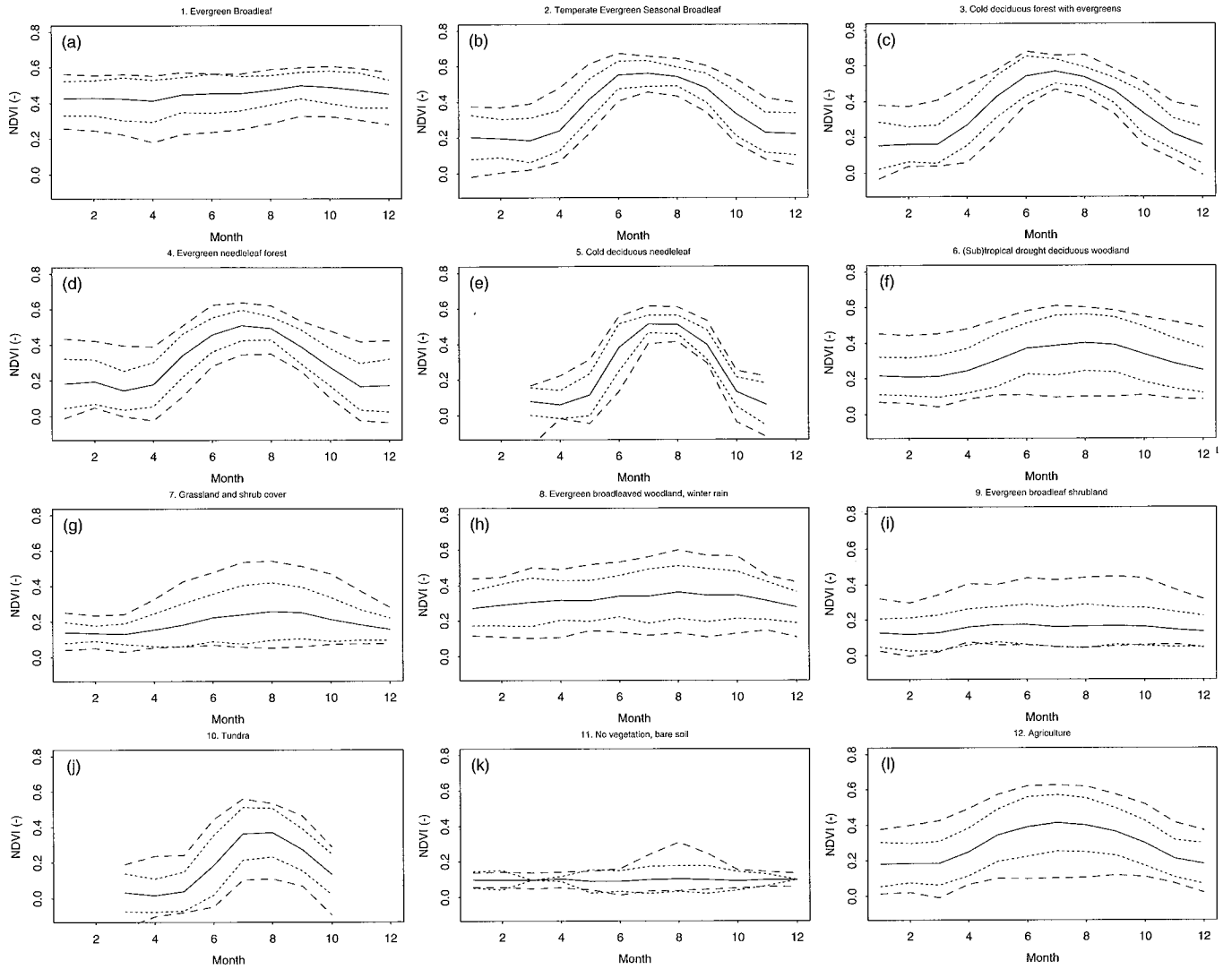


Figure C.5: Normalized difference vegetation index time-series for the 12 landcover classes (a to l) used by Dorman and Sellers (1989). Dotted line = 5%, dashed line = average – standard deviation, solid line = average, dashed line = average + standard deviation, dotted line = 95%.

C.7 Conclusion

The global 1° by 1° NDVI dataset contains useful information on the temporal and spatial distribution of vegetation. Biophysical parameters that are derived from these data will therefore in principle reflect more closely the temporal and spatial variations of vegetation than those previously derived from *in situ* observations and landcover classifications. A limitation to the NDVI data is the presence of suspect data, generally with decreased values, that are due to persistent cloud cover, atmospheric attenuation, solar zenith angle variations, and missing data. The magnitude of inconsistencies in the dataset can be as large as -0.1 to -0.2 NDVI units. Other effects in the NDVI, caused by viewing geometry, misregistration, sensor degradation, and non-linearities in the NDVI

$$P \propto \sum \text{NDVI} * \text{PAR}, \quad (\text{C.3})$$

which assumes NDVI measurements on the ground, we will obtain an error of -25%. Similarly, if we use the same model over a desert, we may obtain a small value for primary production, where there in fact is none. One way to avoid this type of problem is to scale the data to a maximum and minimum NDVI value, and then relate these to known maximum and minimum values of biophysical parameters (see Sellers *et al.* 1996b, Chapter 5, Appendix D).

and channels 1 and 2 relationships, are effectively reduced during processing, mainly by compositing and adjusting for sensor degradation. These deviations are estimated to be an order of magnitude smaller and are further reduced after spatial averaging of the continental data over the 1° by 1° grid. Variations in NDVI caused by the soil background are not accounted for, but these effects will be important to the low range of NDVI values only.

Regarding scaling, the 1° by 1° resolution seems a reasonable compromise between minimizing the amount of data for use in GCMs and retaining enough spatial detail to address the dynamics of vegetation. The current resolution that is used by the SiB-GCM is 4° by 5° , but it is to be expected that future runs will employ higher resolution data as fine as 1° by 1° . At 4° by 5° resolution, the principal vegetation patterns can be discerned; however, it is clear that changes in small areas, for example around desert margins, will be undetectable.

The dataset presented in this paper should be viewed as a basis for specifying landsurface boundary conditions in GCMs. Future global products should retain information on individual channels and viewing geometry, should have advanced ways to correct for atmospheric scattering and absorption, and better ways to identify and eliminate clouds.

Acknowledgments

This research was funded by the NASA Earth Observing System Interdisciplinary science (EOS-IDS) program, Biosphere-Atmosphere Interactions project (contract NAS-531732). Thanks to Piers Sellers for critical reading of the manuscript and comments for its improvement. Computer code that aided in processing the global dataset was developed by Hong Zhang. The NDVI continental datasets could not have been compiled without the contributions of the members of the GIMMS group, in particular Wayne Newcomb, Dave and John Rosenfelder, and Bob Rank. Their efforts are gratefully acknowledged.

Appendix D

The Generation of Global Fields of Terrestrial Biophysical Parameters From Satellite Data

Slightly revised from publication by P.J. Sellers, S.O. Los, C.J. Tucker, C.O. Justice, D.A. Dazlich, G.J. Collatz, and D.A. Randall, 1996, A revised landsurface parameterization (SiB2) for atmospheric GCMs. Part 2: The generation of global fields of terrestrial biophysical parameters from satellite data, *J. Climate*, 9, 706-737.

Abstract

The global parameter fields used in the revised Simple Biosphere Model (SiB2) of Sellers *et al.* (1996a) are reviewed. The most important innovation over the earlier SiB1 parameter set of Dorman and Sellers (1989) is the use of satellite data to specify the time-varying phenological properties of FPAR, leaf area index, and canopy greenness fraction. This was done by processing a monthly 1° by 1° normalized difference vegetation index (NDVI) dataset obtained from Advanced Very High Resolution Radiometer (AVHRR) red and near-infrared data. Corrections were applied to the source NDVI dataset to account for (i) obvious anomalies in the data time-series, (ii) the effect of variations in solar zenith angle, (iii) data dropouts in cold regions where a temperature threshold procedure designed to screen for clouds also eliminated cold landsurface points, and (iv) persistent cloud cover in the tropics. An outline of the procedures for calculating the landsurface parameters from the corrected NDVI dataset is given, and a brief description of source material is provided, mainly derived from *in situ* observations, that was used in addition to the NDVI data. The datasets summarized in this paper should be superior to prescriptions currently used in most landsurface parameterizations in that the spatial and temporal dynamics of key landsurface parameters, in particular those related to vegetation, are obtained directly from a consistent set of global-scale observations instead of being inferred from a variety of survey-based landcover classifications.

D.1 Introduction

The last decade has seen significant progress in the development of landsurface parameterizations (LSPs) for

use within general circulation models of the atmosphere (GCMs). Dickinson (1984) and Sellers *et al.* (1986) designed and implemented LSPs based on biophysical principles and showed that their implementation in GCMs resulted in improved simulation of the continental fields of absorbed radiation, evapotranspiration, and precipitation (Sato *et al.* 1989).

The first generation of biophysical LSPs, the Biosphere Atmosphere Transfer Scheme (BATS) of Dickinson (1984), and the Simple Biosphere model (SiB) of Sellers *et al.* (1986), were designed to provide improved estimates of the exchanges of radiation, moisture, sensible heat, and momentum between the land surface and the atmosphere. The important parameters governing these exchanges are the albedo (radiative transfer), the roughness length (momentum transfer and turbulent exchange of heat and moisture), and the surface resistance (control of moisture flux from the vegetation and soil to the air). The surface resistance replaces the moisture availability functions used in earlier LSPs, see for example Budyko (1974). All GCMs require specification of these parameters or related quantities as time-series global fields. Until the mid - 1980s, these were arbitrarily prescribed as independent boundary conditions, or by using numbers inferred from field measurements. Dickinson (1984) and Sellers *et al.* (1986) developed sub-models for LSPs which calculated these parameters from knowledge of a few vegetation and soil quantities that could be directly measured or easily attributed to specific vegetation types (Table D.1). To obtain global fields for these parameters, the world's landcover types as defined by Kuchler (1983) and Matthews (1983) were lumped into twelve classes (Table D.2), each of which was assigned values for the quantities listed in Table D.1 based on an extensive survey of the ecological literature (Klink and Willmott 1985). The global distribution of landsurface parameters was obtained by combining Table D.1 with Table D.2. This was a difficult

and inexact task in the case of the phenological parameters of leaf area index and canopy greenness fraction which are essential for calculating the desired parameters. Dorman and Sellers (1989) used this approach for the original version of SiB, hereafter referred to as SiB1, to calculate a global climatology of albedo, roughness length, and stomatal resistance.

SiB1 has since been modified to include a more realistic model of leaf photosynthesis and conductance as proposed by Collatz *et al.* (1991, 1992). This leaf-scale model was analytically integrated to describe canopy conductance and photosynthesis as a function of physiological properties (specified for each vegetation type as in Table D.1), environmental conditions (provided by the GCM), and the canopy photosynthetically active radiation (PAR) use parameter, Π , which is defined as the fraction of photosynthetically active radiation absorbed by the green canopy (FPAR) divided by the mean canopy PAR extinction coefficient, \bar{k} : $\Pi = \text{FPAR}/\bar{k}$ (Sellers *et al.* 1992a, Sellers *et al.* 1996a). SiB2 requires definition of global time-varying fields of FPAR, total leaf area index, L_T , and canopy greenness fraction, N , which are of course closely related, to calculate the carbon assimilation rate or gross photosynthesis in addition to the fluxes of radiation, heat, moisture, and momentum. This task could be carried out using the methods described in Dorman and Sellers (1989). However, it is difficult to place much confidence in the accuracy of these survey-derived fields because of the large variations within landcover classes in the spatial and temporal patterns of FPAR, L_T , and canopy greenness fraction, N . To do better, we must make use of satellite data which alone can provide us with a continuous, consistent, global view of the world's vegetation.

This paper outlines a procedure for calculating global monthly fields of FPAR from the satellite-derived normalized difference vegetation index (NDVI) dataset by Los *et al.* (1994). A number of steps are involved in moving from the source NDVI dataset to FPAR and then to the required values of albedo (obtained from spectral hemispheric reflectances, $a_{\lambda,\mu}$), roughness length, (z_0) and canopy conductance, (g_c). In summary,

1. Simple corrections were applied to the 1° by 1° source NDVI data to account for anomalies in the seasonal time-series, solar zenith angle effects, data dropouts, and persistent cloud cover. The resulting product is called the Fourier Adjusted, Solar zenith angle corrected, Interpolated, and Reconstructed (FASIR)-NDVI and is described in detail in sections D.3.1 and D.4.
2. The FASIR-NDVI fields were combined with a landcover classification to derive fields of FPAR. These were analyzed in turn to calculate total leaf area index, L_T , and canopy greenness fraction, N ; see

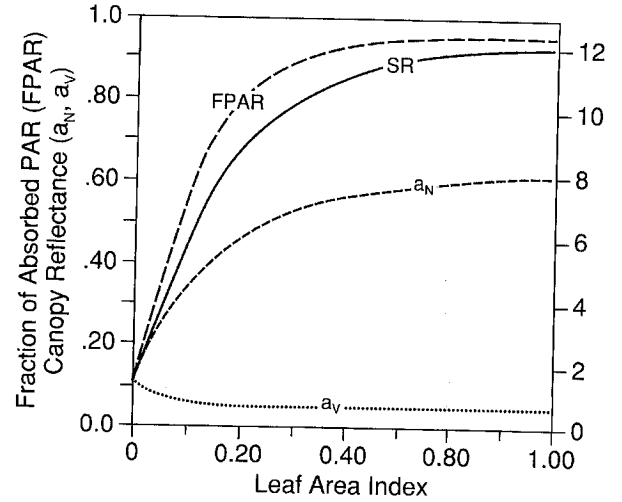


Figure D.1: Variation of visible (a_v) and near-infrared (NIR) (a_N) reflectance, simple ratio (SR) and fraction of photosynthetically active radiation absorbed by the green part of vegetation (FPAR), with leaf area index. (Green canopy, horizontal leaves; from Sellers *et al.* 1992a).

section D.5.

3. The fields of L_T and N were used to calculate hemispheric surface reflectances, $a_{\lambda,\mu}$, and roughness length, z_0 , using simple models; see section D.6. FPAR itself is used directly in SiB2 to calculate canopy photosynthesis, A_c , and conductance, g_c , and hence the surface energy balance; see section D.6 and Sellers *et al.* (1992a).

The satellite data are thus used to specify monthly values of FPAR, leaf area index, and canopy greenness fraction for each 1° by 1° grid area. Additional vegetation and soil parameters are required to further interpret these quantities into higher order parameters (albedo, roughness length, canopy conductance) and also for direct use in the LSP-GCM. These non-satellite-derived parameters are specified from literature sources in much the same way as was done in Dorman and Sellers (1989).

A paper by Sellers *et al.* (1996a) describes the formulation of SiB2 in full, and a paper by Randall *et al.* (1996) describes the performance of SiB2 within a GCM.

D.2 Theoretical Background

The complete formulation of SiB2 is set out in Sellers *et al.* (1996a) and papers referenced from it. For the purpose of illustration, a brief summary of the governing equations is presented below in order to show the role of the principal surface parameters in the energy and heat balance. The total surface energy balance is given by

Table D.1: Summary of parameters used by SiB1 and SiB2 sub-models. Note how some parameters are common to more than one sub-model, ensuring consistency among the derived fields of albedo, roughness, and energy fluxes. Time-varying parameters are denoted by asterisk. (Note that N is used to define daily mean leaf optical properties by weighting 'live' and 'dead' values held in the input parameter set). The same parameter categories apply to SiB2, except that only root depth is assigned for the category 'root physiology, morphology.' In SiB1 and SiB2, total leaf area index, L_T , and the canopy greenness fraction, N , vary seasonally. In SiB1, all vegetation of the same class in the same hemisphere has the same physiology, except for wheat where a simple latitudinal dependence is included; see Dorman and Sellers (1989). In SiB2, L_T and N are defined by vegetation type and satellite data and so vary temporally and spatially within vegetation classes.

	Radiative Transfer	Momentum Transfer	Stomatal Resistance
* Leaf Area Index, L_T	X	X	X
* Canopy greenness fraction, N	X		X
Leaf angle distribution function, $G(\mu)$	X	X	X
Cover fraction, V	X	X	X
Leaf optical properties	X		X
Soil optical properties	X		
Canopy top and base heights		X	
Leaf dimension		X	
Leaf physiological properties			X
Root physiology, morphology,			X
Soil physical properties			X

$$R_n - G = \lambda E + H, \quad (D.1)$$

with

$$\begin{aligned} R_n &= \text{net radiation, } W \text{ m}^{-2}, \\ G &= \text{ground heat flux, } W \text{ m}^{-2}, \\ \lambda E &= \text{latent heat flux, } W \text{ m}^{-2}, \\ H &= \text{sensible heat flux, } W \text{ m}^{-2}. \end{aligned}$$

D.2.1 Albedo

The net radiation, R_n , is given by

$$\begin{aligned} R_n = & \int_0^{4.0 \mu\text{m}} \int_0^{\pi/2} F_{\Lambda, \mu} \downarrow (1 - a_{\Lambda, \mu}) d\mu d\Lambda \\ & + \varepsilon (F_{T, d} \downarrow - \sigma T_s^4), \end{aligned} \quad (D.2)$$

with

$$\begin{aligned} F_{\Lambda, \mu} \downarrow &= \text{incoming radiation flux, } W \text{ m}^{-2}, \\ \Lambda &= (\text{subscript}) \text{ wavelength interval, } \mu\text{m}, \\ \mu &= (\text{subscript}) \text{ cosine of angle of incident radiation,} \\ a_{\Lambda, \mu} &= \text{surface hemispheric reflectance,} \\ \varepsilon &= \text{emissivity } \simeq 1.0, \\ F_{T, d} \downarrow &= \text{incident thermal infrared radiation (TIR),} \\ & \quad (\text{assumed to be all diffuse}), W \text{ m}^{-2}, \end{aligned}$$

$$\begin{aligned} T &= (\text{subscript}) \text{ thermal wavelength interval,} \\ d &= (\text{subscript}) \text{ diffuse radiation,} \\ \sigma &= \text{Stefan-Boltzman constant, } W \text{ m}^{-2} \text{K}^{-1}, \\ T_s &= \text{surface temperature, K.} \end{aligned}$$

In SiB2, the vegetation cover is 'bulked' into a single layer overlying the soil rather than two layers as used in SiB1. A two-stream approximation model is used to calculate hemispherical surface reflectances for incident direct and diffuse visible and near-infrared (NIR) radiation (Sellers 1985). The functions of $a_{\Lambda, \mu}$ in (D.2) are therefore divided into four reflectances (visible-direct, visible-diffuse, NIR-direct, and NIR-diffuse), with the spectral division between visible and NIR wavebands specified at $0.7 \mu\text{m}$, which corresponds to the abrupt change in leaf and chlorophyll optical properties. Dorman and Sellers (1989) presented evidence that the calculation of surface reflectances by this method gave results that compare well with field observations in areas of moderate to dense vegetation cover. In semi-arid and desert areas, the results were not so good because a single set of soil background reflectances was assigned to all arid areas in the world; this is unrealistic (Harrison *et al.* 1990).

Generally speaking, absolute errors or uncertainties in the albedo translate almost directly into errors in the calculation of net radiation and the heat fluxes of (D.1). This is because the surface net shortwave flux is around five times as large, although of opposite sign, as the net longwave flux (Sato *et al.* 1989, Table D.1).

The calculated reflectances and albedo of (D.2) are functions of the surface radiative transfer properties spec-

ified in Table D.1. Of these properties, the leaf spectral characteristics (live and dead) and the leaf angle distribution function can be assigned using published values; within vegetation classes, these parameters do not vary widely temporally or spatially, except when the vegetation is senescent. Soil reflectance usually plays a lesser role in the albedo of vegetated areas, but in arid areas it must be specified from direct observations. The major uncertainty in determining albedo by this method is therefore related to the amount and greenness of the vegetation cover.

Sellers (1987) explored the dependence of canopy reflectance on leaf area index and spectral properties using the two-stream model. It was shown that for a continuous canopy of horizontal leaves, for a specified wavelength interval,

$$a = \frac{\omega}{2} \left(\frac{1-A}{P_1 - P_2 A} \right), \quad (\text{D.3})$$

where

$$\begin{aligned} a &= \text{surface reflectance,} \\ A &= \left(\frac{P_1 - \gamma}{P_2 - \gamma} \right) e^{-2h_a L_T}, \\ \omega &= \text{leaf scattering coefficient,} \\ P_1 &= 1 - \omega/2 + h_a, \\ P_2 &= 1 - \omega/2 - h_a, \\ h_a &= (1 - \omega)^{1/2}, \text{ extinction coefficient for diffuse radiation,} \\ \gamma &= \omega/2a_s, \\ a_s &= \text{soil reflectance.} \end{aligned}$$

Similar expressions were derived for spherical and other leaf angle distributions. In (D.3), we see that reflectance depends strongly on the $e^{-2h_a L_T}$ term, where $2h_a$ is around 1.8 for visible radiation and 0.5 for NIR. In practice, most soil reflectances are fairly dark so the total albedo is weakly dependent on variations in the visible reflectance and more strongly dependent on the NIR contribution (figure E.9). Clearly, arid zones with bright soil backgrounds are the exception to this generalization, but the numerical consequences of applying this assumption do not seem to be serious (see later discussion, section D.9).

D.2.2 Surface Roughness

Turbulent exchange between the surface and the atmosphere determines not only the local-scale transfer of momentum, but also the transport of sensible and latent heat away from the surface. The details of the SiB2 aerodynamic transfer model are written up in Sellers *et al.* (1996a). Here we summarize the relationships between shear stress, aerodynamic resistance, and roughness length. Under neutral conditions

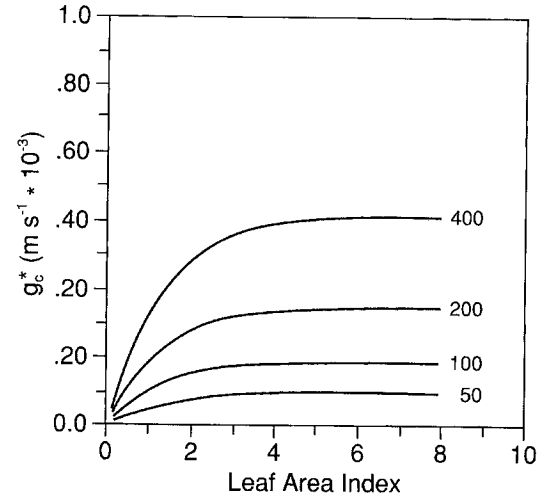


Figure D.2: Dependence of unstressed surface conductance ($g_c^* = 1/r_c^*$) on green leaf area index (from Sellers *et al.* 1992a).

$$\tau = \rho \frac{u_m}{r_a}, \quad (\text{D.4})$$

where

$$\begin{aligned} \tau &= \text{shear stress, kg m}^{-1} \text{ s}^{-2}, \\ \rho &= \text{air density, kg m}^{-3}, \\ u_m &= \text{wind speed at reference height, m s}^{-1}, \\ r_a &= \text{aerodynamic resistance for momentum transfer, s m}^{-1}, \end{aligned}$$

$$r_a = \frac{1}{u_m} \left[\frac{1}{k} \log \frac{z_m - d}{z_0} \right]^2 \quad (\text{D.5})$$

with

$$\begin{aligned} k &= \text{von Karman's constant} \simeq 0.41, \\ z_m &= \text{reference height, m,} \\ d &= \text{zero plane displacement, m,} \\ z_0 &= \text{roughness length, m.} \end{aligned}$$

In (D.4) and (D.5) we see that τ and r_a are related to the natural logarithm of z_0 . The SiB2 turbulent transfer sub-model calculates values of z_0 and d from the list of parameters shown in Tables D.1 and D.7 and yields a very weak exponential dependence on leaf area index (figure D.5). Over the normal range of leaf area index, *i.e.*, $0.5 < L_T < 5.0$, a simple expression can be plotted to the results of Sellers *et al.* (1989) to yield

$$z_0 = z_2 (1 - b_z e^{-h_z L_T}), \quad (\text{D.6})$$

with

$$\begin{aligned} z_2 &= \text{canopy height, m} \\ b_z &\approx 0.91 \\ h_z &\approx 0.0075. \end{aligned}$$

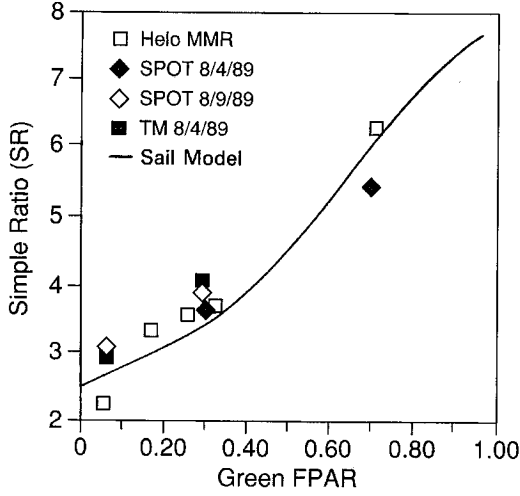


Figure D.3: Relationship between simple ratio vegetation index (SR) and FPAR for the Firsts ISLSCP² Field Experiment (FIFE) study area (redrawn from Hall *et al.* 1992). The SR data were taken from atmospherically corrected satellite and helicopter data. The FPAR data were made from light bar observations (green FPAR only). The line is a simulation produced by the Scattering from Arbitrary Inclined Leaves (SAIL) model (Hall *et al.* 1992).

D.2.3 Photosynthesis and Evapotranspiration

The details of the formulation used to calculate coupled photosynthesis and transpiration are presented in Sellers *et al.* (1992a, 1996a). The model calculates canopy photosynthesis and conductance as the product of three terms:

$$A_c = [V_{\max_0}, F_{\pi_0} \downarrow] [B_1 \cdots B_4] [\Pi] \quad (\text{D.7})$$

$$g_c = [V_{\max_0}, F_{\pi_0} \downarrow] [B_1 \cdots B_6] [\Pi] \quad (\text{D.8})$$

with

$$\begin{aligned} A_c &= \text{canopy photosynthetic rate,} \\ &\quad \text{mol m}^{-2} \text{ s}^{-1}, \\ g_c &= \text{canopy conductance, m s}^{-1}, \\ V_{\max_0} &= \text{maximum leaf catalytic (Rubisco)} \\ &\quad \text{capacity for green sun leaves,} \end{aligned}$$

$$\begin{aligned} F_{\pi_0} \downarrow &= \text{mol m}^{-2} \text{ s}^{-1}, \\ &\quad \text{incident radiant flux of photosynthetically} \\ &\quad \text{active (visible, } 0.4 - 0.7 \mu \text{ m)} \\ &\quad \text{radiation, W m}^{-2}, \\ B_1 \cdots B_6 &= \text{environmental stress factors dependent} \\ &\quad \text{on temperature, relative humidity, and} \\ &\quad \text{soil moisture,} \\ \Pi &= \text{canopy PAR use parameter.} \end{aligned}$$

The two left-hand terms of (D.7, D.8) are dependent on the vegetation physiology (V_{\max_0}), the incident flux of PAR (F_{π_0}), and local environmental conditions ($B_1 \cdots B_6$); see Sellers *et al.* (1992a, 1996a).

The vegetation physiological parameters and the coefficients governing B_1 and B_6 were obtained from published values, see Tables D.4 and D.5 and Sellers *et al.* (1996a). The crucial surface parameter in (D.7, D.8) is the canopy PAR use parameter, Π , which specifies the amount of green vegetation present; it varies from 0 (no vegetation) to around 1.5 (dense, green vegetation) (Sellers *et al.* 1992 a).

$$\Pi \approx \frac{\text{FPAR}}{\bar{k}}, \quad (\text{D.9})$$

where

$$\begin{aligned} \text{FPAR} &= \text{fraction of PAR absorbed by the green} \\ &\quad \text{vegetation canopy,} \\ \bar{k} &= \text{time-mean (radiation-weighted) extinction} \\ &\quad \text{coefficient for PAR.} \end{aligned}$$

FPAR can be approximated by

$$\text{FPAR} = VN(1 - e^{-\bar{k}L_T/V}), \quad (\text{D.10})$$

with

$$\begin{aligned} V &= \text{vegetation cover fraction,} \\ N &= \text{canopy greenness fraction (equation D.29),} \\ L_T &= \text{total leaf area index.} \end{aligned}$$

The conductance, g_c , given by (D.8) is used to calculate the canopy transpiration rate in SiB2. For a dry canopy with negligible energy fluxes to or from the soil, the SiB2 formulation approaches the Penman-Monteith equation

$$\lambda E = \frac{\Delta(R_n - G) + \rho c_p \delta_e / r_a}{\Delta + \gamma(r_c + r_a)/r_a}, \quad (\text{D.11})$$

with

$$\begin{aligned} \Delta &= \text{slope of the saturated vapor pressure versus} \\ &\quad \text{temperature curve, Pa K}^{-1}, \\ \gamma &= \text{psychrometric constant, Pa K}^{-1}, \\ \delta_e &= \text{vapor pressure deficit at } z_m, \text{ Pa} \\ &= e^*(T_m) - e_m, \end{aligned}$$

$$\begin{aligned}
 T_m &= \text{air temperature at } z_m, \text{ K}, \\
 e_m &= \text{vapor pressure at } z_m, \text{ Pa}, \\
 e^*(T_m) &= \text{saturated vapor pressure at temperature } T_m, \text{ Pa}, \\
 r_a &= \text{aerodynamic resistance for heat and water vapor, s m}^{-1}, \\
 r_c &= \text{canopy resistance, s m}^{-1} \\
 &= 1/g_c.
 \end{aligned}$$

In (D.11) the aerodynamic resistance for heat and water vapor, r_a , is closely related to r_a for momentum in (D.4); the value of z_0 for heat and water vapor transport is smaller than that for momentum (Sellers *et al.* 1986).

Under normal daytime conditions, the numerator of (D.11)—the evaporative demand—holds a moderate or high value. The evaporation rate is then largely regulated by the surface resistance, r_c , which is typically 5 or more times as large as r_a for most natural vegetation covers (figure D.2 and Sato *et al.* 1989; Sellers *et al.* 1992a).

D.2.4 Deriving Surface Parameters From Satellite Data

Equations (D.2), (D.4), (D.7), (D.8), and (D.11) define the fluxes of radiation (albedo), momentum (roughness length), photosynthesis, and evapotranspiration (biophysical control of gas exchange and surface heat fluxes), respectively. It should be noted that the governing parameters a , z_0 , and FPAR are not linearly related to total leaf area index, but to its exponent, such that

$$\begin{aligned}
 \text{Albedo, } a, &\propto e^{-2h_a L_T/V}, V, N, \\
 \text{Roughness length, } z_0, &\propto e^{-h_z L_T/V}, V, \\
 \text{FPAR, } &\propto e^{-\bar{k} L_T/V}, V N,
 \end{aligned}$$

where h_a , h_z , and \bar{k} are extinction coefficients and N is the canopy greenness fraction. The extinction coefficients $2h_a$ and k vary around 0.5 for green vegetation (h_z is small and for practical purposes z_0 is dependent on vegetation height to first order and only weakly on leaf area index). Thus we see that the transfers of radiation and mass (H_2O and CO_2) are sensitive to leaf area index at low values of L_T and reach a saturation level at high values of L_T because of an asymptotical increase with L_T .

Sellers *et al.* (1992a) built on work by Dickinson (1983), Asrar *et al.* (1984), Sellers (1985, 1987), Hall *et al.* (1990), and Myneni *et al.* (1992) on remote sensing of vegetation; and on work by Farquhar *et al.* (1980), Ball (1988), and Collatz *et al.* (1991) on plant physiology, to derive the relations between photosynthesis, conductance, and FPAR shown in (D.7, D.8), and also between FPAR and satellite-derived surface reflectances discussed below.

Two remotely-sensed vegetation indices are in common use, defined here as

$$\begin{aligned}
 \text{SR} &= \frac{a_N}{a_V} \\
 \text{NDVI} &= \frac{a_N - a_V}{a_N + a_V}, \quad (\text{D.12})
 \end{aligned}$$

with

$$\begin{aligned}
 \text{SR} &= \text{simple ratio,} \\
 \text{NDVI} &= \text{normalized difference vegetation index,} \\
 a_V, a_N &= \text{hemispheric reflectances, or radiances, for visible and NIR wavelength intervals respectively (sensor dependent).}
 \end{aligned}$$

In the theoretical treatment of Sellers *et al.* (1992a), a_V and a_N are taken as above-canopy reflectances, *i.e.*, the effects of atmospheric absorption and scattering were ignored. In this paper, a_V and a_N are replaced by radiances normalized for incoming solar radiation as observed by a satellite sensor.

Sellers (1987) used a two-stream model to show that for idealized conditions—uniform green canopy, dark underlying surface—the spectral vegetation indices should be proportional to the NIR reflectance, a_N , and to FPAR. It was shown that this useful relationship holds because the broad-band leaf scattering coefficients in the visible ($\omega_V \simeq 0.2$) and the NIR ($\omega_N \simeq 0.95$) are such that

$$\frac{\partial a_N}{\partial L_T} \propto \frac{\partial \text{FPAR}}{\partial L_T} \text{ for all values of } L_T. \quad (\text{D.13})$$

Equation (D.13) holds because the extinction coefficient for PAR flux or visible radiation (k) is roughly double the extinction coefficient for diffuse NIR flux (h_N) within the canopy, or

$$k \simeq 2h_N, \quad (\text{D.14})$$

which may be re-expressed as

$$\frac{G(\mu)}{\mu} (1 - \omega_V)^{1/2} = 2(1 - \omega_N)^{1/2}, \quad (\text{D.15})$$

where

$$\begin{aligned}
 G(\mu) &= \text{relative projected area of leaves in direction,} \\
 &\quad \cos^{-1} \mu \\
 \mu &= \text{cosine of solar zenith angle.}
 \end{aligned}$$

Simply put, equations (D.13), (D.14), and (D.15) hold because the near-infrared reflectance, a_N , which drives the SR and NDVI under most conditions, is proportional to double the pathlength of NIR radiation in the canopy ($e^{-2h_N L_T/V}$), as this radiation must enter, interact, and leave the canopy, while FPAR is proportional to only the one-way penetration and absorption of PAR through the canopy ($e^{-k L_T/V}$). The two parameters, a_N and FPAR, vary with each other if equations (D.14) and (D.15) are

approximately satisfied. For $\omega_V = 0.2$ and $\omega_N = 0.95$, equation (D.15) is exactly satisfied when $G(\mu)/\mu = 0.5$, i.e., a canopy of random leaf orientation exposed to a near-nadir solar flux. In practice, $G(\mu)/\mu$ usually lies between 0.5 and 1.0, and ω_N is somewhat lower, so equation D.15 is still approximately satisfied.

If the soil or background material is relatively dark, so that

$$\frac{\partial a_V}{\partial L_T} \rightarrow 0, \quad (\text{D.16})$$

SR will be mainly dependent on a_N , so

$$\frac{\partial(\text{SR})}{\partial L_T} \propto \frac{\partial a_N}{\partial L_T}, \quad (\text{D.17})$$

it follows then that FPAR is proportional to SR (figure D.3).

The set of relationships set out in (D.13) through (D.17) applies to the case of a horizontally homogeneous canopy overlying a dark soil. Hall *et al.* (1990) carried out a parallel analysis on the case of clumped vegetation and again found that FPAR and a spectral vegetation index (SVI) were usually near-linearly related. In Sellers *et al.* (1992a), these two findings were examined and it was shown that while $\text{SVI} \propto L_T$ relationships may vary widely between vegetation morphologies, the relationships between SVI, FPAR, A_c , g_c , and albedo should be more conservative.

Lastly, Sellers *et al.* (1992a) posited that because the relationships $\text{SVI} \rightarrow \text{FPAR} \rightarrow$ and non-stressed values of A_c , g_c were approximately linear they should be largely scale-invariant. This means that to first order, *spatial averages* of SVI can theoretically be used to calculate *spatial integrals* of A_c and g_c . This should be true whether one considers a canopy varying in depth, a canopy varying in cover fraction, or a canopy which does both. This finding, which is partially supported by the analysis of FIFE data in Sellers *et al.* (1992b), is immensely useful in that it supports our use of coarse resolution satellite SVI for the calculation of GCM grid scale surface parameters and fluxes.

It should be remembered that the analysis described above and a large body of experimental evidence, see for example Hall *et al.* (1992), relate the SVI to the live green material in the canopy, $N L_T$, rather than the total (living plus non-living) leaf area index, L_T .

D.3 Datasets

D.3.1 The Global 1° by 1° NDVI Dataset

One year of data (1987) of the global 1° by 1° monthly composited normalized difference vegetation index (NDVI) dataset discussed by Los *et al.* (1994) was

used to quantify both the spatial and temporal variability of landsurface parameters at monthly intervals, in particular those related to vegetation. This 1° by 1° NDVI dataset was calculated from the first generation Global Inventory, Monitoring, and Modeling System (GIMMS) continental NDVI datasets, which are based on Global Area Coverage (GAC) data (5 by 5 km) collected by channels 1 (red) and 2 (infrared) of the Advanced Very High Resolution Radiometer (AVHRR) on board the National Oceanic and Atmospheric Administration (NOAA) environmental satellites. These datasets were initiated by Tucker *et al.* (1986) specifically for landsurface studies.

Properties of the NOAA-AVHRR satellite-sensor system, such as the polar orbit of the satellite, the short interval between subsequent orbits and the wide viewing angles, allow for data collection of the entire Earth at almost daily intervals. For studies of the land surface, the objective is to compose cloud-free 'clear' views of the surface, eliminating cloud-contaminated or otherwise dubious data. In most regions, the true temporal coverage of the land surface by AVHRR data is severely reduced by cloud cover obscuring the Earth. Further limitations to the data are caused by scattering (molecules, aerosols) and absorption (ozone, water vapor) of radiation in the atmosphere, variations in the sensor viewing angle and illumination geometry, sensor degradation in channels 1 and 2 of the AVHRR, and variations in bidirectional reflectance properties of the Earth's surface (Holben 1986, Los *et al.* 1994). Several steps are included in the processing of the continental NDVI dataset to eliminate erroneous data and to reduce the effects of atmosphere, cloud remnants, and off-nadir viewing. A short description and an evaluation of the most important data processing steps are given below, more detailed discussions are provided in Holben (1986) and Los *et al.* (1994).

1. High and medium altitude clouds were identified and eliminated by the brightness temperature in AVHRR channel 5 with a threshold of 288 K for Africa and 273 K for other continents. This temperature-based threshold does not eliminate data from warm clouds or sub-pixel size clouds. In addition, data from areas with surface temperatures less than 273K were eliminated, resulting in missing data for high latitudes in the Northern Hemisphere during winter;
2. The outer 45 pixels on either side of a scan, corresponding to scan angles of about 42° or greater, were eliminated to avoid large variations in the data as a result of illumination and viewing geometry. Effects of increased atmospheric path lengths and surface bidirectional reflectance distribution function (BRDF) effects as a result of larger solar zenith angles were not eliminated by this cut-off;

APPENDIX D GENERATION OF GLOBAL BIOPHYSICAL PARAMETERS

3. A preflight calibration of channels 1 and 2 data as specified by NOAA (Kidwell 1995) was applied. This preflight calibration includes a normalization in each band for the intensity of incoming solar radiation;
4. The NDVI was calculated from the selected channels 1 and 2 reflectance values and mapped by continent on a stereographic projection. Because of limitations in data storage and processing capacity, no information on individual channel data was retained;
5. The maximum NDVI value for each month was selected for each pixel to obtain monthly maximum value composites. Because atmospheric scattering, absorption, and clouds all act to reduce the NDVI, selecting maximum values increases the contribution of data collected under cloud-free, clear sky conditions (Holben 1986). In the case of persistent cloud or other atmospheric effects, spurious data remain; e.g., Eck and Kalb (1991) reported on the presence of cloud-contaminated data not eliminated by either the temperature threshold or compositing technique in this dataset; Justice *et al.* (1991a) reported decreased NDVI values in the Sahel at the start of the growing season, due to the movement of large humid air masses into the region, associated with the migration of the intertropical convergence zone (ITCZ); and Tucker and Matson (1985) and Vermote *et al.* (1994) described the effect of atmospheric aerosols on the NDVI after the eruptions of El Chichón and Mt. Pinatubo, respectively. Maximum value compositing tends to favor selection of data from the forward-scatter direction (10° in the forward-scatter direction on average with 50% of the data between around 10° in the backscatter direction and 30° in the forward-scatter direction; see Gutman 1991) instead of near-nadir views as was previously assumed (Holben 1986). However, after averaging the NDVI data to 1° by 1° degree the variation in the NDVI as a result of view angle effects is likely to be small;
6. The effect of sensor degradation in AVHRR channels 1 and 2 on the NDVI was accounted for by an approximation developed by Los (1993). It is estimated that this approximation reduces biases between data segments taken at different times to less than 0.002 units of NDVI;
7. The continental datasets are resampled by averaging the pixels over 1° by 1° . Surface water and missing values are excluded from the averaging procedure. Averaging reduces the impact of random errors and in part cancels the effect of minor errors with opposite signs. Minor errors may be produced

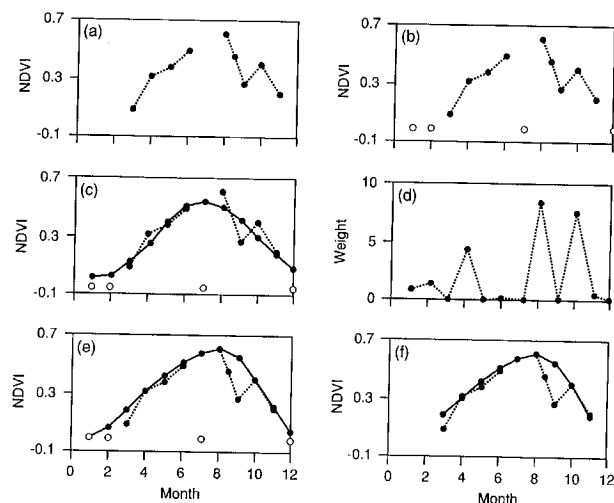


Figure D.4: Steps in the adjustment of NDVI time-series with robust least squares fitting of Fourier series (see items 1-6 in section D.4) (a) NDVI time-series with 4 missing values and one outlier. (b; D.4.1) Missing values are substituted with $NDVI = 0$ prior to fitting of the Fourier series. Note that the original value for July is inconsistent with the rest of the time-series. (c; D.4.2) Curve consisting of the first three harmonics (average, annual, bi-annual cycle) fitted through the data with least squares (equation D.19). (d; D.4.3) Weights calculated by comparing the fitted curve with the original data points. Values above the curve are assumed reliable (weights ≥ 1), values below the curve are assumed spurious (weights < 1 ; equation D.20). (e; D.4.4) Curve calculated with least squares using the weights under (d) Note that points at months 3, 5, 7, and 9 are left out of the fitting procedure (equation D.21). (f; D.4.5, 6) Comparison of a newly calculated value against the original value and its four nearest neighbors to avoid overestimation. Sequences of more than three missing values in the original data are set to missing values. These missing values are dealt with at a later stage in the FASIR procedures (sections D.4.2 and D.4.3).

from a positive bias in the NDVI due to compositing, variations in the NDVI caused by the spectral properties of the soil background, NDVI dependence on view angle, and the effects of inaccuracies in registration and mapping of AVHRR data. These errors are thought to be relatively small and in any case, are impossible to account for without access to the component AVHRR channels 1 and 2 data.

An estimate of the magnitude of errors in the 1° by 1° NDVI data is given in Los *et al.* (1994).

Table D.2: SiB2 vegetation classification derived from the Matthews (1983, 1984) and Kuchler (1983) landcover datasets. The new SiB2 vegetation assignments (in column headed ‘Landcover type’) used at the 4° by 5° resolution are shown together with the original SiB class identifiers (1 through 12; in parentheses in column headed “Landcover type”) used at the 1° by 1° resolution. Note that as SiB2 has only one vegetation layer, there are no longer any two-layer classes (e.g., tree-grass savannah) as in SiB1. The actual number of landcover classes in SiB2 is now only nine as types 6, 7, 8, and 11 are now all assigned C_4 grassland properties. The abbreviations in the “Kuchler” and “Matthews” columns refer to the 32 classes identified in the original datasets. No one-to-one agreement between the 32 Kuchler and Matthews classes is implied. The reconstruction procedure for broadleaf evergreen vegetation types was not applied to class 9 of the original Matthews classification (in parentheses in column headed “Matthews”).

Landcover type	Kuchler	Matthews	N($1^\circ \times 1^\circ$)	Area (10^6 km 2)	SiB1	SiB2
<u>Tall vegetation</u>						
Broadleaf-evergreen trees	B S	1 2 3 (9)	1433	17.2	1	1
Broadleaf-deciduous trees	D Di DBs	5	258	2.2	2	2
Broadleaf and needleleaf trees	M ND SE	10	487	3.9	3	3
Needleleaf-evergreen trees	E Ep	4 7 8 14	2156	14.8	4	4
Needleleaf-deciduous trees	N	16 11	1117	6.1	5	5
<u>Short vegetation</u>						
C_4 groundcover (+ tall vegetation)	DG GBp GD DGp Gsp G Gp	13 15 23 24 25 26 27 28 29	4316	46.4	6	6
(grassland)					7	6
(shrubs + groundcover)	Bs Bz, Bzi Ds Dsi, Bzi DsG GDsp Ss SsG Szp	6 12			8	6
(bare soil)	b	30			11	6
Shrubs with bare soil	Bsp Dsp Dzp	17 19 21	911	9.4	9	7
Dwarf trees and shrubs	L	18 20 22	1252	5.9	10	8
Agriculture or C_3 grassland	n/a	32	2783	26.2	12	9
—Total—			22097	147.8		

D.3.2 Stratification of the NDVI Data Into Landcover Types

A landcover stratification scheme was used to account for the dependency of the relationships between NDVI, land-surface parameters and vegetation type. The landcover classification used for this study is based on the Matthews landcover and Matthews landuse datasets (Matthews 1983, 1984), and the Kuchler (1983) landcover dataset. Both the Matthews and Kuchler datasets have a resolution of 1° by 1° and distinguish 32 main landcover types (Table D.2). The original SiB1 vegetation classification of Dorman and Sellers (1989) was based on these Matthews and Kuchler datasets. The 1° by 1° SiB1 classification was used to process the satellite data, in particular to carry out the solar zenith angle correction and reconstruction procedures described in section D.4.

To accommodate the new photosynthesis-conductance model, the two vegetation layers in SiB1 were reduced to one layer in SiB2 which also involved reducing the number of vegetation classes from 12 to 9, see Table D.2 and Sellers *et al* (1996a). The nine SiB2 vegetation classes shown in Table D.2 and figure E.7 are used to assign surface parameter values.

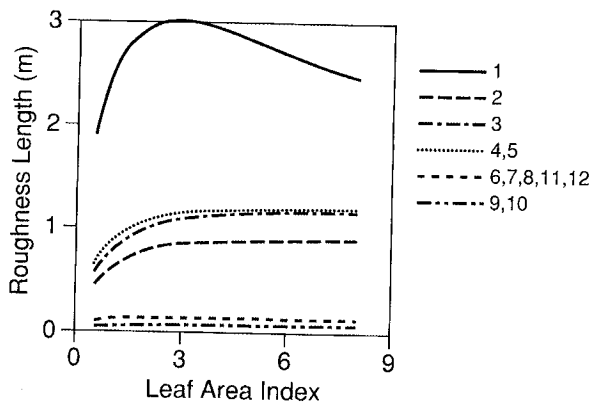


Figure D.5: Dependence of roughness length, z_0 on leaf area index as calculated by the turbulent transfer sub-model of SiB2 (from Sellers *et al.* 1989, 1996a). The numbers in the legend correspond to the numbers of the biome types in table D.2.

The basis of this final landcover dataset is the Matthews dataset. Some modifications were made to obtain closer agreement with the classes and the SiB2 biomes for which the vegetation parameters in Tables D.4 and D.5 were established:

1. For South America, the Kuchler classification replaced the Matthews classification.
2. In North America, the Kuchler landcover type 4 (needleleaf evergreen) replaced the Matthews classification.

3. In Siberia, Kuchler vegetation type 5 (needle-leaf deciduous, mainly Larix species) replaced the Matthews classification, because the Matthews classification does not make a distinction between broadleaf and needleleaf deciduous cover types.
4. In cases where a grid cell contained over 50% agricultural activity as defined in the Matthews landuse dataset, class 9 (agriculture) was assigned (Dorman and Sellers 1989).
5. The Kuchler and Matthews classes were merged to reflect either a C_3 or C_4 cover type: SiB2 class 6 (SiB1 classes 6, 7, 8, and 11) was used to represent C_4 types and SiB2 class 9 (SiB1 class 12 at the 1° by 1° scale) was used to represent C_3 types. A more realistic distribution of C_3 and C_4 types at the 1° by 1° scale will be used for future studies (Collatz *et al.* 1998).

The SiB2 landcover classification is depicted in figure E.7.

D.4 An Adjusted NDVI Product: FASIR-NDVI

To correct the global 1° by 1° NDVI dataset for the errors discussed in section D.3.1, a series of adjustments was developed, collectively referred to as FASIR, which stands for:

- Fourier wave Adjustment,
- Solar zenith angle adjustment,
- Interpolation of missing data, and
- Reconstruction of NDVI data classified as tropical evergreen broadleaf.

Prior to the Fourier wave adjustment, remnants of the terminator effect that were marked by erroneous NDVI values (Holben 1986) were eliminated by discarding all data associated with solar zenith angles larger than 85° . The FASIR procedures were first described in Sellers *et al.* (1994).

D.4.1 FASIR: Fourier Wave Adjustment of NDVI Time-Series

The adjustment of outliers in the NDVI time-series using Fourier series analysis is based on two assumptions: first, the NDVI time-series should be smoothly varying at any given point; and second, the major sources of error defined earlier can only decrease the value of the NDVI. The first assumption is used to identify short-term irregularities (≤ 2 months) in time-series that could be the result

of persistent cloud cover or atmospheric effects (water vapor, aerosols). The second assumption has been used for some time now to justify the calculation of monthly maximum value composites (Holben 1986, Tucker *et al.* 1986). There are some cases where this assumption will not hold, discussed in Los *et al.* (1994), but the effects are trivial in the context of this analysis, and generally much smaller than the effects of the atmosphere or clouds. Fourier series are a summation of sine and cosine functions given by

$$\hat{Y}_i = \sum_{j=1}^m a_j \cos((j-1)\phi_i) + b_j \sin((j-1)\phi_i), \quad (\text{D.18})$$

where a and b are Fourier coefficients, $\phi_i = 2\pi(i-1)/n$ the phase, i ranges from 1 to n , $n = 12$ is the number of points in the sequence, and $m = 3$ is the number of harmonics. The selection of $m = 3$ meets the requirement of smoothness and at the same time incorporates a large part of the seasonal variation in the NDVI. The correction is limited to less than a sequence of outliers of $n/2^{m-1}$ data points in a row, hence for $m = 3$, a sequence of 3 or more outliers will erroneously be incorporated in the adjusted series.

A robust least-squares optimizing method was used to identify and adjust outliers from the general trend in the NDVI time-series. Robust least-squares methods are designed to eliminate data that deviate strongly from a general trend, and could distort the analysis (Hoaglin *et al.* 1983). These methods are generally iterative, and in successive cycles residuals are weighted as a function of the distance to the fitted curve. A modification to the robust least-squares optimizing technique was made to take into account the assumption that errors in the NDVI result in decreased values, hence negative deviations from the fitted curve receive low weights during fitting, and positive deviations receive high weights. The general processing scheme for the Fourier-adjustment procedure is discussed here and shown schematically in figure D.4. A broad outline is as follows:

1. Values are substituted for missing data points prior to fitting the Fourier series. Because the majority of missing values occur during periods of low surface temperature and therefore low greenness values, a low NDVI value, $\text{NDVI} = 0$ is inserted (figure D.4.b).
2. The Fourier series are fitted through the data using the least-squares method (figure D.4.c),

$$(\mathbf{F}^T \cdot \mathbf{F}) \cdot \mathbf{c} = \mathbf{F}^T \cdot \mathbf{Y}, \quad (\text{D.19})$$

where the observed data are

$$\mathbf{Y} = \begin{bmatrix} Y_1 \\ \vdots \\ Y_n \end{bmatrix},$$

the Fourier constants to be solved for are

$$\mathbf{c} = \begin{bmatrix} c_1 \\ \vdots \\ c_{2m-1} \end{bmatrix},$$

and

$$\mathbf{F} = \begin{bmatrix} 1 & \cos \phi_1 & \sin \phi_1 & \cos 2\phi_1 & \sin 2\phi_1 \\ \vdots & \vdots & \vdots & \vdots & \vdots \\ 1 & \cos \phi_n & \sin \phi_n & \cos 2\phi_n & \sin 2\phi_n \end{bmatrix}$$

3. The weights, W_i , are calculated according to distance from the fitted curve (figure D.4.d),

$$W_i = \begin{cases} 0, & \text{if } U_i \leq -k; \\ (1 + \frac{(U_i+r)^4}{k})^4, & \text{if } -k < U_i < -r; \\ 1, & \text{if } -r \leq U_i \leq r; \\ (1 + \frac{(U_i-r)^2}{k})^2, & \text{if } U_i > r \end{cases} \quad (\text{D.20})$$

and

$$\begin{aligned} 0 &\leq W_{i=1} \leq 1 \\ 0 &\leq W_{i=n} \leq 1, \end{aligned}$$

with $U = (Y - \hat{Y})/M$; M is the median of the absolute difference values of Y and \hat{Y} ; $k = 2$; and $r = M/20$.

4. Fourier series are fitted through the data using (D.19), now with the weights W taken into account (figure D.4.e);

$$(\mathbf{F}_W^T \cdot \mathbf{F}_W) \cdot \mathbf{c} = \mathbf{F}_W^T \cdot \mathbf{Y}_W, \quad (\text{D.21})$$

where

$$\mathbf{Y}_W = \begin{bmatrix} W_1 Y_1 \\ \vdots \\ W_n Y_n \end{bmatrix}$$

and

$$\mathbf{F}_W = \begin{bmatrix} W_1 & & W_1 \cos 2\phi_1 & W_1 \sin 2\phi_1 \\ & \ddots & & \\ W_n & & W_n \cos 2\phi_n & W_n \sin 2\phi_n \end{bmatrix}$$

5. Each point is then checked against its original value and the values of its four nearest neighbors ($i-2$, $i-1$, i , $i+1$, $i+2$). The new value is constrained not to exceed the maximum of the 5 original values by more than 2% or to be lower than the original value (figure D.4.f). Notice that the series is cyclic, hence the neighbors to the right for $i = 12$ are $i = 1$ and $i = 2$.

6. Sequences of three or more missing values in the original data are set to missing values after adjustment of the data to avoid inclusion of suspect data (figure D.4.f). The missing values are dealt with by the interpolation and reconstruction techniques, see section D.4.3).

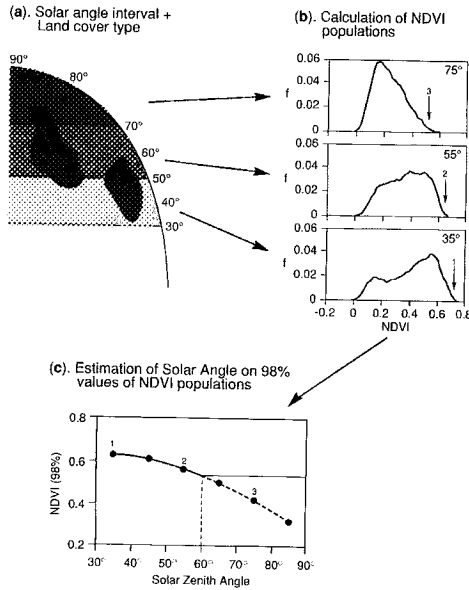


Figure D.6: Schematic of analysis procedure applied to the Fourier-adjusted data (FA) to extract the dependence of observed maximum NDVI (full green canopy) on solar zenith angle. (a) For each monthly dataset, the globe is divided into solar zenith angle classes (The situation for the Northern Hemisphere equinox is shown as an example, so that the solar zenith angle intervals correspond to latitude bands) for solar zenith angle correction. (b) The set of solar zenith angles is combined with the set of vegetation types to produce populations of Fourier-adjusted NDVI data (by solar zenith angle and vegetation type). The 98 percentile of each population is assumed to correspond to a full green canopy. (c) The 98 percentile points for each vegetation type are plotted against solar zenith angle and a simple empirical function is fitted; see equations (D.23), (D.23), and (D.24) in the text. Numbers in plot (b) correspond to numbers in plot (c).

D.4.2 FASIR: Solar Zenith Angle Correction

The NDVI varies with solar zenith angle as a result of increased atmospheric path lengths and surface BRDF effects. Studies on the BRDF properties of vegetation have for the most part been carried out over uniform cover types at the plot scale (Kimes 1983, Holben *et al.* 1986, Deering *et al.* 1992b). Little work has been done to translate the results from ground measurements to observations made at the top of the atmosphere. Lacking

a calibrated, physically-based model, a simple empirical procedure was used to account for solar zenith angle effects. First, we analyzed the entire NDVI dataset to identify a set of dense green vegetation covers for four vegetation morphologies (grass/crops, broadleaf evergreen forests, broadleaf deciduous forests, coniferous forests) which were exposed to a range of solar zenith angles ($20^\circ - 70^\circ$). Solar zenith angles were calculated assuming a nadir view angle, for the 15th day of each month, for an equatorial satellite crossing time according to Price (1991), and for orbits as described in Kidwell (1995).

The monthly NDVI data were stratified by vegetation morphology and solar zenith angle interval, see Figure D.6. These stratified datasets were then combined into annual sets; *e.g.*, data from a broadleaf evergreen type in the Southern Hemisphere collected during December were combined with data from a broadleaf evergreen type in the Northern Hemisphere collected during July having the same solar zenith angle interval. The 98 percentile values of these combined NDVI distributions were then assumed to represent conditions of green, maximum density vegetation cover. These 98% values were plotted against solar zenith angle and a curve was fitted through the data using the form of the equation derived by Singh (1988)

$$y_{98} = k_1(\theta - \pi/6)^{k_2}, \quad (D.22)$$

with $y = (NDVI_{98,0} - NDVI_\theta) / NDVI_{98,0}$, where $NDVI_{98,0}$ represents the 98 percentile of the NDVI distribution for a particular class (*i.e.*, the greenest values) as observed for a zero solar zenith angle. A similar procedure was developed to describe the effect of solar zenith angle on bare soil. It was assumed that the lowest 5% values for bare soil and shrubs (class 7), and bare soil classes (deserts in class 6) represented no-vegetation conditions. The 5% values were extracted and plotted versus solar zenith angle to obtain

$$y_5 = k_3(\theta - \pi/6)^{k_4}, \quad (D.23)$$

with $y = (NDVI_\theta - NDVI_{5,0}) / NDVI_{5,0}$. The parameters k_1 through k_4 were estimated with least-squares. Values of parameters k_1 through k_4 for each landcover class are set out in Table D.3. If no data were available for a vegetation type for solar zenith angles smaller than 30° , a small number, $NDVI = 0.008$, was added to the maximum (98 percentile) NDVI values obtained between 30° and 60° solar zenith angle to allow fitting of (D.22) and (D.23).

With the relationships between NDVI and solar zenith angle established for high and low NDVI values, the equivalent “overhead Sun” value, $NDVI_0$, for an intermediate NDVI for any solar zenith angle is calculated by

$$NDVI_0 =$$

Table D.3: Vegetation cover types with examples of the associated properties: maximum leaf area index, $L_{T,max}$, stem area index, L_s , NDVI at 5% and 98% of NDVI distributions, parameters for the solar zenith angle correction k_1 through k_4 (see equations D.22 and D.23), and the vegetation cover fraction V (equation D.28). For the solar angle correction only, a distinction is made within SiB2 biome 6 between the old SiB1 biome 6, which is treated as morphologically similar to class 1, and SiB1 biomes 7, 8, and 11, which are treated as morphologically similar to the short vegetation classes.

SiB2 biome	$L_{T,max}$	L_s	NDVI _{98%}	NDVI _{5%}	k_1	k_2	k_3	k_4	V
1	7	0.08	0.611	0.039	0.15	2.80	0.52	1.04	0.0
2	7	0.08	0.721	0.039	0.32	1.38	0.52	1.04	0.0
3	7.5	0.08	0.721	0.039	0.28	1.35	0.52	1.04	0.5
4	8	0.08	0.689	0.039	0.19	1.18	0.52	1.04	1.0
5	8	0.08	0.689	0.039	0.19	1.18	0.52	1.04	1.0
6-6	5	0.05	0.611	0.039	0.15	2.80	0.52	1.04	0.0
6-other	5	0.05	0.674	0.039	0.38	1.45	0.52	1.04	0.0
7	5	0.05	0.674	0.039	0.38	1.45	0.52	1.04	1.0
8	5	0.05	0.674	0.039	0.38	1.45	0.52	1.04	0.0
9	5	0.05	0.674	0.039	0.38	1.45	0.52	1.04	0.0

$$\frac{(\text{NDVI}_\theta - \text{NDVI}_{5,\theta})(\text{NDVI}_{98,0} - \text{NDVI}_{5,0})}{(\text{NDVI}_{98,\theta} - \text{NDVI}_{5,\theta})} + \text{NDVI}_{5,0}. \quad (\text{D.24})$$

Equation D.24 assumes a linear variation of the solar zenith angle correction to NDVI over the considered range of NDVI. The solar zenith angle correction is applied to zenith angles of up to 60° and then held constant for higher angles, see figure D.6. The effect of our solar zenith angle correction on the time-series is shown in figure D.7 for a mid-latitude area, with a similar correction for solar zenith angle developed by Singh (1988) shown for comparison; our correction is more conservative, especially for high solar zenith angles.

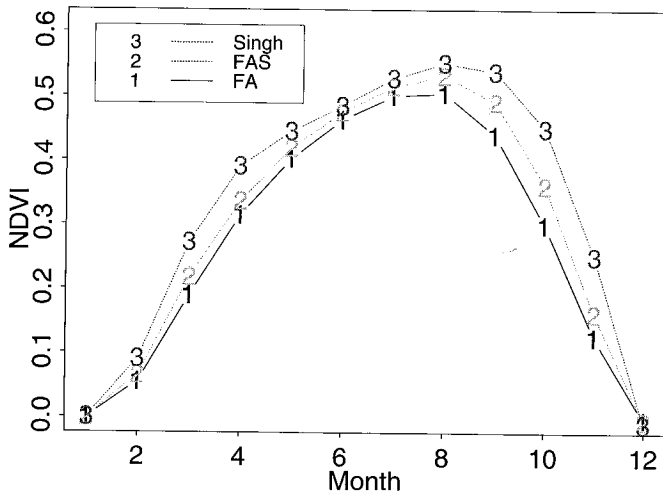


Figure D.7: Illustration of the solar zenith angle correction for a Fourier-adjusted (FA) NDVI time-series of a region in the boreal forest (50.5 N, 88.5 W). The Singh (1988) solar angle correction is shown for comparison.

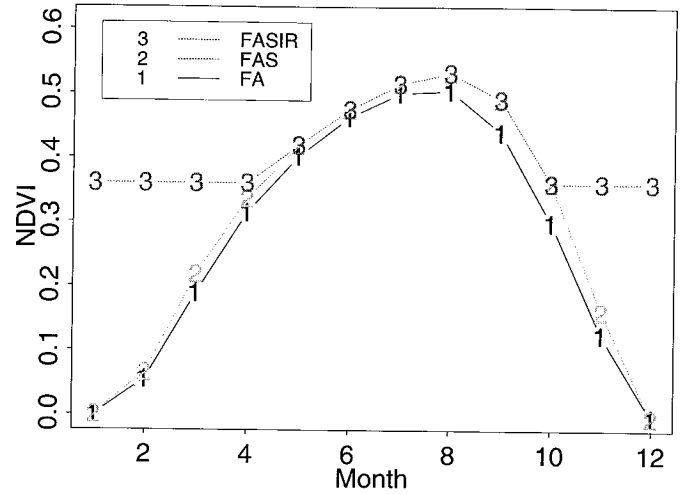


Figure D.8: Example of interpolation for the Fourier-adjusted and solar zenith angle corrected evergreen needleleaf NDVI data of figure D.7 during the Northern Hemisphere winter (50.5 N, 88.5 W).

D.4.3 FASIR: Interpolation of Missing Data

The original NDVI dataset of Los *et al.* (1994) contains data dropouts (missing values) whenever the surface radiative temperature falls below 273 K (288 K for Africa). These missing values present a significant problem at high latitudes during the Northern Hemisphere winter because, given a spurious NDVI of zero, SiB2 will calculate erroneous albedo and roughness length values. This would be particularly damaging for forest areas, because no vegetation would be assigned to an area where trees might project through the snow and influence the albedo and surface roughness. The Fourier-adjustment procedure only allows for restoration of occurrences of fewer than three missing NDVI values in a row.

APPENDIX D GENERATION OF GLOBAL BIOPHYSICAL PARAMETERS

Table D.4: Time-invariant biome-dependent land-surface properties. Most of these are used in the preprocessor (MAPPER) to calculate parameter fields for SiB2. Very few are used directly in the GCM.

Symbol	Definition	Units	1	2	3	4	5	6	7	8	9
<i>Morphological properties</i>											
z_2	Canopy-top height	m	35.0	20.0	20.0	17.0	17.0	1.0	0.5	0.6	1.0
z_1	Canopy-base height	m	1.0	11.5	10.0	8.5	8.5	0.1	0.1	0.1	0.1
z_c	Inflection height (leaf area density)	m	28.0	17.0	15.0	10.0	10.0	0.55	0.3	0.35	0.55
V	Canopy-cover fraction	—	1.0	1.0	1.0	1.0	1.0	1.0	1.0	1.0	1.0
χ_L	Leaf-angle distribution factor	—	0.1	0.25	0.125	0.01	0.01	-0.3	0.01	0.2	-0.3
l_w	Leaf width	m	0.05	0.05	0.08	0.04	0.11	0.001	0.003	0.01	0.01
l_l	Leaf length	m	0.1	0.1	0.15	0.1	0.055	0.04	0.3	0.03	0.3
D_T	Total soil depth	m	3.5	2.0	2.0	2.0	2.0	1.5	1.5	1.5	1.5
D_r	Root depth	m	1.5	1.5	1.5	1.5	1.5	1.0	1.0	1.0	1.0
<i>Optical properties</i>											
$\alpha_{V,l}$	Leaf reflectance visible, live	—	0.1	0.1	0.07	0.07	0.07	0.105	0.1	0.105	0.105
$\alpha_{V,d}$	Leaf reflectance visible, dead	—	0.16	0.16	0.16	0.16	0.16	0.36	0.16	0.36	0.36
$\alpha_{N,l}$	Leaf reflectance near IR, live	—	0.45	0.45	0.4	0.35	0.35	0.58	0.45	0.58	0.58
$\alpha_{N,d}$	Leaf reflectance near IR, dead	—	0.39	0.39	0.39	0.39	0.39	0.58	0.39	0.58	0.58
$\delta_{V,l}$	Leaf transmittance visible, live	—	0.05	0.05	0.05	0.05	0.05	0.07	0.05	0.07	0.07
$\delta_{V,d}$	Leaf transmittance visible, dead	—	0.001	0.001	0.001	0.001	0.001	0.22	0.001	0.22	0.22
$\delta_{N,l}$	Leaf transmittance near IR, live	—	0.25	0.25	0.15	0.1	0.1	0.25	0.25	0.25	0.25
$\delta_{N,d}$	Leaf transmittance near IR, dead	—	0.001	0.001	0.001	0.001	0.001	0.38	0.001	0.38	0.38
$\alpha_{s,V}$	Soil reflectance, vis	—	0.11	0.11	0.11	0.11	0.11	a	a	0.11	0.1
$\alpha_{s,N}$	Soil reflectance, NIR	—	0.225	0.225	0.225	0.225	0.225	a	a	0.225	0.15
<i>Physiological properties</i>											
V_{\max}	Maximum Rubisco capacity top leaf	$\frac{\text{mol}}{\text{m}^2\text{s}}$	$1 \cdot 10^{-4}$	$1 \cdot 10^{-4}$	$8 \cdot 10^{-5}$	$6 \cdot 10^{-5}$	$1 \cdot 10^{-4}$	$3 \cdot 10^{-5}$	$6 \cdot 10^{-5}$	$6 \cdot 10^{-5}$	$1 \cdot 10^{-4}$
ϵ	Intrinsic quantum efficiency	$\frac{\text{mol}}{\text{m}^2\text{s}}$	0.08	0.08	0.08	0.08	0.08	0.05	0.08	0.08	0.08
m	Stomatal slope fact.	—	9.0	9.0	9.0	9.0	9.0	4.0	9.0	9.0	9.0
b	Minimum stomatal conductance	$\frac{\text{mol}}{\text{m}^2\text{s}}$	0.01	0.01	0.01	0.01	0.01	0.04	0.01	0.01	0.01
β_{ce}	Photosynthesis coupling coef.	—	0.98	0.98	0.98	0.98	0.98	0.8	0.98	0.98	0.98
s_2	High T stress fact. (photosynthesis)	K	313	311	307	303	303	313	313	303	308
s_4	Low T stress fact. (photosynthesis)	K	288	283	281	278	278	288	283	278	281
ψ_c	One-half inhibition water potential	m	-200	-200	-200	-200	-200	-200	-300	-200	-200
f_d	Leaf resp. factor	—	0.015	0.015	0.015	0.015	0.015	0.025	0.015	0.015	0.015

To get around the problem of several successive missing NDVI values, a best guess is made about the “effective winter” NDVI value of evergreen needleleaf vegetation by selecting a value at the end of the growing season when the only remaining green component is assumed to be evergreen. For this study, the NDVI value of October is used to replace missing values in areas covered with needleleaf evergreen vegetation during winter. A similar procedure, with a six-month phase shift, was followed for missing winter values in the Southern Hemisphere. Figure D.8 shows an example of the interpolation of missing values.

D.4.4 FASIR: Reconstruction of NDVI Time-Series Over Tropical Regions

The Fourier-adjusted NDVI time-series over the tropics show incontrovertible evidence of serious cloud contamination, *e.g.*, low NDVI values coinciding with the climatological occurrence of rainfall and persistent cloud cover (Sellers and Schimel 1993). Our temporary solution to this problem is to raise the NDVI values for evergreen broadleaf vegetation (class 1 or tropical forest) pixels to the maximum observed for that pixel during the year. The class 9 (drought-deciduous broadleaf) of the source 32 class Matthews landcover data is excluded from class 1 for this procedure because it has highly seasonal vegetation. It is marked by parentheses in Table D.2.

Figure E.8 shows global FASIR-NDVI data for February and August 1987. When comparing the FASIR-NDVI data with the 1° by 1° NDVI dataset of Los *et al.* (1994) it can be seen that the former dataset has higher values over green areas, where we expect the largest impacts due to atmosphere effects and clouds; similar values over deserts, where we expect atmospheric perturbations to be of minor importance; and non-zero values for the boreal forest during the winter (see also figure D.13).

D.5 Calculation of FPAR, L_T , and Canopy Greenness Fraction (N) From FASIR-NDVI

The FASIR-NDVI is taken to be indicative of the amount of green material in the vegetation canopy. FPAR and the green leaf area index, $N L_T$, are calculated from the NDVI using simple relationships discussed earlier. The total leaf area index, L_T , and the canopy greenness fraction, N , are then calculated from analysis of time-series of $N L_T$.

D.5.1 Calculation of FPAR from FASIR-NDVI

The theoretical relation between FPAR and SR, (which is a simple transformation of NDVI: $SR = (1 + NDVI)/(1 -$

NDVI)), was shown to be near-linear in the work of Sellers *et al.* (1992a). Analysis of field data gathered over a range of spatial scales over a Kansas grassland confirmed the near-linearity of this relationship, at least for homogeneous vegetation covers with dark soil backgrounds, see Sellers *et al.* (1992b), Hall *et al.* (1992), and figure D.3.

Assuming linearity, the equation for SR and FPAR can be solved when two points are known. These two points were established using a simple analysis of the NDVI data populations discussed in section D.4.2 and shown in figure D.6.b. The 98% NDVI for tall vegetation types and agriculture is assumed to represent vegetation at full cover and maximum activity with a FPAR value close to 1 (here assumed to be 0.950). The 98% NDVI value of agriculture was used to represent all short vegetation types. The 5% desert value is assumed to represent no vegetation and a FPAR value of 0.001 for all landcover types. The relation between FPAR and SR is then given by

$$FPAR = \frac{(SR - SR_{i,min})(FPAR_{max} - FPAR_{min})}{(SR_{i,max} - SR_{i,min})} + FPAR_{min} \quad (D.25)$$

with

$$\begin{aligned} FPAR_{max} &= 0.950, \\ FPAR_{min} &= 0.001. \end{aligned}$$

$FPAR_{max}$, $FPAR_{min}$ are independent of vegetation type.

$$\begin{aligned} SR_{i,max} &= \text{SR value corresponding to 98\% of NDVI population } i, \\ SR_{i,min} &= \text{SR value corresponding to 5\% of NDVI population } i. \end{aligned}$$

The landcover-type dependent NDVI values for the 98% and 5% of data populations can be found in Table D.3. Note that the 5% and 98% values are the same values used for the solar zenith angle correction and are tied to the same vegetation classification.

D.5.2 Calculation of Green Leaf Area Index From FPAR

The relationship between FPAR and the green leaf area index L_g can be described by an exponential equation (Monteith and Unsworth 1990),

$$L_g = L_{g,i,max} \frac{\log(1 - FPAR)}{\log(1 - FPAR_{max})}, \quad (D.26)$$

where $L_{g,i,max}$ is the maximum green leaf area index defined for vegetation type i . The equation was derived at local levels and is found to be valid for evenly distributed vegetation at regional scales. For clustered vegetation,

e.g., coniferous trees and shrubs, the relation is different; the equation becomes (Huemmrich and Goward 1992):

$$L_g = \frac{L_{g,i,\max} \text{FPAR}}{\text{FPAR}_{\max}}. \quad (\text{D.27})$$

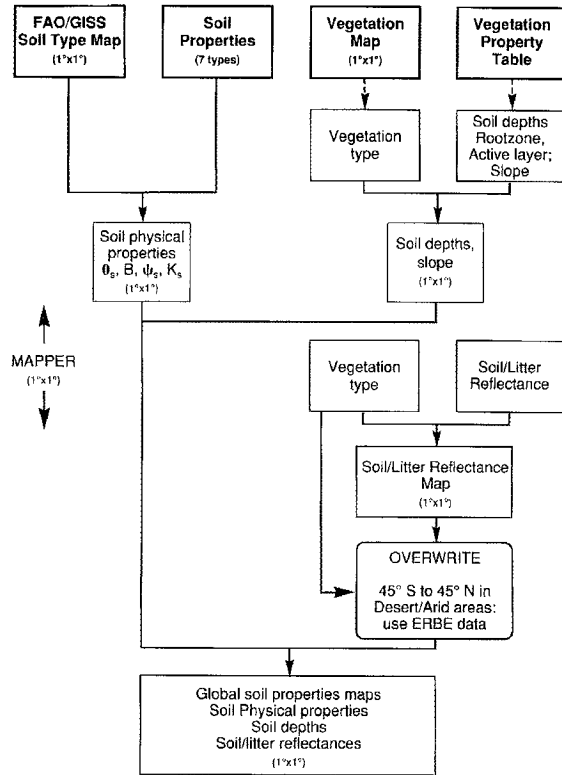


Figure D.9: Schematic of procedures used to generate global fields of soil properties for use in SiB2. All of these procedures are conducted off-line (i.e., prior to the GCM run) in the MAPPER pre-processor program.

Landcover classes 4, 5 (needleleaf deciduous and evergreen), and 7 (shrubland with bare soil) are treated as clustered vegetation types as defined in Sellers *et al.* (1992a). In cases where there is a combination of clustered and evenly distributed vegetation, L_g can be calculated by a combination of equations (D.26) and (D.27):

$$L_g = (1 - F_{cl}) L_{g,i,\max} \frac{\log(1 - \text{FPAR})}{\log(1 - \text{FPAR}_{\max})} + F_{cl} \frac{L_{g,i,\max} \text{FPAR}}{\text{FPAR}_{\max}}, \quad (\text{D.28})$$

where F_{cl} is the vegetation cover fraction. The value of F_{cl} is given in Table D.3 for each landcover class.

D.5.3 Canopy Greenness Fraction and Total Leaf Area Index

It should be emphasized that the FPAR and green leaf area index values described above refer only to the green

portions of the vegetation canopy. It is assumed that a small fraction of the vegetation canopy leaf area index consists of non-green supportive tissues, the stem area index L_s (0.076 for forests, 0.05 for grasslands and crops, Table D.3). An estimate of the proportion of dead leaves within the canopy is provided by the method originally used by Dorman and Sellers (1989) for SiB1. It is assumed that when a deciduous canopy is growing, all the attached leaves are green. After the maximum leaf area is reached, and the canopy starts to lose green leaves, the canopy greenness fraction N is determined by assuming that dead leaves remain within the canopy for one month before falling off or being eaten. Thus the canopy greenness fraction N is given by

$$N = L_g / L_T, \quad (\text{D.29})$$

with

$$\begin{aligned} L_T &= L_s + L_d + L_g, \\ L_d &= L_{g_{n-1}} - L_{g_n} \text{ and } L_d \geq 0, \\ L_g &= \text{green leaf area index, from FPAR,} \\ L_T &= \text{total leaf area index,} \\ L_s &= \text{stem area index.} \end{aligned}$$

Figure E.9 shows FPAR fields for February and August 1987 as calculated by (D.25). Figure E.10 shows L_T fields as produced by Dorman and Sellers (1989) from a survey of the ecological literature as interpreted through SiB1. Figure E.11 shows comparable L_T fields derived from the FASIR-NDVI using equations (D.28) and (D.29). Both figures E.10 and E.11 depict data at 4° by 5° resolution as used by the SiB-GCM. Note that these fields are otherwise directly related to the FPAR fields of figure E.9.

A comparison of figures E.10 and E.11 reveals large differences between the survey-based and satellite-based estimates of L_T . Overall, the original SiB1 values are unrealistically high in the boreal forests and savannah and of course show no spatial variation within natural landcover classes for any given month (Dorman and Sellers 1989). Interestingly, the SiB2 fields show higher summer L_T values for the seasonal boreal forests of eastern Siberia and the Great Plains of North America. Spatially extensive validation datasets corresponding to figures E.9, E.10, and E.11 are simply not available. For the time being, we assume that the SiB2 FASIR-NDVI fields are more accurate than equivalent SiB1 fields because of their basis in direct observation and in the theory supporting the satellite-derived product. Detailed validation of these FASIR-NDVI derived fields must rely on the results of large-scale field experiments, e.g. FIFE (Sellers and Hall 1992) and other work, and will be the subject of future papers.

Table D.5: *Biome independent morphological and physiological parameters. Most of these are used in the preprocessor (MAPPER) to calculate parameter fields for SiB2. Very few are used directly in the GCM.*

Parameter	Description	Units	Value
<i>Morphological parameters</i>			
z_s	Ground roughness length	m	0.05
G_1	Augmentation factor for momentum transfer coefficient	—	1.449
G_4	Transition height factor for momentum transfer coefficient	—	11.785
D_1	Depth of surface soil layer	m	0.02
ϕ_s	Mean topographic slope	radians	1.76
<i>Physiological parameters</i>			
S	Rubisco specificity for CO ₂ relative to O ₂	—	$2600 \cdot 0.57^{Q_t}$
K_c	Rubisco Michaelis-Menten constant for CO ₂	Pa	$30 \cdot 2.1^{Q_t}$
K_o	Rubisco inhibition constant for O ₂	Pa	$30000 \cdot 1.2^{Q_t}$
β_{ps}	Photosynthesis coupling coefficient	—	0.95
s_1	High temperature stress factor, photosynthesis	K ⁻¹	0.3
s_4	Low temperature stress factor, photosynthesis	K ⁻¹	0.2
s_5	High temperature stress factor, respiration	K ⁻¹	1.3
s_6	High temperature stress factor, respiration	K	328
Q_t	Q_{10} temperature coefficient	—	$(T_c - 298)/10$

D.6 Generating the Global Parameter Fields From the Core Datasets

The procedure for making the SiB2-GCM global surface parameter fields consists of combining digital maps (vegetation type and soil type), time-series fields (FPAR, L_T , N) and tables of soil and vegetation properties (soil physics by type, vegetation attributes by type, FPAR, L_T , N) to produce a large but self-consistent set of time-series fields. The core source datasets are:

1. Food and Agricultural Organization / Goddard Institute for Space Studies (FAO/GISS) soil type map: This map, derived by Zobler *et al.* (1986) from analysis of the FAO data base, categorizes the world's soils into seven texture classes on a 1° by 1° grid.
2. Soil properties table: The texture classes specified in (i) above were applied to a soil physical properties dataset of Clapp and Hornberger (1978) to create a table of soil physics properties (Table D.6).
3. Earth Radiation Budget Experiment (ERBE) clear sky surface albedo: The published ERBE (4° by 5°) data of Harrison *et al.* (1990) were used to "paint" in soil reflectances in desert and semi-arid areas (landcover types 7 and desert subclasses in type 6 between 45° S and 45° N; see Table D.2 and next item).
4. Landcover classes: The landcover map of Kuchler (1983) as digitized by Willmott (personal commu-

nication) and the landuse map of Matthews (1983, 1984) were used by Dorman and Sellers (1989) to produce a 1° by 1° vegetation map for SiB1. The distribution of subtropical and tropical C₄ grasslands (Collatz *et al.* 1998) and the extent of tropical forest (Nobre *et al.* 1991) have since been modified to yield a new product, SiB2MAP, see figure E.7.

5. Vegetation properties table: Each vegetation type shown on the map of item (4) above has a set of time-invariant parameters assigned to it (Table D.4, D.5). The role of each parameter is discussed in Sellers *et al.* (1996a). This table corresponds roughly to Table 1 of Sellers *et al.* (1986) and tables 2, 3, and 4 of Dorman and Sellers (1989), except that SiB2 has considerably fewer parameters; see Table 1 of Sellers *et al.* (1996a). The vegetation properties table is broken into the following categories of physical parameters: Vegetation, morphological, and soil-depth parameters are assigned in much the same way as in Sellers *et al.* (1986) and in Dorman and Sellers (1989).
 - (a) Optical properties: Leaf and soil optical properties are assigned as in Dorman and Sellers (1989). Note that the grasslands, croplands, and deserts (classes 6, 7, 8, 9) share one set of properties, broadleaf forests (classes 1 and 2) another, and needleleaf (classes 4 and 5) another. The mixed forest (class 3) properties are described by the mean of broadleaf and needleleaf properties.

APPENDIX D GENERATION OF GLOBAL BIOPHYSICAL PARAMETERS

- (b) Physiological properties: A broad distinction is made between C_3 ($\epsilon_3 = 0.08$) and C_4 ($\epsilon_4 = 0.05$) vegetation (see Tables D.4 and D.5). Other properties, notably the temperature coefficients, vary from type to type. These parameters were obtained from reviews of the ecological literature as partially documented in Collatz *et al.* (1991, 1992).
6. The FASIR-NDVI-derived time-series fields of FPAR, L_T , and N : These were described in the previous two sections.

No direct use of the landcover or soil maps is made from within the GCM as the accessed fields consist of those properties that are directly used in SiB2 and / or GCM calculations, *e.g.*, roughness length, reflectance, FPAR, etc.

Table D.6: Soil texture types, as defined in the global map by Zobler (1986), matched with soil physical parameters from Clapp and Hornberger (1978). B is soil wetness exponent, Ψ_s is soil tension at saturation (m), K_s is hydraulic conductivity at saturation (ms^{-1}), θ_s is soil porosity (volume fraction), see Table D.7.

class	B	Ψ_s	$K_s * 10^6$	θ_s	description
1	4.05	-0.04	176.0	0.40	Sand
2	4.90	-0.07	35.0	0.44	SandyLoam
3	5.39	-0.15	7.0	0.45	Loam
4	7.12	-0.12	6.3	0.42	Clay Loam → Sandy Clay Loam
5	8.52	-0.36	2.5	0.48	Clay → Clay Loam
6	4.05	-0.04	176.0	0.40	Ice
7	5.39	-0.15	7.0	0.45	Organic

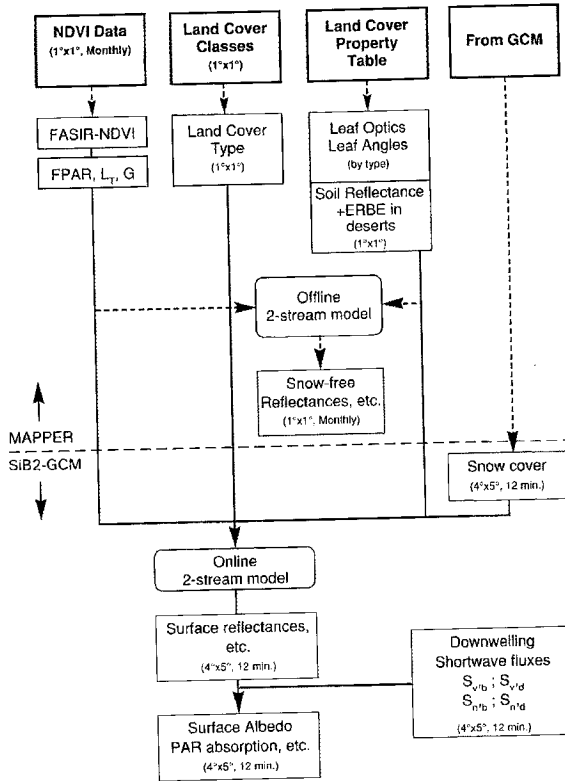


Figure D.10: Schematic of procedures used to generate global surface reflectance and other radiative transfer properties for SiB2. The horizontal dashed line divides off-line preprocessor (MAPPER) tasks from on-line (SiB2-GCM) tasks.

The next four sub-sections describe how these datasets are combined using simple relational rules or through intermediate models to produce the landsurface parameter fields for SiB2. This task is performed by a series of sub-routines in an off-line preprocessor for SiB2 called MAPPER (figures D.9, E.12, E.13, and D.10). The resulting fields, shown in Table D.7, are accessed directly by SiB2 from within the GCM. Generally speaking, the 1° by 1° cells are averaged up to 4° by 5° monthly fields and linear temporal interpolation is used to define the daily value of each parameter between the fifteenth day of each month.

D.6.1 Soil Physical Properties and Reflectance Properties

Figure D.9 outlines the procedure for producing the global soil properties fields. The soil type map (figure E.12) and soil properties table are combined to produce fields of the textural parameters: θ_s , B , K_s , and Ψ_s . The landcover map and the vegetation type-dependent properties of soil depths and slopes are combined to create global fields of these parameters. The depth of the topmost layer is always 0.02 m (D_1); the root zone layer thickness, D_2 , is defined as $D_2 = D_r - D_1$; the recharge zone layer thickness, D_3 , is defined as $D_3 = D_T - D_r$, where D_r is the root depth and D_T is the total depth of the hydrologic active soil layer. Soil or litter background reflectances (visible and NIR) are important parameters for calculating the albedo of sparsely vegetated areas. As a default, the vegetation type-dependent values of soil background reflectance are used to create global fields. In comparisons with ERBE data, this procedure was found to give unrepresentative albedo values for the deserts of Australia and the northwest United States, which were assigned soil reflectance values typical of the Sahara. To remedy this, the ERBE data of Harrison *et al.* (1990) were used to paint in the desert areas (type 7 and desert subclasses in 6 between 45° S and 45° N), see figure E.13. The amalgamated soil properties maps at 1° by 1° are accessed directly by the MAPPER preprocessor of SiB2 without intermediate reference to the soils or landcover maps.

D.6.2 Radiative Transfer Properties

The canopy greenness fields (N) from the FASIR-NDVI product are used with the landcover map and leaf optical properties to create weighted (by live / dead fraction) leaf optical properties for each grid area. These fields plus the soil / litter reflectance fields (previous section) can be used in an off-line version of the two-stream model of Sellers (1985) to calculate monthly 1° by 1° fields of snow-free reflectances. However, these are not accessed by SiB2 from within the GCM. Instead, the soil and leaf optical properties are modified in the presence of snow (Sellers *et al.* 1996a) and a vectorized version of the two-stream model called from within the GCM is used to calculate the actual time- and space-varying surface reflectances. The GCM also supplies fields of the incident shortwave radiation fluxes (visible, NIR, direct beam, and diffuse) for every timestep. These are combined with the reflectance fields and some other derived surface properties to calculate albedo values and the fractions of the incident radiation fluxes absorbed by the canopy and soil; see figure D.10 and Sellers *et al.* (1996a). Figure E.14 shows snow-free albedo fields produced by the off-line model. Examples of SiB2 albedo fields which include the effects of snow may be found in Randall *et al.* (1996).

D.7 Turbulent Transfer Properties

The first-order closure model of Sellers *et al.* (1989, 1996a) is applied off-line to the vegetation properties subset of morphological parameters ($z_2, z_c, z_1, z_s, l_w, l_l, \chi_L$, see Table D.4 and D.5 for definitions) to create look-up tables for each vegetation type of the bulk aerodynamic parameters of roughness length (z_0), zero plane displacement (d), canopy boundary layer transfer parameter (C_1), and soil-to-canopy air-space parameter (C_2). The model is cycled to produce values of these bulk parameters for each vegetation type for leaf area indices ranging from 0 to 8.0 in 0.5 increments. This look-up table (SiB2 file SIBAERO) is combined with the L_T fields and landcover map to produce 1° by 1° monthly snow-free fields of z_0, d, C_1 , and C_2 . Linear interpolation is used between the look-up table values to provide estimates of these parameters for each grid area and month. In the GCM, SiB2 accesses these snow-free fields and adjusts them for the effect of snow accumulation at every timestep. These adjusted values are then used by the non-neutral turbulent transfer sub-model of SiB2 to calculate r_a, r_b , and r_d for each timestep (figure D.11 and Sellers *et al.* 1996a). Figure E.15 shows snow-free roughness lengths calculated by SiB2.

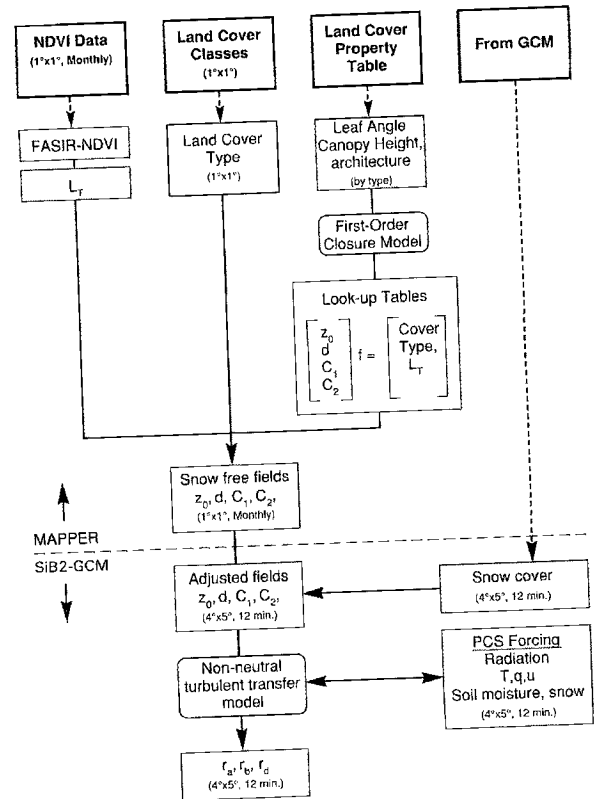


Figure D.11: Schematic of procedures used to generate global fields of turbulent transfer properties for SiB2. The horizontal dashed line divides off-line (MAPPER) tasks from on-line (SiB2-GCM) tasks. PCS stands for physical climate system, other symbols are defined in Table D.4 and D.5.

D.8 Vegetation Biophysical Parameters

Vegetation type and some associated parameters (L_{Tmax} , SR_{max} , SR_{min}) have already been used in the calculation of FPAR, L_T , and N from the FASIR-NDVI fields. An off-line calculation of mean monthly solar (radiation-weighted) angle is used in conjunction with the vegetation properties (optical and leaf angle characteristics) to calculate the 1° by 1° monthly time-mean, radiation-weighted values of the PAR extinction coefficient, \bar{k} . The canopy PAR use parameter, Π , is then calculated from $\Pi \approx FPAR/\bar{k}$ (Sellers *et al.* 1992a, 1996a). Π is combined with other surface parameters in SiB2 to calculate A_c and g_c and from these, the fluxes of radiation, heat, mass (CO_2 and H_2O), and momentum (figure D.12, Sellers *et al.* 1996a). Figure E.16 shows values of Π calculated by SiB2.

APPENDIX D GENERATION OF GLOBAL BIOPHYSICAL PARAMETERS

Table D.7: Parameter fields used by SiB2 within the GCM. In the application described in Randall et al. (1996) all of the following parameters are defined as global fields, generated from the datasets described in section D.6.

<i>Static parameters associated with landcover class</i>		
Z2	z_2	: Canopy top height (m)
Z1	z_1	: Canopy base height (m)
VCOVER	V	: Vegetation cover fraction
CHIL	χ_L	: Leaf angle distribution factor
SODEP	D_T	: Total depth of 3 soil moisture layers (m)
ROOTD	D_r	: Rooting depth (m)
TRAN	$\delta_{V,N}$: Leaf transmittance
REF	$\alpha_{V,N}$: Leaf reflectance
SOREF	$\alpha_{sV,N}$: Soil reflectance
VMAX0	$V_{max,0}$: Rubisco velocity of sun leaf ($\text{mol m}^{-2} \text{s}^{-1}$)
EFFCON	ϵ	: Quantum efficiency (mol mol^{-1})
GRADM	m	: Conductance-photosynthesis slope parameter ($\text{mol (m}^{-2} \text{s}^{-1})$)
BINTER	b	: Conductance-photosynthesis intercept
ATHETA	β_{ce}	: w_c, w_e coupling parameter
BTHETA	β_{ps}	: w_p, w_s coupling parameter
TRDA	s_5	: Slope of high temperature inhibition function (leaf respiration, K^{-1})
TRDM	s_6	: 1/2 Point of high temperature inhibition function (leaf respiration, K)
TROP	298	: Temperature coefficient in GS-A model K
PHC	Ψ_c	: 1/2 Critical leaf water potential limit (m)
RESPCP	f_d	: Respiration fraction of V_{max}
SLTI	s_3	: Slope of low temperature inhibition function (K^{-1})
HLTI	s_4	: 1/2 Point of low temperature inhibition function (K)
SHTI	s_1	: Slope of high temperature inhibition function (K^{-1})
HHTI	s_2	: 1/2 Point of high temperature inhibition function (K)
<i>Static parameters associated with soil type</i>		
BEE	B	: Soil wetness exponent
PHSAT	Ψ_s	: Soil tension at saturation (m)
SATCO	K_s	: Hydraulic conductivity at saturation (m s^{-1})
POROS	θ_s	: Soil porosity (volume fraction)
SLOPE	ϕ_s	: Mean topographic slope (rad)
<i>Time-space varying vegetation parameters from SVI</i>		
APARC	FPAR	: Canopy absorbed fraction of PAR
ZLT	L_T	: Leaf area index
GREEN	N	: Canopy greenness fraction
<i>Parameters derived from the above</i>		
Z0D	z_0	: Roughness length (m)
DD	d	: Zero plain displacement (m)
CC1	C_1	: Bulk boundary resistance coefficient ($(\text{sm}^{-1})^{1/2}$)
CC2	C_2	: Ground-to-canopy airspace resistance coefficient
GMUDMU	$G(\mu)/\mu$: Time mean leaf projection

D.9 Discussion

Significant changes were made in the SiB2 landsurface parameterization with respect to the previous SiB1 version. Most importantly, vegetation-related parameters for the land surface were directly derived from satellite observations, *i.e.*, the 1° by 1° NDVI dataset discussed by Los *et al.* (1994), rather than inferred from groundcover classes.

For the calculation of the vegetation-related parameter fields, two major issues had to be addressed: inconsistencies in the source NDVI data had to be accounted for, and relationships between the NDVI and the landsur-

face parameters had to be established. Correction of the NDVI was hampered by the absence of component channels 1 and 2 data and the lack of information on viewing geometry in the source global dataset. Adjustment procedures were developed based on some assumptions about the properties of NDVI datasets associated with different landcover classes. Some of these assumptions, such as the supposition that most of the major sources of error tend to lower the value of the NDVI, have been largely validated by research and can be used with a high level of confidence (*e.g.*, Holben 1986, Los *et al.* 1994). Other assumptions have not been as thoroughly investigated.

The NDVI data were adjusted with a series of corrections, collectively referred to as FASIR (Fourier-adjustment, solar zenith angle correction, interpolation, and reconstruction). These corrections were applied in a predefined sequence, such that corrections which are less dependent on additional non-NDVI data sources were applied first, and corrections which depended more heavily on additional data used were applied last. Specifically, the Fourier-adjustment uses only the NDVI data and does not require input from an additional data source. A land-cover classification and estimates of solar zenith angle are used for the solar zenith angle correction, however, the outcome of the calculations is not seriously affected by changes in the classification. The interpolation and reconstruction were done specifically for GCM purposes and depend heavily on the landcover classification.

Figure D.14 shows the effect of each of the FASIR corrections by latitude band for July. The average by latitude band of the NOAA-Global Vegetation Index (GVI; see Tarpley *et al.* 1994) is also shown in figure D.14 for comparison. Figure D.13 shows the effect of the FASIR corrections by biome for the entire year.

In general, the Fourier-Adjustment (FA of FASIR) provides a conservative correction to the data, *i.e.*, suspect values are adjusted relative to the position of more reliable data. The procedure may lead to some small overestimations in specific cases, *e.g.*, when a large, sudden change in the amount of vegetation occurs, such as in climates with large seasonality. For these biomes, overestimation could be a problem at the start and end of the growing season. Figures D.14 and D.13 indicate that the FA correction is most significant for biomes with a large fraction of dense, green vegetation cover, where the impacts of cloud contamination and atmospheric water vapor are expected to be strongest. The correction can also be significant for biomes with large seasonality, indicating that an overestimate during the start and end of the growing season is possible. The Fourier-adjustment has a marginal effect over deserts, and an intermediate effect for grasslands, needleleaf deciduous, shrub lands, and tundra. Because the Fourier-adjustment has the greatest effect on areas where NDVI time-series are expected to be most suspect, it is assumed that the improvements provided by this procedure outweigh its disadvantages. For photosynthesis calculations in SiB2-GCM, overestimates in the NDVI at the start and end of the growing season should have only a minor impact, because ambient temperatures are low and will counteract possible overestimates in assimilation rates.

The solar zenith angle adjustment (S of FASIR) incorporates a number of assumptions which have yet to be validated against *in situ* observations. The effect of this correction is greatest for vegetation types at high latitudes/solar zenith angles (tundra and needleleaf) and temperate regions (broadleaf deciduous, mixed needleleaf

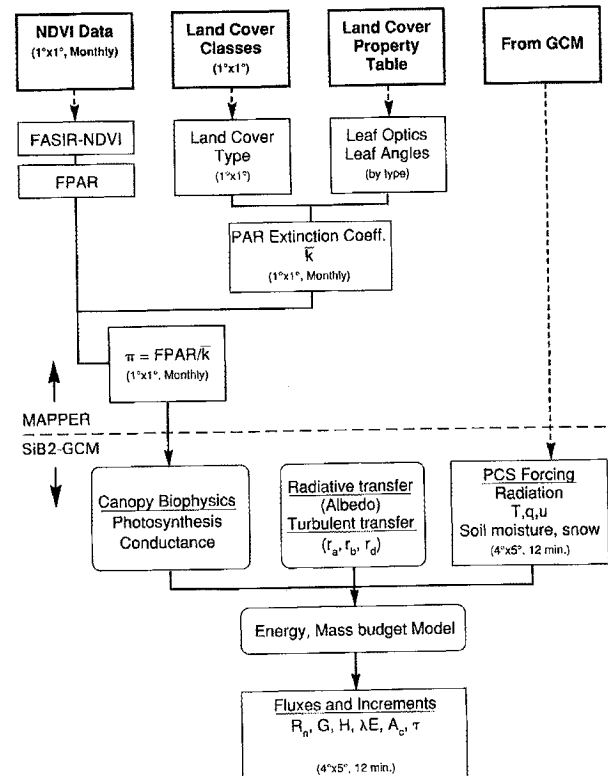


Figure D.12: Schematic of procedures used to generate global fields of surface biophysical properties for SiB2, principally the canopy PAR use parameter, Π . The horizontal dashed line divides off-line preprocessor (MAPPER) tasks from on-line (SiB2-GCM) tasks. Also shown are the connections with other SiB2 sub-models to calculate the surface fluxes and hence the increments in the SiB2 and atmospheric boundary layer prognostic variables (Sellers *et al.* 1996a).

and broadleaf deciduous; see figure D.13). The solar zenith angle correction is more conservative than the one derived from first principles by Singh (1988) (figure D.7). Although there is some uncertainty about this correction, it should improve the data overall and it is likely that any overcorrections are small. View angle effects in the source 1° by 1° NDVI data are expected to be small: the compositing technique favors selection of maximum NDVI values which should be grouped around an average view angle of 10° in the off-nadir forward-scatter direction. View angle effects in the NDVI are relatively small at and around this view direction. Remnants of view angle effects in the 1° by 1° data are confounded with and partially accounted for by the solar zenith angle correction: the correction is derived from the dataset itself, and thus should partially correct for systematic higher or lower deviations due to biases in viewing angle when confounded with solar angle. Residual variations in the NDVI as a result of unconfounded variations in view angle are not accounted for.

APPENDIX D GENERATION OF GLOBAL BIOPHYSICAL PARAMETERS

The interpolation (I in FASIR) of missing data for the Northern Hemisphere evergreen needleleaf vegetation in winter is necessary to obtain realistic estimates of several landsurface parameters in SiB2, in particular those derived from the leaf area index fields such as albedo and roughness length. Failure to provide NDVI estimates for the winter period would effectively set the leaf area index values to zero and result in near-zero roughness lengths and high albedo values. This would remove the effects of the boreal forests on the physical climate system during winter. For lack of an alternative, a best guess of the minimum NDVI value is made by selecting the value at the end of the growing season before any snowfall is likely to have occurred. Overestimation of the NDVI for these higher latitudes outside the growing season is unlikely to lead to excessive evapotranspiration or assimilation rates in SiB2, because of the low ambient temperatures.

The reconstruction (R in FASIR) of NDVI time-series for the tropical evergreen broadleaf vegetation is necessary to correct for the effect of persistent cloud cover and atmospheric water vapor effects associated with tropical forests. Low NDVI values would result in low FPAR and leaf area index estimates. A side effect of the procedure is that all seasonality in the data is eliminated and that areas incorrectly classified as evergreen broadleaf will have high NDVI values throughout the year. The procedure does provide an overall improvement in that it diminishes the number of outliers, especially in very cloudy areas. We have no real alternative approach until higher-resolution, multi-year datasets become available in which cloud-contaminated data can be identified and discarded and water vapor corrections applied.

Errors at the low end of the NDVI, *e.g.*, as a result of variations in the reflective properties of the soil background, are diminished when transforming the NDVI into SR. This is because the transformation tends to compress the lower values of the NDVI, whereas the higher values become stretched. Errors in the NDVI at the low end will therefore have little impact on SR and hence FPAR values.

Relationships between the NDVI and biophysical parameters have been established mainly from *in situ* studies involving individual plant species and high resolution radiometric data. Recently, a number of studies have focused on the extrapolation of the relationship between FPAR and SR from the plot-scale (a few meters) to intermediate spatial scales on the order of 100 m² to 15 km² (Sellers *et al.* 1992b). The results support a near-linear relationship between SR and biophysical properties, and by inference FPAR, over this range of spatial scales (Hall *et al.* 1992). The near-linear properties of the SR - FPAR relationship combined with assumptions on the occurrence of minimum and maximum vegetation activity has encouraged us to calculate global fields of FPAR; total leaf area index, L_T ; and canopy greenness fraction,

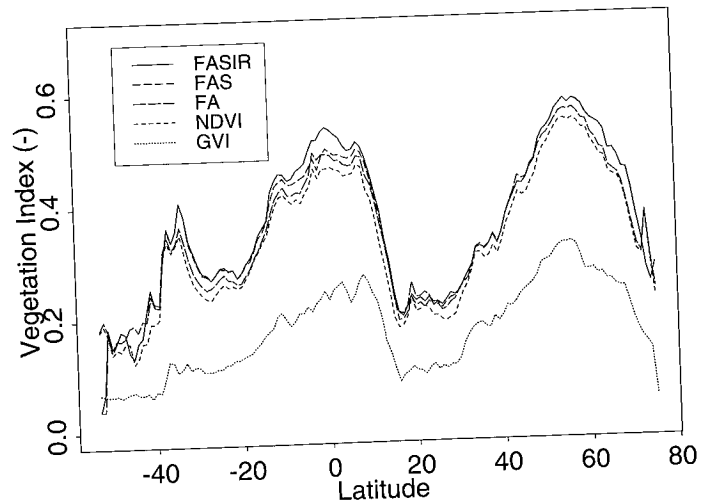


Figure D.13: Effect of Fourier-wave adjustment, Solar zenith angle correction, Interpolation, and Reconstruction on the global NDVI averaged by latitude for the month of July 1987. The Global Vegetation Index (GVI) product (Tarpley *et al.* 1984) is shown for comparison (lowest curve). Averages for each of the products were calculated with missing values set to zero; see text for discussion.

N , from the satellite data. It is doubtful that the near-linearity of the FPAR-SR relationship holds for all land-cover classes and soil backgrounds; it has been suggested that for some cases, *e.g.*, bright soil backgrounds, the relation between FPAR and NDVI may be more linear than the relationship between FPAR and SR (Choudhury 1987, Goward and Huemmrich 1992). Because of the dark soil background assumption, we expect our FPAR estimates to be less reliable for intermediate NDVI values over areas with a bright soil background. For high and low NDVI values we still expect our estimates to be reasonable since the effect of non-linearities should be small close to the end points to which the SR-FPAR relationship was tied. Because FPAR is critical to calculations of vegetation activity, further research is needed to establish a more accurate relationship between FPAR and vegetation indices.

We have more confidence in the estimates of FPAR than L_T . However, we have seen that the essential surface properties are near-linearly related to FPAR rather than L_T , which is used only as an intermediate variable. Therefore our uncertainties in albedo, surface roughness, canopy conductance, and photosynthesis seem to scale directly with the errors in the NDVI (SR) and FPAR rather than with the errors in the estimation of L_T .

To obtain improved parameter fields over the ones described in this paper, a number of items need to be addressed. In the first place, the source satellite dataset could be improved by incorporating individual channel data that are corrected for scattering by atmospheric

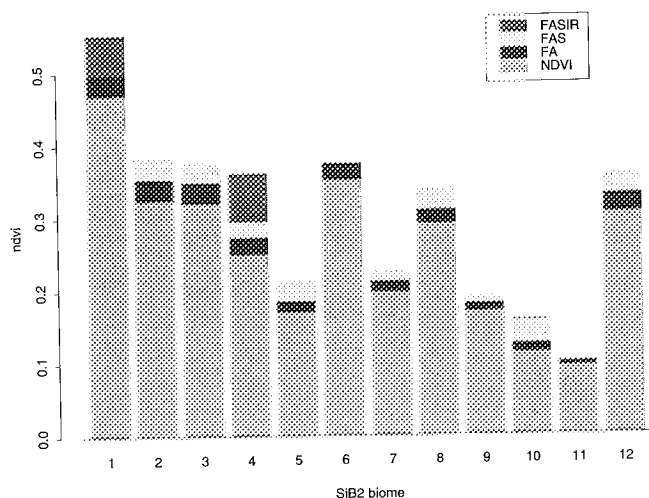


Figure D.14: Average NDVI values by biome for the entire year of 1987 with the subsequent FASIR corrections (Fourier-wave adjustment, Solar zenith angle correction, Interpolation, and Reconstruction) shown for comparison. Missing values were set to zero prior to averaging. See text for discussion.

aerosols and molecules, absorption by atmospheric water vapor and ozone, cloud contamination, and off-nadir viewing and solar zenith angle geometry. Studies are underway to obtain an improved spectral vegetation dataset in which many of these problems are addressed. Further improvements could be expected from future remote sensing devices, such as the MODerate resolution Imaging Spectroradiometer (MODIS), that are designed specifically to address vegetation monitoring. Second, procedures for deriving biophysical parameter fields from the NDVI could also be improved. The results from algorithm development studies reported in Sellers and Hall (1992) could be taken further, particularly by addressing variations due to different vegetation types and soil backgrounds. A third area in which improvements can be made is in the landcover classification used for stratifying vegetation types. A classification based on satellite-derived biophysical parameters, *e.g.*, surface reflectance and FPAR, rather than on a set of inconsistently specified landcover classes, is greatly preferred.

Although the FASIR-NDVI and the relationships used to derive global fields of FPAR and L_T have serious limitations, much was gained over previous attempts to specify global surface parameter fields, *e.g.* Dorman and Sellers (1989). Most important, it has become possible to address realistically the spatial and temporal variability of landsurface parameters within a climate model.

The NOAA - global vegetation index (GVI) dataset (Tarpley *et al.* 1984) was considered as an alternative data source for this work but was thought to be less suitable for our purposes, despite the availability of component channel data retained with the GVI composites. As

described by Gutman (1991), the GVI data tend to be lower than the NDVI because (1) they are not normalized for incoming solar radiation in the respective bands, and (2) because the GVI compositing technique has a strong bias to selecting data from the extreme backscatter direction ($40^\circ - 50^\circ$ off-nadir). Figure D.14 shows a comparison of the global zonal averages of the GVI, NDVI, and FASIR-NDVI data for the month of July 1987. The GVI values are lower overall because the component channel values were not normalized for the solar flux in the visible and near-infrared bands. In addition the GVI and NDVI differ significantly at latitudes below 20° South, although to a lesser extent an overall discrepancy in signature can be found in the entire Southern Hemisphere. The difference in signal here is most likely explained by the different viewing angles associated with the NDVI and GVI, *i.e.*, near forward-scatter and extreme backscatter, respectively. This bias becomes more significant for large solar zenith angles, up to a point where the entire signal from the land surface is lost, both in the GVI as well as in its concurrent channels 1 and 2 data. Goward *et al.* (1994) therefore assign GVI data from solar zenith angles larger than 70° as spurious; however, it is likely that GVI data collected at much smaller solar zenith angles are affected as well.

D.10 Conclusion

The revised Simple Biosphere model, SiB2, of Sellers *et al.* (1996a) has a far smaller core set of parameters than the original SiB1 of Sellers *et al.* (1986). This is due to some simplification (reduction to a single layer of vegetation, incorporation of a much simpler soil moisture stress model) and the use of a more realistic and universal formulation to describe canopy conductance and photosynthesis. The latter was not done in SiB1 at all. In SiB1, the phenologically varying vegetation properties (L_T and N) were prescribed by vegetation type and month; in the case of croplands, a complex procedure was used to describe their seasonal and latitudinal variations (Dorman and Sellers 1989). In SiB2 all of the time and space variations in L_T , N , and FPAR are calculated from the satellite dataset. In summary, the SiB2 dataset has the following benefits over that of SiB1 as written up in Dorman and Sellers (1989):

1. Realistic time-space variations in FPAR, L_T , and N ,
2. Realistic time-space variations in products derived from FPAR, L_T , and N , principally the surface reflectances, surface turbulent transfer characteristics (z_0 , d , C_1 , C_2), and surface biophysical parameters,
3. Improved soil reflectance fields, partially derived from ERBE data. This yields better albedo fields

in the world's desert and arid zones,

4. Improved soil physical properties fields: Global soil texture information is used rather than assigning soil properties by landcover type,
5. Direct use of parameter fields: In SiB1, parameters were accessed through vegetation type. In SiB2, parameter fields are generated off-line and accessed directly from within the GCM. This will allow averaging of properties within the GCM grids from the original 1° by 1° data in future work, and leaves the way open for using finer resolution datasets if necessary.

Finally, a note on the effects of uncertainties in the FASIR-NDVI data on the accuracy of the parameter fields used in SiB2. It was shown in previous sections that errors or uncertainties in the NDVI will translate approximately linearly into errors or uncertainties in FPAR, reflectance, conductance, photosynthesis, and thus evapotranspiration. However, the errors in leaf area index, L_T , are likely to be proportionally far worse due to the generally exponential dependence of green leaf area index (NL_T) on FPAR. In a sense, this does not matter too much, as canopy reflectance, transpiration, and photosynthesis appear to be near-linearly related to FPAR and the Simple Ratio vegetation index (a transform of the NDVI), and only secondarily and non-linearly on leaf area index.

Acknowledgments

This work was funded by a NASA Earth Observing System-Interdisciplinary Science (EOS-IDS) grant (Biosphere-Atmosphere Interactions project). I thank David Strauss of the Center for Ocean-Land Atmosphere studies (COLA), Dept. of Meteorology of the University of Maryland for his advice on Fourier series. I thank the members of the GIMMS group at NASA Goddard Space Flight Center for their assistance in data processing.

Appendix E

Color Figures

E.1 Figures With Chapter 2

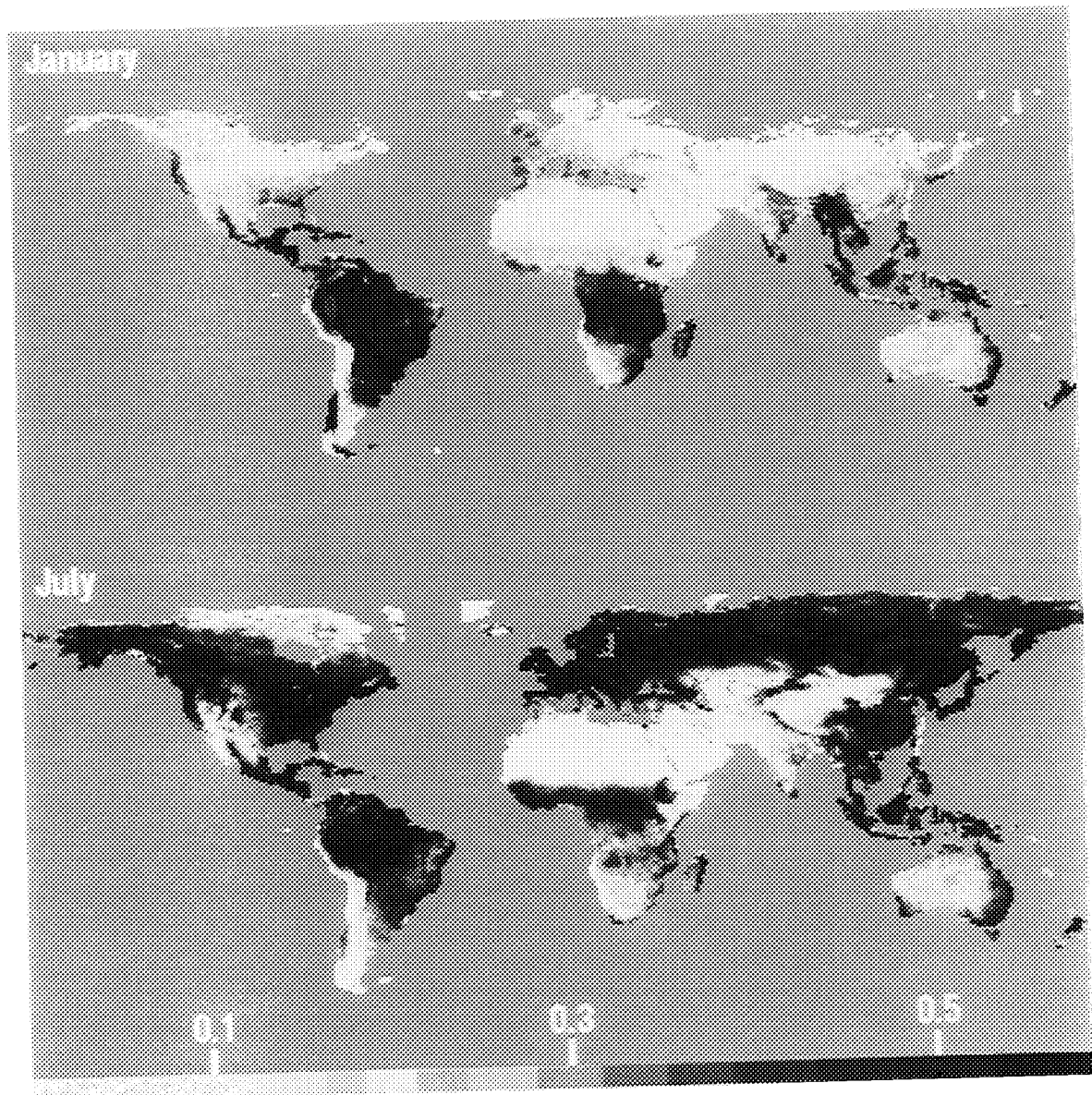


Figure E.1: Global 1° by 1° monthly mean normalized difference vegetation index (NDVI) for 1982–1990. Blue indicates missing data, for the most part occurring in the oceans and snow-covered areas in the Northern Hemisphere during winter. (top) Global 1° by 1° mean for January. (bottom) Global 1° by 1° mean for July.

E.2 Figures With Chapter 9

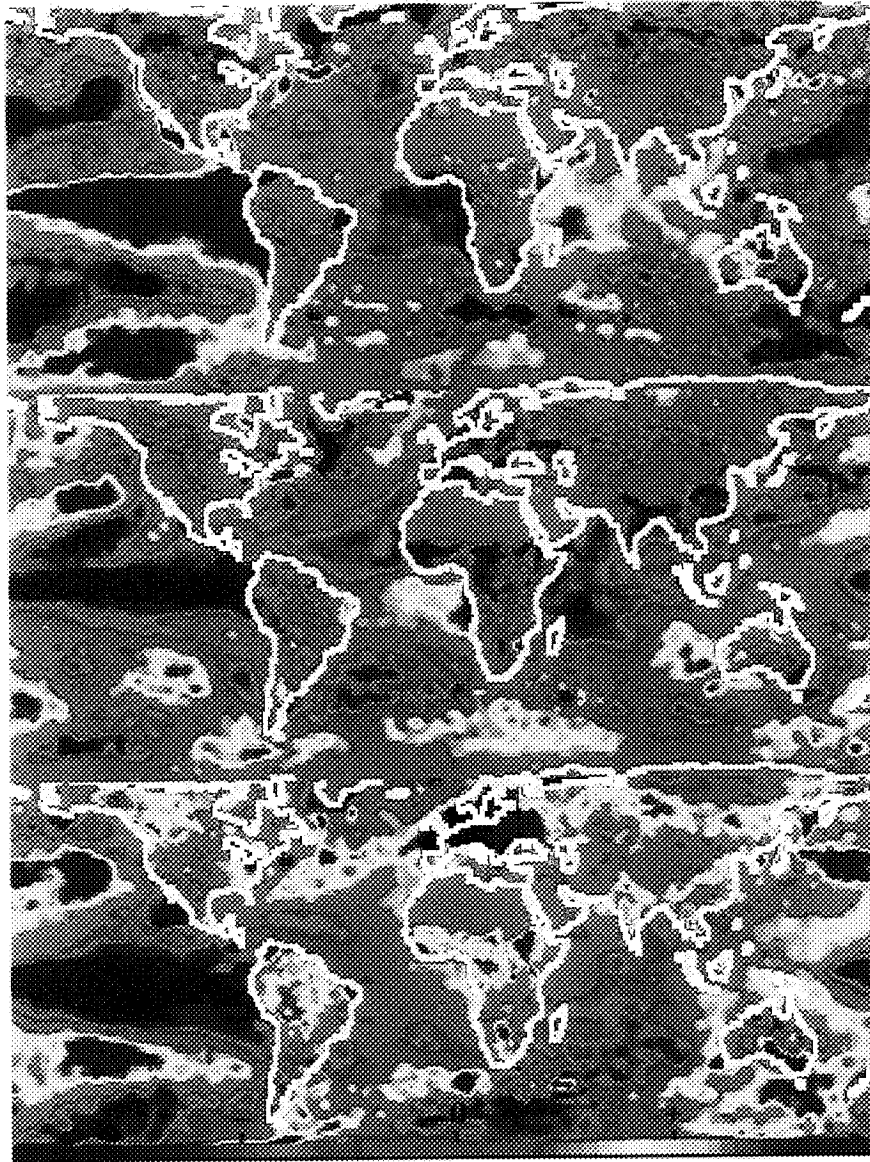


Figure E.2: *Pixel-by-pixel covariances of NDVI and sea surface temperature (SST) anomalies with the synthetic factor loadings of figures 9.2.a and 9.2.c reveal patterns of SST warming and cooling contiguous with land areas of increased and decreased NDVI. NDVI and SST data were scaled by the standard deviation of their respective total populations. Note that for this figure the entire dataset is used. A spatial 3 by 3 median filter was used to suppress noise. (see figure 9.3 for a more detailed description).*

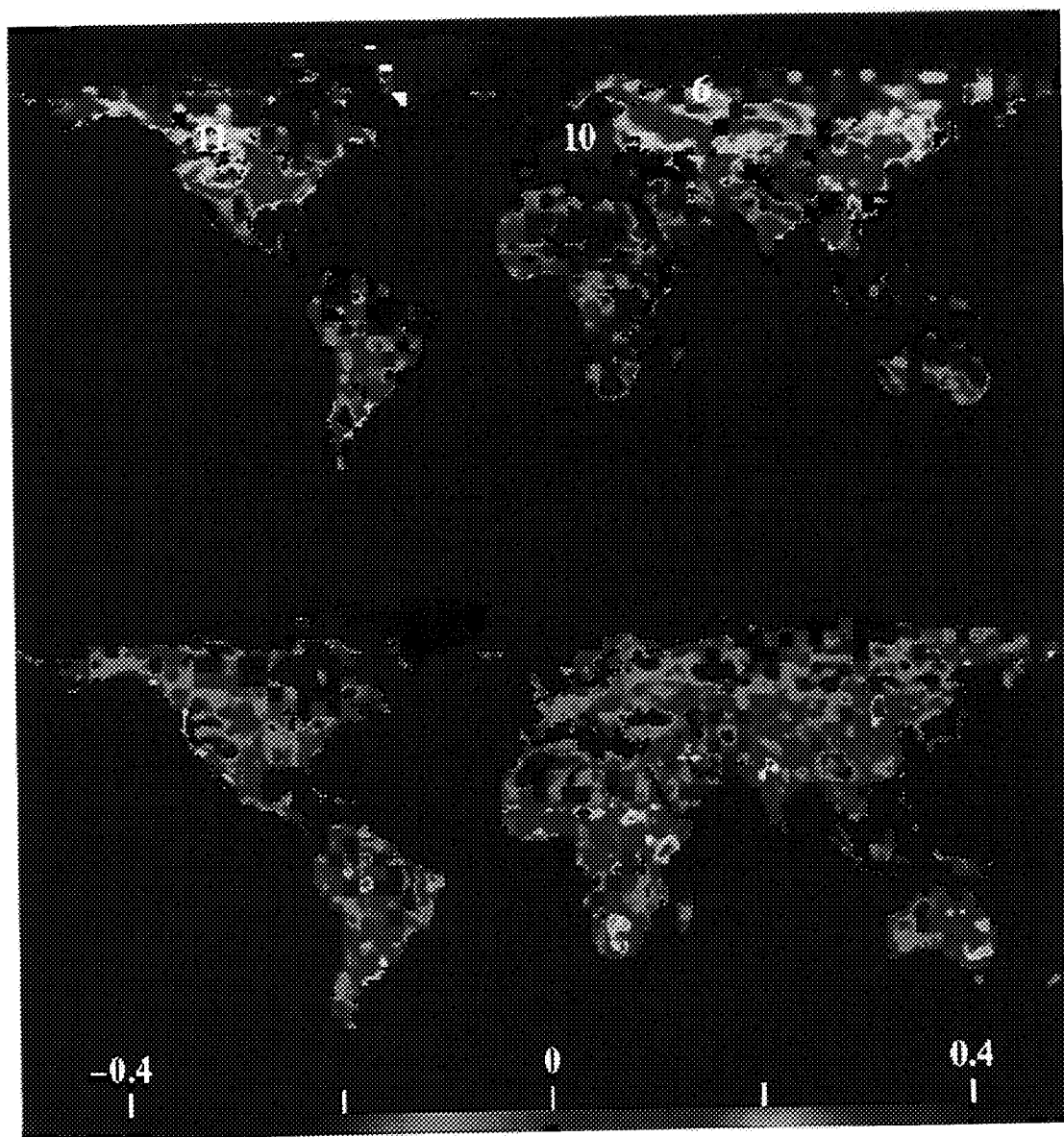


Figure E.3: (a) pixel-by-pixel correlations between NDVI anomaly, and landsurface air temperature anomaly time-series. (b) pixel-by-pixel correlations between NDVI and rainfall anomaly time-series. Air temperature and precipitation data were extrapolated to the spatial resolution of the 1° by 1° NDVI data by using one value for each 5° by 5° window. A 3 by 3 median filter was used to suppress noise. Numbers refer to regions investigated in more detail in figure 9.6.

E.3 Figures With Appendix C

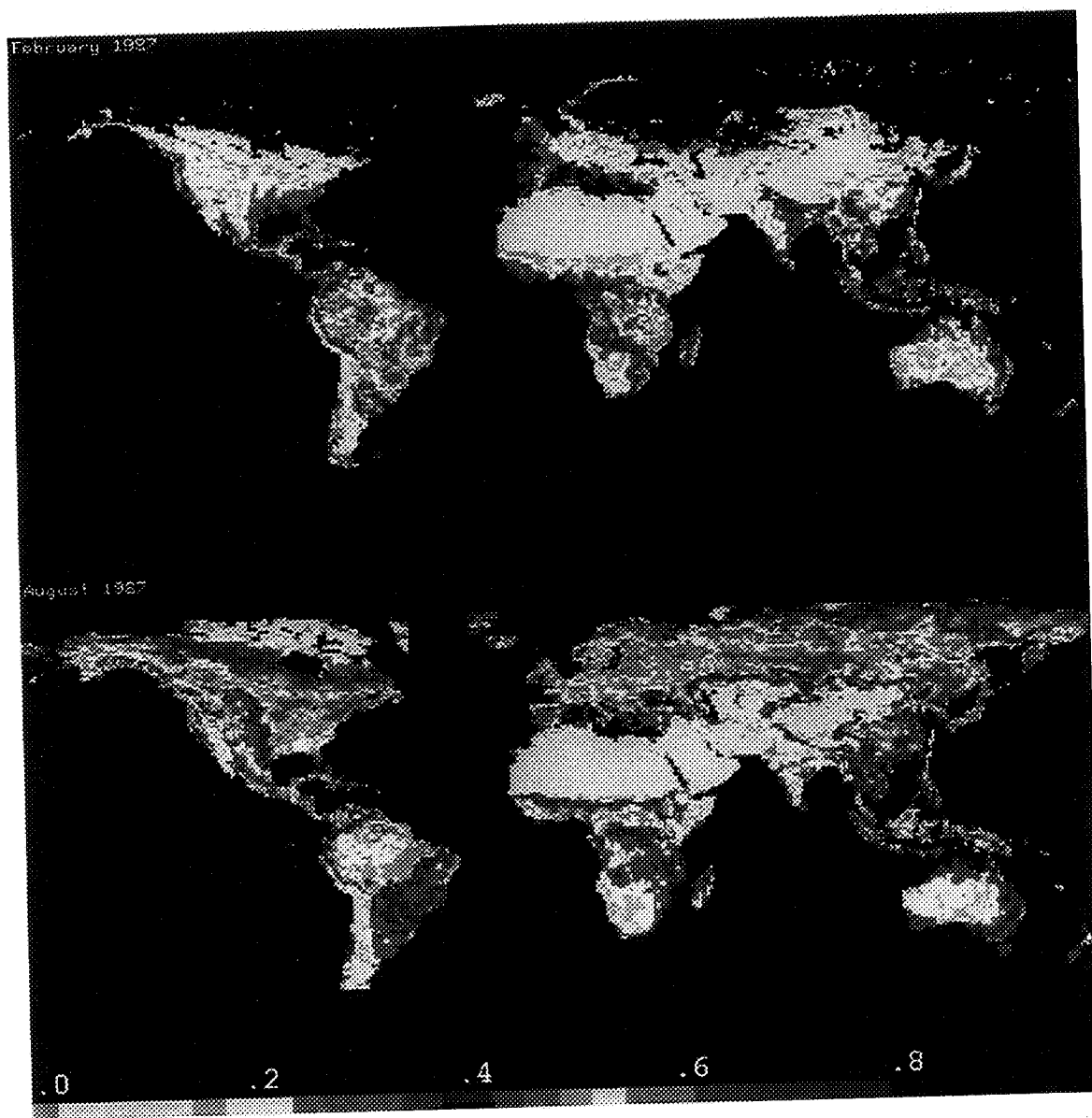


Figure E.4: Normalized difference vegetation index images for February and August 1987.

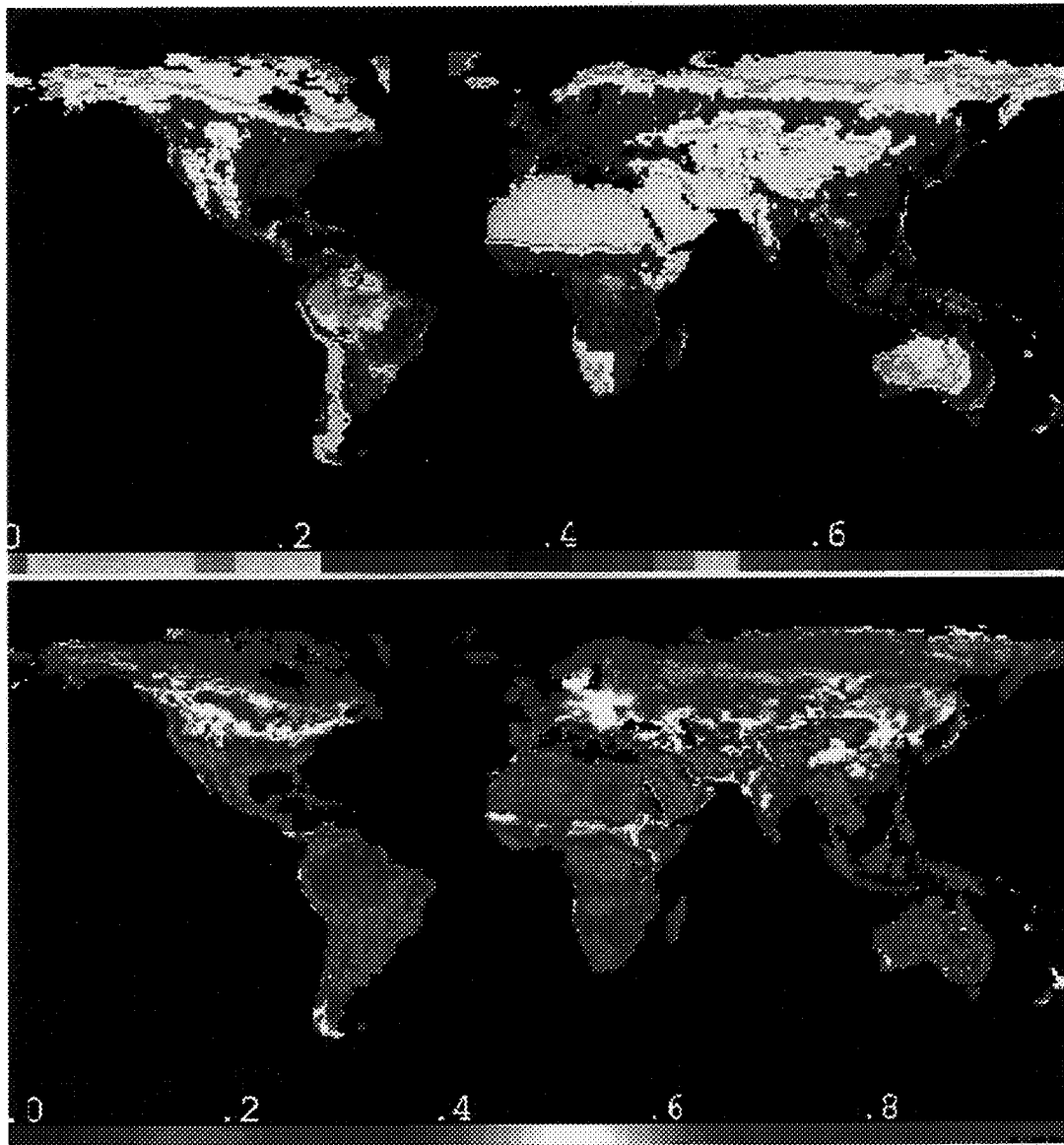


Figure E.5: (a) Average of monthly normalized difference vegetation index datasets for the entire period 1982–1990. Missing values are set to zero. (b) Coefficient of variation for the same period.

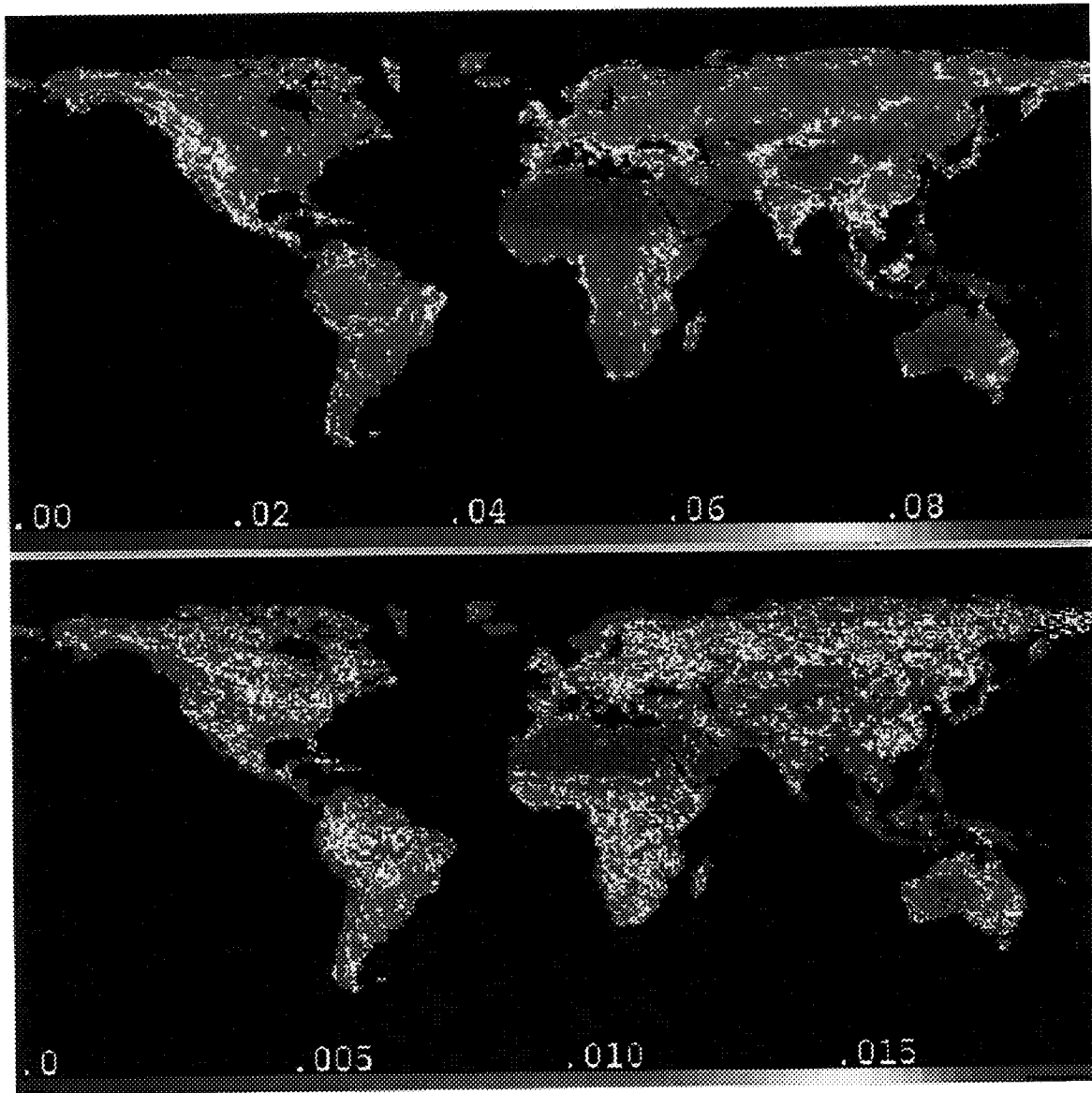


Figure E.6: (a) Average spatial standard deviation and (b) temporal standard deviation of the spatial standard deviation over the landsurface in 1° by 1° cells from each month of 1987. The temporal standard deviation of the spatial standard deviation indicates how spatial variation changes over time, (*e.g.*, from heterogeneous during the wet season to homogeneous during the dry season).

E.4 Figures With Appendix D

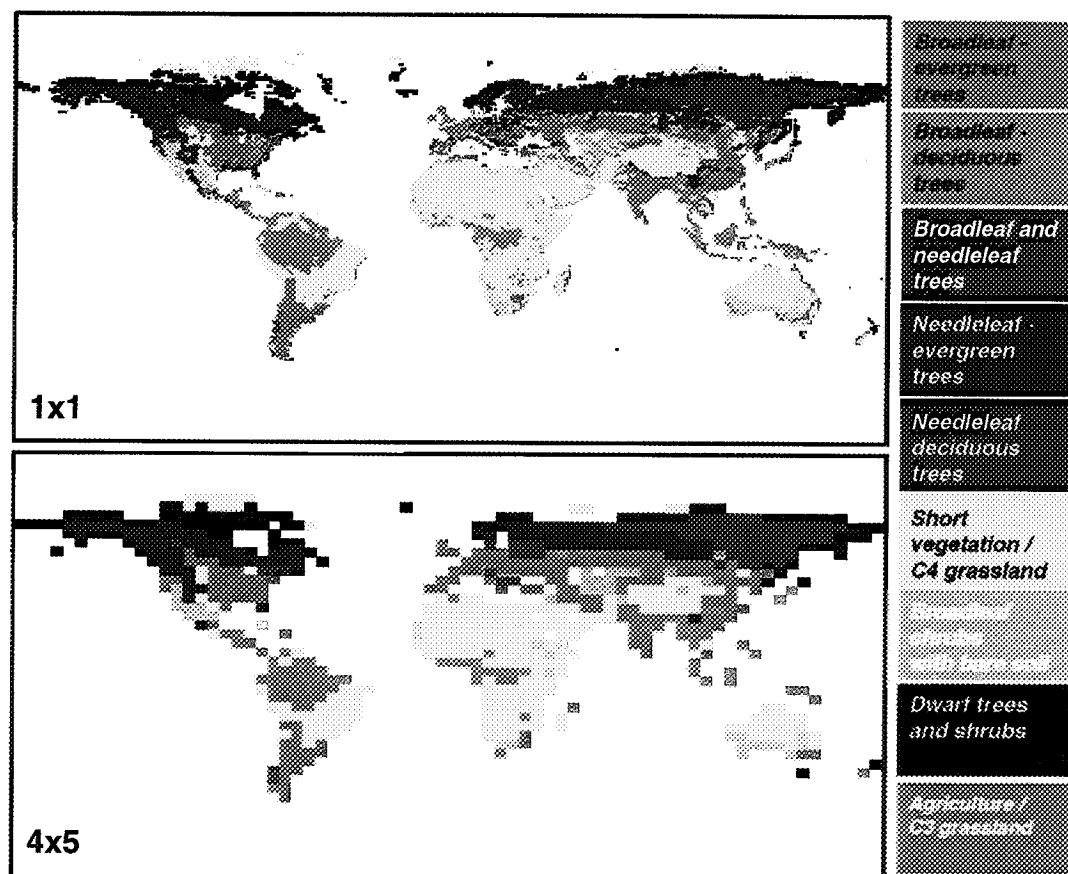


Figure E.7: *SiB2* global landcover classification derived from the Matthews (1983) and Kuchler (1983) 1° by 1° landcover datasets and the Matthews landuse dataset (Matthews 1984), with modifications from Collatz et al. 1998). Data are also shown at 4° by 5° resolution as used by the *SiB2-GCM* in Randall et al. (1996).

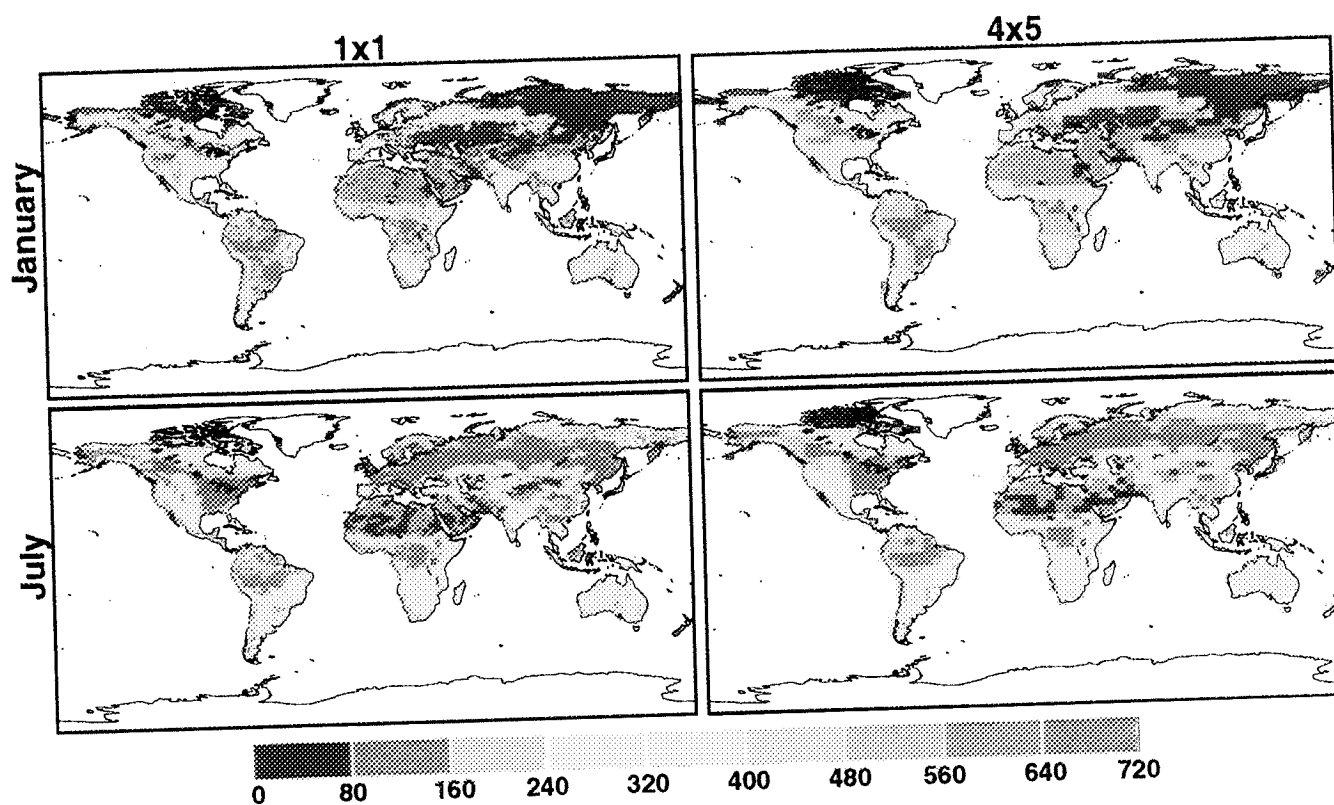


Figure E.8: *FASIR-NDVI* (values are multiplied with 1000) for (a) January 1987 and (b) July 1987. Comparison with the *NDVI* data published by Los et al. (1994) shows overall increased values for green biome types during their growing season (figure D.13). For the winter, *NDVI* data from evergreen needleleaf biome types are restored by the Interpolation (*I* of *FASIR*) procedure.

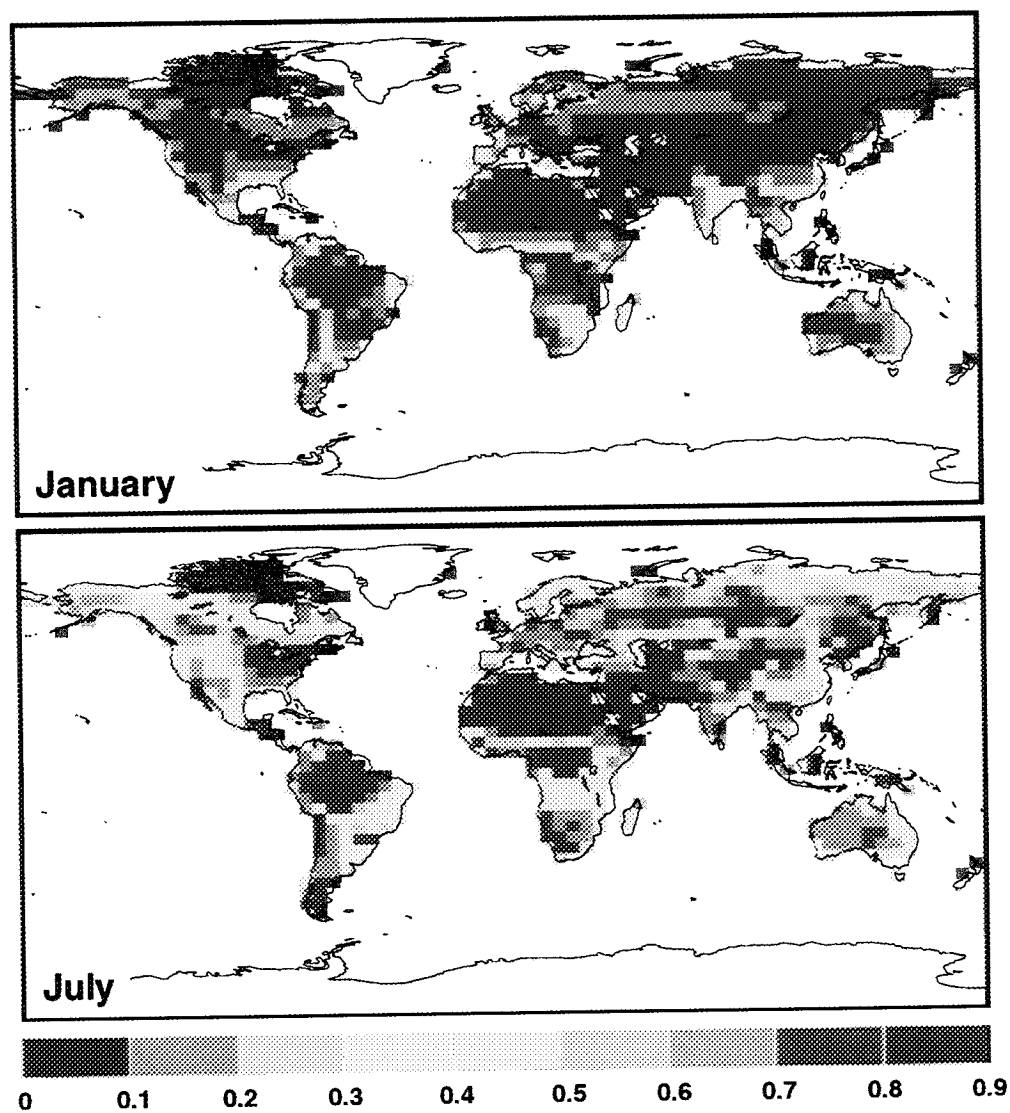


Figure E.9: Global fields of FPAR for January and July 1987 calculated from the FASIR-NDVI data (see text for discussion).

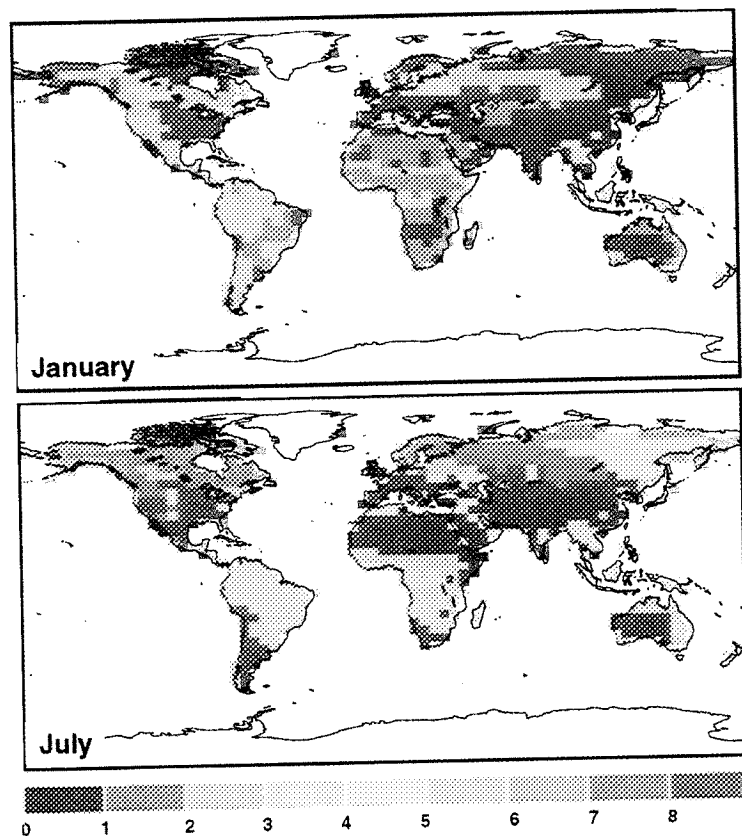


Figure E.10: Global fields of total leaf area index (L_T) for January and July as specified for the original SiB1 model of Sellers et al. (1986). The L_T fields were assigned as monthly-varying values for each vegetation type (with a six-month phase change for the Southern Hemisphere), see Dorman and Sellers (1989) for details.

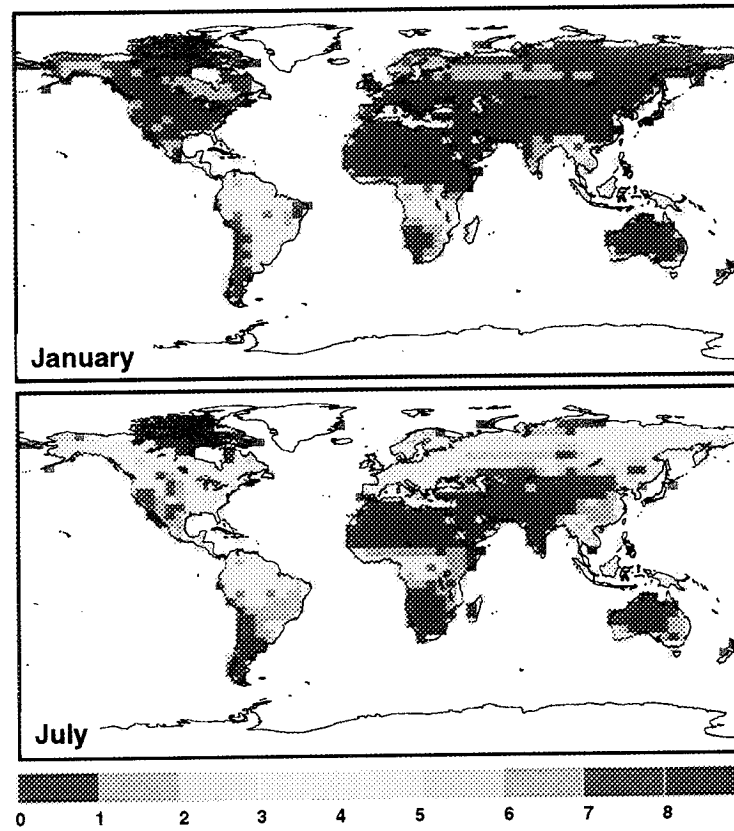


Figure E.11: Global fields of leaf area index (L_T) for January and July 1987 as calculated from the FASIR-NDVI dataset (equations (D.25), (D.28), and (D.29), see text for discussion).

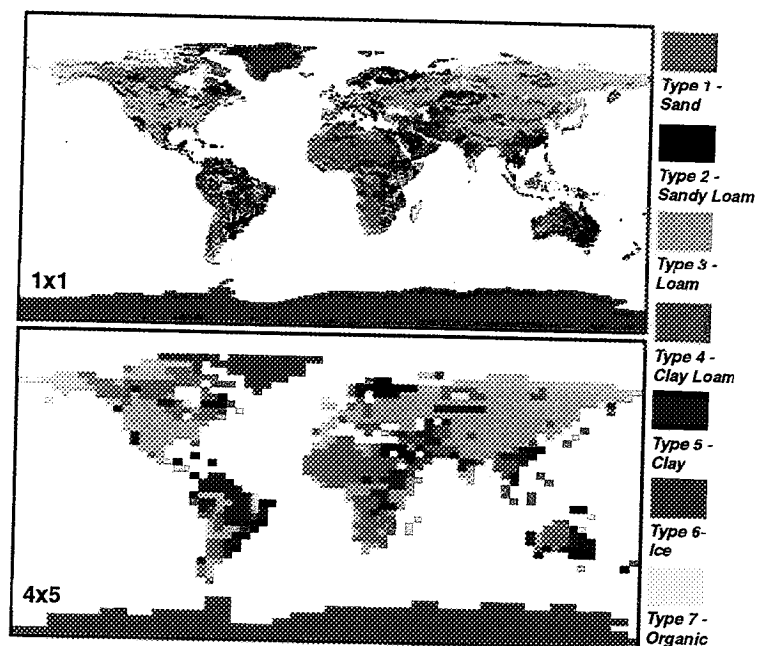


Figure E.12: Soil texture map adapted from Zobler et al. (1986) who processed Food and Agricultural Organization data to create their map. The classes and associated parameters are defined in Table D.6.

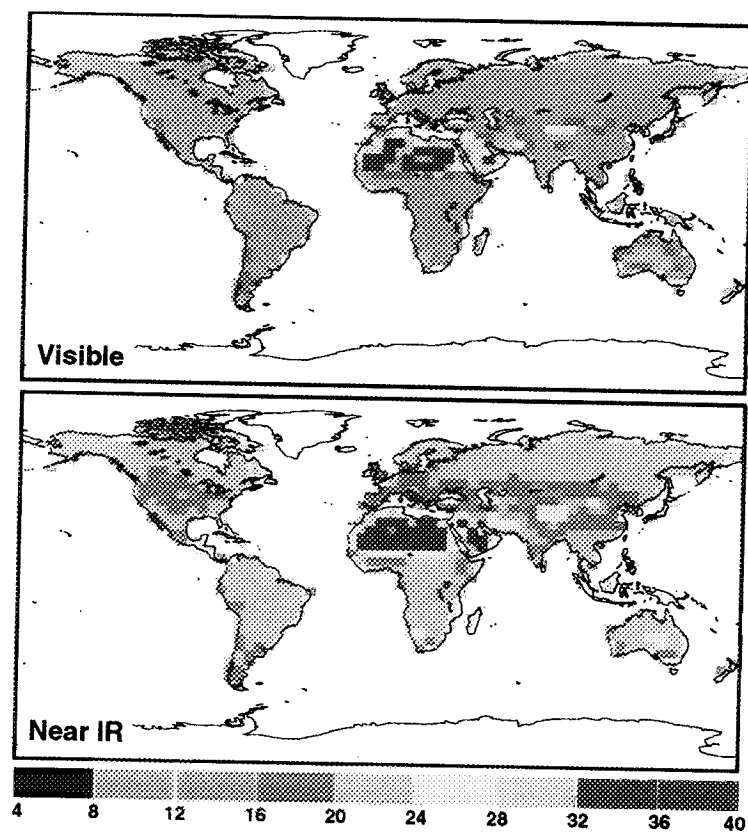


Figure E.13: *Snow-free background soil/ground reflectance values in percentages derived from vegetation classification information and ERBE data, see text.*

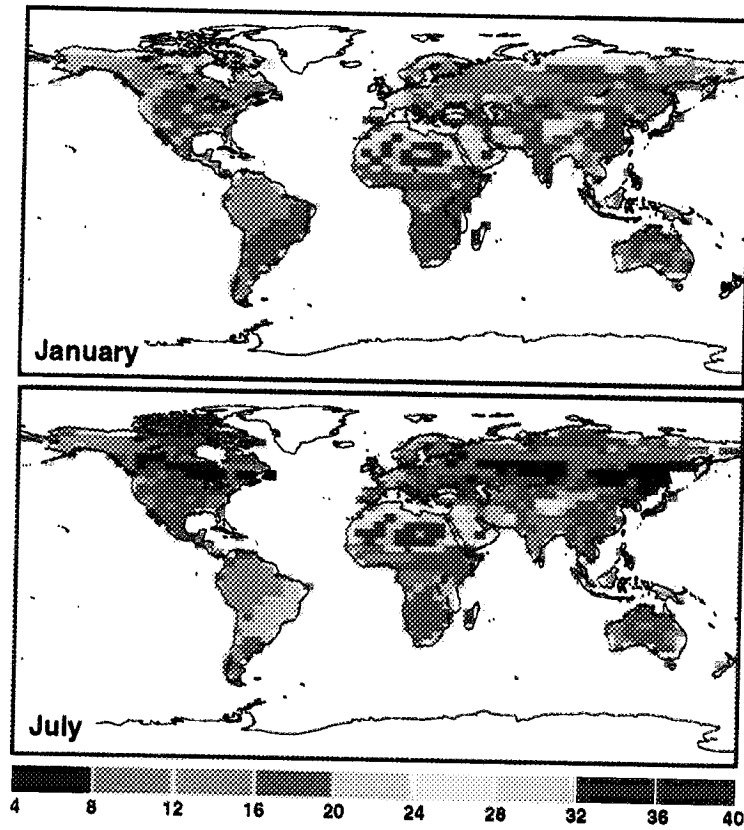


Figure E.14: (a) January and (b) July snow-free clear-sky albedo in percentages produced by an off-line SiB2 calculation following the procedure shown in figure E.13.

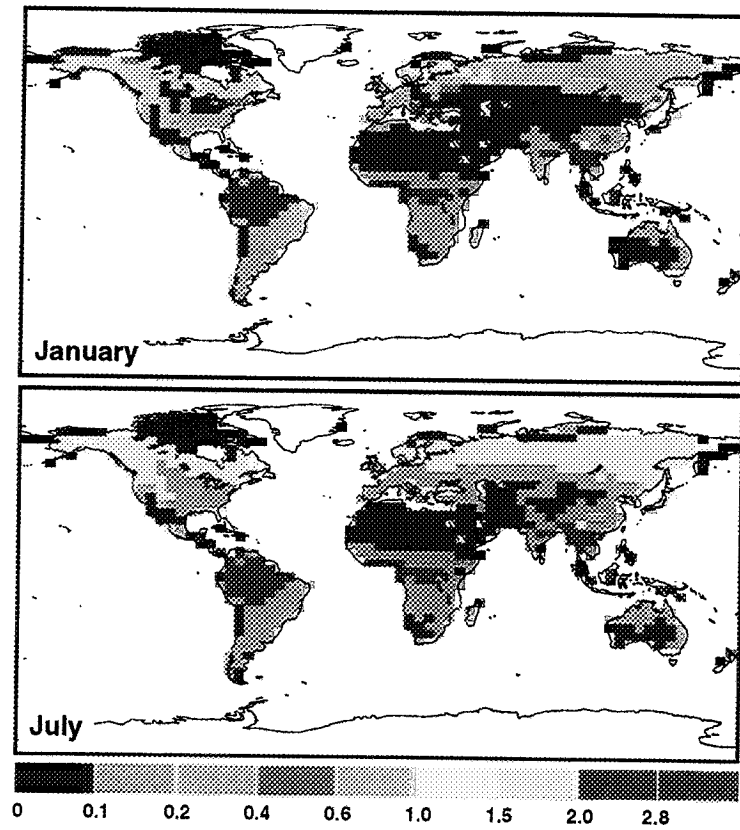


Figure E.15: (a) January and (b) July snow-free roughness lengths (m) produced by SiB2.

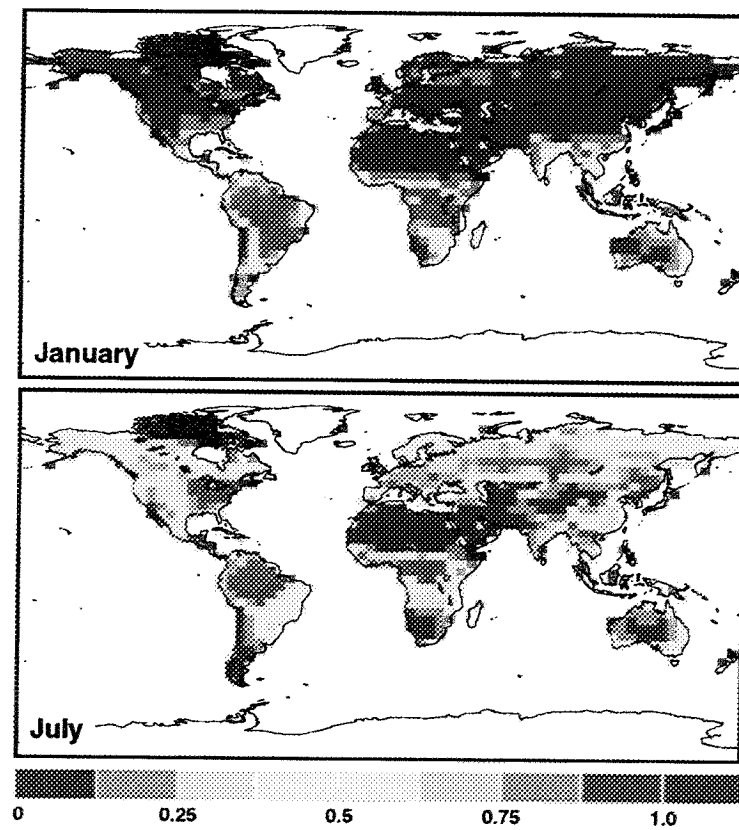


Figure E.16: (a) January and (b) July fields of the canopy PAR use parameter Π produced by SiB2.